Metallic Nanopores for Single Molecule Biosensing

by

Mariam Ayub

Thesis submitted for the degree of

Doctor of Philosophy

of Imperial College

and for the Diploma of Imperial College

May 2011

Department of Chemistry

Imperial College of Science Technology and Medicine

Exhibition Road, London SW7 2AZ

I declare that the work presented within this thesis is my own and that where contributions have been made, these have been clearly acknowledged and referenced.

Mariam Ayub

Abstract

This thesis describes a novel approach to the fabrication and characterisation of metallic nanopores and their application for the detection of single DNA molecules. Metallic nanopores with apparent diameters below 20 nm are produced using electrochemical deposition and real-time ionic current feedback. Beginning with large nanopores (diameter 100-200 nm) milled into gold silicon nitride membranes using a focused ion beam, platinum metal is electrodeposited onto the gold surface, thus reducing the effective pore diameter. By simultaneously observing the ion current feedback, the shrinking of the nanopore can be monitored and terminated at any pre-defined value of the pore conductance in a precisely controlled and reproducible way.

The ion transport properties of the metallic nanopore system are investigated by characterising the pore conductance at varying potentials across the nanopore and concentrations of electrolyte. The results are compared to conventional bare silicon nitride nanopore systems. Chemical modification at the nanopore surface is also studied using thiolisation to reduce the capacitive charging effects observed with metallic nanopores. Further to this, impedance measurements are carried out to study the resistive behaviour exhibited in these systems. An equivalent circuit model is proposed to validate the results obtained from the experimental studies.

To evaluate the suitability of these nanopores for applications in single-molecule biosensing, translocation experiments using λ-DNA are performed. DNA molecules are electrokinetically driven through the nanopore under an applied electric field, hence as the DNA translocates through the pore, current blockade events are detected. Each event is the result of a single molecular interaction of DNA with the nanopore and is characterised by its dwell time and amplitude. Characterisation studies and noise analysis towards the applicability of metallic nanopores as single molecule detectors are also studied and compared to current bare silicon nitride pore systems.

Acknowledgements

First and foremost I'd like to express my sincere gratitude to my supervisors Dr. Joshua Edel and Dr. Tim Albrecht for their continuous support and encouragement throughout the course of my PhD. Their wisdom, patience and invaluable suggestions made my PhD experience both productive and stimulating. The enthusiasm they have for their research was contagious and motivational for me, and this thesis would not have been possible without their constant guidance and critical reading.

All the members of the Edel and Albrecht group, both past and present have contributed immensely to my time at Imperial College. The group has been a source of friendships as well as good advice and collaboration. I am especially grateful for the fun group of Nanopore members. I am also indebted to Dr. Jongin Hong for his assistance in the experimental design of nanopore chips and for his tremendous help and guidance both as a colleague and friend throughout my PhD. I am grateful to students Jessica Clough and Daniel Godfrey for their collaborative work on the impedance spectroscopy and thiol modification studies and to Dr. Margarita Rivera-Hernandez for her help with the STM measurements. I am also thankful to Dr. Kevin Lee and Dr. Mahmoud Ardakani at the London Centre of Nanotechnology (LCN) for teaching me the basics of FIB.

Most of all I would like to express my deepest gratitude to Bharat Lad, who has been by my side throughout this PhD and without whom, I would not have had the courage to embark on this journey in the first place. I thank him for believing in me, and instilling confidence in me when I needed it the most. I am also indebted to him for his constant encouragement, unwavering support and advice in the preparation of this thesis.

Finally to my family and parents to whom I cannot express my appreciation with words, through all my difficulties they have unconditionally provided all the love and support I could have ever wished for. To them I dedicate this thesis for all their years of struggle, guidance and support.

Contents

1 Introduction **13**

1.1 The need for improved biosensing tools 13

1.2 Single molecule detection 14

1.3 Coulter counter 15

1.4 Nanopores 16

1.4.1 Concept 16

1.4.2 DNA analysis 18

1.4.3 Biological nanopores 20

1.4.4 Solid-state nanopores 22

1.4.5 Fabrication of solid-state nanopores 23

1.4.6 DNA translocation through solid-state nanopores 26

1.5 Metallic nanopores 28

1.6 Outline of thesis 32

2 Materials and Methods **34**

2.1 Fabrication of free-standing silicon nitride membrane 34

2.1.1 Depositing silicon nitride films 36

2.1.2 Device microfabrication 36

2.1.3 Photolithography 37

2.1.4 Etching 38

2.1.5 Electron-beam evaporation 39

2.2 Fabrication of nanopores 41

2.2.1 Focused ion beam technique 41

2.2.2 Milling parameters 43

2.2.3 Problems encountered during nanopore fabrication 45

2.3 Sample characterisation 48

2.3.1 Optical microscopy . . . 48
2.3.2 Field Emission Scanning Electron Microscopy (FE-SEM) . . . 48
2.3.3 Scanning Tunnelling Microscopy (STM) . . . 49
2.4 Electrochemical characterisation . . . 50
2.4.1 Faraday enclosure . . . 51
2.4.2 Preparation of electrodes . . . 51
2.5 Microfluidic flow cell . . . 52
2.5.1 Assembly . . . 54
2.5.2 Cleaning of microfluidic cell . . . 55
2.6 Testing nanopores . . . 56
2.6.1 Handling and storage of nanopores . . . 56
2.7 Chemicals and Solutions . . . 57
2.7.1 Potassium Chloride (KCl) solution . . . 58
2.7.2 Potassium tetrachloroplatinate II (K_2PtCl_4) . . . 58
2.7.3 Tris-HCl EDTA (TE) buffer solution . . . 59

3 Characterisation studies of platinum electrodeposition 61
3.1 Electrochemical deposition . . . 61
3.1.1 Redox reactions . . . 63
3.1.2 Kinetic and Mass Transport . . . 63
3.2 Basic concepts of the experimental techniques . . . 65
3.2.1 Cyclic voltammetry . . . 65
3.2.2 Chronoamperometry . . . 67
3.3 Experimental . . . 69
3.3.1 Platinum deposition . . . 69
3.3.2 Electrode fabrication . . . 70
3.3.3 Experimental set-up . . . 71
3.4 Results and Discussion . . . 74
3.4.1 Chronoamperometric measurements . . . 74
3.4.2 Cyclic voltammetry analysis . . . 81
3.4.3 Multi-step deposition . . . 82
3.4.4 Scanning Electron Microscopy (SEM) Characterisation . . . 91
3.4.5 Elemental Analysis . . . 92
3.4.6 Scanning Tunnelling Microscopy (STM) topographic analysis . . . 94

3.5 Summary . . . 96

4 Precise electrochemical fabrication of sub-20 nm metallic nanopores 98

4.1 Background . . . 99

4.2 Experimental . . . 100

4.2.1 Pt deposition . . . 100

4.2.2 Fabrication of initial nanopores . . . 100

4.2.3 Data acquisition and analysis . . . 101

4.3 Preliminary experiments . . . 101

4.3.1 Methodology . . . 101

4.3.2 Results and Discussion . . . 103

4.4 Visual feedback method . . . 105

4.4.1 Requirements for optical measurements . . . 105

4.4.2 Assembly of the PDMS/glass flow cell . . . 107

4.4.3 Optical set-up . . . 109

4.4.4 Results and Discussion . . . 109

4.5 Ionic current feedback (ICF) method . . . 114

4.5.1 Requirements for monitoring the ionic current in real-time . . . 115

4.5.2 Assembly of the PTFE flow cell . . . 115

4.5.3 Bipotentiostatic set-up . . . 117

4.5.4 Results and Discussion: Nanopore array . . . 120

4.5.5 Results and Discussion: Individual nanopore . . . 125

4.5.6 Assessing the reproducibility of the ICF technique . . . 135

4.6 Summary . . . 140

4.7 Appendix . . . 141

4.7.1 Fabrication of PDMS reservoirs . . . 141

4.7.2 Fabrication of glass substrates . . . 141

4.7.3 Wire bonding onto gold contact pads . . . 142

5 Ion transport 144

5.1 Pore conductance theory . . . 145

5.2 Electrochemical Impedance Spectroscopy (EIS) theory . . . 147

5.3 Experimental . . . 150

5.3.1 Buffer solution . . . 150

5.3.2 Data acquisition and analysis . . . 150
5.3.3 Surface modification using thiols . . . 152
5.4 Results and discussion . . . 154
5.4.1 I-V characteristics . . . 155
5.4.2 Salt dependence . . . 155
5.4.3 EIS studies . . . 157
5.4.4 Surface modification using thiol chemistry . . . 171
5.5 Summary . . . 174

6 Detection of DNA using metallic nanopores 176
6.1 Background theory . . . 176
6.2 Experimental . . . 179
6.2.1 DNA material . . . 179
6.2.2 Fabrication of nanopores . . . 179
6.2.3 Experimental set-up . . . 180
6.3 Data Acquisition and Analysis . . . 181
6.3.1 Data Digitisation . . . 181
6.3.2 Filtering and sampling . . . 182
6.3.3 Acquisition protocols . . . 183
6.3.4 Noise characterisation . . . 185
6.4 Results and Discussion . . . 186
6.4.1 DNA translocation through Pt deposited nanopores . . . 186
6.4.2 Mean dwell time and amplitude characteristics . . . 187
6.4.3 DNA translocation through bare silicon nitride nanopores . . . 193
6.4.4 Multiple levels . . . 195
6.4.5 Electrical noise . . . 197
6.5 Summary . . . 198

7 Conclusions and Future work 200
7.1 Conclusions . . . 200
7.2 Future work . . . 205

Bibliography 208

Appendicies 219

List of Figures

1.1 Concept of nanopore experiments 17
1.2 Structure of DNA 19
1.3 DNA translocation dynamics 20
1.4 Structure of biological nanopores 21
1.5 Fabrication of silicon based nanopores 24
1.6 Fabrication of polymer based nanopores 25
1.7 Cross-sectional diagram of nanopore 26
1.8 Translocation characteristics of 11.5 kb dsDNA through silicon oxide pore . 27
1.9 Detection of DNA folding states within nanopores 28
1.10 Metallic nanopore schematic 29
1.11 Examples of metal nanopores 31

2.1 Main steps of metallic nanopore fabrication process. 35
2.2 Photo-lithographic pattern for fabricating silicon nitride membranes. 38
2.3 Shadow mask geometry 40
2.4 Schematic and images of chip structures 41
2.5 FIB and SEM instruments. 42
2.6 FIB chamber and examples of SEM images 43
2.7 SEM images of FIB milled nanopores. 44
2.8 SEM images of membrane. 45
2.9 Examples of nanopore thinning 46
2.10 SEM image of a Au/Si_3N_4 membrane. 49
2.11 Schematic and image of microfluidic flow cell. 53
2.12 Scheme for sealing the nanopore chip onto the microfluidic cell. 54
2.13 Steps for wetting the pore 55

3.1 Electrochemical deposition process. 62
3.2 Schematic diagram of the cyclic voltammetry technique 66
3.3 Schematic diagram of the chronoamperometry technique. 68
3.4 Photomask for the design of Au electrodes on a glass substrate. 70
3.5 Illustration of Au/glass electrode production. 71
3.6 Image and schematic of electrochemical cell 72
3.7 Optical images of the 8-set working electrode (WE). 74
3.8 Current vs. Time plot of deposition process. 75
3.9 Current-time transients at the Au electrodes. 76
3.10 Current plots for varying deposition durations. 78
3.11 SEM images for different deposition durations. 79
3.12 Current-time transients for various K_2PtCl_4 concentrations 80
3.13 Pt-deposition quality at varying K_2PtCl_4concentrations. 81
3.14 Cyclic voltammograms of various metals and solutions. 83
3.15 Cyclic voltammogram of Pt deposition on Au. 84
3.16 Schematic of nucleation and growth mechanisms. 84
3.17 Schematic representation of nucleation potential technique. 85
3.18 Schematics of various nucleation and growth experiments. 87
3.19 Current-time plots of various nucleation and growth experiments. 88
3.20 Optical images of various Pt depositions. 90
3.21 SEM images of Au substrate and Pt deposition. 91
3.22 EDXS spectras showing the elements present for Au and Pt samples 93
3.23 STM image and roughness measurements for Au and Pt deposited surfaces. 95

4.1 Schematic of the three electrode deposition set-up. 102
4.2 Photomask and optical image of Au contact pads. 102
4.3 Current-time plots of the deposition of Pt. 103
4.4 SEM images of before and after Pt deposition. 104
4.5 Schematic of device for optical feedback of deposition. 108
4.6 Images of the optical set-up for the visual feedback. 110
4.7 Current-time plots corresponding to the optical feedback experiments. . . . 111
4.8 Observed visual feedback recording during deposition. 112
4.9 SEM images of Pt-deposited nanopores produced using optical feedback . . 113
4.10 Before and after SEM images with increased reservoir size. 114

4.11 Concept of ionic curent feedback (ICF). 115
4.12 Schematic of PTFE flow cell used for ICF deposition. 116
4.13 Images of experimental set-up for ICF deposition. 118
4.14 Schematic of the computer-controlled electrochemical instrument. 119
4.15 Schematic representation of potentials applied to the ICF system. 122
4.16 Current-time plots of the deposition of Pt. 123
4.17 SEM of nanopore array sample – before and after deposition. 124
4.18 Current-time plots of Pt-deposition in multi-step experiment. 126
4.19 I-V traces and pore conductance of post ICF deposition pores. 127
4.20 Current-time plots of single pore deposition. 128
4.21 Single nanopore I-V traces before and after deposition. 129
4.22 Post-deposition SEM images for various deposition durations. 131
4.23 Normalised current-time plots for a single nanopore for various durations. 132
4.24 Conductances of 23 Pt deposited nanopores. 133
4.25 Current-time transients of 12 subsequent electrodeposition steps. 134
4.26 Enlarged plot of ICF current-time trace. 135
4.27 Pore conductance vs. amount of Pt deposited. 136
4.28 I-V trace of single nanopore – post deposition. 137
4.29 Current-time and SEM images of single-step depositions. 138
4.30 Semi-log plot of pore conductance vs. deposited Pt. 139
4.31 Amount of deposited Pt vs. deposition time. 140
4.32 Wire bonding method between Au membrane and contact pad. 142

5.1 Electrochemical setup for ion transport experiments. 145
5.2 Schematic of a Nyquist plot. 149
5.3 Schematic of a Bode plot. 150
5.4 Screenshots of the EIS modelling editor. 153
5.5 Process of forming self assembled monolayers of thiol. 154
5.6 General nanopore characteristics at 1M KCl concentration. 156
5.7 Salt dependence of Si_3N_4, Au and Pt pores. 158
5.8 Impedance measurements for a Au pore at varying KCl concentration. . . . 160
5.9 Bode plots for 1 mM to 250 mM KCl. 161
5.10 Bode plots for 500 mM to 1M KCl. 162
5.11 Pore conductance results fitted to models. 165

5.12 Solution conductance vs. KCl concentration. 168
5.14 Membrane capacitance vs. KCl concentration. 171
5.15 CV measurements characterisation of modified Au surface. 172
5.16 I-V traces for ion transport across modified and bare Au nanopores. 173

6.1 Schematic of DNA translocation. 177
6.2 Experimental set up for DNA analysis. 180
6.3 Image of the acquisition set-up used for single channel recordings. 182
6.4 Analysis of DNA events using Clampfit software. 184
6.5 Ionic current trace for λ-DNA translocations through a 18 nm Pt pore. . . . 187
6.6 Typical current blockades of λ-DNA in Pt pores. 188
6.7 Amplitude and dwell time histograms for Pt deposited pore. 189
6.8 Current traces of λ-DNA translocation at varying potentials. 190
6.9 Amplitude and dwell time histograms for Pt pore at varying potentials. . . 191
6.10 Frequency of translocation events at varying potentials. 192
6.11 Ionic current trace for λ-DNA translocations through a SiN pore. 194
6.12 Amplitude and dwell time histograms for a SiN pore. 195
6.13 Examples of multiple level events produced by λ-DNA. 196
6.14 Power spectral density plots for SiN and Pt pores. 197

List of Tables

2.1 List of solvents used in this thesis. 58
2.2 List of gases used in this thesis. 58
2.3 List of main chemicals used in this thesis. 60

3.1 Summary of results for varying deposition potential at Au/glass electrode. . 77
3.2 Summary of results for varying deposition duration at Au/glass electrode. . 79
3.3 Summary of results for varying K_2PtCl_4 at Au/glass electrode. 81
3.4 Table of calculated charge and thickness for S1-S4 experiments. 89
3.5 Calculated RMS roughness values from STM measurements. 96

4.1 Summary of results for Pt deposition onto a 16 nanopore array. 106
4.2 Summary of multi-step deposition studies on a nanopore array. 125
4.3 Summary of varying time duration studies on a nanopore array. 130
4.4 Varying V_{dep} at WE1 with a deposition duration t= 60 s. 130
4.5 Assessing the reproducibility of the single step approach. 139

5.1 Summary of CV results for varying KCl concentration in Si_3N_4 pores. . . . 159
5.2 Summary of CV results for varying KCl concentration in Au pores. 159
5.3 Summary of CV results for varying KCl concentration in Pt pores. 163
5.4 Pore conductance measurements using CV technique. 165
5.5 Salt dependence measurements using Randles model. 166
5.6 Salt dependence measurements using Randles with CPE model. 167
5.7 Solution resistivity values obatined from models. 169

6.1 Summary of results for the detection of λ-DNA. 192

Chapter 1

Introduction

1.1 The need for improved biosensing tools

The relevance of DNA as a biological information storage molecule was immediately appreciated when its double helix structure was first proposed by Watson and Crick (1953). DNA contains information that is fundamental in a wide variety of biological processes at the cellular and whole-organism level, ranging from development, reproduction to death. In the 50 years since its discovery, a major branch of genetic research has been stimulated by the anticipated advances in detection and treatment of diseases, and understanding of the processes that occur in nature (Collins, 2003).

A large amount of nucleic acid information resulting from The Human Genome Project (HGP), and (Venter, 2001) has also generated a great demand for the development of faster and inexpensive nucleic acid detection and sequencing methods. For example certain genetic analysis can enable the identification or diagnosis of a disease, facilitating rapid and appropriate treatment for individuals based on their own genomes, Guttmacher and Collins (2002). In an ideal scenario, genetic disorders could be diagnosed at birth in order for treatment to begin at the early developmental stage of life. Genome sequencing could then become routine, making it much easier to identify the genetic basis of diseases or isolate the factors that cause a drug to work in one patient but not another. Such diagnosis requires determining the sequence of chemical base pairs which make up DNA, and identifying and mapping approximately 20,000-25,000 genes of the human genome.

What currently limits the pace of genetic research is the available speed and cost of DNA sequencing. The Human Genome Project and the industrial gene sequencing

efforts currently uses state-of-the-art sequencing technology to extract the genetic codes of individuals at a cost of $10,000 in eight days, Illumina; Metzker (2010); Venter (2001). Much of the cost for biomolecular analysis is expended in sample preparation prior to analysis. Therefore, the current goal for sequencing lies in reducing this time to a matter of hours or even minutes for less than $1,000. Using a high throughput DNA sequencing method which can detect unlabelled molecules or which is capable of detecting trace quantities with increased specificity is highly compelling, Collins (2003).

The availability of such an analysis tool will not only increase the scope of genetic surveillance for infectious diseases but would also bring a dramatic improvement on evolutionary and ecological genomics, Guttmacher and Collins (2002); Metzker (2010). Thus making it feasible for routine healthcare practice and the vision of personalised medicine. At the fundamental level, the ability to manipulate and detect short-lived changes in specific biomolecule concentrations without the use of fluorescent labelling or genetic modification would also be of great utility to researchers probing the dynamics of single living cells, Marziali and Akeson (2001).

1.2 Single molecule detection

In recent years, technological advances have opened the door to a fundamentally different way of studying biology: *one molecule at a time*. The emerging field of single-molecule detection has utilised nanoscale fabrication and manipulation techniques such as electron beam lithography, optical microscopy and scanning tunnelling microscopy (STM) to directly study and probe individual molecules, Deniz et al. (2008); Rigler and Vogel (2008). The ability to monitor biological processes at this fundamental level of sensitivity has given rise to an improved understanding of the underlying molecular mechanisms, Walter et al. (2008).

In a typical single-molecule experiment, the molecule being examined is localised to a discrete volume so that its properties can be distinguished from all the other molecules in the sample, Efcavitch and Thompson (2010); Cornish and Ha (2007). Localisation is generally performed via attachment of the molecule to a fixed surface (eg., glass; bead) or via confinement to a droplet or channel, with passage through the channel controlled by electrochemical gradients, pressure flow, lasers etc, Kapanidis and Strick (2009); Walter et al. (2008).

These approaches provides an insight to the functional and structural interactions

that occur *in vivo*, thus leading to improved instrumentation in genomics and clinical applications which exploit these interactions, Lavery (2002).

Several single-molecule analysis techniques are currently under investigation, (Moerner, 2007; Rigler and Vogel, 2008; Selvin and Ha, 2008; Cornish and Ha, 2007 and Joo et al., 2008) including: AFM, STM, optical tweezers and traps, magnetic tweezers, capillary electrophoresis separation, bio-membrane force probes, steady shear flow, single-molecule fluorescence detection, Förster resonance energy transfer (FRET) probes and combination of optical trapping and mechanical actuators. These techniques have all been used to detect and manipulate individual molecules to elucidate interactions involving DNA, RNA, and proteins.

One of the most promising methods towards producing a cheap and rapid sequencing tool is through the use of nanopores. This involves threading DNA through tiny holes, such that an ionic current signal flowing through the pore becomes blocked when the pore is occupied by the DNA. The concept is that individual bases of the DNA can then be read off one at a time as they pass through the nanopore, making nanopores excellent candidates for instrumentation in high-throughput genomics. The techniques used in this thesis are based on nanopore detection, focusing mainly on the development and characterisation of individual pore systems.

1.3 Coulter counter

The idea of maneuvering individual strands of DNA through holes just a couple of nanometres wide can be seen as a difficult task. However this form of biopolymer transport is a common process in biology. Many biological processes rely on the ability of pores and channels to regulate the transport of ions and biopolymers through cellular membranes (Schatz and Dobberstein, 1996). Examples include gene transfer by transduction (Driselkelmann, 1994), RNA and transcription factor transport through nuclear pore complexes (Bustamante et al., 1995)(Salman et al., 2001), and the uptake of oligonucleotides by membrane proteins, Hanss et al. (1998); Meller (2003). These biological processes have inspired various *in vitro* nanopore experiments using voltage-driven transport of biomolecules, Sakmann and Neher (1995); Hille (2001).

However the concept of detecting molecules passing through a pore outside of a cell was first introduced in the 1950s by Wallace Coulter, (Coulter, 1953). In a Coulter counter, microscale molecules or particles are passed through an aperture under pressure driven

flow. As the molecules pass through the aperture they temporarily displace the volume in the aperture which results in transient current blockades. Since the magnitude of these blockades is approximately proportional to the volume of each molecule, coulter detectors are used for the counting and sizing of various particles.

This technique was first applied on the nanoscale (∼100 nm) by using nuclear-track etched nanopores, developed in the early 1970s, DeBlois and Bean (1970). These pores were produced by using an irradiation source, which formed tracks along a thin foil. Subsequently, the tracks were chemically etched and resulted in the formation of sub-micrometer cone-like openings. Use of these pores resulted in the detection of ∼60 nm particles which were driven under an electric field. It was then envisaged that the use of even smaller pores, would extend the coulter counter concept further. By moving towards nanoscale dimensions, surface effects are predominant and diffusion becomes an efficient mass transport mechanism, Eijkel and van den Berg (2010); Craighead (2006); Tegenfeldt et al. (2004). The main advantage of decreasing the pore diameter is the ability to probe and manipulate single molecules in confined geometries, providing a better understanding of the fundamental processes that are occuring, Sparreboom and Eijkel (2009); Piruska et al. (2010).

1.4 Nanopores

Nanopores use the same sensing principle as a coulter counter and are based on detecting transient interruptions in the ion-current of an electrolyte, induced by the entry, transport and exit of a particular analyte from the pore. Nanopores feature a much smaller inner diameter, between 1 and ∼100 nm. When the nanopore diameter is similar to the cross section of the analyte, this results in the analyte blocking the nanopore to a much larger extent than a microscale aperture.

1.4.1 Concept

The nanopore experimental set-up for detecting individual molecules is simple. The approach consists of a biological, inorganic, or polymer membrane with a single nanopore, as shown in Figure 1.1. The nanopore connects two reservoirs of salt solution on both sides of a membrane, often denoted as *cis* and *trans*. In this experimental geometry the only path between the ionic reservoirs is through the nanopore. When an electrochemical potential is applied between the reservoirs, a measurable ionic current is made to flow through the nanopore. As the analyte molecules are added to the *cis* side of the nanopore, due to

the presence of charge on the molecules, they are driven towards the opposite electrode, present in the *trans* chamber. Their entry into the nanopore results in blockades in the ionic current, which correlates to their molecular properties (e.g., size and charge). Because of its extremely small size, the nanopore completely dominates the resistance of the electrochemical cell.

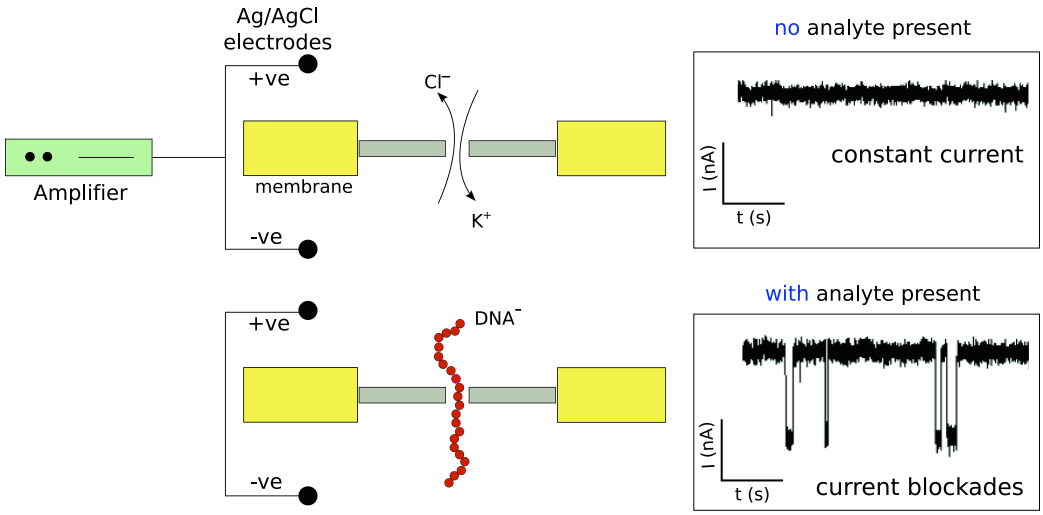


Figure 1.1: Schematic illustrating the detection principle of nanopore experiments. *Top*: a transmembrane potential causes a constant flow of ions through a single pore. *Bottom*: analytes that pass the pore cause temporary current blockades which are further detected and characterised.

The ionic current detection in nanopores uses salt concentrations between 500 mM to 1 M which are much higher than physiological ionic strengths. The measurable conductance is unitary as indicated by a constant-current trace (Figure 1.1) which allows for easier detection of molecule-induced blockades. Under these conditions, different molecules exhibit different levels of blockade. For example, a strongly interacting molecule may block the pore current permanently, whereas rapidly passing molecules may be too fast to be resolved, thereby giving rise to an increase in the current noise.

A distinguishing feature of nanopores is that they can be used to analyse not only small molecules but also long biopolymers, such as DNA and RNA, Healy (2007). The most important advantage of the nanopore technique over other single molecule methods is that molecules can be detected without labelling or surface immobilisation. In most single molecule experiments, labelling with probes such as fluorophores, quantum dots, nanoparticles or with surface anchoring groups (e.g., biotin, His-tag, amines) is commonly used

to detect and localise single biomolecules, Selvin and Ha (2008); Efcavitch and Thompson (2010). Whereas in nanpore experiments unlabelled water soluble molecules are able to give rise to detectable current blockades. Due to their simple electrical sensing principle, nanopores offer one of the least complex and cheapest methods for detecting single molecules.

1.4.2 DNA analysis

The concept of analysing nucleic acids such as DNA and RNA using nanopores was first proposed in the the 1990s, where the realisation of using artificial nanopores to translocate DNA biopolymers had prospects for the detection and discrimination of individual bases, Kasianowicz et al. (1996). The sequential reading of a DNA biopolymer as it translocates through nanopores was also an attractive and novel concept as it allowed researchers to mimic natural biological machinery.

Physical characteristics of DNA

The structure of DNA can be simplified to a linear polymer with repeating sugar-phosphate backbones, Watson and Crick (1953). Under physiological pH conditions (∼7.4) each phosphate group carries a single negative electric charge; making DNA a highly charged polymer. There are four nitrogen containing ring compounds called bases attached to each sugar. The DNA sequence refers to the order in which the four possible bases, Thymine (T), Guanine (G), Adenine (A) and Cytosine (C) are arranged along the molecule. The sequence in which these bases are linked constitutes a form of biological information that can be efficiently decoded and copied to direct the assembly of amino acids into the proteins and to carry out specific biological tasks in the cell, Alberts (1994); Watson and Crick (1953). DNA normally exists in its double stranded form, denoted dsDNA. The chemistry that joins the two DNA strands is what provides the DNA molecule with the ability to manage biological information: hydrogen bonds between opposing bases link the two strands in the double helix, but only in the combinations T with A and G with C. The specificity of base pairing enables the storage and replication of genetic information. Hence the process of sequencing DNA can be simplified to detecting the order in which these bases occur within a strand of DNA, Watson and Crick (1953), Figure **??**.

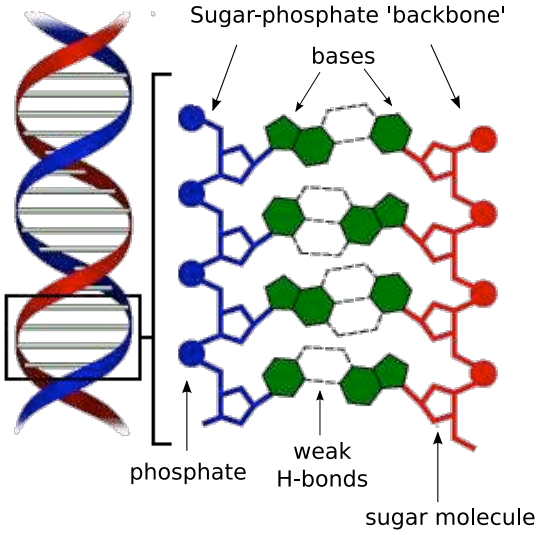


Figure 1.2: The double helix and primary structure of DNA.

DNA translocation dynamics

The dynamics of a DNA strand translocating through a nanopore depend on the following key parameters: (i) the force applied on the DNA molecule; (ii) DNA molecule properties (e.g, cross section, conformation and persistence length); (iii) solution conditions (e.g., ionic strength, viscosity, temperature); and (iv) the interactions between the DNA and nanopore, Healy (2007); Wanunu et al. (2008).

The DNA biopolymer molecules act as flexible long chains in solution that can adopt a large number of conformations, N. Therefore they can be modelled using polymer physics, (Flory, 1953 and Muthukumar, 2007) where the size of the molecule in solution can be represented by the radius of gyration R_g. In the ideal polymer chain, the approximation R_g is defined by:

$$R_g{}^2 = \frac{1}{N}\sum_{k=1}^{N}(r_k{}^2), \tag{1.4.1}$$

where N is the total number of monomers (in the case of DNA, the number of bases) and r_k is the distance of monomer k from the centre of mass co-ordinate.

When the internal diameter of the nanopore is only slightly larger than the biopolymer cross-section, the molecules unfold in order to enter the pore. This unfolding concept subjects the biopolymer molecules to an entropic barrier (Muthukumar, 2007); (Wanunu et al., 2008). As a result, the chain entropy: $S = k_B \ln N$, where k_B is the Boltzmann constant

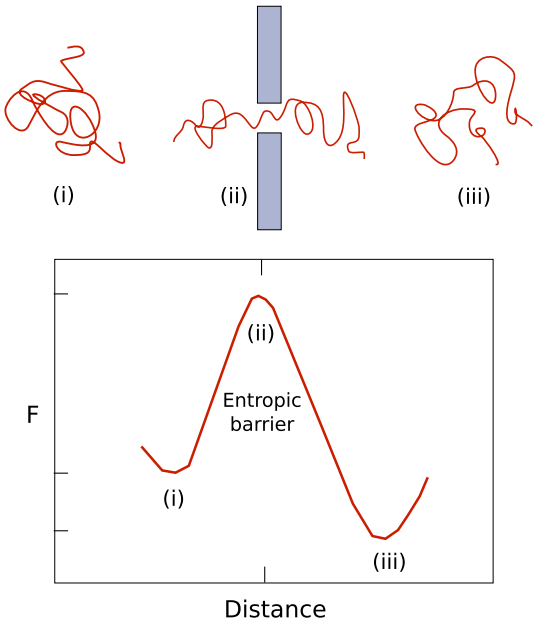


Figure 1.3: Schematic of the general mechanism for DNA translocation through confined channels. The DNA polymer unfolds in order to enter the pore. This unfolding subjects the polymer to an entropic barrier. Adapted from Muthukumar (2007).

can be high, and its free energy F is given by:

$$F = E - TS = E - k_B T ln N, \tag{1.4.2}$$

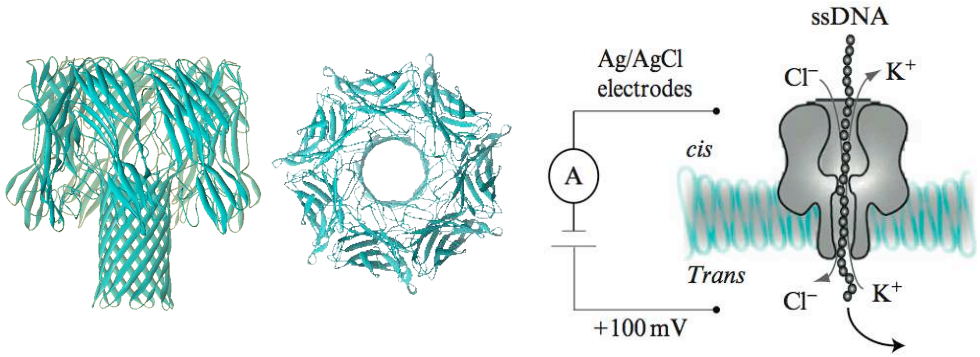
where E is the energy of interaction between monomers and the surrounding solvent molecules and T is the absolute temperature. There can be additional entropic contributions to F due to a reorganisation of solvent molecules accompanying the conformational changes of the chain. When the polymer chain is confined to an environment such as a pore, the number of conformations that can otherwise be assumed by the polymer chain is reduced and as a result the chain entropy decreases and the chain free energy increases, Muthukumar (2007). This effect is depicted in Figure 1.3.

1.4.3 Biological nanopores

The use of biological nanopores for the detection of DNA has evolved from studies aimed at understanding the mechanism of ion channels, Hille (2001); Sakmann and Neher (1995). Biological nanopores are constructed using specific proteins which self-assemble into a lipid bilayer. These proteins are generally referred to as pore-forming and can be applied with excellent reproducibility, Howorka and Siwy (2009b). There are a range of

different pore proteins which can be employed in this way such as *Bacillus subtilis* (used to detect dsDNA, Szabo et al., 1997) and OmpG (porin from the bacterial outer membrane), Conlan et al. (2000). Another recently studied protein is the MspA pore from *Mycobacterium smegmatis*. It has a single, short and narrow channel constriction which has been employed for the sensing of DNA, Butler et al. (2008).

However, efforts in nanopore biosensing have been implemented primarily with the α-hemolysin (α-HL) channel, first demonstrated in Bayley and Cremer (2001). Found in the bacterium *Staphylococcus aureus*, the α-hemolysin pore features a transmembrane channel with a width of 1.4 nm at its narrowest point and allow ions to pass at a high ionic conductance. Its asymmetric structure characterised by X-ray crystallography (Song et al., 1996) is represented in Figure 1.4. Due to its channel width, α-hemolysin is ideal for the detection of ssDNA (diameter of 1.2 nm) translocation. The α-HL nanopore has also been studied extensively as a stochastic sensor for studies into the kinetics of chemical reactions, Bayley and Cremer (2001); Howorka and Siwy (2009b).



(a) Front and top view (b) Experimental set-up

Figure 1.4: (a) The heptameric α-hemolysin (α-HL) pore, PBID structure reference: 7AHL, determined by crystallography (Song et al., 1996) and (b) experimental set-up for ionic current and DNA detection measurements.

In 1996, Kasianowicz et al. were the first to demonstrate the passage of charged DNA molecules through an α-HL nanopore, which resulted in clear temporal current blockades, Kasianowicz et al. (1996). The pore was inserted in an artificially formed lipid bilayer, where DNA molecules in free solution on either the *cis* or *trans*-sides of the pore were translocated across the channel under a constant applied transmembrane electric potential. During translocation, individual ssDNA fragments blocked the passage of electrolyte ions,

which resulted in a ∼80% reduction in the pore current.

In further experiments, discrimination between single-stranded and double-stranded nucleic acids was also shown to be possible as the barrel and limiting aperture of the α-HL pore sterically prevented double-stranded nucleic acids (2.4 nm in diameter) from passing through. Whereas single-stranded nucleic acids with a diameter ∼1.2 nm were small enough to translocate through the pore in a linear fashion. This sub-nanometer difference in size between the single and double-stranded diameters of the nucleic acids was used to selectively filter single-stranded nucleic acids from a mix of single and double-stranded fragments in solution, Kasianowicz et al. (1996); Meller et al. (2000).

The research then advanced to determine characteristic details of the passing molecules. Different RNA molecules (a nucleic acid closely related to DNA) of 100 identical bases were found to cause different current blockade signals, Akeson et al. (1999). Where two populations of long (∼50 bases) homopolymer strands composed of different nucleotides could be distinguished from one another (e.g. single-stranded RNA fragments poly$(A)_{50}$ versus poly$(C)_{50}$). α-HL has since been used extensively to discriminate between DNA and RNA sequences, (Meller et al., 2000), to study DNA unzipping kinetics, orientation of entry, DNA-protein interactions, and peptide transport, Mathe et al. (2004); Nakane et al. (2004); Sauer-Budge et al. (2003).

An important outcome of these studies has been the realisation that the dynamics of biopolymer translocation is governed by its interactions with the nanopore walls, Meller (2003), resulting in small changes in the ionic current, as the biopolymer passes through the pore. This concept was utilised for the detection of small molecules, metal ions, and the discrimination of enantiomer drugs, by employing molecular engineering methods to modify the α-HL nanopore, (Howorka and Siwy, 2009b); (Wanunu et al., 2009). However, the range of sensing applications using α-HL is limited by its fixed dimensions and the delicate lipid membrane.

1.4.4 Solid-state nanopores

Protein pores are particularly attractive for nanopore sequencing as X-ray crystallography can reveal their structure with angstrom resolution, self-assembly facilitates atomic reproducibility from one pore to the next and protein engineering offers an effective tool to tailor their analytical capabilities. However due to the inherent fragility of the lipid bilayer membrane in which these nanopores are suspended, the integration of these pores

into devices and arrays presents major challenges.

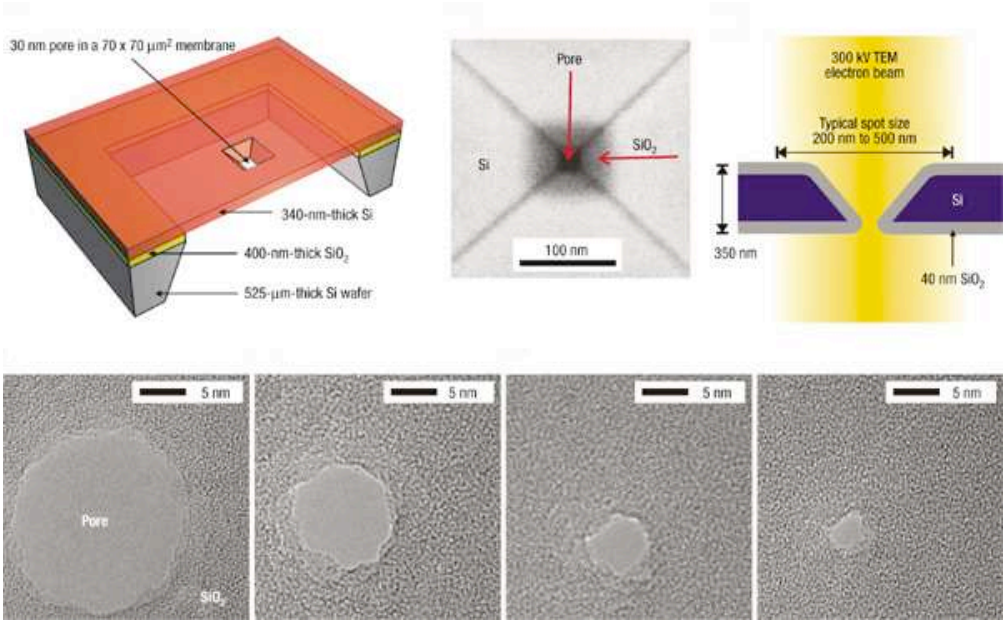
Due to these limitations, experiments with biological pores have stimulated the scientific community to develop nanopores in solid-state support, which are made in robust silicon materials or organic polymers, Dekker (2007). Solid-state nanopores have potential advantages because they are mechanically and chemically more stable, as well as easier to handle. They allow for long recordings over a wide range of external parameters such as temperature, pH and ionic strength. In addition, solid-state nanopores can be more easily integrated into sensing devices, Howorka and Siwy (2009a). Techniques that are currently used for nanopore preparation can be divided into two major categories, Figures 1.5 and 1.6,(i) the drilling and shaping of pores in silicon nitride and silicon oxide materials, Storm et al. (2003) and (ii) the ion-track etching method, DeBlois and Bean (1970). There has also been research on preparing glass pipettes with nanometer openings for use in translocation experiments, Karhanek et al. (2005).

1.4.5 Fabrication of solid-state nanopores

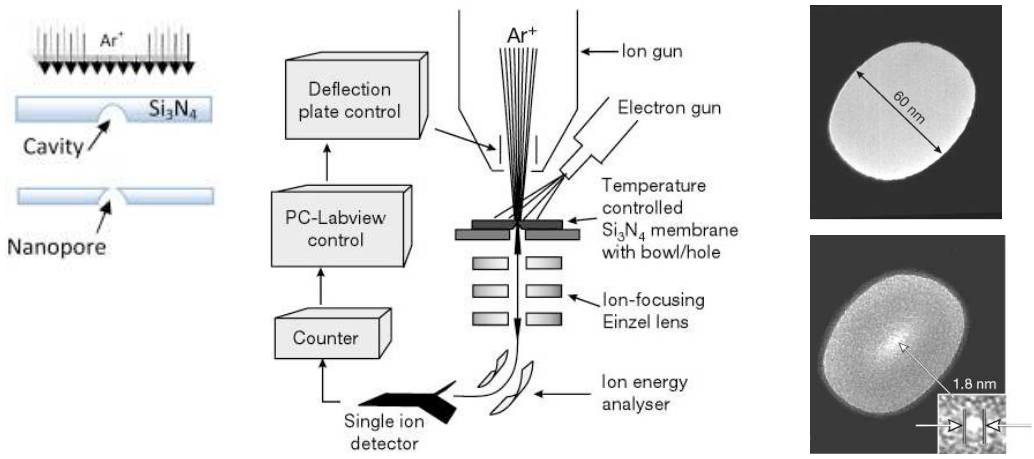
Aiming to address the limitations of biological pores, the first synthetic pore successfully used for DNA analysis was developed by Li et al. (2001). The group produced the nanopore in a thin silicon nitride (Si_3N_4) membrane using an ion beam sculpting technique. In this approach, an energetic beam of Ar^+ ions is used to sputter a Si_3N_4 membrane that contains a bowl-shaped cavity. The sputtering causes thinning of the film, eventually resulting in the formation of a nanopore as detected by leakage of Ar^+ ions. Nanopore sizes down to 1.5 nm have been fabricated using this method, as determined by transmission electron microscopy (TEM).

A similar method for producing silicon dioxide (SiO_2) pores was later developed by Storm and co-workers, Storm et al. (2003). The group substituted the ion beam method with a simpler procedure, in which a focused electron beam (e-beam) of a commercial TEM was used to attain the desired dimensions. A large ($\sim$100 nm) SiO_2 pore was irradiated with an intense beam of 300 keV, which caused the pore to shrink by fluidisation of the SiO_2 layer. The shrinking was reported to be an effect of mass flow at the nanoscale driven by surface tension. Direct visualisation of the process allowed both the controlled fabrication and analysis of the nanopore shape in real-time.

Another approach with a high degree of pore size control is based on polymer films such as poly(ethylene-terephthalate) (PET), Siwy et al. (2003a), polycarbonate (PC) and



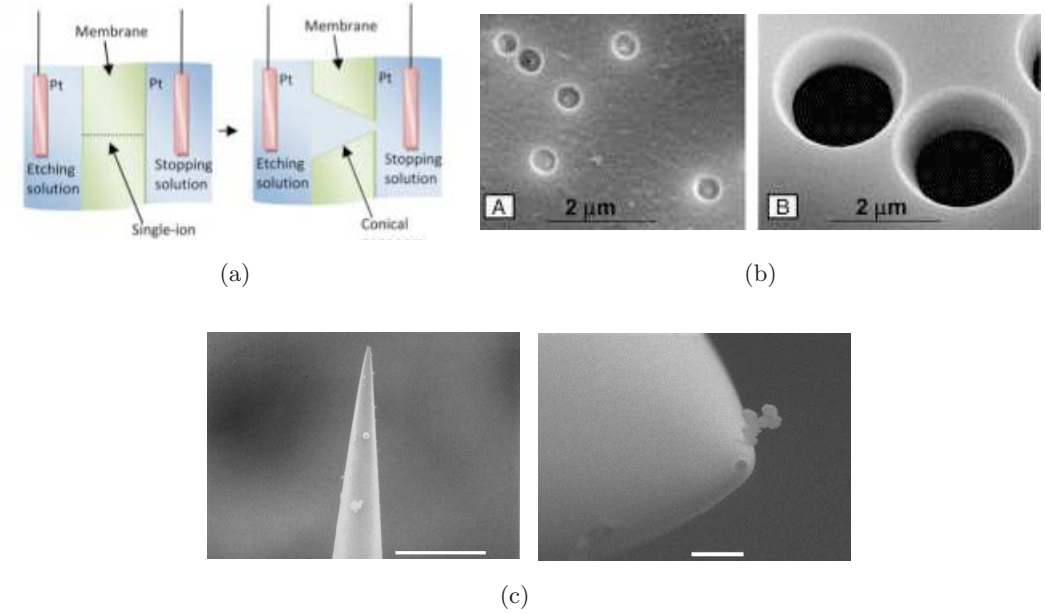
(a) The electron beam technique, schematic of a solid state nanopore and an SEM image of the area where the milling takes place. *Below*: a sequence of TEM images (*Left to Right*) showing the reduction of a silicon oxide nanopore diameter under continuous exposure to a highly focused electron beam, Dekker (2007).



(b) Single nanopore obtained by the ion-beam sculpting technique. Where an original larger pore in a cavity (*Left panel*) obtained by a focused ion beam is closed by applying a defocused ion beam (*Right panel*), Li et al. (2001).

Figure 1.5: Solid-state nanopores prepared in silicon-based materials.

polyimide (PI), as well as mica, Howorka and Siwy (2009b). The technique, known as track-etching begins with the irradiation of the film (usually 1-10 μm in thickness) with energetic heavy ions. These form latent tracks, that are chemically etched to obtain conical shaped pores with the desired nanoscale or microscale dimensions, DeBlois and Bean (1970); Howorka and Siwy (2009a).



(a) (b)

(c)

Figure 1.6: Synthetic nanopores with a high aspect ratio. (a) conical nanopores prepared in 12 mm thick foils of poly(ethylene terephthalate) and (b) polyimide using the track-etching technique, Siwy et al. (2003a). (c) a glass nanopipette fabricated with a commercially available pipette puller, Karhanek et al. (2005).

Nanopores incorporated in thin insulating membranes are highly promising materials, since the nanopore volume can be reduced to a few nanometers in all dimensions, similar to biological membrane channels. In addition, the planar geometry permits high-resolution fabrication and characterisation as exemplified by subnanometer size control for nanopores down to 1-2 nm diameters, Kim et al. (2006).

Structural characteristics

Translocation dynamics of biomoelcules through solid state nanopores are strongly dependent on interactions between biomolecules and the nanopore surfaces. Therefore precise characteristics of the nanopore structure as well as its surface properties is essential. In

2006, Kim and co-workers performed three-dimensional tomographic imaging of solid-state nanopores fabricated using an electron-beam (Kim et al., 2006). The imaging revealed a truncated double-cone pore structure, as illustrated in Figure 1.7. Following this, a series of nanopores in the range 3-15 nm were fabricated and assembled into two-chamber devices to investigate the ion transport properties. These pores typically yield ohmic current-voltage (I-V) curves, the slopes of which were used to define the pore conductance, G, as shown in Figure 1.7 (right panel).

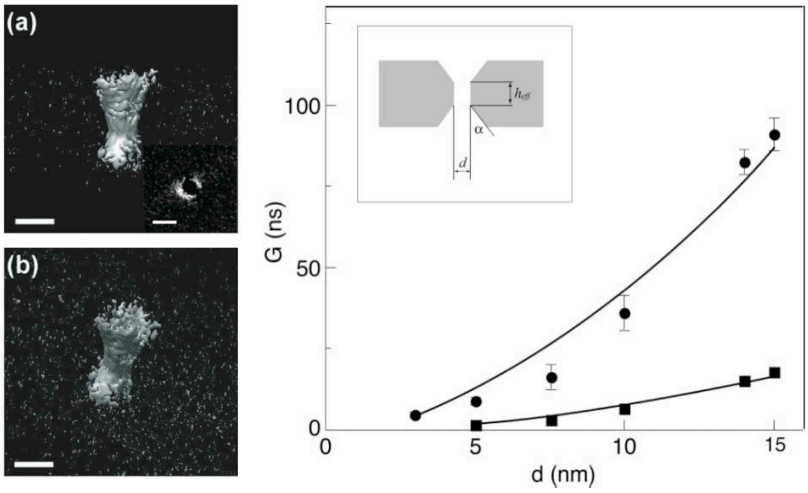


Figure 1.7: (a) 3-D cross-sectional image of a solid-state nanopore fabricated in Si_3N_4 as determined by TEM tomography with an 8 nm diameter (*inset*) (b) tilted view. (c) ionic conductance (G) of solid-state nanopores as a function of their diameter measured in 1.0 M (*circles*) and 200 mM (*squares*) KCl solution. The solid lines represent fits to a geometrical model which assumes a truncated double-cone structure, as shown in the *inset*. Scale bar= 5 nm. Adapted from Kim et al. (2006).

1.4.6 DNA translocation through solid-state nanopores

In recent years, solid-state nanopores have demonstrated utility for sensing single-stranded, (Fologea et al., 2005a) and double-stranded DNA, (Storm et al., 2005); (Heng et al., 2004); (Ayub et al., 2010); (Smeets et al., 2008); (Healy, 2007), ions, (Siwy et al., 2003b) macromolecules, (Heins et al., 2005) and proteins, (Han et al., 2008). In particular, the focus has been on understanding the dynamics of both ssDNA and dsDNA translocations, an example of the typical current-versus-time trace for the detection of dsDNA is shown in Figure 1.8. Quantitative polymerase chain reaction (PCR) has been used to confirm

translocation, demonstrating that the number of current blockade signatures correlates with the amount of DNA in the *trans* chamber, Heng et al. (2004).

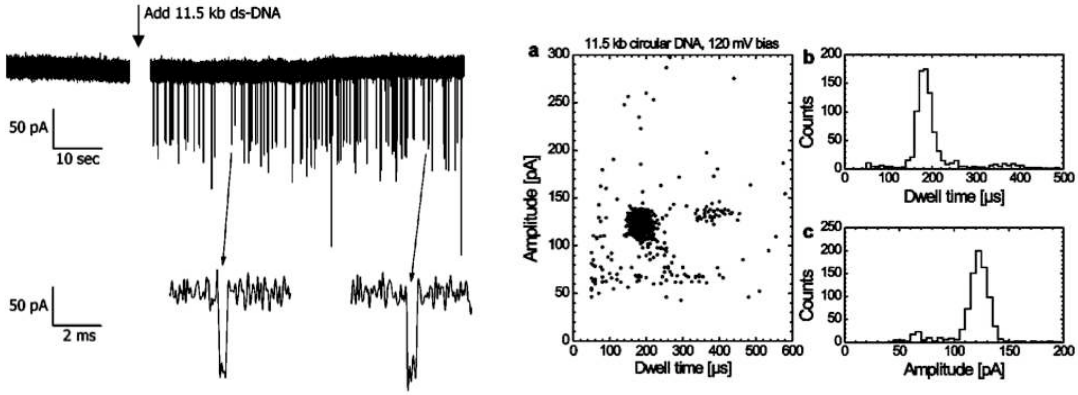


Figure 1.8: *Left panel*: Measured ionic current versus time trace for the translocation of 11.5 kb dsDNA. After addition of DNA to the cis side of the pore, typical spikes in the current are observed corresponding to the interaction of the DNA with the nanopore, (*below*) two individual events are shown at an increased time resolution. *Right panel*: (a) Event scatter plot of events recorded at 120 mV with DNA molecules along with histograms of observed (b) dwell times and (c) amplitudes. Storm et al. (2005).

More focus is now being put towards characterising these solid-state nanopores. Studies concerning DNA folding mechanisms during translocations have shown different event depths (or varying blockade levels in one event) corresponding to molecules translocating individually, unfolded or folded (Li et al., 2003 and Storm et al., 2003), as shown in Figure 1.9.

The effect of DNA conformation on the translocation signal has also been investigated by Fologea et al. (2007). In this study, they showed that linear, circular relaxed, and coiled circular DNA could also be distinguished by the current blockade and translocation time. Using an 18 nm pore, the circular DNA form (5.4 kbp in length) exhibited current blocking that was double the magnitude of that for the linear DNA. The length dependence was also determined from the dwell time and the current amplitude of each event.

Another interesting observation made with solid-state nanopores is the reduction in current during the translocation of a DNA molecule which strongly depends on the electrolyte concentration, Smeets et al. (2006); Chang et al. (2004). Smeets and coworkers found that the surface charge of 10 nm diameter pores fabricated in SiO_2 dominated the pore conductivity at low electrolyte concentration (<100 mM), leading to a nonlinear

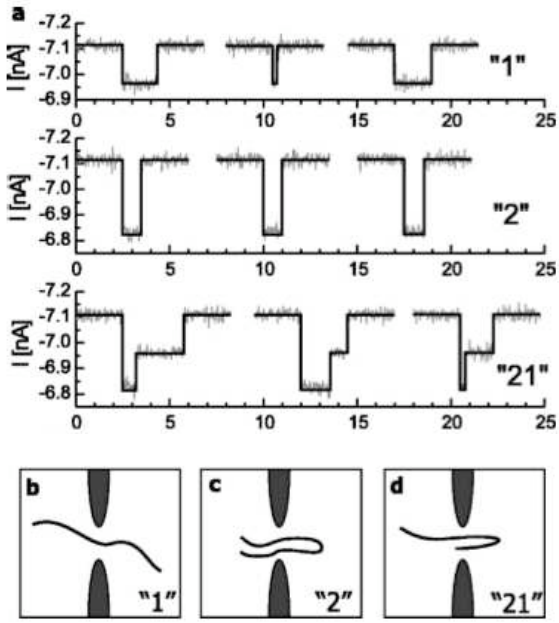


Figure 1.9: Detection of the folding state of single dsDNA molecules with a silicon oxide nanopore. Various types of ion current events (a) are attributed to different folding states of DNA in a nanopore (b, c, d), Storm et al. (2005); Fologea et al. (2005a).

dependence of G on salt concentration. At low salt concentrations, an increase in ionic current was observed rather than a drop as the DNA passed through the pore. As the counter ions shielding the charge of the DNA backbone added a positive contribution to the ionic current. Due to this the DNA molecule introduced a cloud of mobile counter ions into the pore, thereby increasing the number of charge carriers available for ionic transport.

1.5 Metallic nanopores

The successful use of solid-state nanopores in single-molecule translocation studies has resulted in a new and active area of research. The adjustable dimensions and surface characteristics of solid-state nanopores make them a versatile single molecule tool in biology. In addition to this, the physics behind the translocation process in naturally occurring biological pores, and the effects of nanometer-scale confinement can be experimentally addressed.

The results obtained from using nanopores for studies of nucleic acid analysis have also raised prospects for DNA sequencing directly from the ion current blockage signa-

tures (Deamer and Branton, 2002 and Dekker, 2007) however accurate determination of individual bases based on ion current measurements alone either with a biological or solid-state nanopore is unlikely to be feasible. Although the transitions between different homopolymer regions have been detected (Akeson et al., 1999) the detection for the change of a single base within a sequence is overwhelmed by the known noise levels using contemporary ion current measuring techniques, Smeets et al. (2008). Though the direct sequence measurement or base counting using solid-state nanopores may one day be possible, it must occur either optically or by introducing a mechanism for controllably decreasing the translocation rate by several orders of magnitude under high electric field, Branton (2008).

The thesis focuses on the development of metallic nanopores in insulating membranes and their application to single molecule biosensing. Metallic nanopores extend the use of current solid-state nanopore platforms and can potentially be used to overcome the current challenges faced with controlling the translocation process. By coating the solid-state nanopore with a thin metallic layer, an additional localised control at the nanopore can be established, where controlling the electrostatic environment (gating) of the pore becomes feasible through the application of external potentials to the metal film, Taniguchi et al. (2009); Nam et al. (2009); Kalman et al. (2009). Further to this, modifying the chemical properties and shape of the metal pore interior is particularly appealing because it allows the pore to be equipped with desired functionalities, for example the well established and versatile thiol chemistry can be used to functionalise metal surfaces, thus providing better sensitivity.

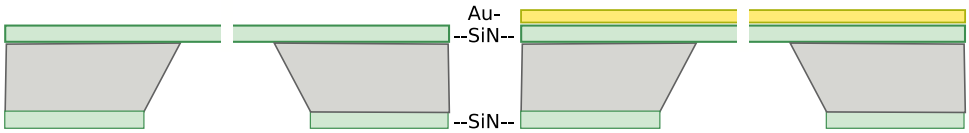


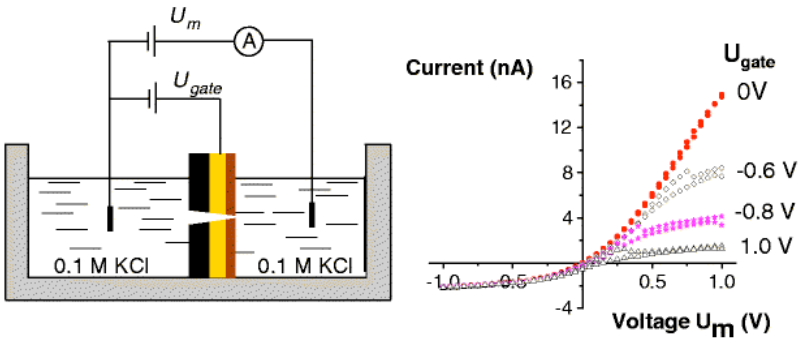
Figure 1.10: Illustration of (*Left*) the conventional solid-state nanopore produced in silicon nitride membrane and (*Right*) the metallic nanopore device developed in this thesis.

In addition, changing the nanopore chemical characteristics can affect the nanopore selectivity to analytes and prevent unwanted irreversible adhesion to the nanopore surface. Chen and coworkers have shown that nanopores modified with thin alumina coatings exhibit enhanced DNA capture rate and lower noise compared with uncoated silicon ni-

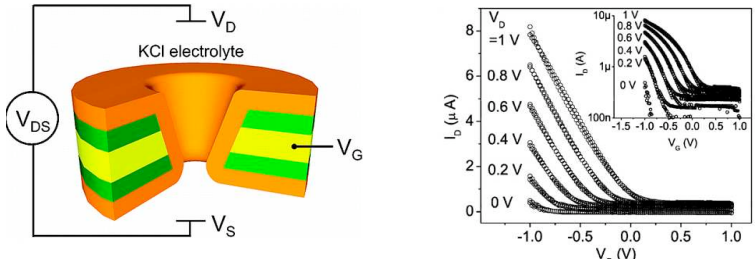
tride pores, attributed to increased positive surface charge, Chen et al. (2004b). Iqbal and coworkers showed that ssDNA transport through hairpin-functionalised nanopores is sequence dependent, suggesting that surface interactions can be tailored for selectivity, Iqbal et al. (2007). Wanunu and Meller (2007) developed a general method for controlling the pH response of the nanopore device by using self-assembled organo-silane molecule coating. Chemical coating can open up various options, from tailoring the coating to specifically slowing down nucleic acids transport, to nanopore functionalisation with enzymes, antibodies etc. If needed, the organic coating can be stripped off and the nanopore can be recycled many times, with little effect on the substrate.

Slowing down the voltage-driven DNA dynamics in solid-state pores is another important challenge, Branton (2008). It is expected that rates on the order of 1-10 μs/base pair or slower are needed for a electronic implementation of the DNA sequence, Dekker (2007); Fologea et al. (2005b). Environmental factors such as increased solution viscosity or reduced voltage have been reported to increase the average translocation time by a factor by increasing the viscosity increase or reducing the voltage, Fologea et al. (2005b). However, these parameters have negative effects on the capture rate of DNA to the pore: DNA collision with the pore is strongly depends on the voltage gradient in the pore vicinity and the solution viscosity. Therefore, the use of viscosity and voltage to slow down DNA translocation results in reduced capture rate and can limit the practicality of the nanopore technique. This can be overcome by the presence of a metallic probe at the nanopore, the DNA can potentially be pulled towards the pore and subsequently slowed down by switching the charge on the nanopore surface. This application can also help increase the nanopore-DNA interactions to better regulate the DNA moving process with little or no negative effects on the rate of DNA capture into the pore.

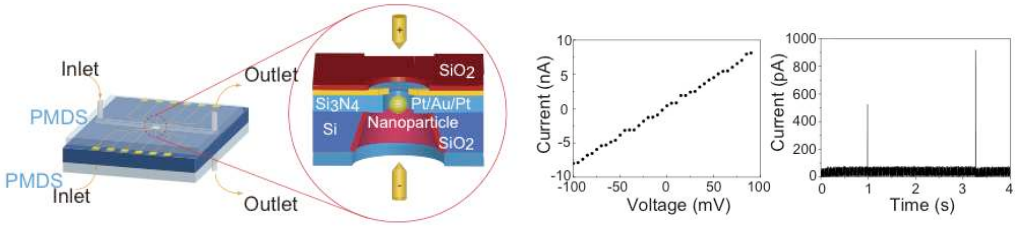
Studies on employing metal films in nanopore devices have recently emerged which focus on using metal coated nanopores prepared by electroless plating (Martin et al., 2001 and Lokuge et al., 2007) or thermal evaporation (Kalman et al., 2009; Taniguchi et al., 2009; Nam et al., 2009 and Chansin et al., 2007). The metallic nanopores have been used to study the ion transport properties and selectivity of protein transport by modulating the charge at the metallic membrane surface, examples of these are presented in Figure 1.11. Physical studies of metallic layers is at the forefront of material sciences, this combined with the capability of chemically modifying (Shufang et al., 2003) and functionalising (Siwy et al., 2005 and Talisman et al., 2009) the surfaces allow the metallic nanopore



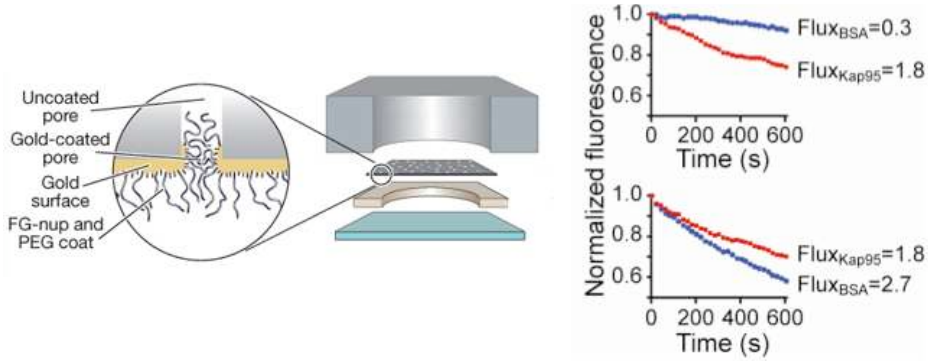
(a) polymer based metallised conical nanopore for controlling ion transport by varying gate voltages, U_{gate}, Kalman et al. (2009).



(b) electrode-embedded nanopores which can be manipulated by the surrounding gate dielectric (TiO_2, orange) and gate electrode (TiN, yellow), Nam et al. (2009).



(c) detection of translocation of Au nanoparticles via electric current between two nanogap electrodes, Taniguchi et al. (2009).



(d) nanopore functionalised with specific binding porins that can mimic the transport selectivity of a nuclear pore complex, Talisman et al. (2009).

Figure 1.11: Examples of recent work using metallised nanopores.

platform to be optimised for both selectivity and specificity, thus providing overall a more sensitive nanopore sensing device.

1.6 Outline of thesis

This thesis reports on the fabrication and characterisation of metallic nanopores in insulating membranes, and their application in single-molecule biosensing. These topics are covered in several relatively self-contained sections. In the first part of this thesis a new process is described which is developed for controlling nanometer-sized metallic pore fabrication. Investigations are carried out to control the thickness and size of the pore, and explore the possibilities to influence its surface composition.

The second part of this thesis discusses the ionic transport properties of the fabricated metallic nanopores. The dependence of salt concentration and electrochemical potential using both ionic current measurements and impedance spectroscopy. In addition to this, a comparative study between metallic nanopores and conventional silicon nitride pores is presented. This is followed by studies of chemically modifying the metallic nanopores using thiol chemistry. The third and final part of this thesis shows DNA translocation through metallic nanopores. We use different electrochemical potentials to study the translocation dynamics and compare these to silicon nitride pores. The outline of this thesis is as follows:

Chapter 2 provides a detailed description of the fabrication method for preparing metallic nanopores and the reagents used along with the design and operation of the microfluidic devices used throughout the thesis. Details of experimental problems encountered and the techniques used to characterise the nanopore surfaces is also presented.

Chapter 3 begins with an introduction of electrochemical deposition, used in the fabrication of our metallic nanopores. A platinum deposition solution is developed and characterised on flat metallic electrodes for optimisation of our fabrication technique.

Chapter 4 reports on a novel fabrication process of metallic solid-state nanopores in which a feedback mechanism is employed to assess its size during the fabrication process. The method uses electrochemical deposition to shrink the size of metallic nanopores by monitoring the ionic current as a feedback mechanism and uses the observed pore conductance to calculate the nanopore diameter in real-time.

Chapter 5 is devoted to studies of the ionic transport characteristics of metallic nanopores under varying electrolyte conditions. Here, a comparison is made with a theoretical model and the system is further characterised using impedance spectroscopy. The results ob-

tained are then compared to bare silicon nitride pores of same dimensions. The use of metallic nanopores is further extended by chemical modification of the metal film using thiols. The method of engineering the metallic nanopores using self-assembled monolayers is presented followed by ionic current measurements which indicate a reduction in noise for modified nanopores.

In Chapter 6 the applicability of the metallised nanopores for stochastic sensing is demonstrated in real-time translocation experiments of single λ-DNA molecules. The pores feature comparable noise to silicon nitride pores and we observe longer DNA residence time of current blockades suggesting an attractive interaction between the DNA and the metallic pore walls.

Finally, the thesis concludes with a discussion of the results achieved, and an outlook on the work planned for the future.

Chapter 2

Materials and Methods

This chapter presents the experimental procedures for fabricating metallic solid-state nanopores in free-standing silicon nitride membranes. These structures are used throughout the thesis for the development of a novel fabrication technique and the characterisation and analysis of both the ion transport and translocation of λ-DNA molecules.

In Section 2.1 the fabrication of solid-state membranes is presented, providing technical specification of pattern designs for photolithography, etching conditions and electron-beam evaporation. These processes are carried out on whole wafer substrates therefore allowing the fabrication of multiple samples simultaneously. Section 2.2 then discusses the set-ups and parameters used for milling and characterising the nanopores. This is followed by an overview of the storage and cleaning procedures employed to thoroughly clean the devices. Subsequently, Section 2.5 provides descriptions of the microfluidic cell design and electrode preparations. A list of all chemicals used in this thesis are then provided in Section 2.7.

2.1 Fabrication of free-standing silicon nitride membrane

The initial steps for preparing the free-standing membrane were carried out at the Cornell Nanoscale Science and Technology Facility and the National Nano Fabrication Centre (NNFC) by Dr. Jongin Hong, Dr. ChiWon Ahn and Mr. Kyungmin Kim. Standard four-inch double side polished Si <100> wafers with thickness of 350 $\pm$10 μm were used as the starting substrate. The whole fabrication process for producing the nanoporous membranes is illustrated in Figure 2.1.

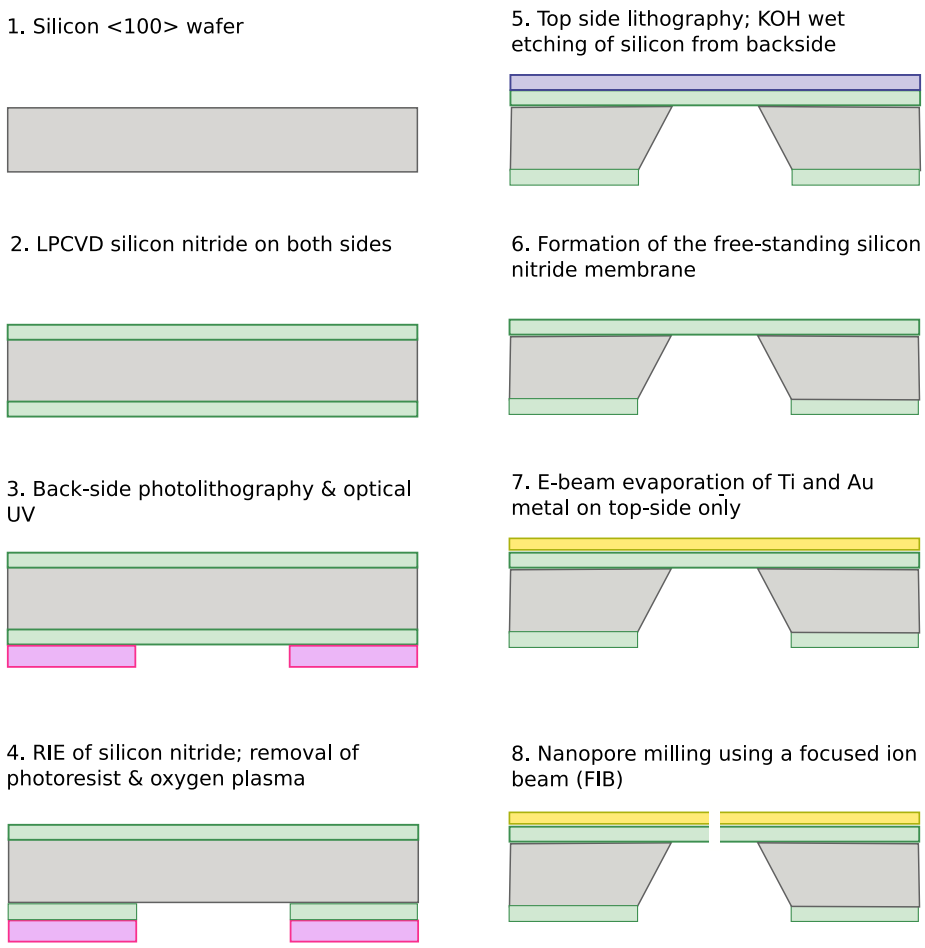


Figure 2.1: Main steps of metallic nanopore fabrication process, steps (1-8) are carried out on whole wafer substrates, the chips are then cleaved and nanopore milling is done on individual samples. (1) Starting with a double polished Si wafer, (2) Si_3N_4 is deposited on both sides of the Si wafer using LPCVD. (3) backside lithography is then carried out by exposure to UV for defining areas for Si_3N_4 etch. (4) Subsequently, reactive ion etching of Si_3N_4 and removal of photoresist is performed. (5-6) Following this, the front side lithography and KOH etching of Si is carried out for the release of the free-standing membrane. (7) Finally, Au/Ti films are thermally evaporated on the front-side of the wafer and then (8) circular shaped nanopores are milled from backside through the membrane with a focused ion beam.

2.1.1 Depositing silicon nitride films

A pre-requisite to making nanopores is the fabrication of solid-state free-standing membranes. The mechanical and electrical properties of the free-standing film directly affect the efficiency and quality of the fabrication of the nanopores, as well as the performance of the nanopores in studying biomolecule translocation. Silicon nitride (Si_3N_4) was chosen as the membrane material as its an excellent insulator with high resistivity (10^{16} Ω·cm) and dielectric strength (10 MV/cm), Gad-el Hak (2006). When sealed properly, Si_3N_4 provides gigaohm-range seal levels comparable to the traditional lipid bilayer used in patch clamping. This allows the detection of very low currents combined with the advantage of high mechanical stability of the membrane.

Si_3N_4 film is deposited on both sides of the silicon wafer using low-pressure chemical vapour deposition (LPCVD) at a temperature of 825 °C, using ammonia (NH_3) and dichlorosilane ($SiCl_2H_2$) gases (MRL Industries Furnace).

$$3SiCl_2H_2 + 4NH_3 \rightarrow Si_3N_4 + 6H_2 + 6HCl \tag{2.1.1}$$

The deposited film is a product of a chemical reaction between the source gases supplied to the reactor (Equation 2.1.1) which results in a silicon-rich nitride layer, with a tensile stress of 150 MPa. This is characterised using ellipsometry and FleXus stress measurements at 670 nm (scan wavelength). The stress is low enough to allow the formation of free-standing membranes. The thickness of the deposited nitride film can also be controlled with sub-nanometer resolution in the LPCVD process. Wafers with Si_3N_4 thicknesses between 50 nm upto 240 nm were produced as a starting substrate for all experiments conducted within this thesis.

Subsequently, multiple membrane templates (50 μm × 50 μm) are then fabricated on the silicon substrate wafer using standard photolithography techniques.

2.1.2 Device microfabrication

Device microfabrication combines photolithography, etching and electron-beam evaporation techniques. Photolithography is one of the most fundamental processes in semiconductor and MEMS manufacturing, combining high precision patterning with batch fabrication capabilities. Shadow masks protecting specific areas on the sample and exposing other areas allow precise control over microfabrication by selective photoresist removal and cre-

ating patterns of interest. Ultra-violet (UV) light passes through a mask onto a substrate, which is coated with a UV-sensitive photoresist. The light exposes the photoresist, which transfers the pattern from the mask to the substrate. The photoresist is developed in a chemical etchant, resulting in a polymer structure. This structure was used as a mask for subsequent processing steps including metal deposition and etching. Conventional photolithography is capable of producing features down to several hundred of nanometers, which is primarily dictated by the resolution of the mask and the wavelength of the UV light. Photolithography was used to define the areas for: (i) reactive ion etching of silicon nitride and (ii) wet etching of exposed silicon leading to the release of free-standing silicon nitride membranes. Electron beam evaporation was used to deposit nanometer thin layers of metal films. Further details of the techniques used are outlined below.

Patterns for photolithography

Photolithographical patterns were designed using the AutoCAD 2007 software (Autodesk, UK) and printed as a transparency shadow mask on polyester film. The pattern used for preparing free-standing silicon nitride membranes is shown in Figure 2.2. It consists of 240 chips with dimensions of 5 mm x 5 mm, this size was selected for ease of handling and to maximise the number of devices that could be prepared on a single wafer. These contain a smaller window size of 600 μm x 600 μm in the centre for defining the membrane template (used in the process for releasing the free-standing silicon nitride films). Two of the chips with their dimensions are exemplified in Figure 2.2 (*inset*) with a separation of 360 μm between each chip.

2.1.3 Photolithography

Photolithography was used to define square window patterns on the backside of the wafer for the fabrication of free-standing membrane. This was accomplished by coating a layer of photoresist, which was selectively exposed to UV light through an optical mask.

Megaposit SPR220-7 (Rohm & Hass, Germany) was exposed and developed for the patterning of membrane templates (windows 600 μm $\times$ 600 μm), which were etched by reactive ion etching in the next fabrication step. The wafers were spin coated with a primer of hexamethyl- disiloxane (HMDS, 30 s, 3000 rpm) promoted improved adhesion. This was followed by spin coating a layer of SPR220-7 photoresist, which was deposited

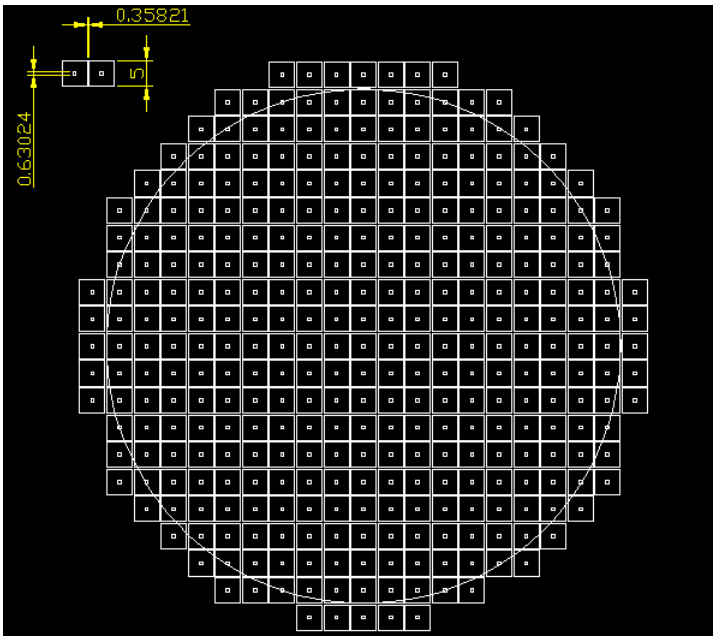


Figure 2.2: Photo-lithographic pattern for fabricating free-standing silicon nitride membranes. Whole 4 inch wafer pattern incorporating 240 functional chips. *inset*: example of 2 chips (enlarged) with dimensions of chip design with the outer square size of 5 x 5 mm and inner square size (membrane template from backside) of 600 μm x 600 μm. Initial CAD design by Dr. M. Kim, Drexel University, USA.

at a rate of 1.7 krpm. Samples coated with SPR220-7 were soft baked for 100 seconds at 90 °C and then additionally baked for 100 seconds at 115 °C, to ensure good adhesion of the layers to the substrate. This produced a resistive layer thickness of 10 μm.

The shadow mask with the desired pattern (Figure 2.2) was then aligned to the substrate, following the guidelines of the mask aligner used. The wafer was then exposed to the UV radiation for periods of 20 seconds. The pattern was developed by soaking the substrate in Microposit developer (LDD26W, Rohm & Haas, Germany) for 30 seconds, followed by rinsing with ultra pure water and blowing dry under a stream of nitrogen.

2.1.4 Etching

Once the membrane templates had been patterned on the wafer, two different etching methods were used to remove material to form the free-standing membranes: (i) dry etching, where ions bombarded the substrate and etched away the material in a vertical direction and (ii) wet etching, where the material dissolved when it was immersed in a chemical solution.

Reactive ion etching

The Si_3N_4 was removed from the patterned wafers using a technique known as reactive ion etching (RIE). In RIE, the wafer substrate was placed inside a reactor and the etching gas was introduced. A plasma was then created in the gas mixture using an RF power source, breaking gas molecules into ions. By applying a bias voltage, the ions were accelerated towards, and reacted at, the surface of the substrate etching away the material in a vertical direction. The etching was carried out using the RIE 10NR (Samco) at 8 mbar (CHF_3 50, O_2 2.5 sccm, 50 W) with an etching time of approximately 60 minutes.

Wet etching

Following this, the front-side of the wafer was coated with a thick layer of photoresist. Then using the Si_3N_4 as a mask, the exposed Si substrate was anistropically etched in potassium hydroxide (KOH, Sigma) solution (30 wt., 80 °C, etching time, $\sim$ 8 h), yielding free-standing 50 x 50 μm^2 membranes.

2.1.5 Electron-beam evaporation

With the aim of preparing metallic nanopore structures, metal films were deposited on pre-fabricated Si_3N_4 membranes. The metal evaporation was performed in high vacuum (< 2 x 10^{-6} Torr) using an electron beam evaporator (KVE T-C500200, Korea Vacuum). Electron-beam evaporation is a form of physical vapour deposition in which a target surface is bombarded with an electron beam, given off by a charged tungsten filament under high vacuum. The electrons in the beam carry high kinetic energy, which at collisions with atoms in the solid target surface transform their kinetic energy into heat. As a result, this process can in very short time melt and transform the target atoms into the gaseous phase. These atoms then precipitate into solid form, coating everything in the vacuum chamber (within line of sight) with a thin layer of the anode material, Movchan (2006).

Metal evaporation was carried out on the front-side of the pre-fabricated wafers. First, a 10 nm titanium (Ti, 99.99%, Testbourne Ltd) film was deposited onto the wafer. This was followed by the deposition of either 50 nm or 100 nm thick gold layer (Au, 99.999%, Good Fellow) on top. Ti was used as the adhesive layer as it readily formed nitrides and oxides with adjacent layers, thereby improving the adhesion between the gold and silicon nitride layers, Gad-el Hak (2006). Au metal was employed because of its high electrical conductivity, which enabled for enhanced sensitivity. Additionally, Au is ex-

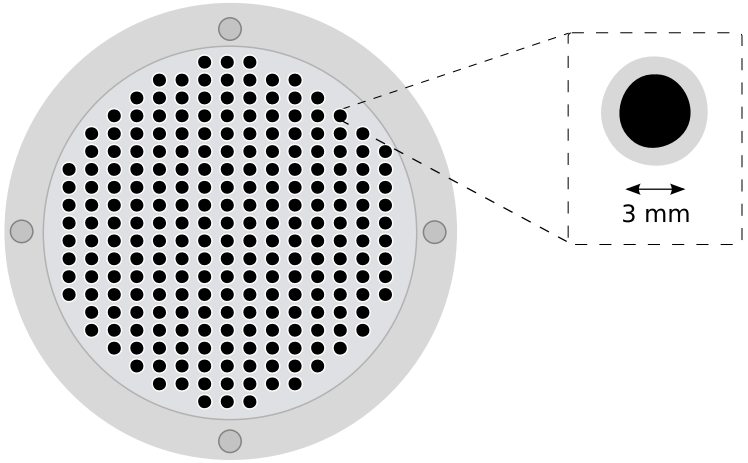
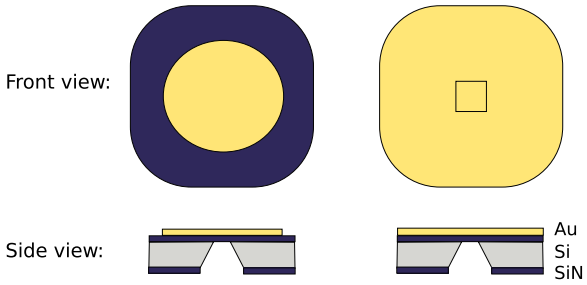


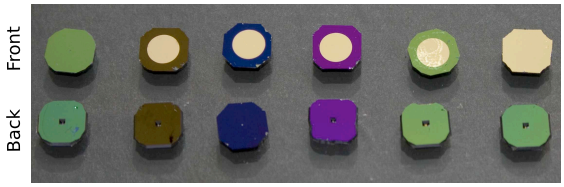
Figure 2.3: Geometry of the shadow mask used for the selective deposition of Ti/Au layers. In the centre of each 5 mm chip, 3 mm holes are milled into the metal plate shadow mask as shown and the structure is aligned to the 4 inch fabricated wafer. The final construct is sealed from the edges using screws to secure the wafer inside.

tremely biocompatible and its surfaces can be easily modied using SAMs, allowing for the direct immobilisation of thiolated probes (as discussed further in Chapter 5). The film thicknesses and evaporation rates were monitored by a quartz crystal microbalance. Two different chip structure were created following e-beam evaporation: (i) Au/Ti deposited as 3 mm circular shape at the centre of each 5 mm chip with the use of a shadow mask, Figure 2.3, (ii) whole wafer deposition, where the entire 5 mm area of each chip was covered with the Ti and Au layers from the front-side.

5 mm x 5 mm sample chips were then prepared by cleaving the final fabricated wafer. The cleaving was carried out using a diamond tip scribe at the flat edge of the wafer in one chosen direction. This involved holding the wafer in place by placing a ruler (or a microscope slide) on top of the polish side and making a scratch across the wafer in a chosen direction along the edge of the ruler (or microscope slide). The wafer was then cleaved by gently rolling the diamond tip scribe over the scratch but on the opposite side of the wafer. The sequence was repeated for all the remaining chips on the wafer. Due to the intrinsic brittleness of the silicon wafer, special care had to be taken to prepare samples of a uniform shape. The substrates were subjected to solvent cleaning to remove dust and organic impurities. Figure 2.4 shows a schematic of the individual chip structures produced and an image of the different chips designs used throughout this thesis.



(a) Geometry of the 2 different chip structures produced after e-beam evaporation.



(b) Image of various chip designs used throughout this thesis. The different colours correspond to the thickness of LPCVD grown Si_3N_4.

Figure 2.4: (a) Schematic diagram and (b) image of nanopore chip structures used throughout this thesis.

2.2 Fabrication of nanopores

Various techniques have been employed to create solid-state nanopores with the most popular being the use of a focused ion or electron beam for fabricating pore diameters below 50 nm. In this thesis, nanopores were fabricated using the focused ion beam technique for: (i) pore shrinking experiments using Pt deposition (ii) comparative ion transport studies of bare silicon nitride and gold coated nanopores and (iii) DNA translocation experiments. Nanopores with diameters between 20-150 nm were fabricated in pre-patterned bare Si_3N_4 and Au coated Si_3N_4 membranes. The following section outlines the technique and the parameters used for milling.

2.2.1 Focused ion beam technique

The focused ion beam is a tool commonly used for the imaging and dissection of semiconductor devices. Its operation is based upon a focused beam, which is is rastered across the material surface, emitting secondary electrons that are detected and synchronised with a

TV signal to form an image. During this research a Carl Zeiss 1540 Crossbeam system, as shown in Figure 2.5 was used. The system comprises of a Gemini SEM column with an add-on Orsay Physics Canion 31 FIB column. Both beams share the same vacuum space and hence all the fabrication and visual characterisation can be done in a single run without breaking the vacuum and without exposing the sample to air during the process.

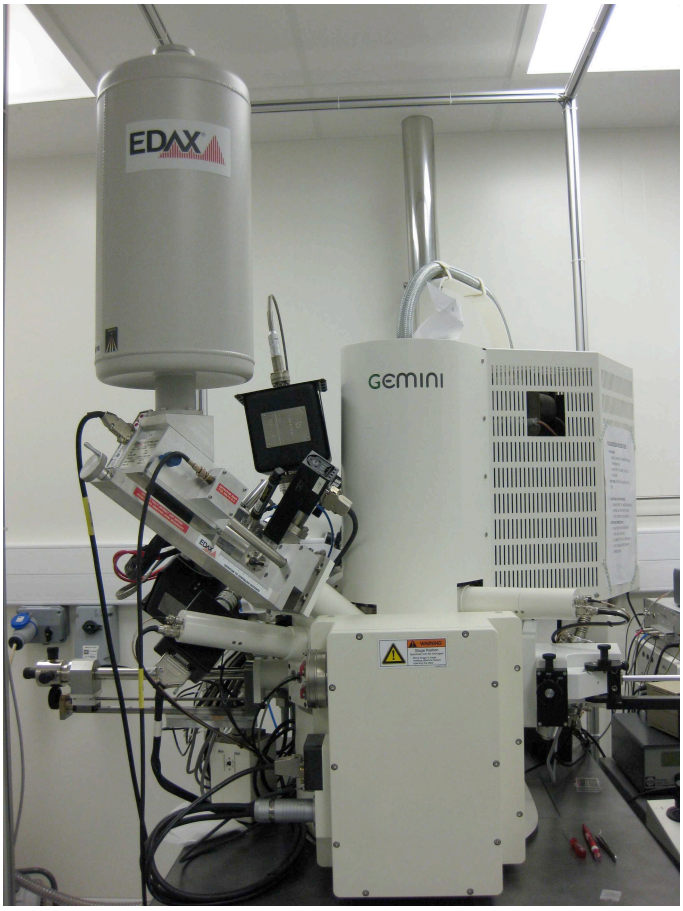


Figure 2.5: Cross-beam Leo 1540 at the London Centre of Technology, UCL. The SEM column is vertical, labelled Gemini. The FIB column is mounted 54° from the vertical axis on the left. The system also has an energy dispersive X-ray spectroscopy system; the coolant storage tank is shown in the picture labelled EDAX.

The FIB produces and directs a stream of high-energy ionised gallium atoms (Ga^+), focuses them using electric fields and directs them onto the sample for both milling and imaging. These Ga^+ ions are large and energetic enough to allow the sputtering/etching of material from the incident surface. The membranes were initially exposed to an oxygen plasma (SPI Plasma-Prep II) and directly mounted onto the FIB stage, using carbon tape (G3939, Agar Scientific) with the backside of the membranes facing up. Each membrane

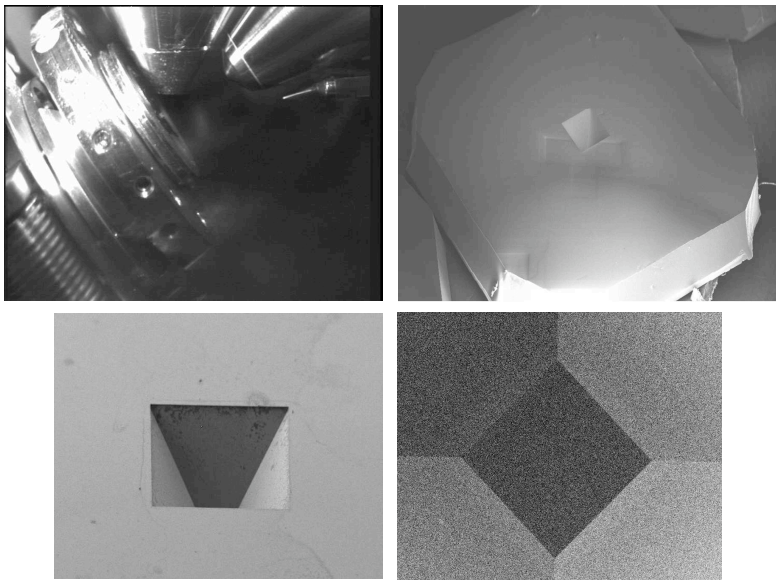


Figure 2.6: *Top left,* TV image of the FIB chamber showing the SEM and FIB columns aligned to the sample stage at 54°, with a working distance of 5 mm; *Top right*: SEM image of the whole 5 mm chip from backside (140 x magnification) and *Bottom*: SEM and FIB image of free-standing membrane from backside once the beams are aligned (at 2 Kx and 10 Kx, respectively).

was then grounded using thin carbon tape leading from the edge of the membrane onto the stage. Following this, the FIB and SEM beams were aligned by adjusting the stage at an angle of 54°, with a working distance (WD) of 5 mm. This allowed for the milling and imaging to be recorded simultaneously. A TV image of the configuration inside the chamber is shown in Figure 2.6.

2.2.2 Milling parameters

Feature-mill software, incorporated in the milling operation, allowed the creation of complex designs by milling of geometry such as circular/polygon shapes and text. Circular holes with defined dimensions were created using this software. The parameters for milling these included magnification, dwell time (milling time per pixel) and beam current. In this mode the ion beam could scan in a line from one side to the other in the user defined object displayed on the computer screen. The dwell time of the beam exposure was calculated by using the milling time, the size of the milling object, the increment style and the number of layers. The beam movement was controlled by two scanning frequencies, (i) X scan, for control in horizontal direction and (ii) Y scan, for vertical control. To

achieve a sufficient small beam diameter, the ion acceleration voltage was set to 30 keV and the milling current to 1 pA. This resulted in a probe size of 8 nm and provided better resolution than higher currents.

The magnification was another parameter which affected the resolution of the patterning as it defined the field area within a 1024 x 1024 pixel array. For obtaining nanopores with diameters of less than 50 nm, a magnification of over 100 Kx was used. Furthermore, the focus and stigmatism of the ion beam were carefully adjusted, and the quality of the beam was checked by drilling holes in a sample membrane. Figure 2.7 shows typical nanopores milled using the FIB with diameters of 25; 45; 70; and 100 nm ±5 nm, measured using the scale feature in the FIB software. As various thicknesses of Si_3N_4 and Au/Si_3N_4 were used, the parameters were adjusted accordingly to ensure the beam was able to mill all the way through the membrane to create the nanopores.

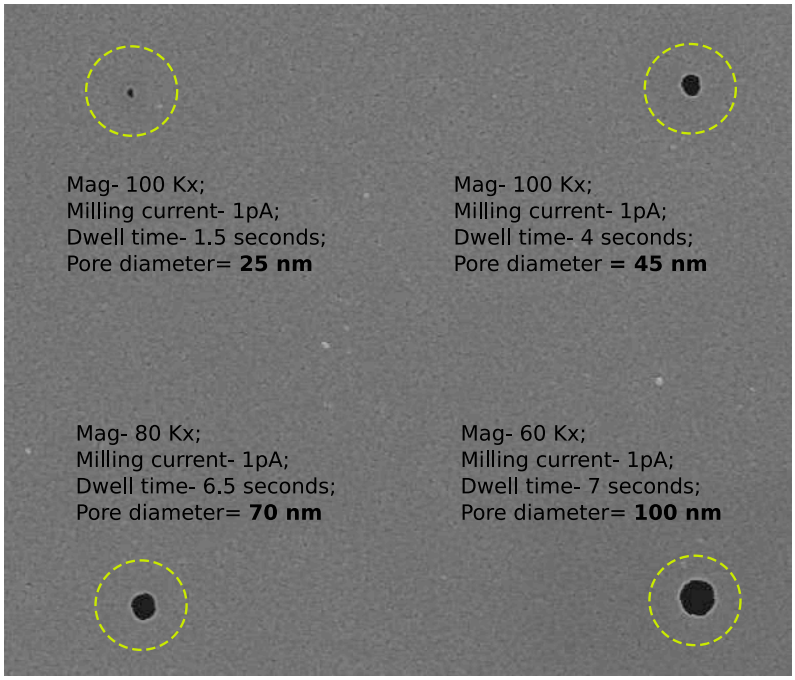


Figure 2.7: SEM images of nanopores milled using the focused ion beam technique. The image is of 4 different pores milled through a Au/Si_3N_4 membrane. The parameters used for milling were adjusted according to the final pore size required. Magnification of image set to 30 Kx.

2.2.3 Problems encountered during nanopore fabrication

The ion beam milling procedure discussed above although straightforward, had three specific problems which occurred repeatedly:

Residual layers due to un-etched Si_3N_4 and cracks in the membrane

The whole procedure of photolithography and reactive ion etching would ideally result in a sample with a free-standing membrane having clean pyramidal walls ready for FIB processing as shown in Figure 2.6. However, at times the resulting devices had residual layers of un-etched Si_3N_4 or cracked edges which had been damaged during the microfabrication process and therefore it was not possible to mill nanopores in these devices. Two such sample are shown in Figure 2.8. If we compare this sample with the one shown in Figure 2.6, we see that the width of the membrane and the sidewalls are rough and uneven and the free standing membrane show cracks which made the membranes non-functional.

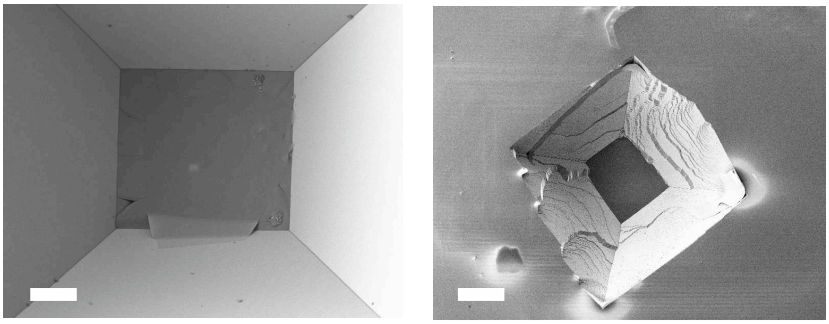


Figure 2.8: SEM images of membrane. *Left*: from backside, showing residual layers covering the membrane and cracks on the edges, scale bar 20 μm. *Right*: incomplete etching of Si results in uneven edges, scale bar 100 μm.

Sample charging in FIB

The FIB uses ionised gallium for imaging and milling. So when these charged ions strike an insulating surface or a conductor which is not properly grounded, a charge starts to build up, Shaffner and Veld (1971); Zeiss (2007). One immediate effect is instability in the FIB imaging and milling. The FIB image starts to move depending on the severity of the charge build up. To avoid sample charging, the sample needs to be properly grounded. Initially, silver paint (G3648, Agar Scientific) was used to ground the chips to the SEM stub. This provided a very good and quick grounding mechanism. One problem realised on repeated

application and removal of silver paint was the presence of stray particles of silver paint on the thin films. These stray particles caused severe charging and depending on their location, it was not possible for the nanopores to be milled in the membrane. To avoid this problem, silver paint was replaced by conducting carbon tape (G3939, Agar Scientific) which could be easily applied and removed and the charging reduced significantly.

Thinning of material

During the milling process, it was realised that if a certain area was scanned above 50 Kx magnification for more than 10-15 seconds, the beam started to erode away the material from that location, due to the high beam intensity. Another phenomena was detected after the milling step, where close inspection of the nanopore FIB and SEM images revealed that the nanopore orifice was surrounded by a 'halo-like' ring (Figure 2.9). Across this ring region, the contrast gradually darkened until it reached the grey value of the Si_3N_4 membrane.

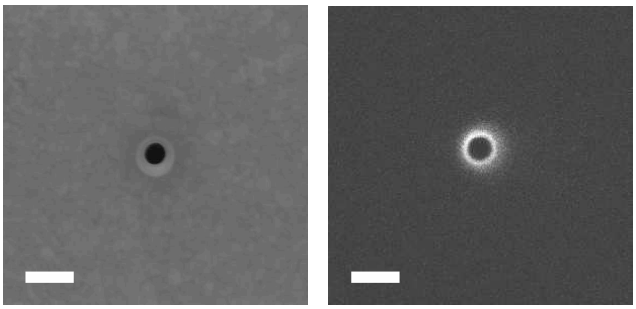


Figure 2.9: Thinning of material around the periphery of the nanopore. *Left*: SEM image from the Au (front-side) of a 60 nm pore. *Right*: FIB image of the same pore (Si_3N_4, back-side) with a white halo ring around the edges exhibiting the contrast variation observed after milling.

Due to the amorphous nature of Si_3N_4, the observed contrast could be dominated by the variation in mass-thickness. Mass-thickness contrast arises from incoherent elastic scattering of electrons. So during imaging as the electrons go through the specimen, they are scattered off axis by elastic nuclear interactions (Rutherford scattering), Reimer (1998). So it is expected that high-mass regions of a specimen would scatter more electrons than low-mass regions of the same thickness. Similarly, thicker regions will scatter more electrons than thinner regions of the same average mass, (Goodhew and Humphreys, 2001). Therefore thicker and/or higher mass areas will appear darker than thinner and/or

lower-mass areas. The specimen thickness can also be related to the attenuation of the transmitted intensity by-

$$\Delta I/I_0 = 1 - e^{-Q\Delta t} \quad (2.2.1)$$

where, Q is the total elastic scattering cross-section depending on the atomic number Z, and Δt is the thickness change. Therefore, the bright halo-like ring indicated that the periphery of the nanopore was surrounded by a membrane region of decreased thickness.

Spatial resolution of FIB

The ability of FIB to mill quickly through an arbitrary material was derived from the sputtering mechanism by which atoms are ejected from the surface and the near surface of the target, Orloff et al. (2005). The sputter yield, defined as the number of atoms ejected per incident ion, is high (typically >2) for 30 keV Ga^+ impinging on most materials. This is because the incident ion can transfer much of its kinetic energy to a target atom, and thereby overcome the surface binding energy, E_s , or the bulk displacement energy, E_d.

Modelling the interaction between an incident ion and a target atom as an elastic two-body collision, the maximum transferrable energy, E_{max}, is found to be (Landau and Lifshitz, 1976):

$$E_{max} = \frac{4M_1M_2}{(M_1+M_2)^2}E_0 \quad (2.2.2)$$

where E_0 is the kinetic energy of the incident particle, and M_1 and M_2 are the masses of the incident ion and the target atom, respectively. Equation 2.2.2 indicates that the incident kinetic energy can be most efficiently transferred to the target when the masses of the incident and target atoms are closely matched. Nevertheless, hundreds to thousands of electronvolt are transferred in typical collisions with 30 keV Ga^+ ions, even for targets with dissimilar masses.

Although the sputtering process makes FIB milling effective, it also limits the spatial resolution that can be achieved. The 30 keV energy of incident Ga^+ ions from an FIB greatly exceeded E_s and E_d, which are typically several electronvolt. A single incident ion therefore generates a cascade of collisions within the target, in which many atoms became displaced or sputtered. The lateral extent of the collision cascade is typically about 10

nm. Hence milling structures with critical dimensions in the single nanometer range can become extremely difficult.

2.3 Sample characterisation

Microscopic and spectroscopic techniques were used to characterise membranes and nanopores both at the micro- and nanometer scale. The use of all the techniques presented below were essential in controlling the device fabrication reproducibility.

2.3.1 Optical microscopy

Optical microscopy was used for initial sample characterisation (e.g., general cleanliness, uniformity of Au/Ti layers and calculation of dimensions) and for membrane visualisation using DIC mode. Optical microscopy was conducted using an Olympus DP71 light microscope, with magnifications in the range from 5 x to 100 x, connected to a computer provided with digital image capture software.

2.3.2 Field Emission Scanning Electron Microscopy (FE-SEM)

A high resolution FE-SEM (Leo Gemini 1525) was used routinely for 2D imaging of nanopore and membrane surfaces. It allowed characterisation of film uniformity and quantitative calculations of large areas with a resolution down to a few nanometers. Image contrasts observed in SEM were formed by local potential difference between different material surfaces, which was caused by differential charging, Wells (1974). Substrates were fixed to a SEM stub using carbon adhesive pads (G3347N, Agar Scientific). The optimal conditions for imaging were low beam current, low magnification, low accelerating voltage and relatively high scan speeds.

Au/Si_3N_4 films and Pt depositions were visualised with the FE-SEM at 5 keV or 10 keV, with a working distance (WD) of 5 mm. High magnification images (above 100 Kx) were used for characterising individual nanopore dimensions using the scale bar feature provided on the software.

In comparison to the amorphous Si_3N_4 surface, when scanning from the front-side of gold coated membranes, the polycrystalline gold films exhibited strong contrast variations in SEM images, resulting from Bragg reflections of randomly orientated crystalline grains within the Au film, Goodhew and Humphreys (2001). Nanopores were located under the

SEM by increasing the EHT voltage to 20 keV at low magnification, which accelerated the electrons through the column and resulted in a higher contrast with the Si_3N_4 membrane showing up as a faint square outline, Figure 2.10.

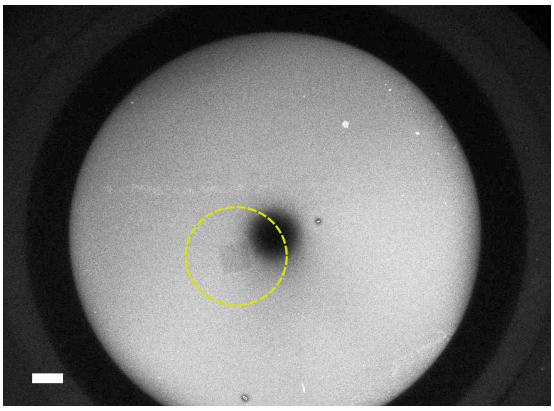


Figure 2.10: SEM image of a Au/Si_3N_4 membrane (front-side). A faint square outline of the Si_3N_4 membrane is seen at 120 x magnification as the EHT value is increased upto 20 keV, resulting in the membrane becoming more visible for tracking. Scale bar= 50 μm.

Elemental analysis using the FE-SEM

The SEM was also fitted with the Oxford Instruments INCA energy dispersive x-ray spectrometer (EDXS), which allowed for the chemical composition studies of the membrane films. EDXS analysis was carried out for comparative studies in Au coated and Pt deposited nanopores.

2.3.3 Scanning Tunnelling Microscopy (STM)

STM was used as a non-invasive technique to study the surface topography and roughness, and to estimate grain size of metal deposits. It also allowed for a general assessment of the deposit growth quality and reproducibility. STM measurements were carried out using Agilent 5500 STM (Agilent Technologies), equipped with a 1 μm x 1 μm x 0.7 μm scanner and an electronics module. The STM was positioned inside a Faraday cage and placed on a vibration isolation table. A hermetically sealed, top-down configuration was used which provided complete isolation of the electronics and scanning elements from the imaging environment.

The nanopore chip was mounted onto a stand-alone sample plate and connected to the module. Manual mirrors were used to allow lateral positioning of the tip relative to

the substrate. Tungsten (W) STM tips were employed in these measurements, prepared in-house electrochemically using KOH etching. Areas ranging between 50 nm^2-1 μm^2 were analysed with a current setting of 1 nA and scan rates between 0.6-0.8 nm^2 s^{-1}. All measurements were taken using the PicoImage^{TM} software, provided with the instrument.

The principle of operation was based on a feedback loop. An extremely sharp W tip was brought in close proximity of the membrane surface. Electrons tunnelling between the surface and the tip, produced an electrical signal. The tip slowly scans across the surface at a distance of only an atom's diameter. It is raised and lowered in order to keep the signal constant and maintain the distance. Recording the vertical movement of the tip made it possible to study the structure of the surface. A profile of the surface was then created and from that a computer-generated contour map of the surface was produced. Processing of all STM images was carried out using WSxM 5.0, Nanotec software.

2.4 Electrochemical characterisation

Electrochemical measurements were carried out throughout the thesis for various characterisation purposes including: (i) Pt electrodeposition studies of film uniformity (ii) ion transport properties across Si_3N_4 and Au coated nanopores and (iii) initial control experiments for DNA translocations. In all measurements the reference electrode (RE) was a silver wire with a silver chloride coating, Ag/AgCl (detail for the preparation of these electrodes is provided in Section 2.4.2) and platinum wire was used as the counter electrode (CE) for the characterisation studies on platinum electrodeposition. Cyclic voltammetry (CV) and chronoamperometry (CA) were conducted using commercially available potentiostats; 760C bipotentiostat from CH Instruments, (Texas, USA) and Reference 600 from Gamry (PA, USA) with the relevant software provided. CVs were recorded by applying a voltage to the RE electrode and measuring the current flowing through the working electrode (WE). CA in bipotentiostatic mode was utilised in Pt electrodeposition studies.

DNA translocation experiments required sensitive electrical equipment to measure the small currents passed by individual pores. For this an Axopatch 200B patch-clamp amplifier (Molecular Devices) with a 16-bit digitiser (1440A, Molecular Devices) was employed. Detailed descriptions of all set-ups adopted in this thesis are given in the relevant chapters.

2.4.1 Faraday enclosure

All electrical recording experiments were carried out in a conducting enclosure (Faraday cage) to shield the sensitive acquisition electronics from external electrical noise. Steel or aluminum boxes, ∼80 x 60 x 60 cm in dimensions with rigid side-walls >1 mm thick were used throughout the thesis. For low ionic current measurements, the faraday cage was grounded via the common ground in the patch-clamp amplifier. Vibration isolation was an important consideration in these measurements as external noise (e.g., from other laboratory equipment) could be transmitted through a laboratory bench into the box and resulted in substantial noise in the signal.

Therefore the Faraday cages were mounted onto anti-vibration tables. Finally, it was essential that the electrodes within the box were: (i) as short as possible (to reduce access resistance) and (ii) firmly secured, to prevent their vibration. While a single Faraday cage was effective at isolating the system from external noise, a secondary Faraday cage was used to shield the experimental set-up inside and to minimise any internal sources of noise.

2.4.2 Preparation of electrodes

In most nanopore studies, silver/silver-chloride (Ag/AgCl) electrodes have been used in conjunction with KCl-rich solutions for the transport of ions across the nanopore. The electrodes are reversible as they allow current to flow in both directions. However, under a constant applied potential, there is one dominant reaction for each of the Ag/AgCl electrodes:

- At the anode: $Ag(s) + Cl^- \rightarrow AgCl(s) + e^-$
- At the cathode: $AgCl(s) + e^- \rightarrow Ag(s) + Cl^-$

Ag/AgCl electrodes were employed in all ionic current recordings (Chapter 5) and electrodeposition experiments (Chapter 4) due to their long-term chemical stability, predictable junction potentials, and superior low-noise electrical performance (Ives and Janz, 1961 and Axon-Guide).

Ag/AgCl electrodes were prepared from Ag wire by either: (i) chlorodisation in 500 mM HCl solution using Pt wire as the counter/reference electrode or (ii) treatment with a weak hypochlorite solution (Axon-Guide and Purves, 1981). The preferred approach was chlorodisation, as the thickness of the AgCl coating could be controlled easily, resulting in high reproducibility. Electrodes were produced from 250 μm diameter silver wire

(<99.99%, Sigma-Aldrich), using lengths of 30 mm. These electrodes had a large reactive surface area, which prolonged their working life and minimised the access resistance.

Before treatment, the electrodes were thoroughly cleaned and roughened by abrasion using emery paper, and then immersed in 1% (w/v) NaClO (Fisher Scientific) in water. After treatment, the electrodes were rinsed with distilled water. The electrodes were then stored in the dark to prevent UV conversion of AgCl back to Ag. It was observed that good electrodes had a rough texture and a dull grey colour.

Immediately before use, the electrodes were electrically balanced in solutions of the experimental buffer by either: (i) using the open circuit potential (OCP) technique of the potentiostats, or (ii) using the pipet offset function on the patch-clamp amplifier, before carrying out DNA translocation experiments. Little to no potential adjustment was required for good electrodes. A sign of poor or degraded electrodes was the development of white patches and a requirement to rebalance the potential offset.

Pt wire (2 mm in diameter, 99.99% Sigma Aldrich) was used as the counter electrode in electrodeposition characterisation experiments in a standard three electrode cell and as the anode in the chlorodisation of Ag/AgCl electrodes.

2.5 Microfluidic flow cell

A microfluidic flow chamber was required for successful and reliable single channel recordings. Furthermore, a flow cell simplified the fast exchange of solution buffers during the experiment. Several considerations were taken into account when designing the cell. Firstly, the chip must function as a membrane barrier between two solutions such that the nanopore would be the only junction between the two solution compartments. Secondly, each compartment should be able to accommodate an electrode so that an electrophoretic force can be applied on the molecules. Finally, measurements involving the potentials applied at the nanopore, required an electrical connection to the membrane surface for which specific, easily accessible inlets were crucial.

In our experiments, PTFE (Teflon®) was used as the material for a vertical cell design. This was made up of two part; top (*cis*) and bottom (*trans*) chambers. A dielectric constant of approximately 2.1 (Dupont, 2005) made Teflon an excellent material to prevent charge transfer between the two chambers. The nanopore chip was mounted at the bottom of the *cis* chamber and a circular glass coverslip was affixed at the bottom of the *trans* chamber, which allowed for visual inspection. A 1 mm hole drilled into the side of the

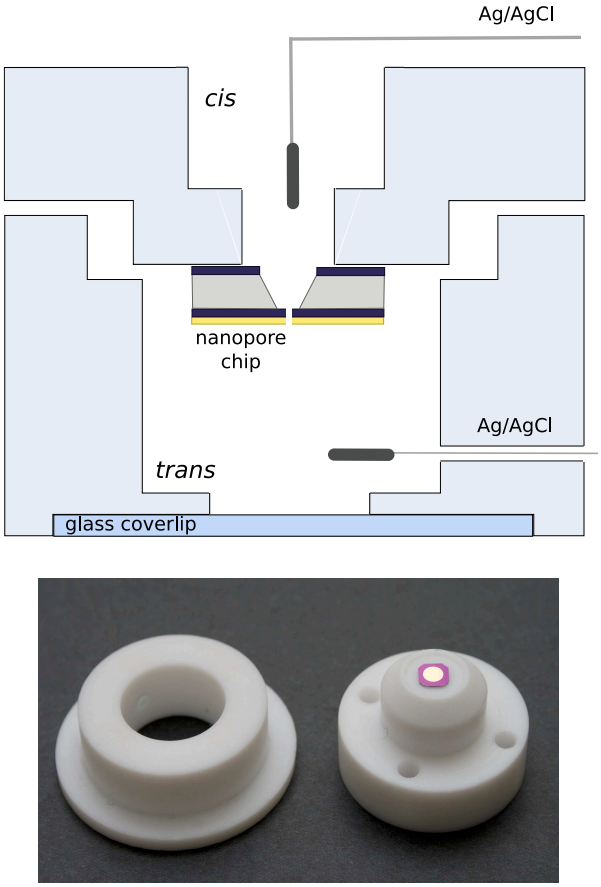


Figure 2.11: Microfluidic flow cell. *Top*: a schematic illustration of the generic flow cell used throughout the thesis. Cell chambers are made from PTFE. Thin layers of kwik cast epoxy are used to mount the nanopore chip and the circular glass coverslip to the chambers. The nanopore acts as the only junction between the *cis* and *trans* chamber solutions. Ionic current through the nanopore is measured using two Ag/AgCl electrodes immersed in the two chambers as shown. 0.5 mm grooves are milled into the sides of the *cis* chamber to allow for electrical contact to the Au coated membrane. The electrodes inlets are sealed with the epoxy and the platform is tested for leaks before measurements. *Bottom*: image of the two chambers components that make up the microfluidic cell, the nanopore chip is mounted on the *cis* chamber as shown.

trans chamber allowed for an electrode to be placed in the bottom solution. Another hole was drilled into the side of the *cis* chamber to insert the top electrode into.

A schematic of the generic cell assembly used throughout this thesis is shown in Figure 2.11 along with an image of the PTFE microfluidic cell. If changes have been made, these will be described in the relevant chapters.

2.5.1 Assembly

As the solid-state nanopores were fabricated in a vacuum, subsequent wetting was problematic. Generally, LPCVD deposited silicon nitride surfaces are hydrophobic to prevent adsorption of organic and other non-polar species from the air, Gad-el Hak (2006). Due to this reason the nanopore surfaces are difficult to wet. Bubbles and other sources of contamination also introduce fluctuations and therefore need to be avoided. To introduce an aqueous environment to the pore, a clean, hydrophilic surface is required. This was accomplished in a reproducible way by appropriate cleaning and assembly techniques as outlined below, Figures 2.12 and 2.13. The protocol used for pore wetting was adopted from Selvin and Ha (2008).

The nanopore chip was exposed to an oxygen plasma for ∼4 mins, from each side (SPI Plasma-Prep II) and then mounted at the bottom of the *cis* chamber using a silicone epoxy (Kwik-Cast, World Precision Instruments). This was applied using tweezer tips and the epoxy cured in less than 10 minutes, making it very easy and quick to work with. Immediately following curing, the chip was wetted to avoid any accumulation of dust. This was done by applying ∼5 μl of propan-2-ol to the *cis* side of the chip and then by turning the chip, the trans side was also treated with propan-2-ol. The pore wetting process is illustrated in Figure 2.13.

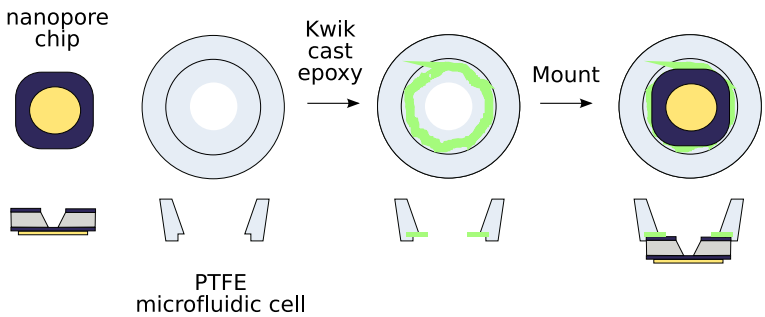


Figure 2.12: Scheme for sealing the nanopore chip onto the microfluidic cell.

For Au coated nanopores where an electrical contact was required at the membrane surface, thin gold-plated adhesive film (250 μm thick, 3M Farnell) was used. The adhesive film was affixed at the edge of the membrane leading out from the side of the chamber where specific grooves were machined onto the Teflon to guide the connection towards the outlet.

Ag/AgCl electrodes were then inserted from the inlets and sealed with the kwik-cast epoxy. KCl buffer solution was then added to both sides and the nanopore chip was flushed several times to ensure removal of the methanol and to obtain fluidic combinations that were miscible. Finally the cell was filled with the KCl buffer solution (~2 ml volume on each side) and the *cis* chamber containing the nanopore was fitted into the *trans* chamber.

To disassemble the cell, small tweezers were used to carefully pull out the Ag/AgCl electrodes from the inlets. The *cis* chamber containing the nanopore chip was removed and rinsed thoroughly with distilled water. The chamber was then immersed in hexane for the kwik-cast epoxy resin to swell, after which the chip was released and cleaned for storage. Same method was used for the *trans* chamber, which was directly immersed in hexane to remove the glass coverslip and any remaining residues of the epoxy resin.

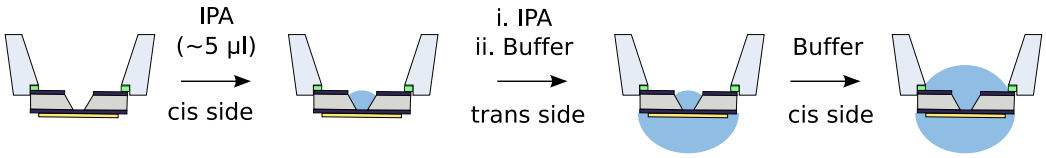


Figure 2.13: Steps for wetting the nanopore. Propan-2-ol (IPA) was used as the wetting agent, following this, the chambers were flushed with KCl buffer from both sides.

2.5.2 Cleaning of microfluidic cell

A 3:1 mixture of concentrated sulphuric acid (H_2SO_4, Sigma) to 30% hydrogen peroxide (H_2O_2, Sigma) (known as 'piranha solution') was used to clean the microfluidic cell components (teflon compartments; circular glass coverslips) and the process was carried out in a fumehood. Once the mixture was stabilised, it was further heated to 65 °C to sustain its reactivity. The hot solution was used to remove any organic contaminants on the microfluidic cell surfaces from previous experiments. The process usually required 20-30 minutes, after which time the parts were removed from the solution and washed

thoroughly in distilled water, followed by ethanol rinses. Due to the self-decomposition of hydrogen peroxide, the piranha solution was freshly-prepared for each use and the waste solution was then neutralised and disposed *in situ*.

The components were then dried thoroughly under a stream of nitrogen. When required, detergent washing steps, NaOH (1 M) or HCl (1 M) washes, or rinsing with an EDTA solution (e.g., 10 mM) to remove traces of divalent metal ions were also employed.

2.6 Testing nanopores

The current-voltage (I-V) characteristics of each nanopore were checked prior to any experiments. Nanopores typically exhibit ohmic I-V curves in the range of ±500 mV. Cyclic voltammetry was carried out to check if the resistance R of the nanopore was more than a factor of two from the expected resistance calculated using the following equation for cylindrical nanopores:

$$R = \rho \left(\frac{h}{\pi r^2} + \frac{1}{2r} \right) \tag{2.6.1}$$

Where, ρ was the resistivity of the salt solution (depending on the concentration used), r the radius of the nanopore inferred from the SEM measurements, and h, the nominal thickness of the membrane (in our case, 50-350 nm depending on the membrane, i.e., bare Si_3N_4 or coated with Au/Ti). If the resistance observed was higher than the expected value, the nanopore was replaced. Detailed ion transport characterisation studies of nanopores used in this thesis are presented in Chapter 5.

2.6.1 Handling and storage of nanopores

Due to the robust materials used to construct these structures, the nanopores used in this thesis were highly stable. Pores fabricated using FIB could be used repeatedly and upto several weeks whilst withstanding extreme conditions such as high salt concentrations, pH and temperatures. Nanopores were handled with small Delrin tweezers (TedPella, Inc) to prevent scratches to the surface. However at times working with thin membranes (< 200 nm thickness; Si_3N_4; Au films) resulted in cracks being observed. Furthermore the nanopores became blocked during measurements. Some of the most common problems encountered during measurements included: (i) no ionic current through the nanopore or very high currents, (ii) air bubble formation at the surface or (iii) presence of KCl crystals

which at times blocked the area where the nanopore was located. The following section describe the respective diagnoses and solutions that were implemented.

(i) No ionic current through nanopore: If there were problems with the electrical signal, first the electrodes were tested to make sure they were balanced and not degraded, next the soldering connection of these to standard electric wire was tested using a standard multimeter (IsoTech). If a nanopore showed high noise features or large capacitive behaviour, randomly changing conductance levels or total blockades of ionic current, the device was replaced and the experiment was restarted.

(ii) Small air bubble formation at the nanopore surface: This could normally be seen by eye and was either flushed away or exposed to an oxygen plasma. This had to be done carefully to avoid breaking the membrane containing the nanopore. Initial care was taken by degassing the buffer solution before the experiments; this was done by placing the solution into a vacuum flask and removing the gas with a vacuum pump. An ultrasound bath (at low setting) was also used to help remove dissolved gases.

(iii) Presence of KCl crystals blocking nanopores: It was important to make sure all buffer solutions were filtered using 0.02 μm filter to prevent crystallisation. However if crystals were observed at the nanopore or in the set-up, the nanopores were flushed with KCl several times and the chambers were refreshed with a new batch of buffer.

Nanopores were stored in small plastic boxes containing thin polyurethane membranes (Agar Scientific) and were ideal for the safe transit of these devices. The membrane films were highly elastic and chemically inert and were able to deform around the individual 5 mm devices and hold them firmly in place. Between experiments, the nanopores were rinsed with ethanol solution and dried in nitrogen air. Following this they were cleaned in an oxygen plasma and were stored in ethanol solution in individual vials for next use.

2.7 Chemicals and Solutions

All gases, solvents and chemicals used throughout the thesis are listed in Tables 2.1 - 2.3. All solutions were prepared using high impedance deionised Milli-Q water (resistivity 18.5 MΩ cm at 22°C $\pm$2°C) and filtered through 0.02 μm filters (Anotop, Whatman, Maidstone, UK) prior to use. The compounds were weighed on a four figure analytical balance (ABS265-s Mettler-Toledo). All pH measurements were taken using a standard S20 pH meter from Mettler Toledo, calibrated using buffer solutions of pH 4, 7 and 9 (Sigma Aldrich).

Chemical	Supplier	Grade
Acetone	Sigma	ACS reagent ≥99.5%
Propan-2-ol	Sigma	ACS reagent, ≥99.5%
Ethanol	Sigma	ACS reagent, ≥99.5% absolute
Hexane	Sigma	ACS reagent ≥99.5%

Table 2.1: List of solvents used in this thesis.

Chemical	Supplier	Grade
Oxygen	BOC gases	99.95%
Argon	BOC gases	99.999%, high purity
Nitrogen	BOC gases	99.999%, high purity

Table 2.2: List of gases used in this thesis for (i) electrochemical characterisation studies and (ii) general fabrication and cleaning purposes.

2.7.1 Potassium Chloride (KCl) solution

All experiments throughout this thesis were carried out in KCl salt solution. Because of possible contaminants, the KCl and other buffer components were of highest possible purity. KCl from Fluka (>99.99%) was used which contained less than 0.0005% of trace metals. An aqueous 3 M stock solution of KCl was prepared in water. This was left for 1 hour on a magnetic stirring plate to fully dissolve the KCl. Solutions were refreshed every few days due to the formation of crystals that would be transferred into the device. Various concentrations of KCl were employed in this thesis to act as a buffer component as well as for general use in dilution and storage. All buffer solutions were stored at 4°C ±2°C.

2.7.2 Potassium tetrachloroplatinate II (K_2PtCl_4)

Potassium tetra-chloroplatinate (K_2PtCl_4, 99.99% Sigma Aldrich) was employed in platinum electrochemical deposition experiments on Au coated nanopores (Chapter 4). Where $PtCl_4^{2-}$ ions were reduced to form Pt metal at the Au nanopore surface (Equation 2.7.1) under an applied potential to the WE.

$$PtCl_4{}^{2-} + 2e^- \rightarrow Pt + 4Cl^- \tag{2.7.1}$$

Low concentrations (between 1 mM-200 mM) of the Pt complex were prepared in buffer solution and fresh aliquots were used in each experiment. The chemical solution was stored at 4°C ±2°C.

2.7.3 Tris-HCl EDTA (TE) buffer solution

DNA translocation experiments were carried out in 1 M KCl salt solution containing 10 mM Tris-HCl and 1 mM EDTA. The purpose of the TE buffer was to protect the DNA from degradation. Tris was used as a buffering agent to keep the solution at a defined pH.

Trizma base (Tris-base, Sigma), Ethylene diamine tetra-acetic acid (EDTA, Sigma) and KCl amounts were combined and made upto 1 litre in volume with water. The pH of the solution was then checked and adjusted to pH 8.0 using Hydrochloric acid (HCl, Sigma ACS reagent, 37%). The solutions were filtered through a filter of 0.02 μm and aliquots of these (20 ml each) were stored at 4°C ±2°C in sterilised vials.

Chemical	Supplier	Grade
Potassium tetra-chloroplatinate (II)	Sigma	99.99%, trace metals basis
Potassium chloride	Fluka	>99.99%, trace metal basis
Perchloric acid	Sigma	99.999%, trace metals basis
6-Mercapto-1-hexanol (MCH)	Sigma	purum, ≥97.0% (GC)
Sulphuric acid	Sigma	ACS reagent, 95.0-98.0%
Hydrogen peroxide	Sigma	ACS reagent, ≥30%
Nitric acid	Sigma	ACS reagent, ≥90.0%
Sodium hypochlorite	Fisher Scientific	General purpose grade, 8% Cl
Ammonia	VWR BDH	Analytical reagent, 28%
Potassium hydroxide	Sigma	ACS reagent, ≥85%, pellets
Sodium hydroxide	Sigma	ACS reagent, ≥97%, pellets
Hydrochloric acid	Sigma	ACS reagent, 37%
Trizma Base (Tris-Base)	Sigma	99.9%
Ethylene diamine-tetraacetic acid (EDTA)	Sigma	99.995%

Table 2.3: List of main chemicals used in this thesis for (i) preparation of nanopores (ii) electrochemical studies and (iii) translocation experiments.

Chapter 3

Characterisation studies of platinum electrodeposition

In this chapter, electrochemical deposition of platinum is investigated and characterised as a fabrication tool for constricting large (100-150 nm ± 10 nm) nanopores in Au/Si_3N_4 membranes. Platinum reduction using a solution of potassium tetra-chloroplatinate and potassium chloride is developed and studied at thin film Au electrodes, fabricated on glass substrates i.e. with respect to reduction potential, electrolyte concentration, and deposition duration. A variety of growth patterns are observed and characterised by chronoamperometry (CA), cyclic voltammetry (CV), scanning electron microscopy (SEM), energy dispersive X-ray spectroscopy (EDXS) and scanning tunnelling microscopy (STM).

The first section of this chapter gives a brief overview of the theoretical aspects of electrochemical deposition and the techniques used to gain information on the reaction taking place. The second section then provides details of the experimental work conducted to characterise the deposited platinum films and discusses the results obtained.

3.1 Electrochemical deposition

Electrochemical deposition is a versatile technique by which a thin metallic coating can be obtained on to the surface of another metal, Schlesinger and Paunovic (2000). This is achieved by simple electrolysis of an aqueous solution containing the desired metal ion or its complex. The metal ions in the aqueous solution are reduced to form a solid metal by the passage of an electric current (Figure 3.1), Scholz (2002). The rate of electrodeposit production can be controlled by the current and the resulting fine grained structures can

allow for an accurate control (0.1 nm) of layer thickness, (Bard and Faulkner, 2000; Scholz, 2002).

Electrochemical deposition is typically used in industry for the plating of metals, Paunovic and Schlesinger (2006). However in this work, its application to the synthesis of nanostructured materials is of particular interest. Although there are various other techniques which can be employed for thin film coating (Kanani, 2004) such as thermal spraying, sputter deposition and vapour deposition; electrodeposition is particularly attractive due to its relatively low cost, simple set-up and because it can be performed at room temperature, Riley et al. (1987). Its versatility is also a key advantage, as a broad range of materials may be deposited on various substrates, Kissinger and Heineman (1996); Ross (1994). Precise control is achievable on the composition of the deposited material, its crystallographic structure, texture and grain size, Schlesinger and Paunovic (2000). Artificial material structures such as multi-layers, i.e. a sandwich of thin layers with different compositions can also be obtained with relative ease, Ross (1994).

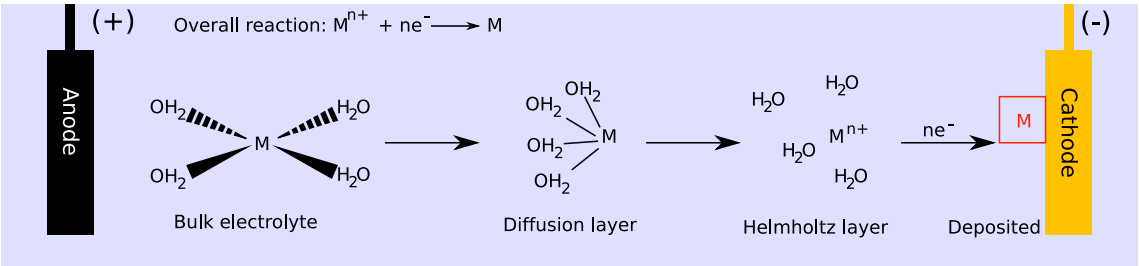


Figure 3.1: Diagram showing the general process of electrochemical deposition in solution. Adapted from Rao and Trivedi (2005).

Figure 3.1 shows the reduction mechanism for an electrochemical deposition of a simple solvated metal salt [$M^{n+} + ne^- \rightarrow M$], where M^{n+} is the metal ion, ne^- is the number of electrons and M is the deposited metal. The metal salt dissociates in water to positively charged metal cations M^{n+}. The sample, the solution and the anode electrode form together the electrical circuit over which a potential difference can be applied. The cathode electrode, which is to be plated, is negatively charged, and it attracts the positively charged M^{n+} cations, Kissinger and Heineman (1996). Meanwhile the negatively charged anions are attracted to the positively charged anode electrode. The electron current (ne^-) in the external circuit completes the loop and reduces the M^{n+} cations to the metallic form, M. At the anode, electrons are removed from the metal M, oxidising it to M^{n+} cations

and hence replenishing the supply. Thus, the anode dissolves as ions into the solution, enabling the concentration of the metal salt to remain constant, Rao and Trivedi (2005).

In electrodeposition baths, a supporting electrolyte is added to increase the conductivity of the solution (Paunovic and Schlesinger, 2006; Rao and Trivedi, 2005). When a ligand is used as a complexing agent, it is always added many folds in excess (relative to the stoichiometric reaction), Rubinstein (1995). This is primarily because, after formation of the required electro-active complex species, it should be available continuously throughout the deposition process. The presence of excess of ligand enables the continuous supply of the electro-active species and also ensures the rapid formation of the electro-active complex from the M^{n+} ions that are brought into the solution by the anodic reaction [$M \rightarrow M^{n+}$], (Raub and Muller, 1967; Schlesinger and Paunovic, 2000).

3.1.1 Redox reactions

The electrodeposition process typically proceeds by oxidation or reduction of species in a solution, Bard and Faulkner (2000). The standard electrode potential for an electrochemical reaction is the potential where the rate of the reduction and oxidation reactions are equal at standard conditions of concentrations, pressure and temperature. The Nernst equation relates the standard electrode potential, E_0, to the electrode potential E with concentrations of the reactant and product $\{ox\}$ and $\{red\}$, it is written as:

$$E = E_0 + \frac{RT}{nF} In \frac{\{ox\}}{\{red\}} \tag{3.1.1}$$

where R denotes the standard gas constant (8.314510 J K^{-1} mol^{-1}), T is the absolute temperature in Kelvin, n is the number of electrons transferred and F is the Faraday's constant. E_0 is the potential when $\{ox\}$ or $\{red\}$ are at equal concentration. The Nernst equation describes the behaviour of a redox reaction at equilibrium. By equilibrium it is implied that no net change in concentration of either $\{ox\}$ and $\{red\}$ is occurring. However if the equilibrium is shifted, the Nernst equation can tell us the final state to expect, Bard and Faulkner (2000); Shriver and Atkins (1990).

3.1.2 Kinetic and Mass Transport

Two factors can affect the rate of the redox reaction, the first is the speed at which electrons are transferred between reactants in the vicinity of the electrode, and the second is how

quickly reactants can reach the electrode from the bulk solution. These cases are referred to as kinetic and mass transport limited reactions (Albery, 1981; Bard and Faulkner, 2000; Schlesinger and Paunovic, 2000), which are defined below.

(i) Kinetic transfer- for an electron to be transferred between an electrode and ions in solution, the ions must approach the electrode whilst displacing the solvent and absorbed molecules in the process.

(ii) Mass transport- ions and molecules can travel from the electrolyte to the electrode as a result of random motion (diffusion), electrolyte flow (convection) or electrophoretic forces (migration), Newman and Thomas-Ayea (2004). If the kinetics are similar in rate or faster than mass transport, then the concentration of the reacting ions is depleted at the electrode/electrolyte interface, producing a concentration gradient. The concentration gradient leads to diffusion which contributes to the mass transport. Migration of electroactive species is usually diminished by the addition of inert ions that carry the current but do not participate in the electrode reactions. Hence the rate of the electrode reactions depends on electron transfer kinetics and surface reactions such as adsorption and crystallisation (Albery, 1981; Paunovic and Schlesinger, 2006).

The electrolysis of species is commonly performed using a constant current forced through the electrochemical cell, while the electric potential is monitored. Under conditions of mass transfer control (i.e. when the kinetics of the electrode reaction does not limit the current), the potential shifts when the concentration of electroactive species at the electrode surface is reduced to zero (Albery, 1981; Riley et al., 1987). The time needed for this depletion of the species, the transition time τ, is given by the Sand equation:

$$\tau^{1/2} = \frac{nF\left(\pi D\right)^{1/2} C}{2I} \tag{3.1.2}$$

where I is the current (in mA), C is the bulk concentration (in mol cm^{-3}), and D is the diffusion coefficient expressed in cm^2 s^{-1}, (Bard and Faulkner, 2000; Scholz, 2002).

Alternatively, a desired potential can be chosen, which is then maintained by the instrument while the necessary current used to maintain that potential is monitored, Schlesinger and Paunovic (2000). The electrode potential is directly associated to the energy change of the electrode process through the relationship: $\Delta G_0 = -nFE_0$, Wang (1994). When the electrode potential is made more negative relative to the standard reduction potential for an electrochemical reaction, the reduction current increases because the rate of electron transfer of the reduction increases. In the electron transfer controlled

potential region, there is a linear relationship between the potential and the logarithm of the deposition current known as the Tafel linearity, which can be calculated using the Butler Volmer equation, Scholz (2002). However, the current can also be limited by other factors such as mass transfer and preceding chemical steps (Paunovic and Schlesinger, 2006; Walsh, 1991).

3.2 Basic concepts of the experimental techniques

At an electrode surface, two fundamental electrochemical processes can be distinguished, faradaic and non-faradaic, Bard and Faulkner (2000). Faradaic currents result from the electrochemical reactions occurring at the electrode surface and are governed by Faraday's law, Bard and Faulkner (2000).

Under certain conditions, a given electrode-solution interface shows a range of potentials where no charge-transfer reactions occur, this is because the reaction is either thermodynamically or kinetically unfavourable, Bard and Faulkner (2000); Scholz (2002). However, non-faradaic processes such as adsorption and desorption can occur. These processes can change the structure of the electrode-solution interface with potential variation and solution composition. They do not involve any electrochemical reactions (charge transfer) and only cause accumulation or removal of electrical charges on the electrode and in the electrolyte solution near the electrode (Bard and Faulkner, 2000; Kissinger and Heineman, 1996).

3.2.1 Cyclic voltammetry

Cyclic voltammetry (CV) is the most widely used technique for acquiring quantitative information for electrochemical reactions and the thermodynamics of redox processes (Bard and Faulkner, 2000; Monk, 2001). It is sensitive to the mechanism of deposition and therefore provides information on structural transitions such as nucleation and growth steps of electrodeposition, as well as interactions at the surface. CV makes available information about the type of reactions observed in the system and the potentials at which they occur, Bard and Faulkner (2000).

Prior to an electrochemical deposition study, CV is used to determine the range of potential to be applied for deposition. This study uses a three electrode arrangement. The general view of a cyclic voltammetric experiment is given in Figure 3.2. A linear potential waveform is applied as a function of time, whereby the electrode potential is swept between

the cathodic, E_c, and anodic, E_a, limits at a constant rate. The corresponding current is recorded as a function of the varying potential. For the cathodic scan, the current has a negative sign as the applied potential decreases, whilst for the anodic scan the current has a positive sign as the applied potential increases, Bard and Faulkner (2000).

The resultant current of the system involves the Faradaic current due to the various electrochemical phenomena occurring on the electrode surface such as electron transfer redox reactions and adsorption processes in addition to the capacitive current due to the double layer charging at these potentials, Hamann et al. (2007); Rubinstein (1995). Apart from this, the kinetic parameters and the mechanism of different heterogeneous reactions occurring on the electrode surface can also be determined.

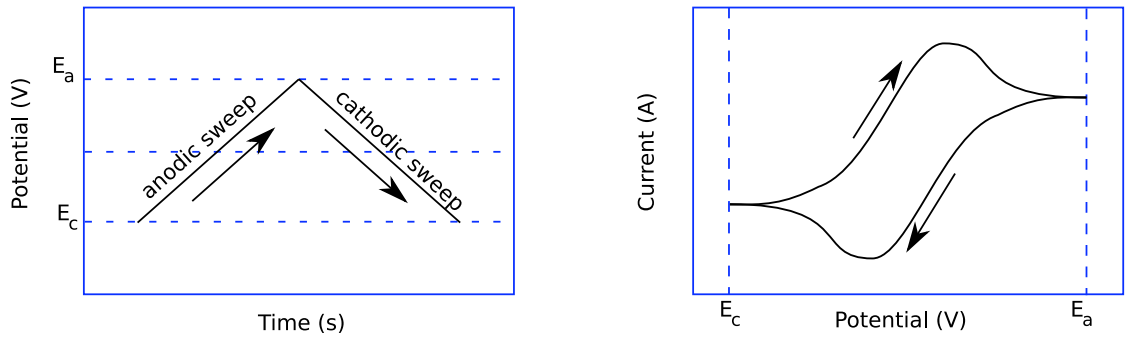


Figure 3.2: Schematic diagram of the cyclic voltammetry technique *Left*: illustration of the potential waveform applied to the system as the function of time and *Right*: the response recorded as a current vs. potential profile.

For a typical single electron reversible redox reaction of the type, $O + ne^- \rightarrow R$, the rate of charge transfer is always greater than the rate of mass transfer at all potentials and the redox reaction is under diffusion control. The ratio of concentrations of oxidant and reductant species of a reversible reaction is given by the Nernst equation (3.1.1) and a concentration gradient exists within the region near the electrode surface known as a Nernst diffusion layer. Here the concentration gradient of the electroactive species is linear. Also the Nernstian equilibrium is always maintained at the electrode surface and at all the potentials, Hamann et al. (2007).

When the potential of the electrode is made more negative, the surface concentration of the reactant O decreases progressively. Thereby the concentration gradient is increased, which results in an increase in the current. On reaching the electrode potential where O is reduced, the surface concentration of O decreases from its bulk value in order to

satisfy the Nernst equation and the concentration gradient is set up. As a result a current proportional to the concentration gradient at the electrode surface flow, Albery (1981); Wang (1994). Due to the diffusion of ions, the concentration gradient does not remain constant and it starts to decrease. At the same time, the electrode potential is also continuously changing, leading to a further decrease of surface concentration of O until it effectively reaches zero concentration (Albery, 1981; Bard and Faulkner, 2000). Once the concentration of O reaches zero, the gradient decreases due to the accumulation of reduced species R, in the vicinity of the electrode surface, hence the current flow also decreases. Overall, this behaviour gives rise to the peak shaped current-potential profile as shown in Figure 3.2 (right panel). Using similar arguments as for the forward sweep, it can be seen that the current change on reverse sweep also exhibits a peak shaped response of the opposite sign.

3.2.2 Chronoamperometry

Chronoamperometry (CA) is an electrochemical method in which a step potential is applied and the current response, i, is measured as a function of time, t. This is a useful method for the quantitative analysis of a deposition process, where the working potential is fixed during the experiment. Additionally, it can also be used to determine the amount of charge for deposition (Kissinger and Heineman, 1996; Paunovic and Schlesinger, 2006).

At the beginning of the transient experiment the potential of the working electrode is held at E_{i}. At $t = 0$ the potential is instantaneously changed to a new value E_{h}, and corresponding current time response is recorded as shown in Figure 3.3. This $i - t$ response is comprised of two components: the current due to charging the double-layer and the other due to the electron transfer reaction with the electroactive species. The extent to which both occur simultaneously depends on the initial, E_{i}, and the final value, E_{h}, of the potential.

In order to determine the exact form of current-time dependence for a planar electrode, the Cottrell equation, Hamann et al. (2007) is used:

$$I = nFACD^{1/2}\pi^{-1/2}t^{-1/2} \tag{3.2.1}$$

It may be observed from Figure 3.3 that the current falls as $t^{-1/2}$. There is also a capacitive component of the current which decays exponentially in time according to the following equation:

$$i = \frac{E}{R_s} e^{-t/R_s C_d} \tag{3.2.2}$$

Here R= resistance (ohms), C = capacitance (F).

This capacitive current decays rapidly and therefore is only significant when looking at short times. The result of this potential step is similar to an electrical circuit, with a resistor, R_s, representing the solution resistance and a capacitor, C_d, representing the double layer at the electrode/solution interface. Hence for a potential step, there is an exponentially decaying current with a time constant, $\tau = R_\mathrm{s} C_\mathrm{d}$.

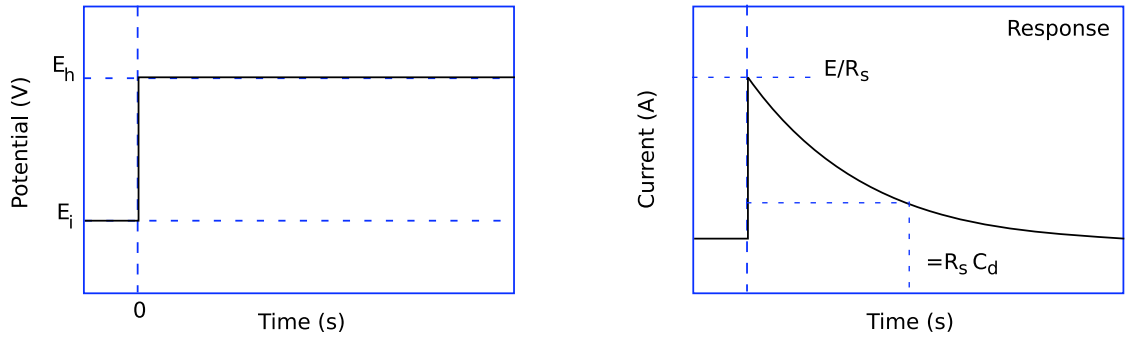


Figure 3.3: Schematic diagram of the chronoamperometry technique. *Left*: illustration of the potential-time profile applied during experiment, $\mathrm{E_i}$ is the initial value and $\mathrm{E_h}$ is the potential where no reduction of oxygen occurs and *Right*: the corresponding response of the current due to changes of the potential. Adapted from Hamann et al. (2007).

At the beginning of the transient experiment the potential of the working electrode is held at E_i. At $t = 0$ the potential is instantaneously changed to a new value E_h, and corresponding current time response is recorded as shown in Figure 3.3. In order to determine the exact form of current-time dependence for a planar electrode, the Cottrell equation, Hamann et al. (2007) is used:

$$I = nFACD^{1/2}\pi^{-1/2}t^{-1/2} \tag{3.2.3}$$

It may be observed from Figure 3.3 that the current falls as $t^{-1/2}$. This feature is frequently used as a test for this type of process and its gradient can be used to calculate the diffusion coefficient D_0 (Bard and Faulkner, 2000; Hamann et al., 2007). The result of a potential step is similar to a simple electrical circuit, with a resistor, R_s, representing

the solution resistance and a capacitor, C_{d}, representing the double layer at the electrode/solution interface. Therefore the behaviour of the current, i, with time, t, when applying a potential step of magnitude, E is given by:

$$i = \frac{E}{R_s} e^{-t/R_s C_d} \tag{3.2.4}$$

Hence for a potential step, there is an exponentially decaying current with a time constant, $\tau = R_{\mathrm{s}} C_{\mathrm{d}}$.

3.3 Experimental

3.3.1 Platinum deposition

The electrodeposition of platinum metal onto gold surfaces is developed and characterised in this section. Pt metal was chosen as a proof-of-concept for electrodeposition experiments and the method can be extended to other metals also. The Pt metal is noble in its character and has a low emf (electromotive force) value (+1.188 $\mathrm{M/M^{2+}}$), Rao and Trivedi (2005). Therefore it is extremely easy to reduce its ions and as a consequence it tries to remain in its metallic state (Baumgartner, 1988 and Rao and Trivedi, 2005). For these studies, a plating bath of potassium tetra-chloroplatinate ($\mathrm{K_2PtCl_4}$, 99.99% Sigma Aldrich) complex was developed with potassium chloride (KCl; Fluka, >99.99%) acting as a supporting electrolyte. The $\mathrm{PtCl_4^{2-}}$ ions were reduced at the Au surface to form Pt using the following reduction reaction:

$$PtCl_4{}^{2-} + 2e^- \rightarrow Pt + 4Cl^- \tag{3.3.1}$$

It was possible to calculate the mass of platinum deposited on the working electrode as this was proportional to the number of moles of electrons transferred (Equation 3.3.2).

$$m = \frac{QMw}{nF} \tag{3.3.2}$$

where m is the mass of the deposit produced at the electrode (in grams), Q is the total electric charge (in Coulombs) required for the process, Mw is the molecular weight (gram/mol), n is the number of electrons transferred and F is Faraday's constant (96485 C $\mathrm{mol^{-1}}$).

3.3.2 Electrode fabrication

In order to deposit and characterise the platinum metal layer electrochemically, glass substrates (65 mm x 25 mm) were patterned with metallised gold electrodes. A photomask for this was designed using Clewin 4.0 (WEI software), Figure 3.4. Each substrate contained eight electrodes to allow for a range of parameters and conditions to be varied at different electrodes easily. An optical image of the enlarged electrode from the photomask is also shown in the figure.

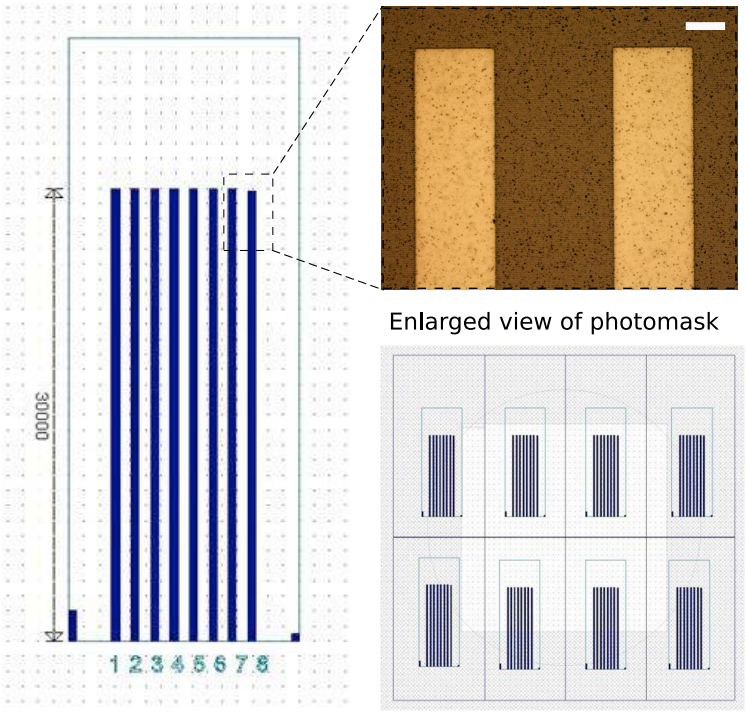


Figure 3.4: Photomask for the design of Au electrodes on a glass substrate. *Left*: Single substrate enlarged showing 8 electrodes per substrate. Single electrode length 3000 μm; width 500 μm. *Top right*: enlarged optical image of the photomask showing two electrode structures printed onto Photoplot film. *Bottom right*: CAD design of photomask which allowed fabrication of 8 individual substrates simutaneously. Each glass slide had the dimensions 65 mm x 25 mm. Dots and dash lines in the CAD file act as guidelines for drawings and were not printed onto the final photomask.

The image from the Clewin design was converted using GebRef software with a final resolution of 2032 x 8000 dpi. The electrodes were patterned using a FP-8000 Raster Photo-plotter (Mega Electronics Ltd, UK) an instrument which drew the image on a piece of light sensitive film (Photoplot film 457 x 305 mm) with a laser diode light source. The

printing process was performed in a darkroom to load and process the film using only a fluorescent green light (900 mm, 30 W). This was followed by a wet chemical process, where the film was developed and fixed at 30 °C (K Series Photoplot developer and fixer, 5L). Finally the photomask was rinsed with DI water and air dried.

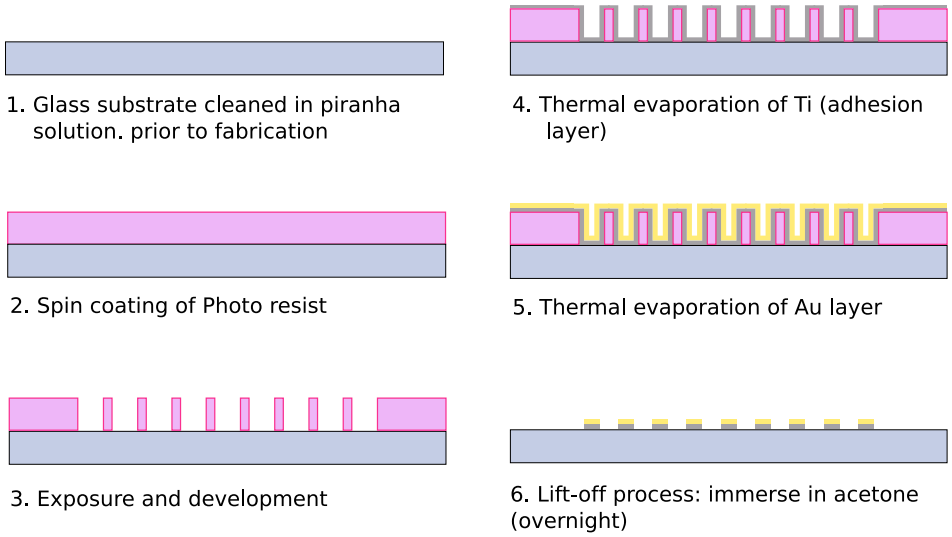


Figure 3.5: Schematic illustration of lift-off process to produce the Au/glass electrodes.

The glass substrates were cleaned using piranha solution (H_2SO_4:H_2O_2= 3:1) for 10 minutes, as described in Section 2.5.2 and a photoresist with 400 nm thickness was spin-coated on top. Using the photomask, the glass substrate was exposed to UV light which allowed the structures from the photomask to be transferred to the substrate. A schematic of this process is shown in Figure 3.5. A set of 8 thin-film gold electrodes were fabricated by depositing the metals through the patterned resist mask using thermal evaporation (Auto 500 coating system, BOC Edwards). Due to the weak bond strength between Au and glass, which can cause Au film to peel-off after it is deposited, a thin titanium adhesive layer (10 nm) was first deposited. Following this, the 100 nm thick gold films were deposited. Metal on top of the mask was removed by selectively etching the underlying resist so that the metal which was deposited directly onto the substrate remained intact. The thickness of the metal films were determined using the Dektak Profiler 8.0.

3.3.3 Experimental set-up

A three electrode system was employed in these studies and the set-up for this is illustrated in Figure 3.6. All measurements were performed using a commercial potentiostat,

(CH760c, Electrochemical Workstation, CH Instruments). The instrument was controlled via a personal computer (PC) using the CHI 7.20 software. All electrochemical potentials were measured with respect to a Ag/AgCl reference electrode (model CHI-111). A large area platinum gauze was employed as the anode and connected to the positive pole of the potentiostat, which functioned as a counter electrode, and the Au patterned glass substrate as the cathode was connected to the negative pole of the potentiostat, which functioned as the working electrode. The electrochemical cell was designed with a luggin capillary (as shown in Figure 3.6) which was used to bring the potential measuring point in close proximity to the working electrode under investigation. The capillary was also filled with the depositing solution and had a large enough opening to accommodate the reference electrode and a smaller opening to insure diffusional movement of the electrolyte solution. Hence the design minimised any iR drop (potential drop due to solution resistance) within the electrochemical cell.

The electrochemical cell was placed in an in-house Faraday cage to reduce current noise and voltage noise (by the reference and working electrode). The Faraday cage was electrically connected to the ground. Depositions were carried out on each electrode at room temperature. The electrolyte solution was degassed by bubbling high purity Argon (Ar) gas for 15 minutes prior to every measurement. The cell was then blanketed with Ar flow during the measurements.

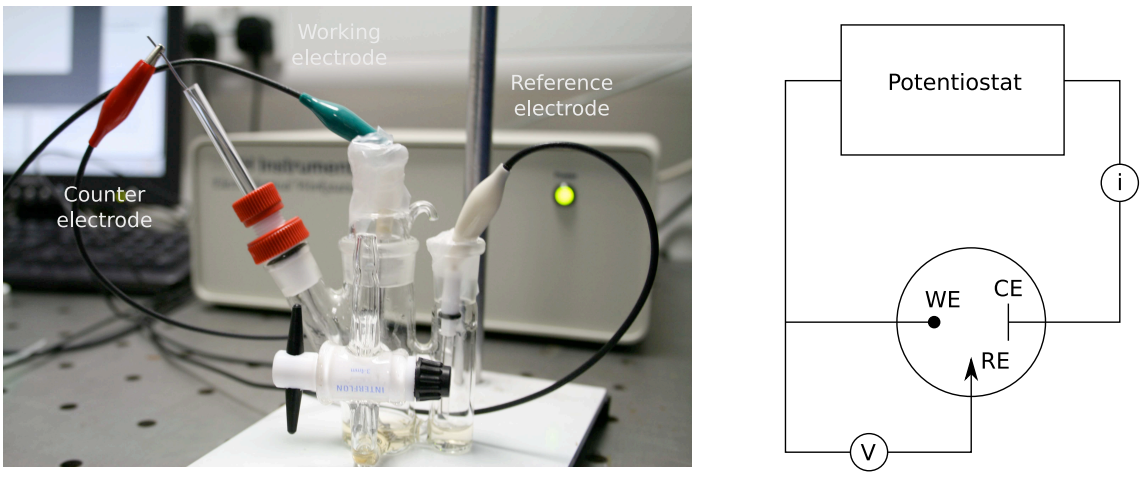


Figure 3.6: *Left*: Optical image and *Right*: schematic of the three electrode electrochemical cell configuration used for Pt deposition characterisation studies; notations: WE (working electrode), CE (counter electrode), and RE (reference electrode).

Pretreatment of the working electrode (Au patterned glass substrate) was carried out to improve the quality of electrodeposition. Surface cleaning was designed to remove contaminants from the substrate, as the presence of contaminants caused poor adhesion and prevented deposition. For this purpose, the Au/glass substrate (WE) were pre-cleaned sequentially in acetone; isopropanol and H_2O prior to their use. This process was followed by exposing the substrate to an oxygen plasma (SPI Plasma Prep-II) which resulted in the surfaces becoming hydrophillic.

The Au patterned glass substrate was then aligned and connected to an in-house prepared 8 set WE connector (part; 3M Gold-8 0.3, RS Components) as shown in Figure 3.7. The substrate was then tested using a multimeter to ensure that each electrode was completely closed without any breaks/ scratches due to the lift-off step and for mechanical stabilisation of the chip. Chronoamperometry (CA) studies of platinum electrodeposition were performed using an aqueous solution of 10 mM K_2PtCl_4/100 mM KCl, as the supporting electrolyte. The glass substrate containing the Au fabricated electrodes was immersed into the aqueous solution and connected to the 8-set WE, which was externally connected with a crocodile clip, serving as the WE. Ag/AgCl and Pt wire were connected to the terminal crocodile clips as the reference electrode (RE) and counter electrode (CE) respectively. Following this an electrochemical cleaning of the electrode surface was carried out by connecting the Au/glass electrodes to the WE and applying potential sweeps between $\pm$500 mV in 50 mM H_2SO_4 using cyclic voltammetry.

Chronoamperometry was then used to deposit the platinum on the surfaces of Au/glass electrodes at a constant potential for a fixed duration. The CA response was measured for 5 seconds after a potential step from 0 mV, where no redox electrolysis occurred, to the defined deposition potential vs. Ag/AgCl. Different parameters were varied including concentration of plating solution; deposition potential and time to analyse and characterise the deposition rate, grain size and surface roughness of the films.

After electrodeposition the sample was rinsed with water and dried under a stream of nitrogen. The resulting electrodeposition morphologies were assessed using CV, FE-SEM and STM, to study the Pt and Au surfaces. FE-SEM images were recorded at 5 keV or 10 keV to enable clear visualisation of Pt grains. At these operating voltages surface charging was observed occasionally, Shaffner and Veld (1971). Quantitative analysis of Pt particle size was performed using the STM (Agilent 5500) and measurements were carried out on the deposited areas ranging between 50 nm^2-1 μm^2 and analysed with a bias current

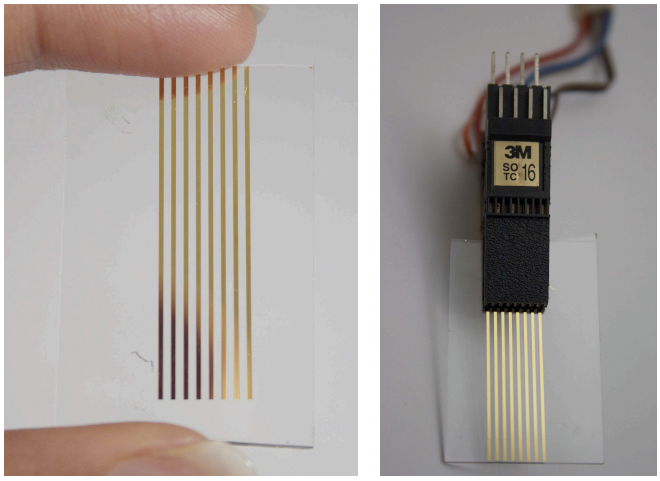


Figure 3.7: Optical images of the 8-set working electrode (WE). *Left*: Au/ glass substrate, *Right*: the substrate attached to an 8 set WE connector; allowing 8 independent experiments to be carried out in the electrochemical cell by exchanging the terminal wire each time.

setting of 1 nA and scan rates between 0.6-0.8 nm^2 s^{-1}.

3.4 Results and Discussion

3.4.1 Chronoamperometric measurements

Platinum was electrochemically deposited onto thin film Au electrodes (each of size 500 μm x 3000 μm) by applying a constant DC potential. The patterned glass substrate containing the fabricated 8 electrodes were immersed into a deposition solution of 10 mM K_2PtCl_4 with a supporting electrolyte of 100 mM KCl. The terminal wire of each electrode was exchanged between new measurements with the 8-set WE crocodile clip externally (as described in the experimental section).

The typical recorded deposition current vs. time scan at an individual Au/glass substrate electrode is plotted in Figure 3.8. A deposition potential (V_{dep}) of -200 mV is applied to the WE and monitored over a course of 200 s. The current-time (i-t) curve can be divided into three sections: (i) at the very beginning of the deposition, a current peak of a few seconds is observed, going from a negative value of -89.4 μA towards 0. This is due to the exchange of metal ions at the metal-solution interface as the electrode is introduced into the aqueous solution. The simplest model of the metal-ion interface is the Helmholtz double layer (Bard and Faulkner, 2000) which consists of two equal and opposite layers of

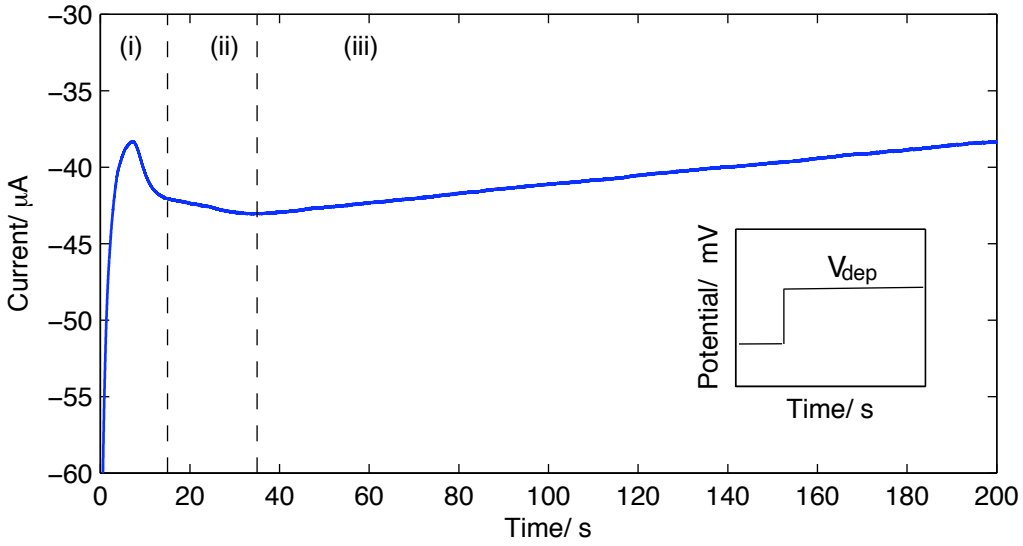


Figure 3.8: Typical deposition current versus time scan observed during the deposition of Pt on a single Au electrode from a solution of 10 mM K_2PtCl_4 and 100 mM KCl (*inset*: the applied potential V_{dep}=-200 mV as a function of time, t).

charges; one on the metal and the other in the solution. This double layer is equivalent to a parallel plate capacitor (Bard and Faulkner, 2000; Shriver and Atkins, 1990). The layer in the solution is lined up at a fixed distance which is determined by the hydration sphere of hydrated ions, Bard and Faulkner (2000); Scholz (2002).

The current peak in the first section originates from this electrical double layer at the metal-electrolyte interface which is charged during the initial few seconds of the deposition. Subsequently, the deposition current remains constant for a longer period of time, indicated by section (ii). However with increasing electrode surface area due to the deposition, there is a gradual increase in current over time, where the overlap of Pt growth centres are followed by outward growth into the solution. This is seen in section (iii). The deposition current for an individual Au electrode amounts to less than 38.2 μA. The start of the film growth becomes apparent by a significant increase of the current due to the larger deposition area during the film formation. Since the current is a function of the deposition area, the current gain indicates the increase in film size.

Varying deposition potential

The effect of varying potential on the deposition rate was studied using the chronoamperometry technique. Figure 3.9 presents plots of current versus deposition time at four

different potentials. The depositions were performed on the set of 8 electrodes. In the case of the highest potential (V_{dep}= -100 mV), only a faint current increase was observed starting after a 2-3 seconds of deposition, whilst in the case of the lowest potential (V_{dep}= -400 mV) the current rose immediately.

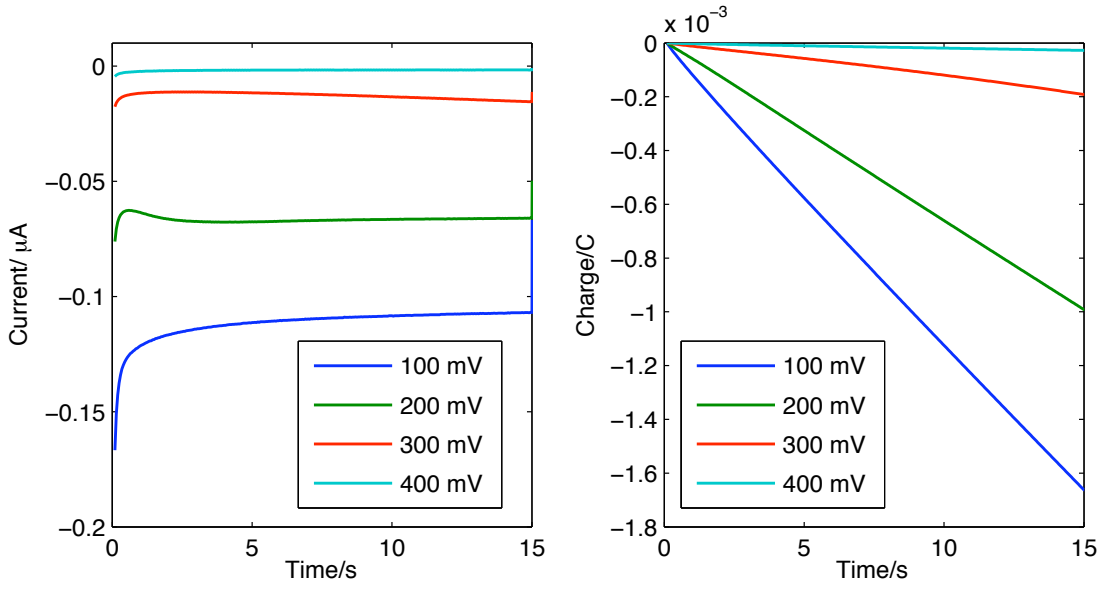


Figure 3.9: *Left*: Current-time transients resulting from various potential experiments at individual Au electrodes. *Right*: Charge-time plot for the different potentials applied at Au electrodes. The applied potentials are indicated in the relevant plots.

It should also be noted that the deposition current increases from -0.11 μA to a less negative value of -0.052 μA, with decreasing potential. Thereby inducing a higher charge deposition rate. This is explained by Faraday's law (using Equation 3.3.2) where mass is proportional to the charge (Q). Which meant more mass was deposited at higher currents in the same time leading to a faster growth of the films. Therefore, the time needed for growing a film of certain thickness reduced with increasing potential. By integrating the deposition current-time curve, the total amount of deposited charge ($Q = \int I\, x\, dt$) was also calculated.

The plot of charge-time for these experiments is plotted in Figure 3.9. A delay of 1.5 seconds was used for these calculations to avoid the non-faradaic components i.e. currents for double layer charging. Table 3.4 shows the calculated charge for the different potentials applied. For the lowest potential (V_{dep}= -400 mV) a charge of -0.0017 C was determined. By using the charge (Q) derived from the i-t curves, the amount of Pt deposited and its

V_{dep}/ mV	Charge/ C	Calculated film thickness/ nm	Deposition rate/ nm s^{-1}
-100	-2.76 x10^{-5}	0.32	0.02
-200	-1.92 x10^{-4}	2.26	0.15
-300	-9.92 x10^{-4}	11.66	0.78
-400	-0.0017	19.54	1.30

Table 3.1: Table showing the calculated charge and thickness values for the various deposition potentials applied (V_{dep}) at the Au/glass working electrode.

thickness could also be estimated. For V_{dep}= -200 mV, the amount of Pt deposited was 0.194 μg. The thickness was calculated using Equation 3.4.1 below:

$$T = \frac{\left(\frac{Mw}{nFD}\right) \times Q}{A} \tag{3.4.1}$$

Where T is the thickness (nm); Mw is the molecular weight (195.08 g/mol); n is the number of electrons transferred; F is Faraday's constant (96485.309 C mol^{-1}); A is the surface area of the electrode (m^2); D is the density of Pt= 21.45 g/cm^2; and Q is the charge (C).

So for a V_{dep}= -200 mV, a 2.26 nm Pt film thickness was calculated. By decreasing the potential down to -400 mV, it was found that initial reduction between -280-400 mV were crucial in producing adherent Pt films. It was likely that the evolution of H_2 bubbles occurred during the electrodeposition of platinum, as once Pt is deposited, it is a highly efficient surface for the electrocatalytic reduction of protons to hydrogen gas, Rao and Trivedi (2005). Furthermore, the presence of adsorbed hydrogen gas bubbles could locally prevent electrolyte contact to the surface, thereby hindering electrochemical reduction and metal deposition (Penner, 2001; Rao and Trivedi, 2005). As a result, this dynamic formation and loss of hydrogen gas from the surface during electrodeposition can cause inhomogeneous electrodeposition rates and an increase in surface roughness of the platinum deposit.

Varying deposition duration

The effect of varying deposition duration on the deposited Pt layer is investigated in this section. The time duration of Pt deposition (t) was varied between 60-200 seconds. Each

run was carried out on a new Au/glass electrode with all other parameters kept constant during the investigation; V_{dep}= -300 mV; using a 10 mM K_2PtCl_4/100 mM KCl system.

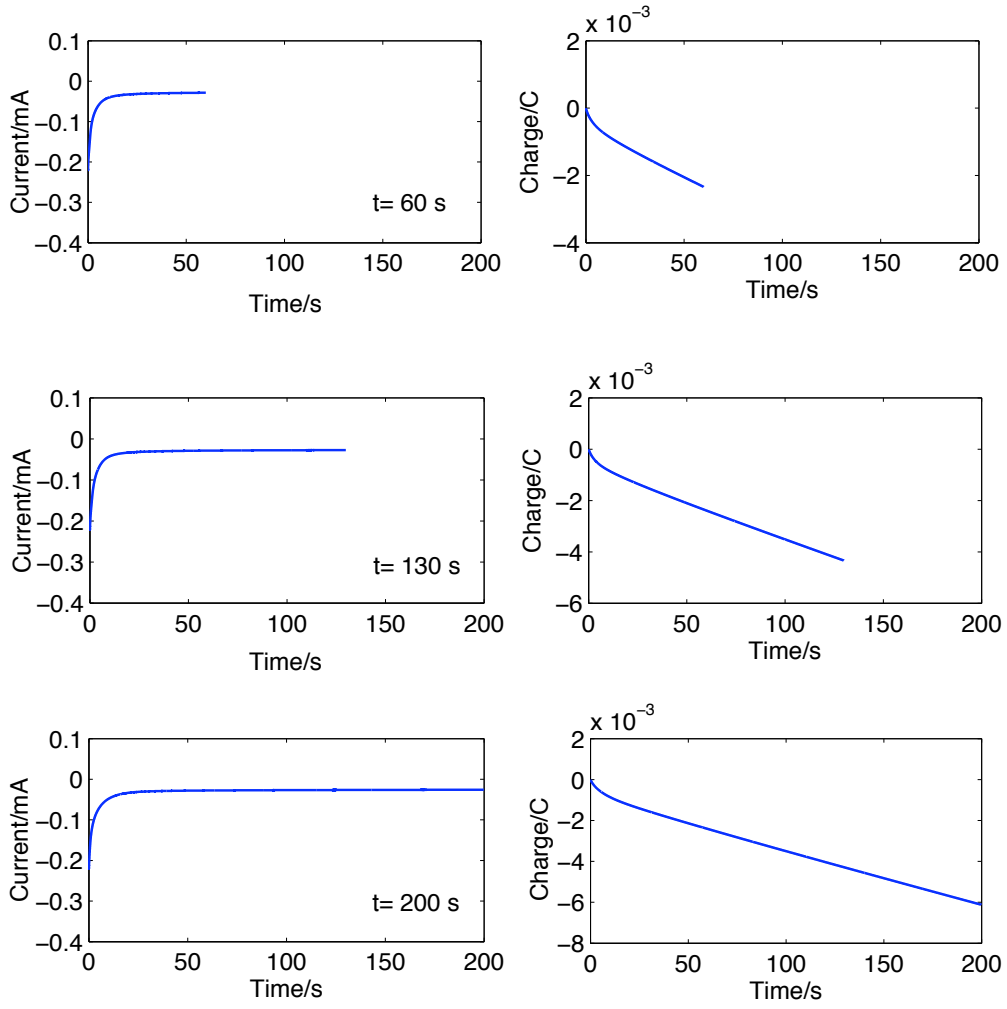


Figure 3.10: *Left*: Current-time transients resulting from deposition duration experiments (t= 60 s; 130 s and 200 s) at individual Au electrodes. *Right*: Corresponding charge-time plot for the different potentials applied at Au electrodes.

Figure 3.10 shows the results for three different times used, t= 60 s, 130 s and 200 s. It can be seen that at lower times (t= 60 s) the deposition current at the end of the run was approximately I=- 28.7 μA. As the duration of deposition was increased to 130 s (I= -26.6 μA) and then upto 200 s (I= -23.1 μA), a general trend was observed where the current increased over time, due to the increase in surface area of Pt deposits. The charge and thickness values for each run were calculated and are tabulated in Table 3.2. These show the overall increase in Pt film thickness as the duration was increased. The deposition rate were comparable as expected as no other changes were made to the system.

V_{dep} duration/ s	Charge/ C	Calculated film thickness/ nm	Deposition rate/ nm s^{-1}
60	-0.0023	17.60	0.29
130	-0.0043	32.62	0.25
200	-0.0061	46.02	0.23

Table 3.2: Table showing the calculated charge and thickness values for the various depostion durations (t= 60 s, 130 s and 200 s) applied at the Au/glass working electrode.

Figure 3.11 presents the SEM images obtained for these measurements which allowed us to understand the effect of varying the time for deposition in more detail. Overall the SEM image of the deposits exhibited brighter contrast corresponding to the Pt grains and the darker grey regions due to the Au film, Goldstein (2003). For the shorter deposition time (t= 60 s), the Pt deposits were sparse, with the Pt grain nuclei spread across the surface resulting in poor coverage. However as the time duration was increased, the SEM exhibited nuclei overlap and formation of compact grains. At a time duration of 200 s, a dense and compact coverage by Pt electrodeposit was observed indicating that a longer time duration was a crucial parameter in film growth, under the conditions investigated.

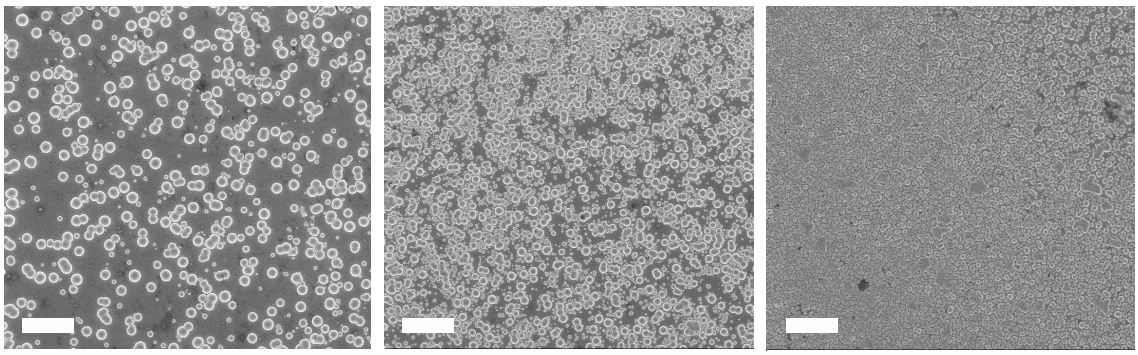


Figure 3.11: Scanning electron micrographs for the different deposition durations investigated. (*Left*) t= 60 s (*Middle*) t= 130 s (*Right*) t= 200 s. V_{dep} in all cases set to -300 mV. Scale bar= 50 nm.

Varying concentration of the metal complex

This section discusses the effect of varying the K_2PtCl_4 concentration over the range 2.5 mM-10 mM in order to investigate its effect on the deposition rate of Pt films. All experiments were carried out with a set duration of 300 s and a deposition potential V_{dep} of -280 mV. Figure 3.12 shows the i-t curves and charge-time plots for the three different concentrations studied.

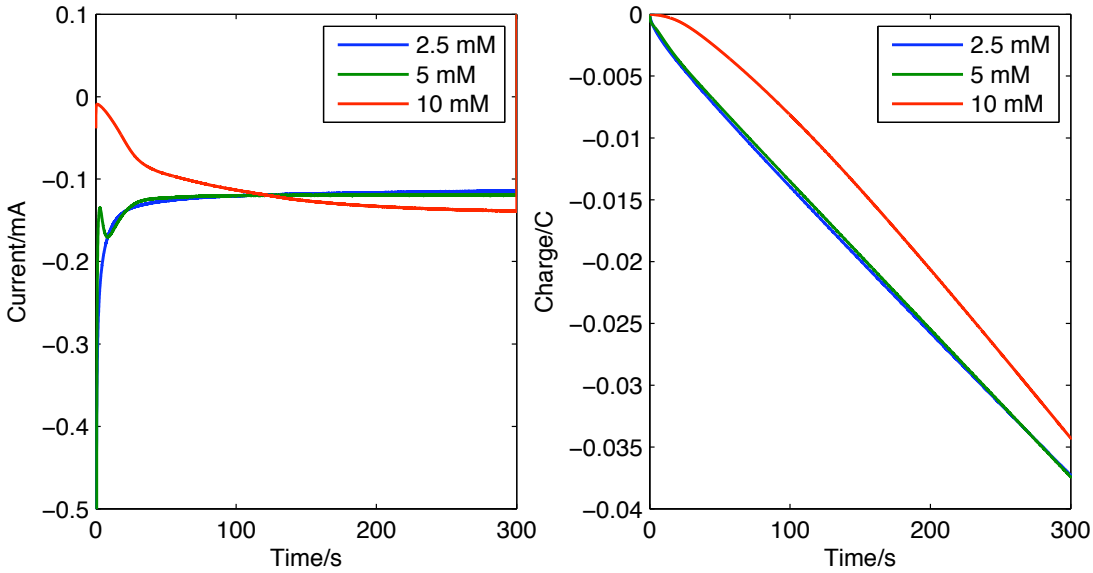


Figure 3.12: *Left*: Current-time transients resulting from various K_2PtCl_4 concentration experiments at individual Au electrodes. *Right*: Charge-time plot for the different concentrations used at Au electrodes. The V_{dep} in all three measurements was set to -280 mV.

The calculated total number of Pt molecules used up during deposition (based upon the amount of current passed through the system) is tabulated in Table 3.3 using the formula: number of electrons transferred (noe)= Q/e, where Q is the charge (C) and e is the electron charge (1.602 x10^{-19} C). Since $PtCl_4^{2-}$ reduction reaction involves two electrons ($PtCl_4^{2-}$ + 2 e^- → Pt^0 + 4 Cl^-), noe was divided by 2. For the 2.5 mM K_2PtCl_4 concentration, approximately 1.074 x10^{17} molecules were used up. This value was similar to what was observed for 5 mM and 10 mM runs with a consistent deposition rate between 0.22-0.24 nm s^{-1} for all measurements.

However, when the samples were observed under the optical microscope, the deposited structures were irregular and highly porous at the lower concentration (2.5 mM) compared

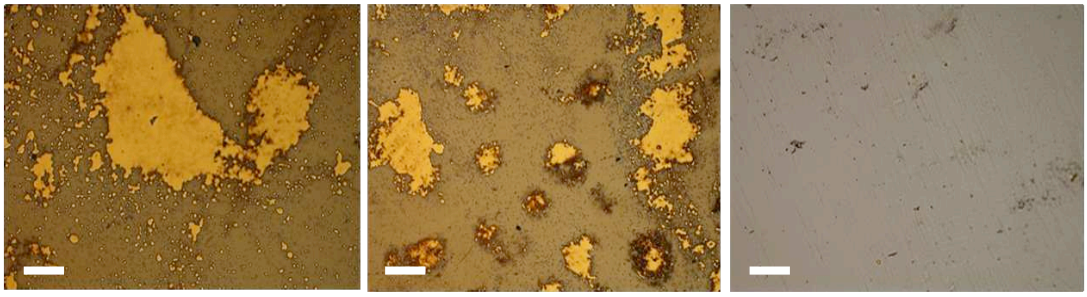


Figure 3.13: Optical images taken with Nikon L150 Eclipse optical microscope at 100 x showing the different quality of Pt depositions when the plating solution K_2PtCl_4 concentration was varied. (*Left*) 2.5 mM (*Middle*) 5 mM and (*Right*) 10 mM. Scale bar= 20 μm.

$[K_2PtCl_4]$/ mM	Charge/ C	No. of Pt_{mol}	Deposited thickness/ nm	Deposition rate/ nm s^{-1}
2.5	-0.0344	1.074 x10^{17}	66	0.22
5.0	-0.0381	1.189 x10^{17}	71	0.24
10	-0.0384	1.119 x10^{17}	73	0.24

Table 3.3: Table showing the deposition thicknesses and rates calculated when concentration of K_2PtCl_4 was varied. The number of Pt molecules consumed during deposition, Pt_{mol}= *noe*/2, *noe* (number of electrons transferred)= Q/e.

to a uniform film exhibited for the higher concentration (10 mM). The SEM images for these are provided in Figure 3.13. The difference in the deposits can be explained by the number of ions that were available for discharging. As the concentration was lowered during deposition, it created a depletion layer near the working electrode resulting in poor deposits. Whereas at high concentration, many ions were available in solution for deposition resulting in a uniform film and consistent deposits.

3.4.2 Cyclic voltammetry analysis

Cyclic voltammetry was used to study the reactions taking place at the electrode surfaces and to confirm the structure of the Pt deposits. Figure 3.14 depicts voltammograms of Au/glass substrate electrode performed in the presence and absence of $PtCl_4^{2-}$ ion solution. The CV curve in Figure 3.14 (top panel) shows the Au coated glass substrate working

electrode cycled in 50 mM H_2SO_4 exhibiting the typical characteristics of an Au electrode surface, Ross (1994). Figure 3.14 (middle panel) corresponds to a cyclic voltammogram of the Au surface in the supporting electrolyte (100 mM KCl) in the absence of K_2PtCl_4 solution showing the corresponding hydrogen and oxygen evolution of Au surface. The CV curve in Figure 3.14 (bottom panel) shows the behaviour of the $PtCl_4^{2-}$ ion solution supported by 100 mM KCl, where platinum reduction; re-oxidation to platinum ion and the oxide reduction peaks are presented at potentials of -300 mV; +900 mV; and +50 mV, respectively. These correspond well to typical potential ranges observed in literature for platinum, Jerkiewicz et al. (2004). All scans were taken at room temperature under inert conditions at a scan rate of 50 mV s^{-1}.

Following deposition, the electrode is cycled in 50 mM H_2SO_4 to study the electrodeposited Pt surface structure. The CV curve for this is shown in Figure 3.15. The curve is typical of that observed for the polycrystalline platinum in an acidic media, Baumgartner (1988). On the anodic sweep starting from +1000 mV, the formation of surface oxide is observed. On the reverse scan at +400 mV the surface oxide is subsequently removed, giving rise to a well defined stripping peak. In the centre of the voltammetric curve (between 0 mV and +250 mV) is the double layer region where the capacitive processes takes place. At more negative potentials, the typical hydrogen evolution and adsorption peaks are observed. Reproducible CVs were obtained by recording ten continuous scans in the direction from +1000 mV to -500 mV. In total more than 50 experiments were performed which all showed similar behaviour to the cases illustrated herein.

3.4.3 Multi-step deposition

The multi-step deposition technique was used to get a better understanding of the Pt deposition mechanism for the plating bath developed. The general mechanism of nucleation and growth can be described by five individual steps, these are illustrated in Figure 3.16, Venables et al. (1984). Firstly the metal ion complex arrives at the electrode surface either by convection or diffusion. Electrons are then transferred to the ion from the cathode as shown in step (ii). In step (iii) the metal ion is either partially or completely desolvated before further metal ions diffuse to the surface (iv) and coalesce (v) to form a nucleation site.

These steps play a crucial role in determining grain sizes. In order to achieve fine-grained thin film deposits, the generation of these nucleation sites needs to be interrupted

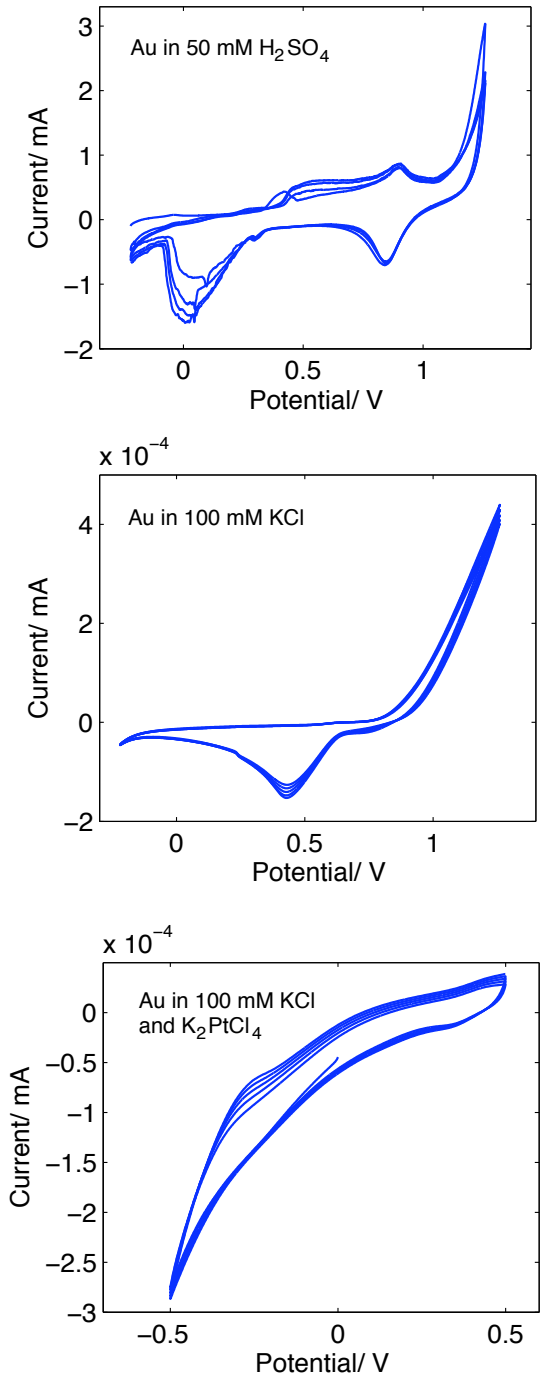


Figure 3.14: Cyclic voltammograms. *Top*: Au/ glass substrate electrode in 50 mM H_2SO_4 solution. *Middle*: Au/glass substrate in 100 mM KCl and *Bottom*: Au/glass substrate in 100 mM KCl in the presence of 10 mM K_2PtCl_4, reproducible scans were obtained after five cycles. The scan rate for all measurements was set to 50 mV s^{-1}.

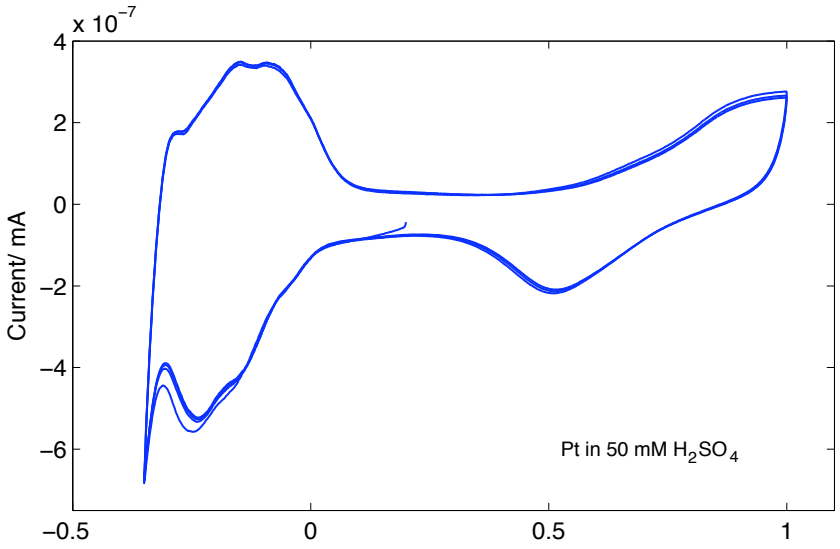


Figure 3.15: Cyclic voltammogram of Pt deposited layer on the Au/ glass substrate electrode in 50 mM H_2SO_4 solution. The scan rate was set to 50 mV s^{-1}.

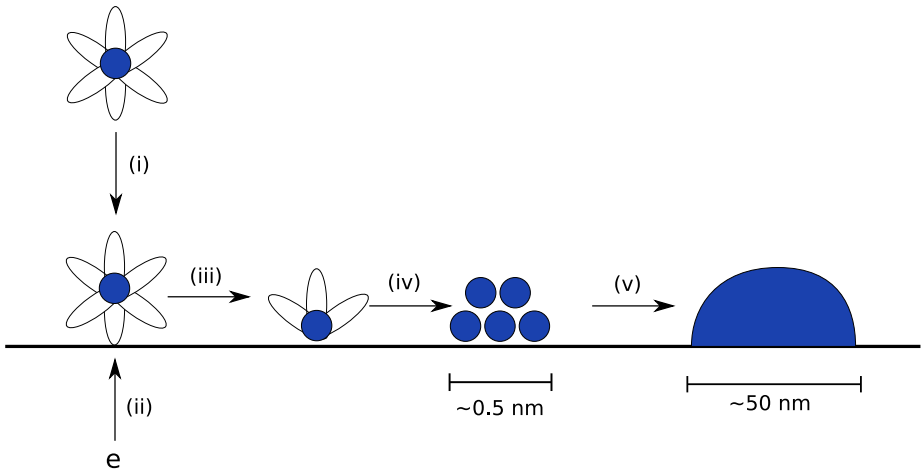


Figure 3.16: Schematic illustrating the general mechanism of nucleation and growth. Growth of a large scale deposit proceeds in a number of stages: (i) transport of the metal ion complex to the electrode surface (ii) electron transfer (iii) partial/complete desolvation (iv) surface diffusion (v) formation of stable nuclei and finally growth of nucleus and overlapping towards film formation. Adapted from Venables et al. (1984).

(Scharifker and Hills, 1983; Scheludko and Todorova, 1952). This can be achieved with the multi-step technique in which a reduction potential, followed by a relaxation potential is applied repeatedly. This oscillation of potential disrupts the flow of electrons which facilitates coalescence of ions that form a nucleation site. If the application of the relaxed and reduction potentials is timed correctly and implemented for a significantly long period, a thin film of metal will eventually form (Sprague and Gilmore, 1994; Venables et al., 1984).

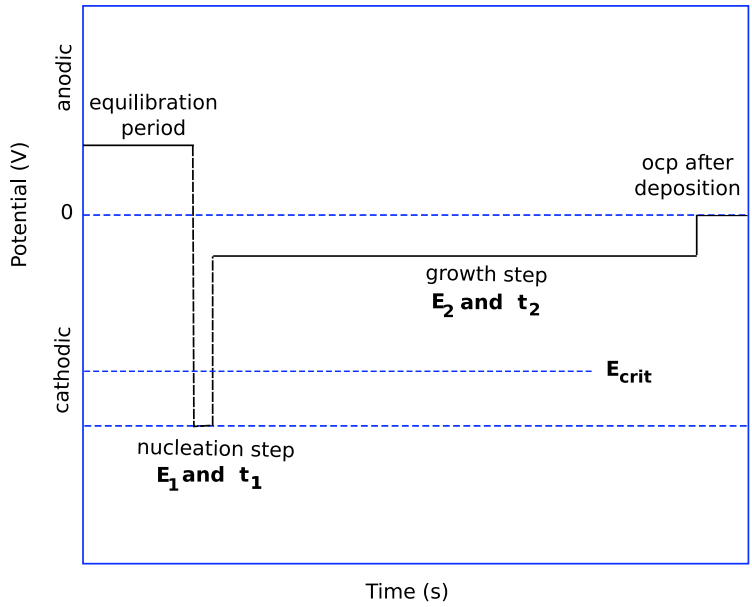


Figure 3.17: Schematic representation of the nucleation potential technique. Potential E_1 allows nuclei formation on the substrate and potential E_2 is a less negative potential suitable for controlled nuclei growth.

Typically two types of growth mechanisms can be observed for the growth of electrodeposited thin films; instantaneous and progressive nucleations, Scharifker and Hills (1983). The presence of either depends upon the rate of nucleation. In the case of instantaneous nucleation, the growth rate of a new phase is high but the number of formed active nucleation sites is low, Venables et al. (1984). In comparison, whilst progressive nucleation is slow, it occurs on a large number of active sites, resulting in the growth of compact grains. The latter is achieved through strategically interrupting the nuclei formation process using the multi-step technique. Interruptions are short and spaced enough to allow, in a following step, controlled growth of the nuclei (Ueda et al., 2002; Venables et al., 1984).

The multi-step technique requires critical information of important parameters as il-

lustrated in Figure 3.17. The technique (Scharifker and Hills, 1983) is characterised by the pulses E_1 and E_2 and their corresponding pulse durations t_1 and t_2. This allows for an efficient way to control the particle size distributions of electrodeposits. The method is based on the knowledge of the critical potential for the system, E_{crit}, which is the minimal potential that has to be applied in order to allow the formation of nuclei.

The first step that was applied, E_1, had to be more negative than E_{crit} to ensure reduction of $PtCl_4^{2-}$ to Pt. The second step, E_2 needed to be more negative than the open circuit potential (OCP) to avoid redissolution but more anodic to prevent new nuclei formation. Duration of the steps was also important, t_1 had to be of the order of milliseconds to avoid the formation of a great number of nuclei, and t_2 had to have values ranging from 40 to 300 s to allow a controlled growth (Penner, 2001; Venables et al., 1984).

In order to determine E_{crit} and E_1 parameters, a cyclic voltammetry was performed on a 10 mM K_2PtCl_4/100 mM KCl system, as shown in Figure 3.14 (bottom panel). This shows a CV starting on open circuit potential (V_{ocp}) conditions (0 mV) and going on cathodic direction up to a potential of -500 mV to avoid secondary cathodic process. The potential sweep is then reversed towards the anodic direction at +500 mV to avoid oxygen evolution. Under these conditions the platinum reduction peak at -300 mV is observed and re-oxidation at +50 mV. We observe the beginning of the platinum reduction at the critical potential (E_{crit} = -180 mV). Thus, nucleation potential E_1 was set between -200 mV and -500 mV to avoid hydrogen evolution and secondary cathodic processes. This potential is applied over a nucleation period t_1 which is in the order of milliseconds to enhance nuclei formation only. The growing potential (E_2) was set to to a more negative value than the V_{ocp} and so it was important it did not exceed E_{crit} in such a way that nuclei formation was inhibited, as well as redissolution of platinum deposit. This growing step potentially enhanced the controlled growth of existing nuclei. Therefore the growing conditions were chosen as; E_2= -300 mV and t_2= 300 s.

Four different types of experiments were carried out with varying E_2 and t_2 and t_1 parameters, these are illustrated in Figure 3.18. Sample 1 (S1) was used as the control where a constant deposition potential V_{dep}= -300 mV was applied for a duration of t= 300 s. Further to this, a single nucleation step (sample 2, S2) was tested and the protocol for this is illustrated in Figure 3.18 (middle panel). Here the parameters were set as follows; E_1= -500 mV ; E_2= -300 mV ; t_1= 0.1 ms; t_2= 300 s. For sample 3 (S3) a double nucleation step technique was used, where the nucleation step of E_1 and t_1 was repeated.

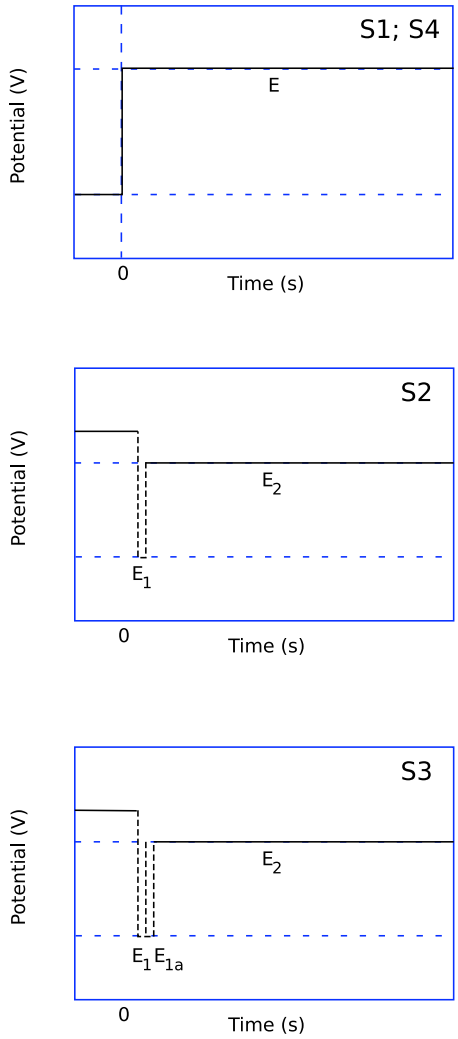


Figure 3.18: Schematic representations of the different nucleation and growth experiments carried out on individual Au/glass electrodes. *Top*: S1, control experiment, V_{dep}= -300 mV; *t*= 300 s. *Middle*: S2, using a single nucleation step, E_1= -500 mV; E_2= -300 mV ; t_1= 0.1 ms; t_2= 300 s. *Bottom*: S3, using a double nucleation step, E_1= -500 mV ; t_1= 0.1 ms; E_{1a}= -500 mV; t_{1a}= 0.1 ms; E_2= -300 mV ; t_2= 300 s. Potential E_1 and E_{1a} allows nuclei formation on the substrate and potential E_2 is a less negative potential suitable for controlled nuclei growth.

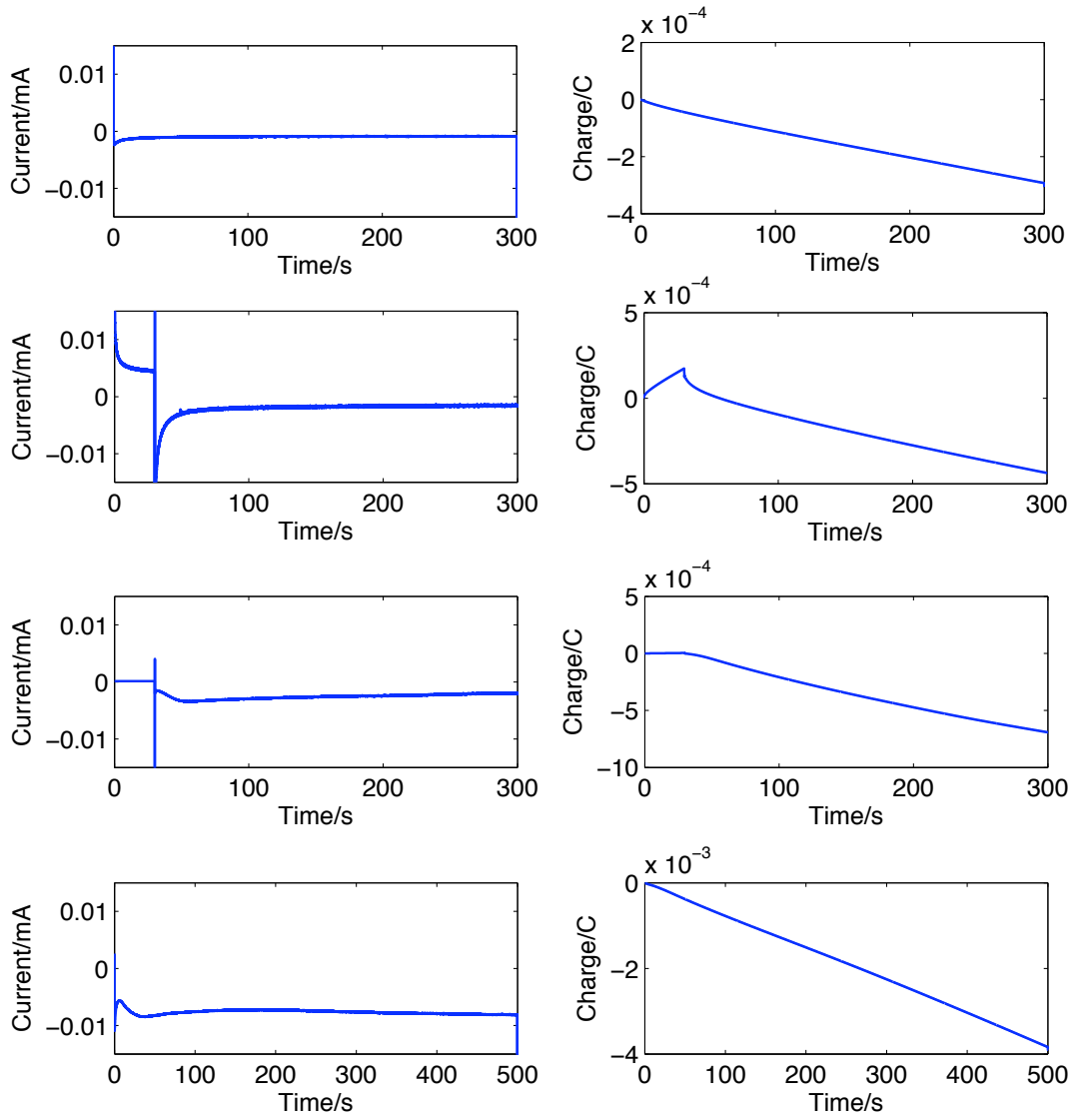


Figure 3.19: Current-time transients resulting from the different nucleation and growth steps applied at individual Au electrodes. *From top to bottom:* S1, S2, S3 and S4 with corresponding charge-time plot for the different samples.

Sample	Charge/ C	Calculated film thickness (nm)
S1	-0.0082	56.50
S2	-0.0052	39.43
S3	-0.0007	5.65
S4	-0.0127	95.80

Table 3.4: Table of calculated charge and thickness values for S1, S2, S3 and S4 experiments at the Au glass electrode substrate.

The additional step, assigned as E_{1a}= -500 mV was set with a time duration of t_{1a}= 0.1 ms. Finally a further control was used where the deposition potential was kept constant as described for S1 (V_{dep}= -300 mV) but with a longer duration of 500 s.

The results obtained for the control depositions experiments (S1 and S4) are presented in Figure 3.19 (top and bottom panel), respectively. Here the behaviour of the current is shown when a -300 mV potential is applied to the system. The results are similar to what we observe for the typical chronoamperometry measurements as discussed in Section 3.4.1. For the case of S1, the current initially rises within the first few seconds due to discharging effects and then remains constant until there is an increase in surface area of Pt deposits, which corresponds to a progressive increase in current over the 300 s run. For S4 (Figure 3.19), the same behaviour is observed, however after ∼320 s, the current stabilises and remains constant for the remaining time. The change in the current induced by the potential also indicates that at short times (<300 s) a progressive deposit of particles is achieved. However at longer times (S4, t= 500 s) the growth of the larger grains becomes limited by diffusion due to a depletion layer established around the grains, Venables et al. (1984).

For the multi-step depositions, the behaviour of the current indicates two steps; a 'nucleation process' at the start and a 'growth process' when it stabilises. For S2, the results for which are plotted in Figure 3.19, it can be observed that during the first step (E_1) a typical nucleation curve for electrodeposition is observed, Scharifker and Hills (1983). This is followed by an increase of the current, indicating a possible growth of the Pt grains. For S3, the same trend is seen with the exception of an additional nucleation step.

Optical images of Pt deposition at each individual electrode following the multi-step

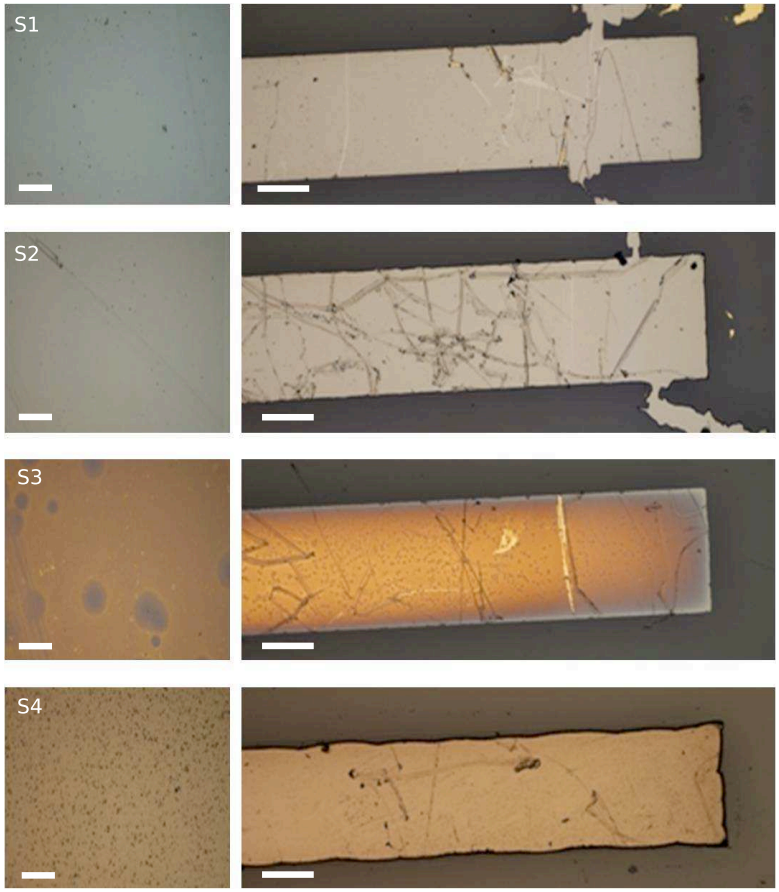


Figure 3.20: Optical images of Pt surfaces (samples S1, S2, S3 and S4) at 100 x after depositions including individual images of the electrodes at 20 x magnification.

procedure were also investigated and are shown in Figure 3.20. For nucleation step experiments (samples S2 and S3) the images showed uneven films and sparse deposition. Whereas for samples S1 and S4 (where no nucleation step was applied) uniform Pt layers with consistent deposits were achieved. The corresponding charge-time plots for all four measurements are provided in Figure 3.19. For samples S1 and S4, a much higher deposited charge is obtained, whereas for S2 and S3, the resulting charge is between -0.0007 to 0.00127 C, respectively. By calculating the thickness values from these plots (provided in Table 3.4), it was observed that the constant deposition experiments S1 and S4 also gave the greatest thickness values compared to the S2 and S3 under the same conditions. From this it was concluded that with the constant deposition method, the growth of Pt film were achieved more efficiently than that obtained with the multi-step method.

3.4.4 Scanning Electron Microscopy (SEM) Characterisation

The Scanning Electron Microscope (SEM) was used to characterise the surfaces of the Au and Pt deposits for all deposition experiments carried out. SEM imaging was performed on a LEO Gemini 1525 SEM. The substrates were affixed to conductive carbon tape (G3939, Agar Scientific) and loaded on specimen mounts for SEM imaging. The WD was set to 5 mm and all measurements were conducted at either 5 kV or 10 kV for high resolution imaging.

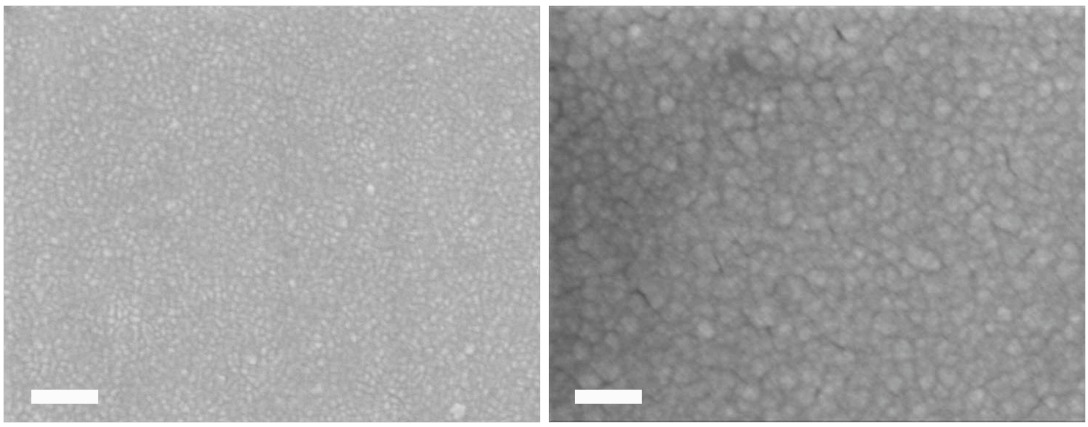


Figure 3.21: Scanning electron micrographs for (*Left*) Au layer on glass substrate and (*Right*) Pt electrodeposited layer. Scale bar= 200 nm.

Figure 3.21 (left panel) shows a typical SEM image of a gold (Au, 100 nm film thickness) electrode prepared for electrodeposition. A smooth Au surface is observed, with no observ-

able cracks or pores with grain size less than 20 nm ±5 nm. In contrast (Figure 3.21, right panel) the SEM of the electrode following electrodeposition of Pt reveals structures similar to bulk Pt films (Baumgartner, 1988; Ross, 1994). Both the polycrystalline gold and platinum films exhibited strong contrast variations in SEM images, resulting from Bragg reflections of randomly orientated crystalline grains, Goodhew and Humphreys (2001). Overall the SEM images showed a uniform layer and relatively flat topography.

3.4.5 Elemental Analysis

Energy dispersive X-ray spectroscopy (EDXS) was used for chemical characterisation of the Au and Pt electrode surfaces and to confirm the composition of both metal layers. In SEM, the sample was exposed to an extremely narrow beam of high energy electrons. Some of these electrons reflected from the surface of the sample, allowing this to be viewed on a monitor screen in the form of a 'back-scattered' electron image, Wells (1974). Other electrons were able to lose energy by interacting with the atoms present in the sample, prompting the emission of X-rays; every chemical element reacted differently in terms of the quantity of X-rays produced, Goldstein (2003).

This function was built in the SEM instrument (LEO Gemini 1525 SEM) where the working distance (WD) was set to 15 mm with an aperture size of 60 μm. Figure 3.22 shows the scans obtained using the INCA Energy software (Oxford Instruments). Individual areas of 500 nm x 500 nm were scanned for the Au electrode surface and the electrochemically deposited Pt surface. The information was plotted as a spectrum of energy versus relative counts of the detected X-rays.

The spectrum obtained for the Au/glass electrode showed a clean Au crystalline surface, indicating a clean surface for deposition. The peaks observed for the Au surface were observed at 2.409; 2.204; 2.117; 2.123 keV corresponding to emissions of X-rays specific for an Au element and were validated using the INCA Element feature, within the software. For the Pt deposited films on the Au surface, again the peaks corresponded to the presence of Pt at 9.973; 8.267; 2.331; 2.050; 2.046; 2.127 keV. A small amount of oxygen and a negligible quantity of carbon was also detected for both analyses. The carbon contamination was common in these measurements and was due to prior cleaning of samples with acetone and from the carbon conductive tape (G3939, Agar Scientific) which was used to affix the samples to the stage. The results obtained from these measurements validated the presence of Pt metal on the surface, which was electrochemically deposited onto the

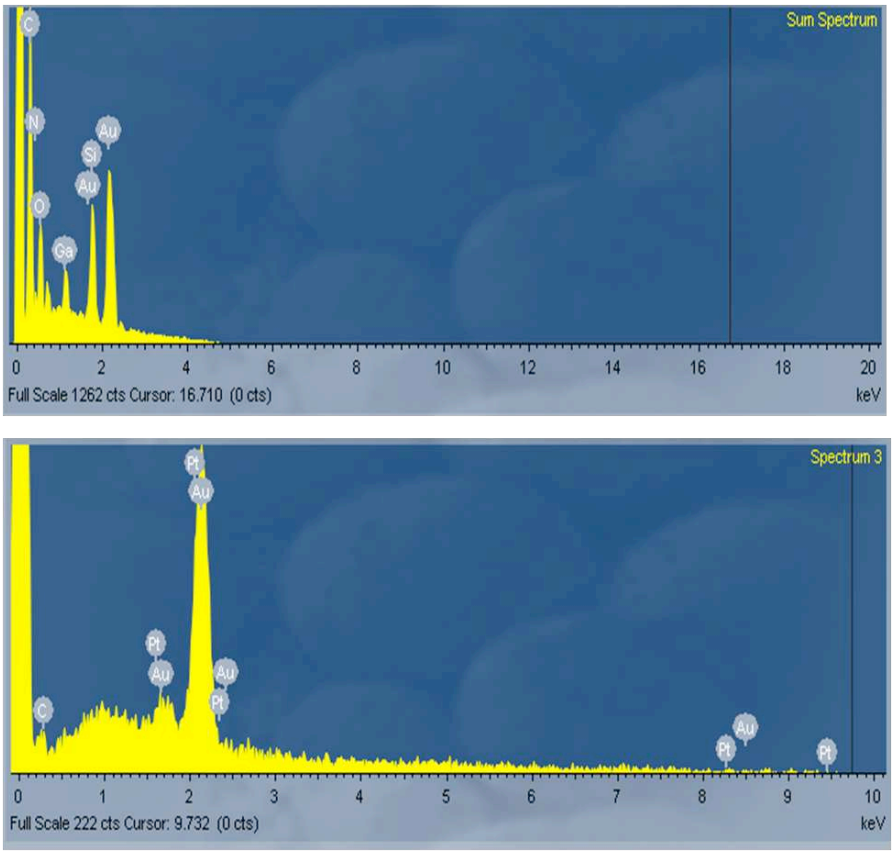


Figure 3.22: EDXS spectras showing the elements present for (*Top*) Au and (*Bottom*) Pt samples scanned. With relevant counts of Au (2.409; 2.204; 2.117; 2.123 keV) and Pt (9.973; 8.267; 2.331; 2.050; 2.046; 2.127 keV) detected corresponding to typical peaks observed for these metal, Goldstein (2003).

Au from the aqueous plating bath.

3.4.6 Scanning Tunnelling Microscopy (STM) topographic analysis

Scanning Tunnelling Microscopy (STM) allowed for a general assessment of the deposit growth quality and reproducibility. STM measurements were carried out using Agilent 5500 STM (Agilent Technologies). A hermetically sealed, top-down configuration provided complete isolation of the electronics and scanning elements from the imaging environment. The STM was housed in a Faraday cage and placed on a vibration isoltation table.

Areas ranging between 50 nm^2-1 μm^2 were analysed with a current setting of 1 nA and scan rates between 0.6-0.8 nm^2 s^{-1}. All measurements were taken using the PicoImage^{TM} software, provided with the instrument. The variations in tip height were recorded as a Tungsten (W) tip was scanned repeatedly across the sample, producing a topographic image of the surface. Using this, a computer-generated contour map of the surface was produced. Processing of all STM images was carried out using WSxM 5.0, Nanotec software.

The typical STM images recorded for the Au and Pt deposited films from the aqueous solution are shown in Figure 3.23. These images confirmed the spherical form of Au and Pt grains already observed by SEM. For an Au sample, a fairly flat surface was observed with grain sizes <20 nm. Following Pt deposition, (V_{dep} of -300 mV; t= 120 s) the resulting surface showed larger grain sizes due to Pt deposits and a rough texture. A longer deposition time duration of 400 s was also used (with all other parameters kept constant) to study the difference in film quality over time. The STM scan for this is provided in Figure 3.23 (top panel). This image shows a less rough surface as the Pt film grows during electrodeposition becoming more compact, at this point fewer individual Pt grains were detected due to the formation of overlapping growth centres. A histogram of grain distribution was also constructed by scanning large-scale areas of three samples (Figure 3.23, bottom panel). This showed the number of grains detected with a specific height. Using a Gaussian fit, the average height for each sample was calculated and is provided in Table 3.5. After acquiring the STM images it was possible to measure the 1-D surface roughness on a line in the horizontal direction, this was carried out over a 400 nm^2 profile. The root mean square (RMS) roughness was determined (Equation 3.4.2) with the software from 342 pixels.

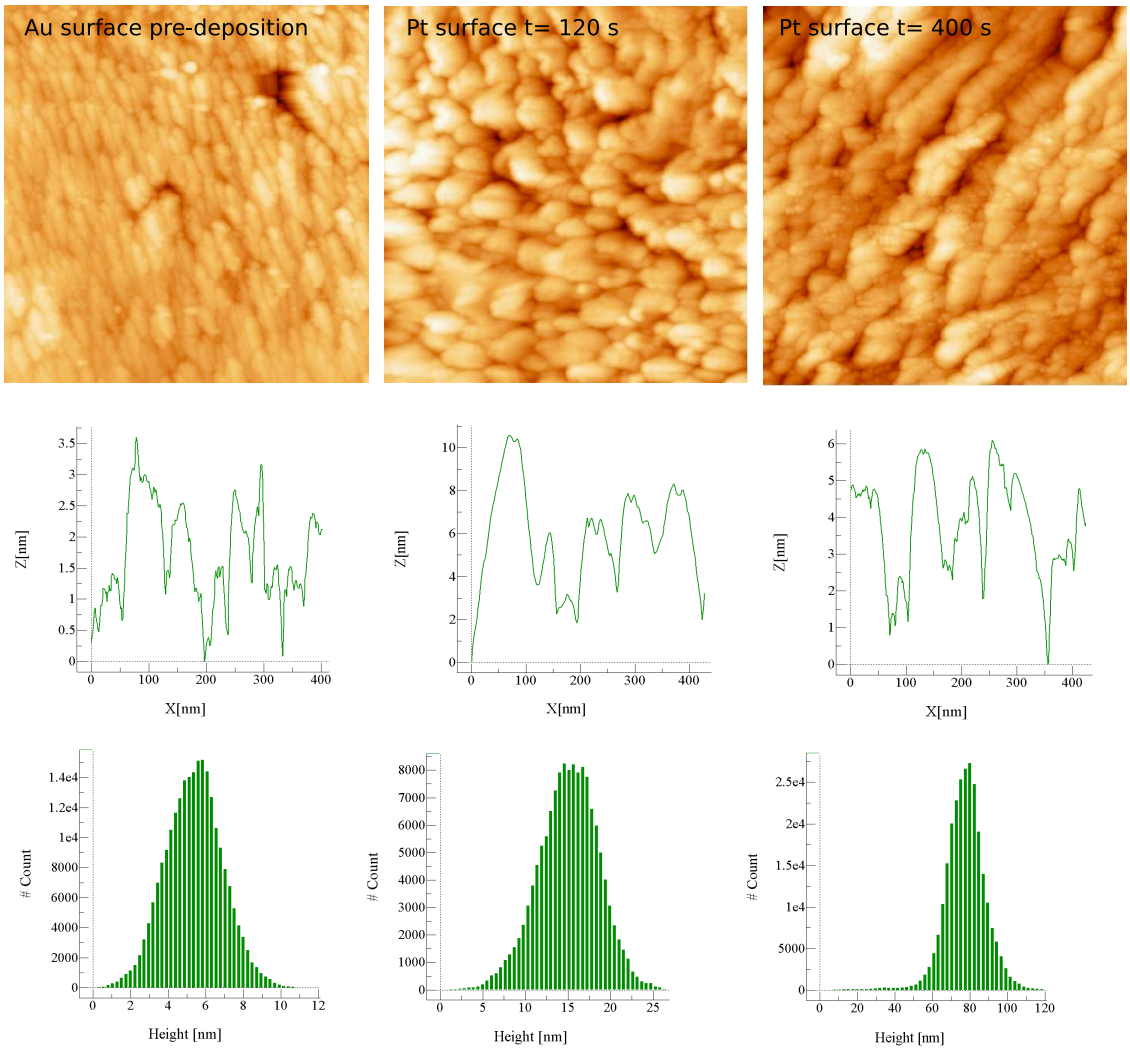


Figure 3.23: STM image and roughness measurements for the gold and platinum deposited surfaces. *Top:* (i) 2-D image of the Au surface prior to deposition, prepared by thermal evaporation. (ii) 2-D image of Pt surface prepared by the application of a constant potential in 10 mM K_2PtCl_4/100 mM KCl, V_{dep}= -300 mV for t= 120 s. (iii) 2-D image prepared by the application of a constant potential in 10 mM K_2PtCl_4/100 mM KCl V_{dep}= -300 mV for *t*= 400 s. *Middle and Bottom:* The profiles along the dotted line are associated with the image and show the overall roughness. The histogram of grain distribution carried out for both Au and Pt samples show the numbers of grains with specific heights. All topographic scan dimensions were set to X= 100 nm, Y= 100 nm, Z= 100 nm.; histogram and line measurements were carried out on large scale areas of 400 nm^2.

Sample	RMS roughness/ nm	Average height/ nm
Au surface pre deposition	1.51	5.42
Pt surface, t= 120 s	11.07	15.14
Pt surface, t= 400 s	3.54	77.92

Table 3.5: Table of calculated RMS roughness using Equation 3.4.2 and the average height of Pt film derived for each sample.

$$RMS = \sqrt{\frac{1}{N}\sum_{i=1}^{N} r_i^2}, \tag{3.4.2}$$

where r_i is the profile in nanometers. The results obtained for the 1-D surface roughness of Au and Pt deposited films are shown in Figures 3.23 (middle panel). The image displays the magnitude of variation in shape fluctuation along the line direction, further demonstrated in the plot of height as a function of distance along a single line. The average height and the root means square (RMS) roughness of the Au surface were determined as 5.42 nm, and 1.51 nm respectively. Similarly post-deposition (t=120 s), the Pt film produced grain sizes between 30-40 nm with an average height of 15.17 nm and RMS= 11.07 nm. For t= 400 s, an average height of 77.92 nm was calculated with an RMS= 3.54 nm. Indicating the surfaces obtained post-deposition had a low surface roughness and were suitable for the application of thin film growth, as discussed in Chapter 4.

3.5 Summary

In summary, a method to deposit platinum has been developed and characterised with a view on controlling the size of our metallic nanopores. Platinum was deposited on fabricated gold electrodes from a solution of 10 mM K_2PtCl_4 and 100 mM KCl at room temperature. The growth conditions were tuned to obtain uniform layers of the Pt film with a metallic conductance. Parameters including $PtCl_4^{2-}$ complex concentration; reduction potential and time duration were examined. Along with multi-step experiments which utilised the separation of nucleation and growth towards forming smaller grain sizes. The Pt deposited surfaces obtained were smooth and homogenous without cracks or pores. STM measurements gave an average RMS value of 3.54 nm for a deposition duration of

400 s, indicating a low surface roughness. The grain sizes observed with SEM and STM were between 30-40 nm showing the control over deposits in the conditions investigated.

The characterisation studies carried out provide us with important information on the distinct system parameters that are required for the optimisation of Pt deposition using the developed plating bath. Further work looks at the integration of electrochemical deposition with a feedback mechanism to control the dimensions of metallic nanopores.

Chapter 4

Precise electrochemical fabrication of sub-20 nm metallic nanopores

Declaration: The work presented in Section 4.5.5 is also published in M. Ayub et al, 'Precise electrochemical fabrication of sub-20 nm solid-state nanopores for single-molecule biosensing'. Journal of Physics: Condensed Matter, 2010, Volume 22, 454128.

This chapter presents the work conducted on developing a novel and simple fabrication technique to produce metallic nanopores with apparent diameters below 20 nm. Section 4.1 presents an overview of the current solid-state nanopore fabrication methods and hence serves as a precursor to the techniques developed and presented in this chapter. In particular, it outlines the limitations of current methods and emphasises the need for better control of pore dimensions during the fabrication process. Section 4.2 then discusses the general experimental set-up of the fabrication studies, a brief overview of the chemicals and material employed is provided, as well as a description of the equipment used to conduct this investigation. Subsequently Section 4.3 discusses the preliminary experiments carried out for fabricating nanopores using electrochemical deposition in the absence of a feedback mechanism.

The remainder of this chapter presents two different techniques that have been proposed and tested to provide greater control of pore dimensions during the fabrication process. Firstly, the use of a visual feedback method is considered in Section 4.4, followed by an ionic current feedback (ICF) method in Section 4.5. For each method, details of the set-up, the necessary steps required for sample preparation and the studies conducted for characterising the proposed methods are presented. These sections then present the

results of the studies carried out and a discussion on the findings. A summary of the conclusions drawn from the work presented in this chapter are presented in Section 4.6.

4.1 Background

As discussed previously in Chapter 1, metal nanopores may provide improved sensitivity and control of the physical characteristics of a nanopore surface and its interaction with molecules under investigation (which can allow for various applications eg. surface modification, etc.). Whilst electrophoretic translocation of DNA, RNA and proteins through nanopores has enabled both detection and structural analysis of these complex biomolecules, (Dekker, 2007; Fologea et al., 2005a; Han et al., 2008) in the measurements considered in this work, the pore must be comparable to the size of the analyte molecule in question. Hence control over the nanopore size is critical.

Currently, the most widely used fabrication methods are based on focused electron or ion beams and thus require (scanning) transmission electron microscopy (STEM) and focused ion beam (FIB) instrumentation (Storm et al., 2003; Li et al., 2001). However, although very small pores are achievable using these approaches, several issues remain. These include the requirement of using very thin, mechanically less stable membranes, particularly for pore diameters in the single digit nanometer range; device-to-device reproducibility; control of the surface properties at and inside the nanopore and finally, the fabrication cost. Therefore, there is an increasing interest in controlling nanopore sizes for both bare insulating membranes and metallic nanopores with more effective techniques.

Since commencing work in this field the research conducted in this group has primarily focused upon developing novel architectures for control and selectivity of bio-molecules. Developments within this project were based on work done by C. Martin et. al towards fabricating gold nanotube membranes (Wang et al., 2006; Yu et al., 2003) and the fabrication of the Pt glass electrode (Zhang et al., 2006) which presented the possibilities of controlling the properties at the nanopore interface through external, electrostatic gating and chemical functionalisation, Nishizawa et al. (1995). Subsequently, the fabrication method discussed here is based on the use of electrochemically depositing Pt metal to consistently shrink the size of metallic nanopores. The objective of the work presented here is to develop a method which permits the control of nanopore sizes during the fabrication process whilst avoiding the need for overly complex or expensive methods. Furthermore, if sufficiently versatile, such a method could be scaled up to fabricate larger nanopore arrays

and can applied to the fabrication steps of other instruments which require a control of metal fabrication down to a few nanometers. However, in this chapter the focus remains upon the development of such an approach to fabricate highly sensitive single molecule sensors. In order to satisfy the given criteria a feedback mechanism is necessary such that the deposition process (and hence the pore size) may be observed and so controlled in real-time. As mentioned above, two such feedback approaches are considered here; the first is based upon a visual observation of the deposition process and the latter is based upon the ion conductance through the nanopore. Both feedback methods are tested to evaluate their performance in controlling pore sizes to the required tolerance.

4.2 Experimental

4.2.1 Pt deposition

The electrodeposition of platinum metal onto gold coated nanopore surfaces is presented in this chapter. For these studies, a plating bath of potassium tetra-chloroplatinate II (K_2PtCl_4, 99.99% Sigma Aldrich) complex is used with potassium chloride (KCl; Fluka, >99.99%) acting as a supporting electrolyte. The $PtCl_4^{2-}$ ions are reduced at the Au nanopore surface to form Pt using the following reduction reaction:

$$PtCl_4{}^{2-} + 2e^- \rightarrow Pt + 4Cl^- \tag{4.2.1}$$

The development and full characterisation of the plating bath employed in this study is discussed in Chapter 3.

4.2.2 Fabrication of initial nanopores

The initial large size nanopores used throughout this chapter were prepared as described in Section 2.2. Briefly Si_3N_4 membrane of thicknesses between 50-240 nm were metallised from one side with 10 nm Ti and 100 nm Au layers. Both individual pores and arrays of 100 nm diameter were then milled into the membrane using a focused ion beam. The exact dimensions and properties of these pores are described in the relative sections.

Prior to measurements, the nanopore chips were exposed to an oxygen plasma to remove any organic contaminants. Subsequently, the chips were wetted to avoid any accumulation of dust. This was done by applying ~5 μl of propan-2-ol to the cis side of the chip and then by turning the chip, the trans side was also treated with propan-2-ol.

4.2.3 Data acquisition and analysis

All deposition measurements were performed using a commercial potentiostat, (CH760c, Electrochemical Workstation, CH Instruments). The instrument was controlled via a personal computer (PC) using the CHI 7.20 software. All electrochemical potentials were measured with respect to a Ag/AgCl reference electrode. The flow cell was in which the experiments were conducted was placed in an in-house Faraday cage and electrically connected to the ground. Depositions were carried out at room temperature. The electrolyte solution was degassed by bubbling high purity argon (Ar) gas for 15 minutes prior to every measurement.

4.3 Preliminary experiments

Subsequent to the studies conducted in Chapter 3 on the electrodeposition of Pt on flat surface, this section looks to apply the findings to a nanopore and verify that the observed deposition characteristics are reproducible for a nanopore containing membrane.

4.3.1 Methodology

A three electrode configuration was employed for the studies in this section, whereby deposition took place on the entire surface of the nanopore membrane. A schematic of the experimental set-up is presented in Figure 4.1. Nanopores used for these measurements consisted of a 16 nanopore array with dimensions of 100 nm with a distance of 5 μm between each pore. The pores were milled into a 100 nm Au; 10 nm Ti and 200 nm Si_3N_4 thick membrane using the FIB technique.

The electrodeposition process requires that the chip be held in place in a stable manner within the solution; hence the chip was adhered to a glass slide using KwikCast epoxy. In order to achieve an electrical connection to the chip for the deposition process, contact pads were patterned and fabricated onto the slide prior to adhering the chip. An electrical connection between the contact pad and the chip was then achieved using a wire bond, Figure 4.2. Discussions of the protocol used for the wirebonding and patterning of the contact pads are provided in Appendix 4.7.2 and 4.7.3, respectively.

The three electrode configuration used was connected to the potentiostat. Here, a Pt wire (250 μm thickness; 5 cm length) was used as the counter electrode (CE) and Ag/AgCl as the reference electrode (RE). The Au coated membrane was connected to the working

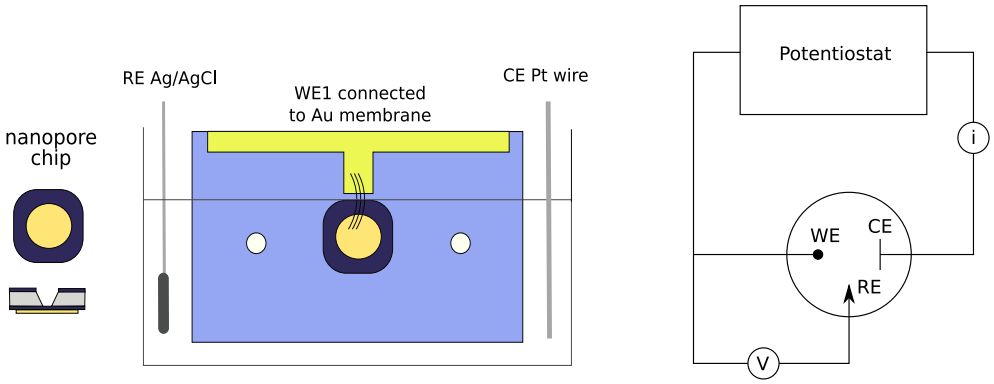


Figure 4.1: Schematic of the experiment. *Left*: A 3 electrode configuration is used and the nanopore containing the 16 nanopores is immersed in the deposition solution completely. *Right*: Circuit for the connections to a potentiostat. notations: WE (working electrode), CE (counter electrode), and RE (reference electrode).

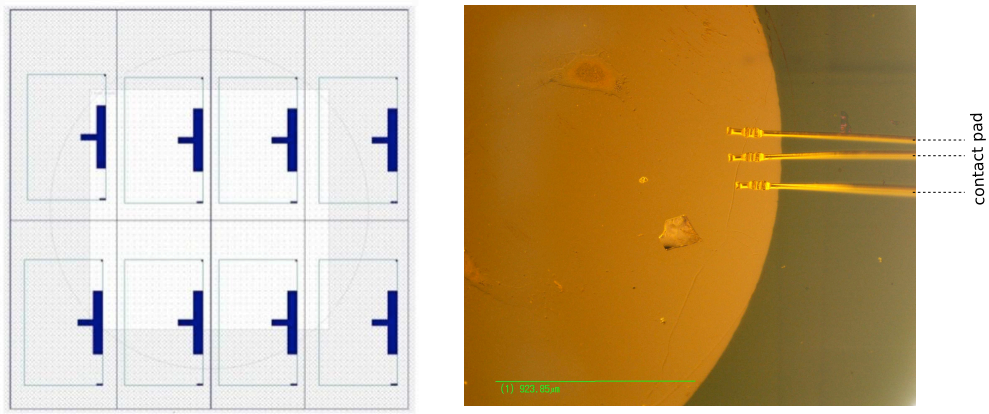


Figure 4.2: *Left*: Photomask for the design of Au contact pads on a glass substrate. Each glass slide had the dimensions 65 mm x 25 mm. Dots and dash lines in the CAD file act as guidelines for drawings and were not printed onto the final photomask. *Right*: Optical image of Au wedge bonding at the edge of a nanopore chip (front view, *yellow*- gold layer; *green*- silicon nitride layer). The three bonds shown lead towards the contact pad patterned on the glass substrate, which is externally connected to the WE1 terminal.

electrode (WE1) terminal by wire bonding onto the Au contact pad. The crocodile clip for WE1 was then attached to the contact pad outside of the solution to allow for external control of the potentials that were applied.

4.3.2 Results and Discussion

Pt deposition at nanopore arrays

Platinum was electrochemically deposited onto the Au metal coated nanopore array containing 16 nanopores of 100 nm ±5 nm dimensions, from a solution of 10 mM K_2PtCl_4 and 100 mM KCl. The chronoamperometric measurements were carried out by immersing the Au membrane into a electrochemical cell as illustrated in Figure 4.1. The typical recorded deposition current vs. time trace obtained at an individual nanopore membrane is plotted in Figure 4.3. The deposition parameters were set to a time duration t= 140 s and V_{dep}= -300 mV.

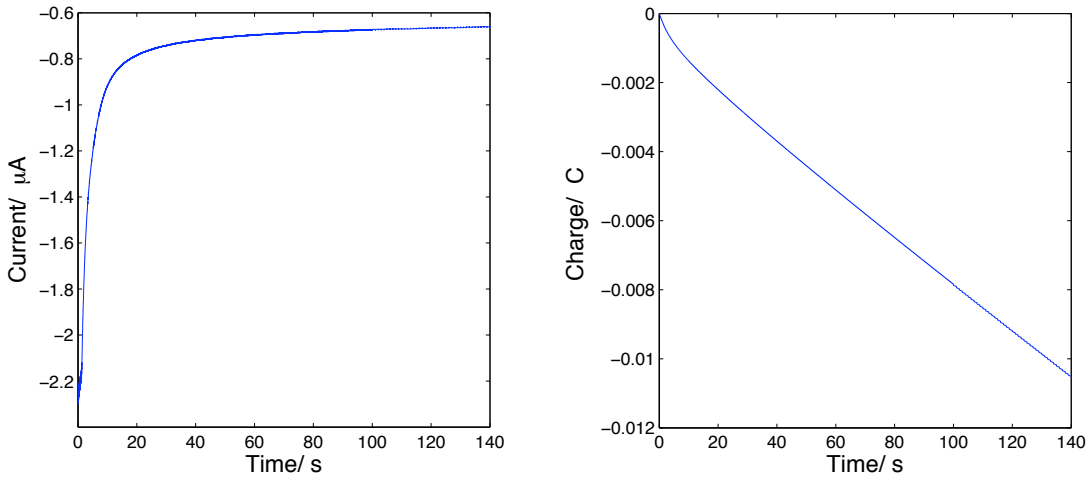


Figure 4.3: Current-time transients resulting from the deposition of Pt on an array of 16 nanopores with intial pore diameter of 100 nm ±5 nm each. The deposition is carried out from a solution of 10 mM K_2PtCl_4 and 100 mM KCl, at a V_{dep} of -300 mV, t= 140 s.

By integrating the deposition current-time curve, the total amount of deposited charge (Q= $\int$I x dt) was also calculated. The plot of charge-time for this experiment is provided in Figure 4.3. A delay of 1.5 seconds was used for determining the charge, in this case a total of -0.0104 C was transferred during the deposition with a final Pt film thickness of 49.2 nm, calculated using Equation 3.4.1.

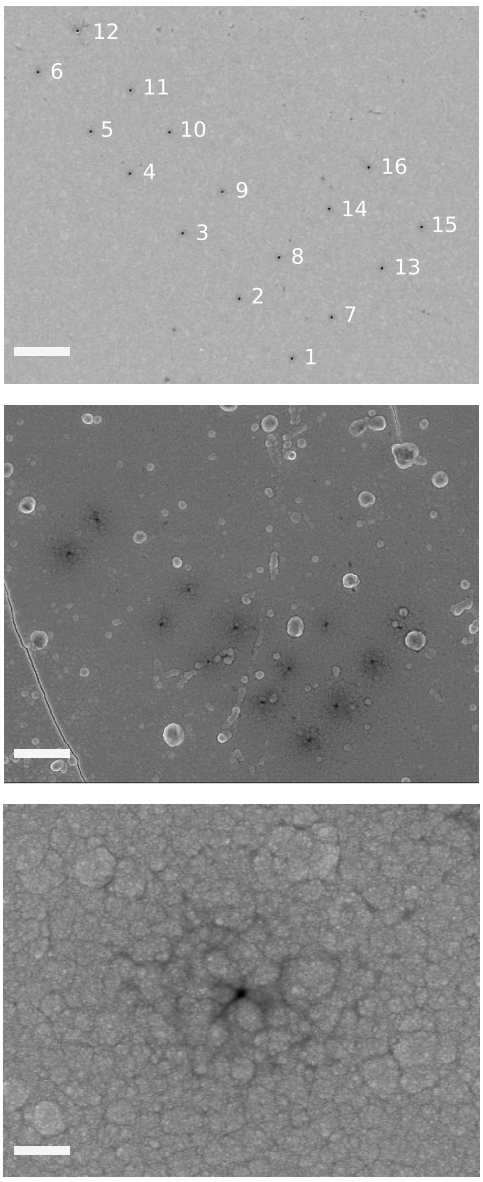


Figure 4.4: Scanning electron micrographs (*Top*) before and (*Middle*) after the deposition of Pt at the 16 nanopore array. Each pore is numbered corresponding to the initial and final dimensions tabulated in Table 4.1. Scale bar= 4 μm. An average diameter value of 66 nm is obtained across all nanopores fabricated using the electrochemical deposition technique. *Bottom*: close up of a single pore (centre) from the array showing deposition around the periphery of the pore. Scale bar= 200 nm.

SEM imaging

SEM imaging of the pores before and after deposition revealed a reduction in pore size. Figure 4.4 shows the nanopore array with initial pore diameters of 100 nm and the subsequent post deposition pore diameters. From the figure, the growth of Pt deposits is evident and by using the scale bar feature provided in the SEM software, the pore dimensions were determined and are plotted in Table 4.1. The experiment was successful in demonstrating the use of electrochemical deposition for controlling the size of the metallic nanopores. Uniform nanopore arrays were observed post deposition. In addition to this, the thickness and granularity of the deposit were observed to be consistent with the results of Chapter 3.

However in order to achieve a particular pore size accurately and consistently the temporal variation in pore size must be observed during deposition, such that the process may be stopped when the desired pore size is reached. Therefore a monitoring form or a feedback mechanism is necessary to control the deposition process; the subsequent sections of this chapter discuss the use of a visual feedback method (Section 4.4) and an ionic current feedback method (Section 4.5).

4.4 Visual feedback method

The first generation of nanopore shrinking techniques considered here use an optical imaging method which allows for real time *in situ* studies of the electrochemical deposition process. The visual was achieved using an inverted optical microscope composed of a light source and condenser above the stage pointing down, whilst the objective and turret were positioned below the stage pointing up. Hence by performing the deposition process with this set-up, the pore shrinking could be observed.

4.4.1 Requirements for optical measurements

In order to initiate and observe the depositions using this optical technique, the nanopore chip needed to fulfil several requirements.

Firstly, the chip had to be affixed to a robust platform so that it could be mounted onto the stage of the microscope. The same Au patterned glass substrate design discussed in Section 4.3 was used in this case. However the platform had to incorporate a sealed compartment to allow for a small volume of deposition solution to be filled. The dimensions

#	Pre deposition		Post deposition	
	width/ nm	height/ nm	width/ nm	height/ nm
1	105.8	104.5	69.4	67.5
2	101.8	102.6	69.6	68.4
3	101.5	102.6	63.4	68.5
4	103.3	102.6	66.8	69.3
5	100.8	101.8	46.5	50.3
6	100.8	101.8	62.5	65.5
7	101.0	102.8	71.1	68.9
8	101.5	101.8	69.6	69.5
9	100.8	101.8	71.0	69.2
10	100.8	101.8	63.5	68.5
11	101.5	101.5	48.2	49.5
12	100.8	101.8	64.5	69.9
13	101.0	101.5	69.4	72.1
14	100.8	101.8	66.8	69.3
15	101.0	101.5	68.6	68.3
16	100.8	101.8	63.5	66.5

Table 4.1: Summary of results for the deposition of Pt onto a 16 nanopore array. The pore dimensions of individual pores have been inferred from SEM measurements using a scale ruler provided in the interface software. #: labelled nanopore (from 1-16) from the SEM image in Figure 4.4.

of this also had to accommodate the RE and CE electrodes. Furthermore, it was important that the platform also facilitated the easy exchange of solution and handling of the flow cell.

Secondly, the metal coated side of the membrane had to be oriented to permit its visualisation during deposition. Therefore the nanopore metallic layer side of the chip was placed facing down, in view of the microscope objective. In order to achieve an even deposition distribution both at the entrance to the nanopore and inside, it was necessary that the nanopore was fully submerged within the deposition solution; hence forming two reservoirs (top and bottom). The geometry of the bottom reservoir also had to be controlled so that the distance between the membrane and the microscope objective was within focusing range. Figure 4.5 shows a schematic of the microfluidic flow cell that was assembled for the optical imaging experiments, and its photograph is provided in Figure 4.6.

4.4.2 Assembly of the PDMS/glass flow cell

The assembly of the flow cell commenced by drilling access holes (1.6 mm in diameter) into the patterned glass substrate. Prior to this, the nanopore membrane was wire bonded to the contact pads on the glass substrate, as discussed in Section 4.3. The glass substrate was then plasma-bonded to a pre-shaped poly(dimethylsiloxane) (PDMS) to increase the thickness of the top reservoir, shown in Figure 4.5. A sufficiently thick PDMS layer was necessary to avoid resistive losses in the electrodes, whilst the diameter of the holes were sufficiently large so that the reservoirs could be filled easily. The procedure for fabricating the PDMS moulds is provided in Appendix 4.7.1.

The bottom reservoir was then constructed by adhering spacers (SecureSealTM, Grace Biolabs) of known thicknesses (120; 240; 360 μm) in layers and sealed using a glass coverslip. This coverslip had a thickness of less than 200 μm and was at a distance of 30 μm from the membrane; such that the membrane was in the focal plane of the microscope. The volume of the cell was <1 ml and was filled with the deposition solution; 10 mM K_2PtCl_4 and 100 mM KCl. The flow cell was filled by injecting the deposition solution into the fluidic channels and then relying upon capillary action to fill the reservoirs.

In a typical experiment, the glass slide, coverslip and PDMS were cleaned by piranha solution and sonication in a solution of deionised water and ethanol prior to use. After sonication, both surfaces were hydrophobic. The coverslip and glass was rendered hydrophilic

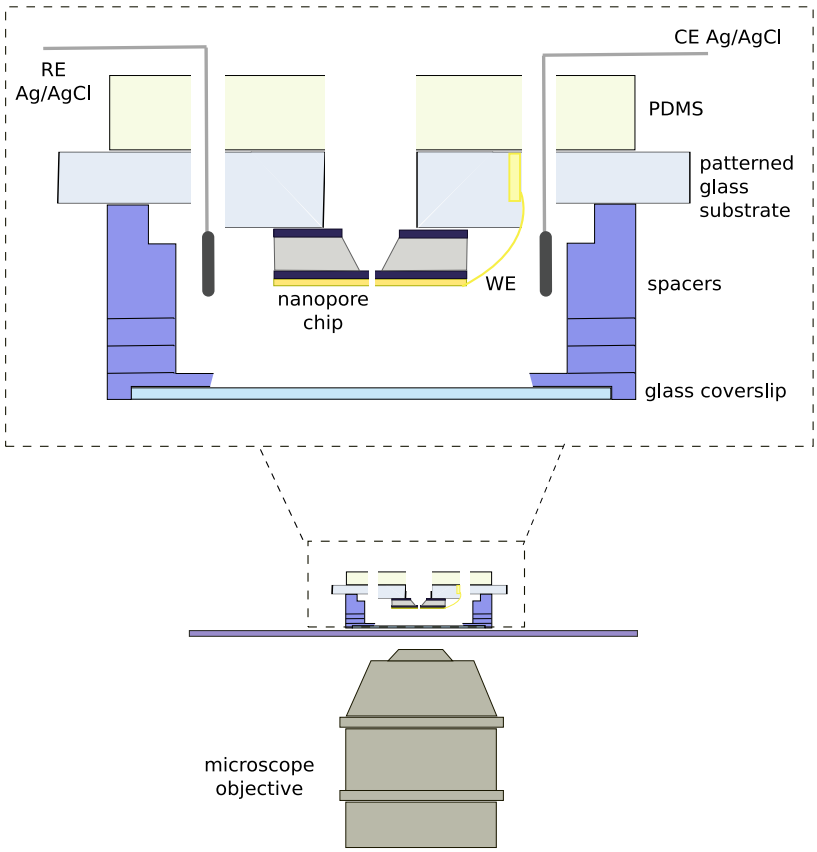


Figure 4.5: Device for real time optical feedback of electrochemical deposition. Schematic of device (not to scale). In this configuration, the CE and RE are positioned into the device using clamp holders. WE is connected via an external contact pad leading to the Au coated nanopore membrane. Spacers cut into frames are used to build the bottom reservoir, which is at a distance of 80 μm from the glass coverslip. The microscope objective is represented for reference.

by exposure to an oxygen plasma for 2 minutes and were then irreversibly bonded to each other. The plasma treatment made the surfaces hydrophilic and negatively charged, which led to strong electro-osmotic flow. A major challenge was to eliminate pressure-driven flows in the cell, which was achieved by ensuring that all channels and reservoirs were at the same pressure. For this, the entrances of each channel were connected to the bottom reservoir. The microfluidic flow cell was then mounted onto the stage of the inverted optical microscope.

The crocodile clip terminal for WE was attached to the contact pad outside of the solution to allow for external control of the potentials that were applied. The RE and CE electrodes were inserted in the distal end of the bottom reservoir using 30 cm tall clamp

holders which were placed on the side of the microscope set-up. These clamps extended above the microscope objective with the aid of a light sturdy aluminum block.

In between experiments, the cell could be dis-assembled and both pieces of glass thoroughly cleaned. The patterned glass substrate that formed the top of the cell was used for numerous experiments with no detectable change in its performance.

4.4.3 Optical set-up

The optical setup consisted of a custom-built confocal microscope with imaging capabilities. In this configuration, the light source was a bright field mercury lamp (Olympus). The selected light entered the body of the microscope (Olympus IX71) and was directed to the nanopore chip through a Olympus 20 x objective. The image was collected by the same objective and was then directed to an electron-multiplying CCD (emCCD) camera (Cascade II, Photometrics). This camera had a pixel size of 16 μm.

An additional 1.6 x post-objective magnification was used to observe the nanopore array. The imaging array was set to 512 x 512 pixels and the data was collected using the RSImage software provided with the camera. A frame rate of 34.3 ms was used for all recordings. Figure 4.6 shows an image of the entire optical set-up integrated with the potentiostat measurements for deposition. The potentiostat, optical microscope and the position of the PDMS/glass flow cell on the microscope stage are annotated as 1, 2 and 3 respectively. A close up of the stage is also shown in the figure, here the RE (white), CE (red) and WE (green) terminals are held in place using clamp holders. A close up of the PDMS/glass flow cell from the view of the optical microscope (bottom) is also provided.

4.4.4 Results and Discussion

Chronoamperometric measurements

Platinum was electrochemically deposited onto the Au metal coated nanopore array, containing 16 nanopores of 100 nm ±5 nm dimensions, from a solution of 10 mM K_2PtCl_4 and 100 mM KCl.

The chronoamperometric measurements were carried out simultaneously whilst observing the deposition process visually under an optical microscope. The typical recorded deposition current vs. time scan at an individual nanopore membrane is plotted in Figure 4.7. The deposition parameters were set to a time duration, t, of 160 s and V_{dep}= -300 mV. The typical features are observed during deposition where we observe a sharp peak at

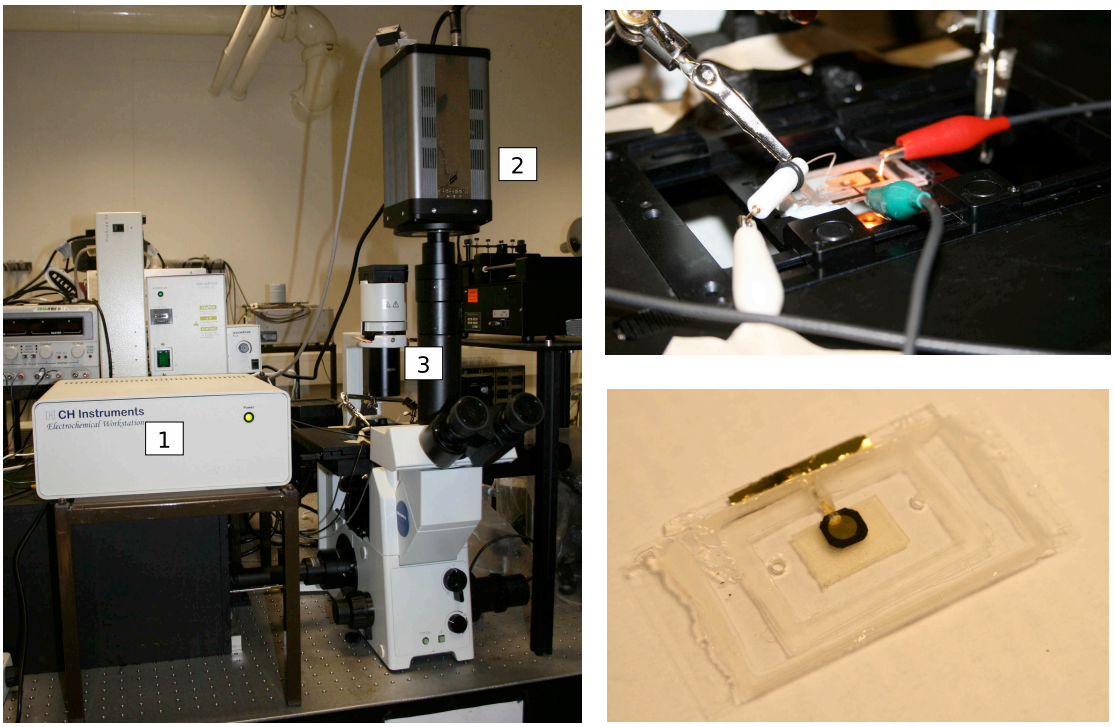


Figure 4.6: *Left*: Image of the optical set-up for the visual feedback of electrochemical deposition at a nanopore array. The potentiostat, optical microscope and the position of the PDMS/glass device on the microscope stage is annotated as 1; 2; 3 respectively. *Top right*: a close up of the stage shows the flow cell and the electrical connections of RE (*white*), CE (*red*) and WE (*green*) terminals held in place using clamp holders. *Bottom right*: Image of the 65 mm x 25 mm PDMS/glass flow cell.

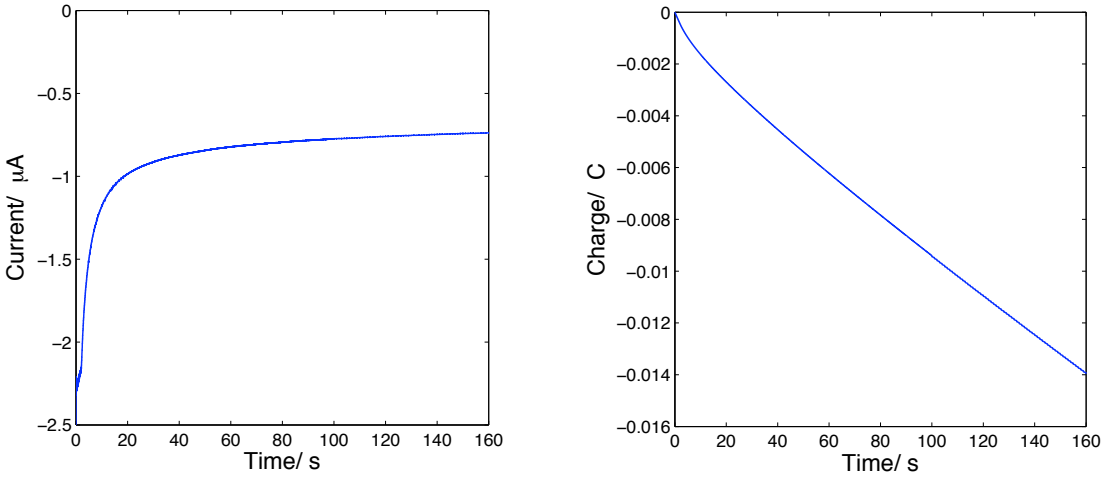


Figure 4.7: Current-time transient traces corresponding to the direct visualisation feedback experiment conducted on an array of 16 nanopores (each with an initial pore diameter of 100 nm) for a time duration t of 160 s and V_{dep}= -300 mV.

the beginning of deposition due to discharging effects at the Au metal surface, the current value remains constant up until ∼30 seconds, from there onwards, a gradual increase in the current value is observed corresponding to an increase in the area of deposited surface on the initial Au surface. The plot of charge-time for this experiment is also provided in Figure 4.7. A delay of 1.5 seconds was used for determining the charge to eliminate any current arising from the initial capacitive discharging of the metal, in this case a total of -0.0139 C was transferred during the deposition with a final Pt film thickness of 93.5 nm.

Direct visual feedback

The deposition process on the Au coated nanopore array was recorded using an emCCD camera. The parameters for the visual feedback were set using the RSImage software where the area investigated was cropped and post processed with an additional 1.6 x magnification. Figure 4.8 shows a sequence of screen shots from the video recording corresponding to the electrochemical deposition experiment results presented in Section 4.4.4.

The bright circular areas here are the nanopores, in this case the array consists of 16 nanopores each with a 100 nm diameter and a spacing of 5 μm. The video shows the Au metal nanopore surface over the deposition duration of 160 s as Pt is deposited. Here the entire image becomes darker over time corresponding to the general nucleation and

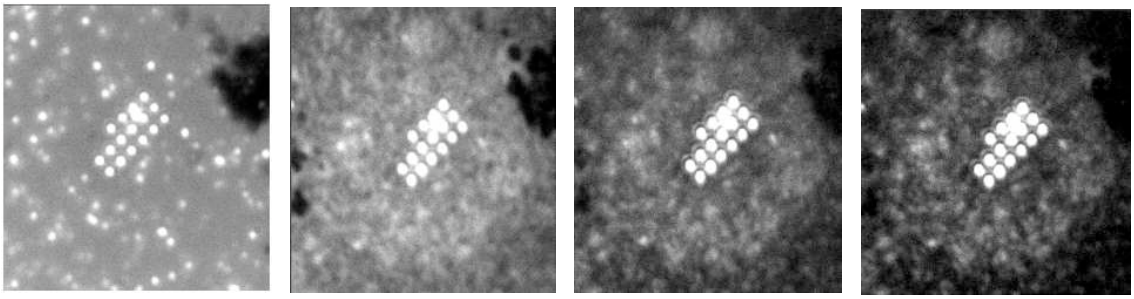


Figure 4.8: Bright field images showing a sequence of four screen shots from the visual feedback recording, corresponding to the electrochemical deposition experiment results presented in Section 4.4.4. *Left to right:* 0 s, 55 s, 130 s and 160 s. The experiment was carried out for a total time duration of t= 160 s.

growth steps of the Pt layer deposits. A marked reduction in light intensity and visibly smaller nanopores had been anticipated for this visual feedback method. However there is no clear observation of pore size shrinkage or reduction in light intensity through the pores over time. The deposition was extended for another 30 s, however this again did not have any effect on the light intensity or pore size.

In order to determine whether the pores shrank post deposition, SEM imaging was carried out on the membrane surface. The chip was dis-assembled from the glass/PDMS cell and cleaned in ethanol and deionised water. Prior to any imaging, the membranes were exposed to an oxygen plasma for two minutes to remove any contaminants. Figure 4.9 shows SEMs of the nanopore array post-deposition. The light grey areas correspond to Pt deposits and the small dark circles are the nanopores. Two of these nanopores have been enlarged for clarity and are shown in Figure 4.9 (bottom panel). It was observed that areas surrounding the pores infact showed little or no deposition.

This could be caused by the restricted depth of the bottom reservoir for focusing, which limited the volume of solution and produced undesirable deposits. To overcome this, the area in the bottom reservoir was increased by incorporating thicker adhesive spacers, however this resulted in low resolution of imaging. The SEM image of this test is presented in Figure 4.10 and clearly shows an even distribution of deposit and a shrunk nanopore, similar to the results obtained in the preliminary experiments.

Furthermore, the visual feedback method for nanopore fabrication had several other drawbacks. The gold contact electrodes were subject to corrosion, so they could only be used for a small number of experiments. Also, electrochemistry on the contact pad

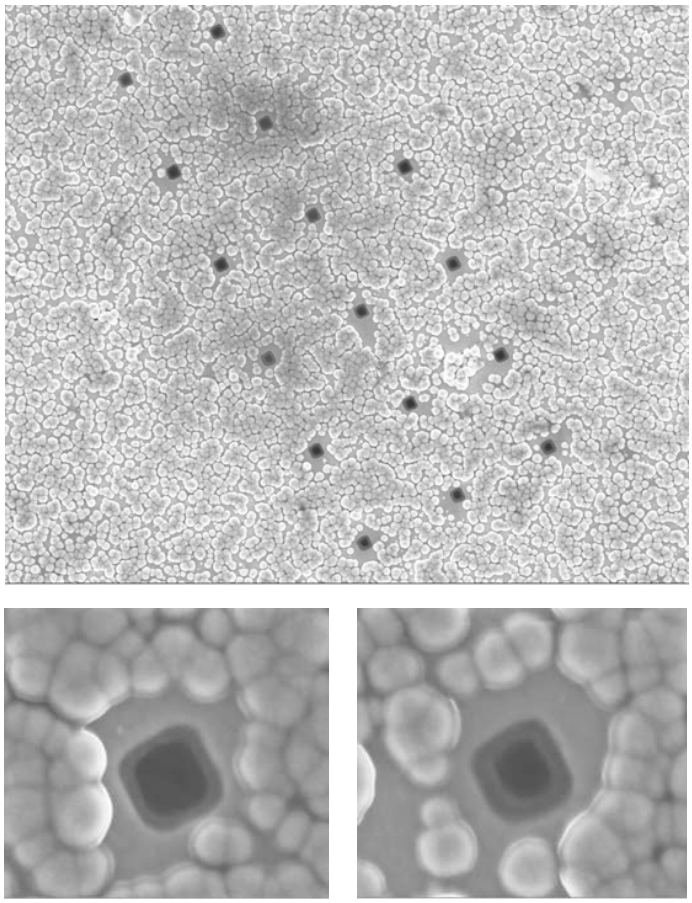


Figure 4.9: *Top*: SEM images of an array containing 16 nanopores post electrodeposition using the visual feedback method. It was evident from the array image that no deposition occurred around the edges of the nanopore. *Bottom*: Two nanopores have been enlarged for clarity showing little or no deposition at the periphery of the pores.

electrodes changed the chemical composition of the solution, leading to a gradual fouling of the solution. The 34.3 ms frame-rate of the video monitor was too slow to visualise the crucial steps of the deposition process. Also, the feedback parameters were ill-controlled, depending on the contrast in the monitor and the ambient light intensity. Subsequently, it was difficult to obtain any systematic real time information from the recording data.

Therefore the second generation of the feedback method was pursued and resolved many of these difficulties.

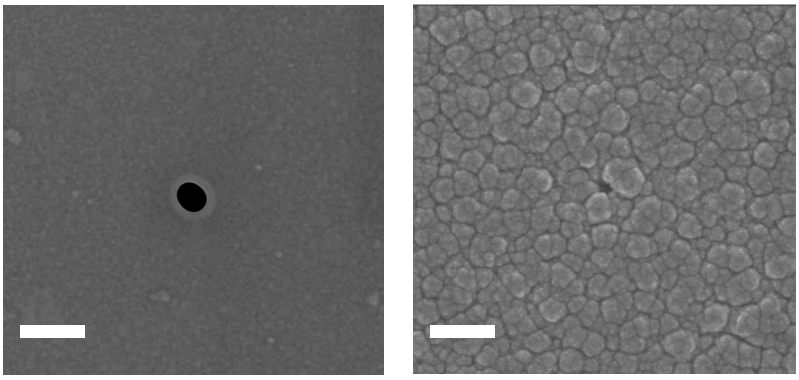


Figure 4.10: *Left*: SEM images of a single nanopore from an array of 16 pores. Initial pore size was 100 nm. *Right*: post deposition this reduced to ∼44 nm. V_{dep}= -300 mV, t= 120 s. Scale bar= 200 nm.

4.5 Ionic current feedback (ICF) method

Subsequent to the trial of the visual feedback method in Section 4.4, a second generation of feedback control is proposed in this chapter, which is based upon the ionic current through the nanopore and is termed the Ionic Current Feedback (ICF) method.

Following ion transport studies across nanopores (which will be presented in Chapter 5), it was envisaged that one could use the ionic conductance through the pore to monitor the shrinking process in aqueous conditions. As shown in Figure 4.11, the Au coated nanopore membrane is between two separate chambers which are filled with deposition solution (10 mM K_2PtCl_4 and 100 mM KCl). With a fixed bias voltage applied across the membrane and the pore being the only conducting channel, the shrinking of the pore radius would result in a decrease in the ionic current through the pore, which could be monitored with pico-ampere-precision.

For this a bipotentiostatic configuration was implemented which allowed for two working electrodes to function independently. Here a reducing potential was applied at the Au nanopore membrane to deposit the Pt from solution and simultaneously a constant potential was applied between two Ag/AgCl electrodes to form a steady state current through the pore. As the pore conductance was derived from the geometry and diameter of the pore, it was possible to calculate the pore size as the nanopore shrank due to the deposition.

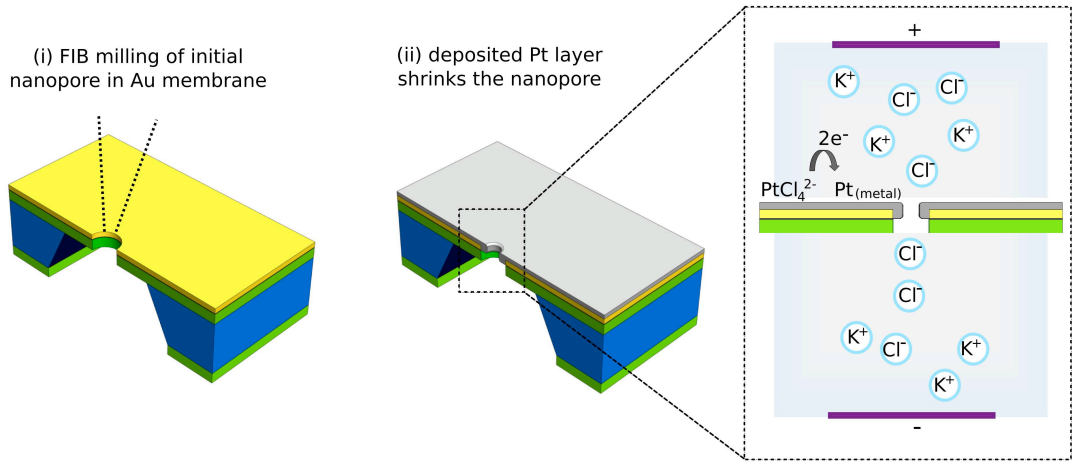


Figure 4.11: Concept of the Ionic Current Feedback (ICF) technique. (i) Starting with initial pores milled in the Au/Si_3N_4 membrane using FIB, (ii) the pore is further shrunk using electrochemical deposition of Pt on the Au surface. The pore shrinking process can be observed in real time by measuring the ionic current through the pore simultaneously in a bipotentiostatic configuration.

4.5.1 Requirements for monitoring the ionic current in real-time

In order to be able to initiate depositions and monitor the ionic current across the nanopore simultaneously, the nanopore chip needed to full several requirements:

Firstly, the chip had to function as a membrane barrier between two solutions such that the nanopore would be the only junction between the two solution compartments; hence the ionic current through the pore could be monitored independently. Secondly, each compartment had to accommodate an electrode so that a bias potential could be applied to drive the ions across the pore. Finally, measurements involving the potentials applied at the nanopore, required an electrical connection to the membrane surface for which specific, easily accessible inlets were crucial.

4.5.2 Assembly of the PTFE flow cell

The sample cell formed from a PDMS mould and a glass slide for the visual feedback measurements (Section 4.4) had the advantage that the PDMS moulds were easy to make in large numbers and could be disposed after use. For certain applications a PDMS/glass-

based flow cell can be sufficient. However, for the tests conducted in this study, an all-PTFE platform was employed. This allowed for all experiments to be done on the same platform reducing the systematic errors in the measurements. The device could be easily assembled/dis-assembled therefore speeding up the process for running experiments.

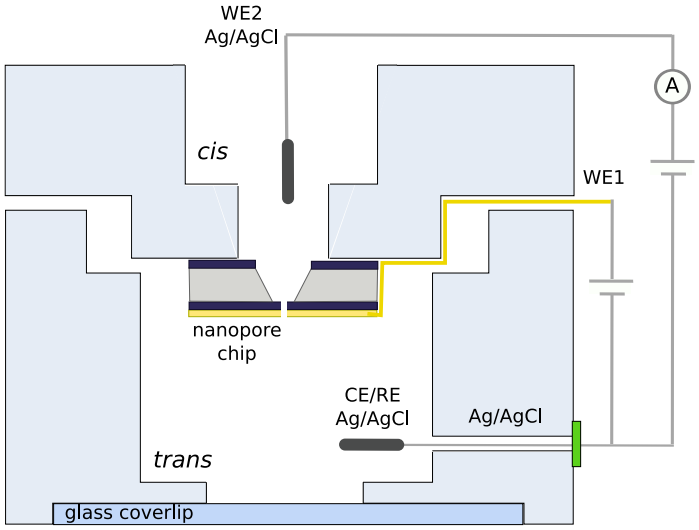


Figure 4.12: Simplified schematic of the PTFE flow cell constructed for the ionic current feedback (ICF) measurements. Thin layers of kwik cast epoxy are used to mount the nanopore chip and the circular glass coverslip to the chambers. The nanopore acts as the only junction between the top and bottom reservoirs. Ionic current through the nanopore is measured using two Ag/AgCl electrodes acting as WE2 and a combined CE/RE, immersed in the two reservoirs as shown. 0.5 mm grooves are milled into the sides of the cis chamber to allow for electrical contact to the Au coated membrane using gold plated adhesive film. The electrodes inlets are sealed with the epoxy and the platform is tested for leaks before measurements.

The design for the PTFE cell was similar to that of the PDMS cell, with minor modications to facilitate the ionic feedback measurements. A schematic of the final flow cell design is presented in Figure 4.12. As with the visual feedback set-up, the PTFE flow cell consisted of two reservoirs (top and bottom). As mentioned in Section 4.4.4, the gold layer of the patterned contact electrodes employed previously, corroded and hence limited the reproducibility of results. To avoid this issue and so completely bypass the need to pattern and wire-bond contact pads to the glass substrate, gold-plated adhesive film (250 μm thickness, 3M Farnell) was used to form the electrical contact to the membrane elec-

trode; this was connected to the edge of each membrane and was directed through the outlet hole milled in the bottom reservoir.

Prior to measurements, the membrane was subjected to an oxygen plasma for 2 minutes and then flushed with ethanol in order to remove any organic contaminants and to enhance the hydrophilicity of the nanopore surface. The nanopore membrane was affixed between the two compartments with Kwik-Cast^{TM} epoxy resin (World Precision Instruments) rendering the nanopore the only electric connection between the top and bottom reservoirs. The epoxy resin was also used to cover and electrically isolate the sides of the silicon chip. The Ag/AgCl electrodes used in this study were prepared as described in Section 2.4.2 and were located 5-10 mm away from the membrane. Under these conditions, the measured ion currents were found to be independent of the relative electrode-membrane distance, confirming that the majority of the potential drop across the flow cell indeed occurred at the nanopore. Finally a grounded Faraday cage was used to shield the flow cell from electrical interference.

4.5.3 Bipotentiostatic set-up

A bi-potentiostatic configuration of two working electrodes was used with independent potentials applied for both the ionic current feedback (ICF) and deposition of metal. Figure 4.13 shows images of the 4-electrode configuration used for the ICF experiments and consists of; a Ag/AgCl electrode that is a combined counter/reference electrode (CE/RE); the Au film on the membrane which is connected as working electrode 1 (WE1) and an additional Ag/AgCl electrode acting as working electrode 2 (WE2) that drives the ionic current through the nanopore. The potential of WE1 is set independently to control the electrodeposition process on the membrane.

The bipotentiostatic electrodeposition experiments were performed using a CH Instruments 760c bipotentiostat (CH Instruments, USA). Here, a constant deposition potential V_{dep} is applied to the Au coated membrane and simultaneously a bias potential V_{bias} across the nanopore using the Ag/AgCl electrodes. Hence, the electrodeposition process on the membrane surface could be initiated (or stopped), while maintaining a constant bias potential between WE1 and CE/RE to monitor the ion current.

As a result of the electrodeposition process, the diameter of the nanopore decreases and its length increases. This leads to a decrease in the pore conductance (Equation 4.5.1) and thus a decrease in the ionic current, Smeets et al. (2006). Once the desired value of

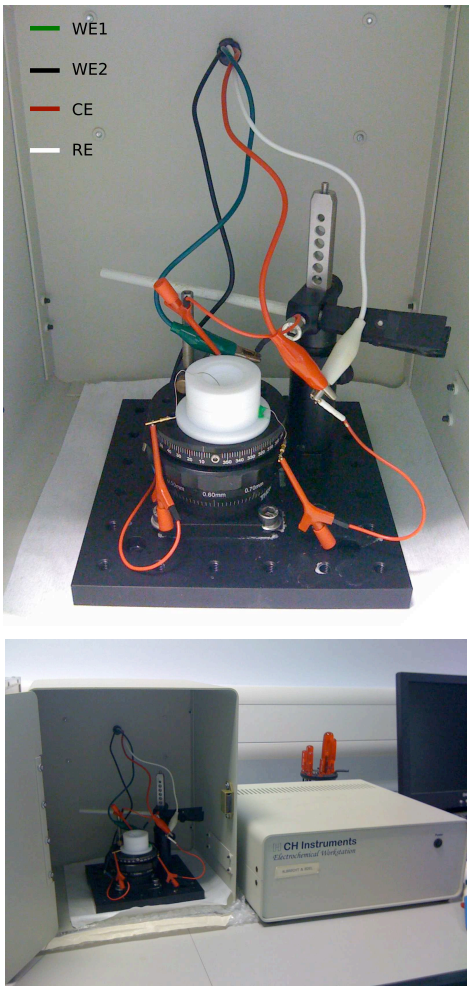


Figure 4.13: Images of the experimental set-up used for the ICF experiments conducted. The WE1, WE2, CE, RE cables leading from the bipotentiostat are fed through the back of the Farady cage and connected to the relevant terminals/electrodes inside. The PTFE flow cell is secured in place using a mastic adhesive on the stage shown.

the ionic current has been reached, the potential of WE1 can be either switched off or increased to a higher potential, where the electrodeposition process no longer takes place, completing the fabrication process. The pore conductance G during the measurement can be calculated from a simple geometrical model:

$$G = \frac{\pi}{4}\frac{d^2}{L}\left(\mu_K + \mu_{Cl}\right) n_{KCl}\, e + \pi \frac{d}{L} \cdot \sigma \cdot \mu_K \tag{4.5.1}$$

d is the pore diameter, K^+ and Cl^- are the electrophoretic mobilities of K^+ and Cl^-, n_{KCl} is the number density of K^+ or Cl^- ions, σ is the surface charge density and e, the elementary charge. The pore length L corresponds to the membrane thickness. Note

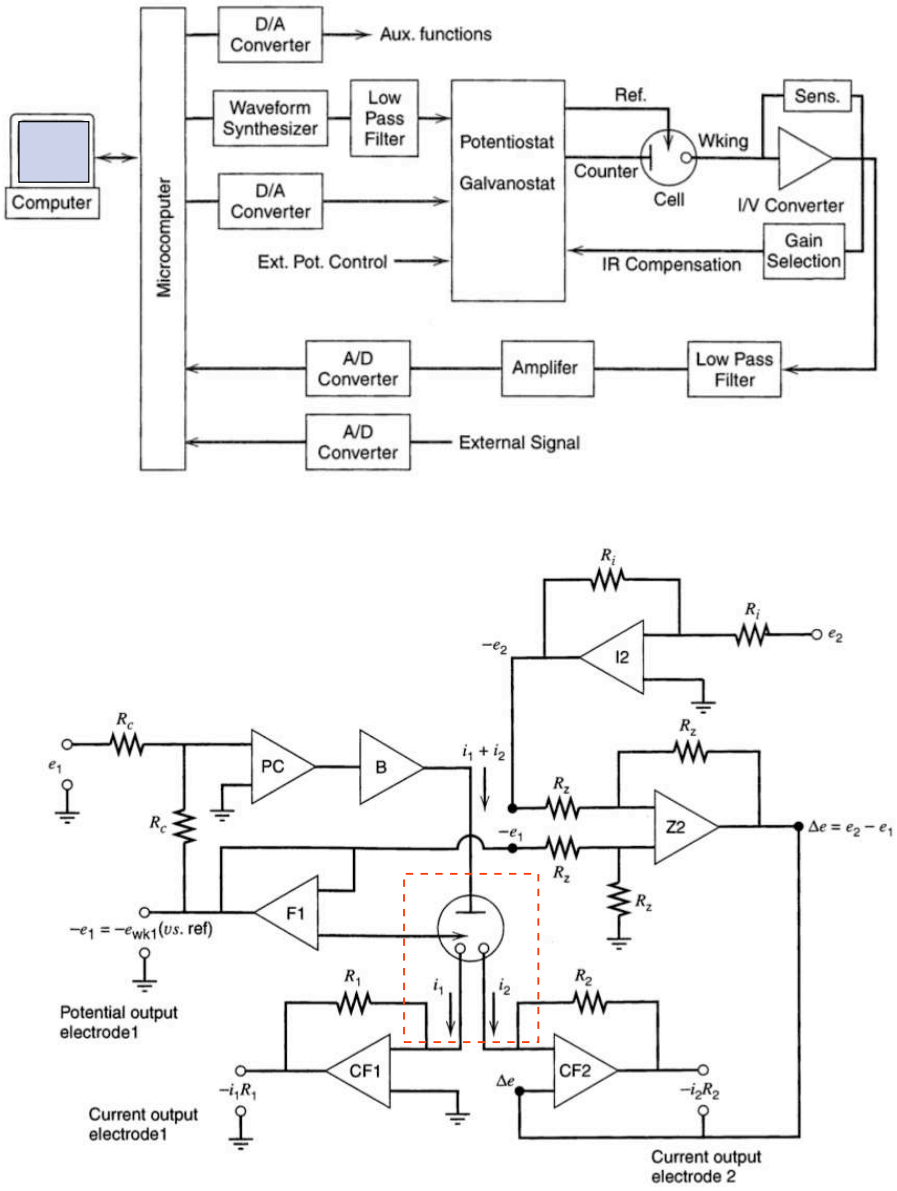


Figure 4.14: *Top:* Schematic diagram of the computer-controlled electrochemical instrument (CH Instruments 760c). Here a waveform synthesiser produces the desired scan signal (e.g., a triangular wave), and the D/A converter generates a dc bias signal. These two signals are then fed to the bipotentiostat. *Bottom:* Bipotentiostat circuit. On the left is the standard potentiostat system, which is devoted to working electrode 1 (WE1). On the right is a network for controlling working electrode 2 (WE2). Adapted from Bard and Faulkner (2000).

that equation 4.5.1 only provides an estimate for the pore conductance and applies to cylindrical nanopores with a net negative surface charge density, high aspect ratios L/d and diameters larger than the Debye screening length, Siwy and Fulinski (2004a).

As mentioned, the experiments required simultaneous control of two working electrode interfaces. The block diagram of the set-up is shown in Figure 4.14 (top panel), Bard and Faulkner (2000). Here a waveform synthesiser produces the desired scan signal (e.g., a triangular wave), and the D/A converter generates a dc bias signal. These two signals are then fed to the bipotentiostat. The overall circuit for the bipotentiostat is shown in Figure 4.14 (bottom panel). The circuitry for a three electrode (WE1; RE; CE) potentiostat is shown in the left part of Figure 4.14. The second electrode (WE2) is controlled by the elements in the right half of the figure.

This circuit employed the first working electrode (WE1) as a reference point for the second working electrode (WE2). Therefore it was possible to set WE1 at any desired potential, e_h with respect to the reference, then WE2 was offset with respect to the first by $\Delta e = e_1$ - e_2, where e_2 was the potential of WE2 with respect to the reference.

The amplifiers (I2 and Z2) served as inverting and zero-shifting stages. They allowed the desired potential e at the input to be set without concern for the value of e_1. This was of particular importance when e_1 and e_2 were varied independently in time.

4.5.4 Results and Discussion: Nanopore array

In this section, the performance of the ICF method is assessed for a range of conditions; initially the method is applied to nanopore arrays (Section 4.5.4) so that its performance can be evaluated across multiple samples in one test. However as nanopore arrays consist of a larger effective ion conductance area, they are not able to assess the sensitivity of the ICF method. Hence, Section 4.5.5 repeats the range of tests conducted for the arrays on single pore membranes.

In order to test the ICF method, the ionic current measured during deposition was compared to that measured using cyclic voltammetry (Section 2.6) both prior and subsequent to deposition. In this case sweeps of ±500 mV were applied across the nanopore and the resulting current-voltage (I-V) characteristics were measured.

However the Pt deposition need not be completed in a single step starting from the initial Au nanopore and ending with the target pore diameter. Instead the deposition process may be stopped and started several times in between, hence achieving a multi-step

deposition. So between each step, I-V measurements were made and compared to those of the ICF. Hence the ICF method was analysed over a wide range of deposition times, using different initial pore sizes. The nanopore arrays were subjected to the ICF deposition approach using the electrode arrangement discussed in Section 4.5.3. The deposition was then performed using both a single-step and a uniform multi-step sequence.

For the single-step deposition sequence, a constant deposition potential of -300 mV was applied to WE1 for 200 s whilst a bias potential of +200 mV was applied between WE2 and CE/RE. I-V measurements were carried out before and after the deposition in 100 mM KCl. A schematic of this approach is illustrated in Figure 4.15 (top panel).

For the uniform multi-step approach, a potential of -300 mV was applied to WE1 for steps of 100 s each. A schematic of this approach is illustrated in Figure 4.15 (bottom panel). During each deposition step a bias potential of +200 mV was applied between WE2 and CRE and the ionic current was monitored through the pores. The I-V measurements were carried out at each deposition interval in 100 mM KCl by sweeping the potential between -500 mV and +500 mV.

Single step deposition

Chronoamperometric measurements

The chronoamperometry technique facilitates the monitoring of the ionic current through the nanopore whilst simultaneously monitoring the resulting current from the applied potential for Pt deposition. Figure 4.16 shows current-time transient scans for the deposition current (blue curve) and ionic current feedback (green curve) observed when Pt was deposited over 200 s using the four electrode configuration. The ionic feedback current show an initial sharp increase which is produced by capacitive charging effects at the electrodes, the current then gradually decreases over the duration of the deposition as a result of the pore shrinking. The ionic feedback current decreases as the Pt deposition current begins to increase (at approximately 80 s) and continues to do so over the deposition duration, this corresponds to the Pt deposition as discussed in Section 3.4.1 for a flat gold surface. A total of -0.0437 C was transferred over the course of the deposition process with a final Pt film thickness of 112.5 nm.

I-V measurements

I-V measurements of the nanopore were conducted before and after the deposition

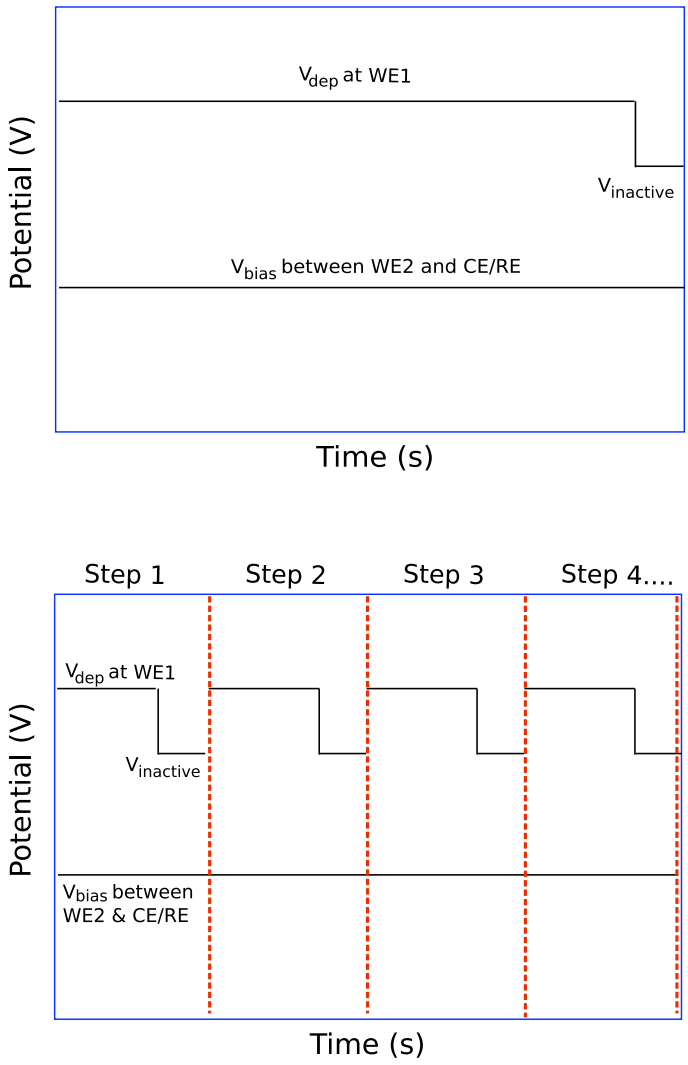


Figure 4.15: Schematic representation of potentials applied to the ICF system using a bipotentiostat. *Top:* 1^{st} approach- for depositing Pt and measuring the ionic current feedback, where a constant potential V_{dep} was applied to WE1 for 200 s at -300 mV (including 2 s at a lower negative potential where no faradaic processes occur). Simultaneously a bias potential V_{bias} was applied between WE2 and CRE (Ag/AgCl electrodes), respectively. *Bottom:* 2^{nd} approach- showing the multi-step depositions, each lasting for 100 s, between which I-V measurements were carried out (represented by *red dotted line*) in 100 mM KCl to derive the pore conductances, notations: WE1 (nanoporous membrane); WE2 (Ag/AgCl electrode); CE/RE (Ag/AgCl electrode).

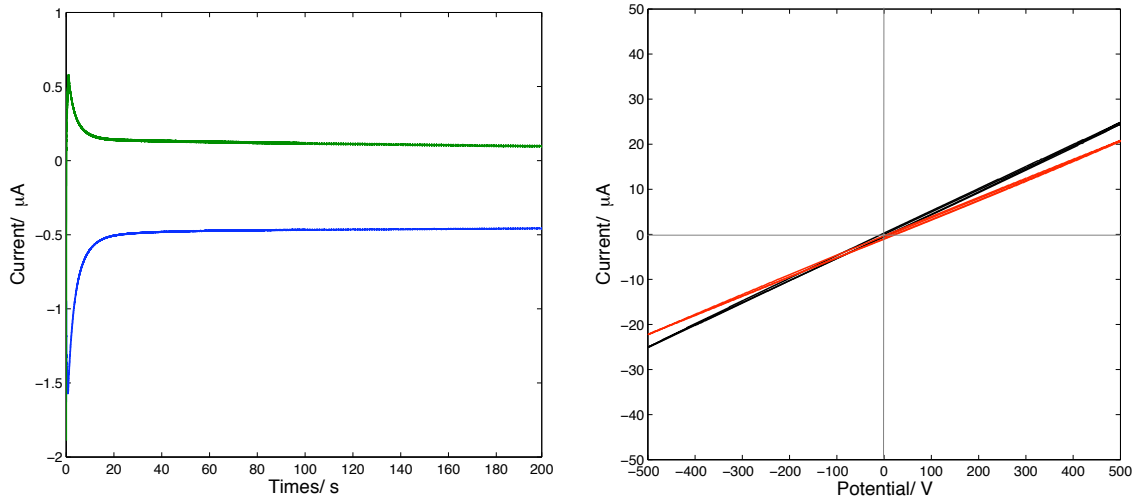


Figure 4.16: *Left:* Current-time transient curves measured for the deposition of Pt at V_{dep} of -300 mV; t= 200 s current response for the deposition (*blue curve*) and ionic current feedback (*green curve*). As the Pt is deposited, the ionic current gradually decreased over time until reaching a lower limit of ∼6.32 μA. *Right:* I-V traces for an array of 16 nanopores, acquired via cyclic voltammetry in 100 mM KCl; before (*black curve*) and after (*red curve*) Pt deposition.

process by applying sweep potentials between ±500 mV across the nanopore array in 100 mM KCl. The I-V measurements for this are shown in Figure 4.16; the gradients of which are the pore conductance, G.

Before the start of the experiment, the conductance per pore gave a value of ∼2.81 μS, where the average initial pore diameter was 150 nm. After depositing the Pt on the Au nanoporous membrane, we observed that the current passing through the pore dropped and a final pore conductance of ∼2.13 μS was obtained. These values were compared to the conductance calculated from the chronoamperometry measurements in Section 4.5.4; by using the applied bias potential of +200 mV and its resulting current (green curve), the conductance (G=I/V) was found to be ∼1.97 μS at 200 s.

The pores were characterised using SEM. Figure 4.17 shows a typical SEM image of a nanopore milled in the thin Au/Si_3N_4 membrane (Au/Ti 100 nm; Si_3N_4 240 nm), with a diameter of 150 nm ± 5 nm. The SEM image of the nanopore following electrochemical deposition of Pt (200 s). Figure 4.17 (right panel) reveals a highly symmetrical final pore, with a diameter of 93 nm ±10 nm; the Pt deposits around the pore in a circular manner without distorting the shape of the pore. The electrodeposited Pt was comparable to

results achieved in the characterisation of Pt films in Chapter 3 and exhibited similar structures with spherical formed particles of platinum between 30-40 nm in size.

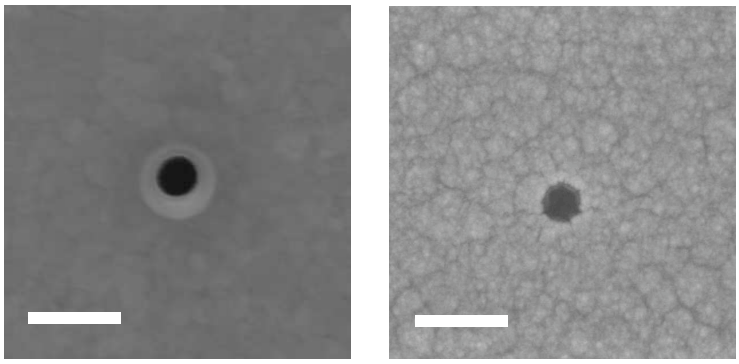


Figure 4.17: Scanning electron micrographs of a single nanopore from an array of 16 pores. *Left:* before and *Right:* after Pt deposition. V_{dep} = -300 mV, t= 200 s. Final pore diameter was 93 nm. Scale bar= 200 nm.

Multiple step depositions

Chronoamperometric measurements

As mentioned previously, the multi-step deposition process consisted of four deposition steps each lasting for 100 s. Figure 4.18 shows the deposition current obtained over the course of 400 s. The main characteristics observed for each step of the multi-step deposition procedure correspond to those of the single-step results. Hence, Figure 4.18 (left panel), which presents the deposition current for each step shows a gradual increase in the current as the Pt layer grows on the surface of the membrane. The deposited charge and thickness values calculated for each step using Equation 3.4.1 are provided in Table 4.2.

Correspondingly, the ionic current plotted in Figure 4.18 (right panel) is seen to gradually decrease over the duration of each deposition step. Starting from an ionic current value of ∼22.45 μA for the first step (green curve) as the deposition steps are performed, a gradual decrease in ionic current is observed, reaching a lower limit of 2.76 μA (blue curve- fourth step).

I-V measurements

I-V measurements for the multi-step approach were taken between each deposition step by sweeping the nanoporous membrane between ±500 mV in 100 mM KCl. The conductance calculated from these sweeps were compared to the conductance values obtained

Step	Conductance/ μS	Deposited charge/ C	Pt thickness/ nm
1	112.25	6.131 x10^{-5}	28 nm
2	93.11	5.720 x10^{-5}	27 nm
3	39.45	3.834 x10^{-5}	18 nm
4	13.80	2.901 x10^{-5}	13 nm

Table 4.2: Summary of results obtained for the multi-step deposition studies (Section 4.5.4) carried out at an array of 16 nanopores with initial diameters of 100 nm.

from current-time transient curves during measurements – as done for the single-step case in Section 4.5.4. A typical I-V measurement for all four steps in this experiment is shown in Figure 4.19 and the conductance values of each step calculated from the ICF and I-V measurements are plotted in Figure 4.19 (right panel).

It can be seen from comparisons of the I-V and ICF measurements, that there is a variance in pore conductances obtained during measurements. Although the ICF curves are quantitatively larger, qualitatively the results of both measurements show a decrease in pore conductance with each subsequent deposition step. The quantitative discrepancy between the two series' may be a result of the different solutions used during the measurements, however further work is necessary to verify this.

4.5.5 Results and Discussion: Individual nanopore

Having conducted a study on the performance of the ICF method on nanopore arrays, in this section its performance is assessed with single nanopore membranes. As the effective conductance area for an individual nanopore is much smaller than that of an array, this section presents studies that examine the sensitivity of the ICF method. Furthermore, as only one nanopore is tested at a time, the initial size of the nanopore (determined during the milling process discussed in Chapter 2) can be varied. Hence the sensitivity of the ICF method can be studied for a range of initial nanopore sizes. As with the tests conducted for nanopore arrays, here, two main categories of experiments were performed; single step and multiple-step.

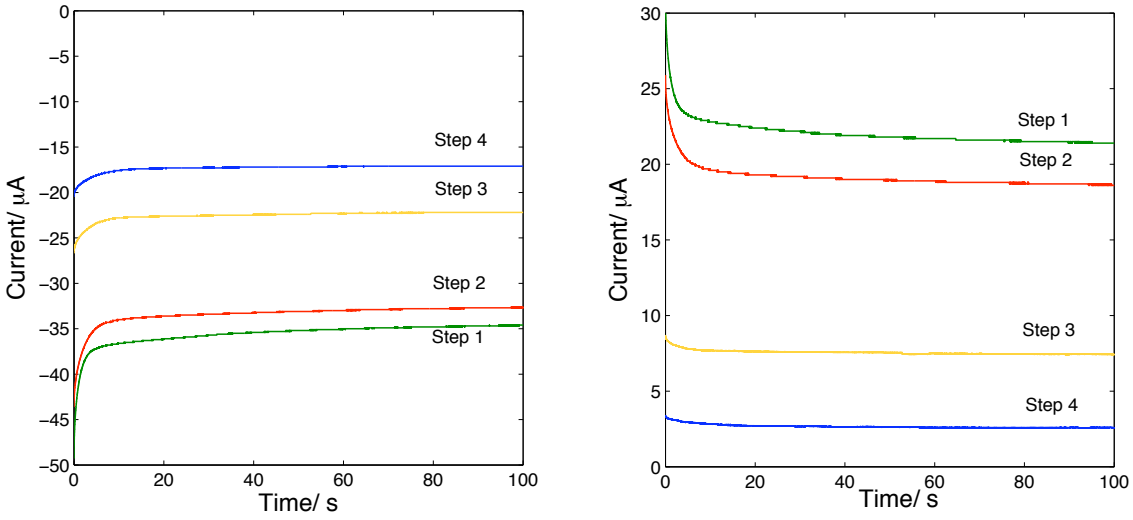


Figure 4.18: *Left:* Current-time transient curves measured for the deposition of Pt at V_{dep} of -300 mV. The multi-step approach consisted of 4 steps, each lasting for t= 100 s (total= 400 s). *Right:* Corresponding ionic current feedback curves measured simultaneously as the Pt deposition took place across the Au/ Si_3N_4 membrane. V_{bias}= +200 mV.

Single step deposition

The tests conducted for a single-step deposition process on individual nanopores largely followed the study conducted for nanopore arrays in Section 4.5.4. However, here a wide range of parameters were varied in order to conduct a thorough characterisation of the ICF method on single-step deposition processes. Hence, tests were performed for a varying deposition duration; 40 s, 80 s, 120 s and 160 s. The deposition potential was also varied between -250 mV to -400 mV.

The results of a typical single step deposition experiment are presented in Figure 4.20, where the ionic current is plotted in blue and the deposition potential in black. The V_{dep} applied in this case was -300 mV and a V_{bias} of +200 mV. The plot shows the typical features discussed previously; the ionic current presents an initial peak due to capacitive effects which then decreases as the pore shrinks. The deposition current exhibits a gradual increase as a result of the increase in conductive surface area. SEM images of the nanopore were taken before and after the deposition process and are presented in Figure 4.21 inset. The figure shows the pore to have shrunk from ∼100 nm to ∼16 nm. I-V tests were conducted before and after the deposition process also, these are plotted in the figure in

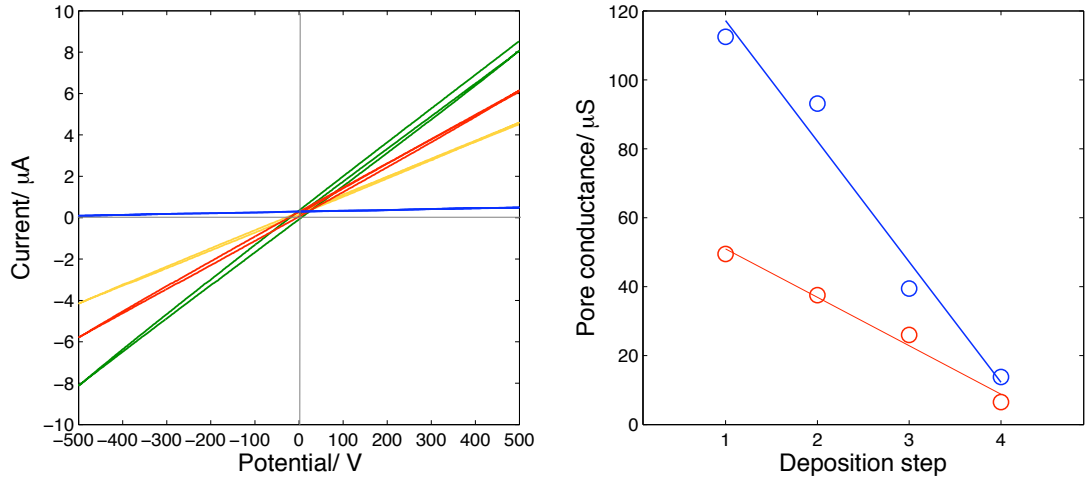


Figure 4.19: *Left:* I-V traces for an array of 16 nanopores with an intial average d= 150 nm acquired via cyclic voltammetry in 100 mM between each deposition step. *Right:* Plot of pore conductance versus the deposition step. Conductance values obtained from the slope of I-V measurements (*red circles*) and ICF curves (*blue circles*) at t=100 s, respectively.

black and red, respectively. As is evident from the figure, the gradients of the curves (and hence pore conductance) decreases after deposition, indicating a reduction in pore size. I-V tests and SEM before and after deposition have been performed for all the tests discussed in this section.

The second series of tests presented here consist of four individual nanopore membranes with an initial pore diameter of 100 nm ±5 nm. All four membranes were subjected to the ICF approach with a constant deposition potential of -300 mV in a deposition solution of 10 mM K_2PtCl_4 and 100 mM KCl. However the duration of the deposition process applied to each pore was varied. Figure 4.23 present the SEM images of the four membranes for deposition times of 40 s, 80 s, 120 s and 160 s, respectively. The final pore size achieved in these experiments range from $\sim$ 95 nm for 40 s to 27 nm for 160 s. As is evident from the 40 s SEM image, the deposited Pt is sparse and progressivley increases in density with the longer duration tests. As a result it is clear that by controlling the deposition duration, a given pore size can be achieved.

In correspondence to the SEM images for each run, the normalised ionic current time graphs for samples 40 s to 160 s are plotted in Figures 4.22. Due to discrepencies in the initial pore diameter, the starting ionic current varied for each membrane and hence the

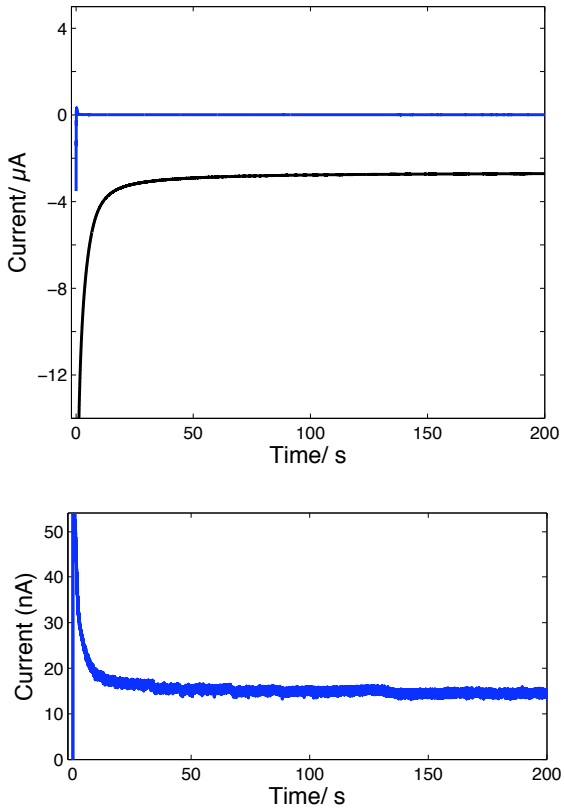


Figure 4.20: *Top:* Current-time transient curves measured for the deposition of Pt at V_{dep} of -300 mV; t= 200 s current response for the deposition (*black curve*) and ionic current feedback (*blue curve*). As the Pt is deposited, the ionic current gradually decreased over time until reaching a lower limit of ∼15.64 nA. *Bottom:* enlarged view of the ionic current during measurement to clearly see the drop in current as the pore shrinks.

plots have been normalised to cancel this effect. As is evident in all of these figures the ionic current decreases with time, this has been explained in the previous section to be a result of pore shrinkage, which reduces the ionic current. Also evident is that the final normalised current value decreases with increasing deposition durations. Hence at 40 s the final normalised current is 0.74 ±0.14, 0.73 ±0.10 for 80 s, 0.48 ±0.06 for 120 s and 0.33 ±0.12 for 160 s. Correspondingly for 40, 80, 120 and 160 s the conductance was found to be 3.95, 3.51, 3.06 and 2.53×10^{-7}S, respectively, Table 4.3. As expected, with increasing deposition duration the conductance decreases. Therefore, by observing the conductance of the nanopore during the deposition process, the pore size can be approximated in real-

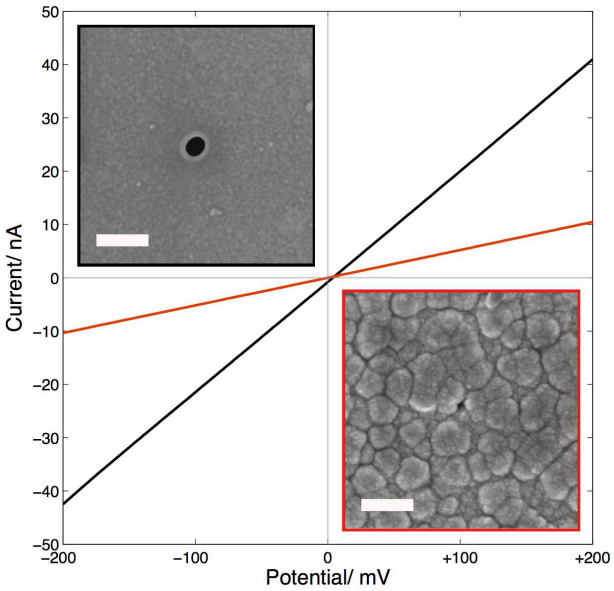


Figure 4.21: Typical I-V traces obtained corresponding to the single step measurements carried out at an individual nanopore. Acquired via cyclic voltammetry in 100 mM KCl; before (*black curve*) and after (*red curve*) Pt deposition. *inset*: Corresponding SEM images for the initial Au/Si_3N_4 pore (d=100 nm) and post-deposition Pt nanopore, d= ∼16 nm, determined by SEM scale feature. Scale bar= 200 nm.

time.

As an example, a series of conductance values have been plotted in Figure 4.24 against their corresponding pore diameters. The pore diameters were measured through SEM and the conductance was obtained through I-V measurements after the deposition process. The figure presented here represents a complete array of tests conducted for a V_{dep} of -300 mV and a V_{bias} of +200 mV. Based upon the current-time readings during the deposition process, the deposition can be terminated at the required ionic current value and hence pore diameter (the relation between which can be approximated from the figure).

Tests were also conducted for three different deposition potentials; -250 mV, -300 mV and -400 mV with a deposition duration 60 s each. The results of this series of tests are tabulated in Table 4.4, where the pore diameter and conductance values are presented for before and after the deposition process. The charge and film thickness of the deposited Pt is also provided. The results show that as the deposition potential increases to a higher negative value, the final pore diameter and hence the conductance decreases accordingly. The thickness of the deposited Pt also increases with the increasing deposition overpotential.

Time s	Current/ μA	G/ μS	Final pore diameter/ nm
40	0.74 ±0.14	3.95	95 nm
80	0.73±0.10	3.51	82 nm
120	0.48 ±0.06	3.06	58 nm
160	0.33 ±0.12	2.53	28 nm

Table 4.3: Summary of results obtained for the time variation studies carried out at an array of 16 nanopores with initial diameters of 100 nm.

V_{dep}/ mV	Pore diameter/ nm		Conductance/ nS		Pt deposition	
	initial	final	initial	final	Charge/ C	Thickness/ nm
-250	100	74	273.4	185.5	1.002 x10^{-6}	67 nm
-300	102	67	291.2	162.2	1.211 x10^{-6}	81 nm
-400	100	61	267.2	136.5	1.455 x10^{-6}	97 nm

Table 4.4: Summary of results obtained for varying V_{dep} at WE1 with a deposition duration t= 60 s; V_{bias}= +200 mV for all measurements.

Multiple step depositions

As with the experiments conducted for the nanopore arrays in Section 4.5.4, here multiple step experiments have been conducted on single nanopore membranes. The studies discussed here largely follow those of Section 4.5.4 in terms of deposition potentials, ICF biased potentials and deposition solution concentration. Furthermore, as with the previous multi-step study, I-V measurements were conducted between each deposition step in order to compare the conductance measured by the ICF approach to that of I-V measurements. The multi-step deposition experiment presented here was carried out with a deposition potential of -350 mV and with the same deposition solution described above on a nanopore with an initial diameter of 100 nm.

The total deposition duration was of 240 s and has been divided into 12 uniform steps of 20 s each; all of which were performed with the same V_{dep}. The current-time traces

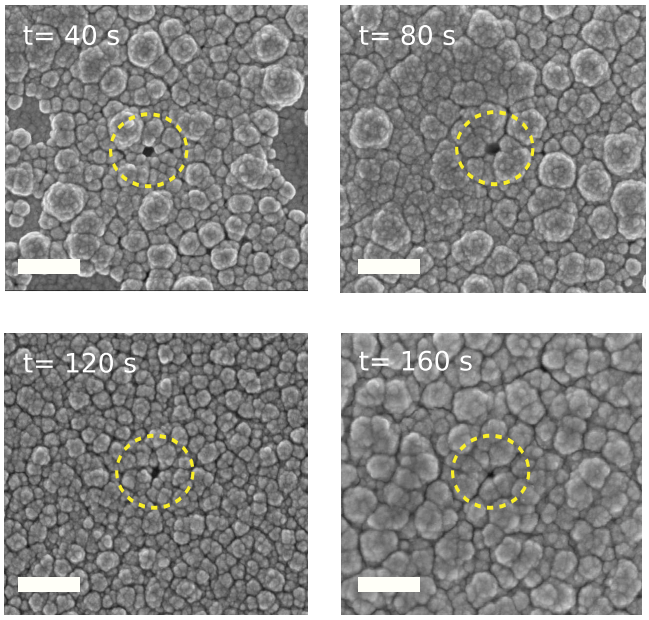


Figure 4.22: Scanning electron micrographs post-deposition for the different time durations investigated at a single nanopore using the ICF technique. For t= 40 s, d= 95 nm; for t= 80 s, d= 82 nm; for t= 120 s, d= 58 nm; for 160 s, d= 28 nm. V_{dep} in all cases set to -300 mV; V_{bias}= +200 mV. Scale bar= 1 μm for top panel 200 nm for bottom panel.

for each step are presented in Figure 4.25 and show that the ion current decreases during each deposition run (whilst electrodeposition is taking place). Importantly, the current of each step begins at approximately the same final current level in the preceding step. This confirms that the deposition process is stopped, when the potential at WE1 is switched back to high potentials. The ion current-time plots of steps 1 and 12 are enlarged for clarity and are presented in Figure 4.26. Due to the larger pore size in the first step, the ionic current through the pore dominates the overall current in the system and hence the current is seen to decrease with the absence of any capacitive effects described previously. However for the final step, the pore diameter is sufficiently small to permit the capacitive charging effects to dominate the overall current response; hence the current initially increases in the first two seconds prior to decreasing in the remainder of the deposition period.

The pore conductance of each step has been calculated using the corresponding final current values and the applied voltage, these are plotted in Figure 4.27 against the amount of Pt deposited. As is expected, the conductance decreases with increasing deposited mass. More importantly, the decay agrees very well with the exponential line of best fit (dashed

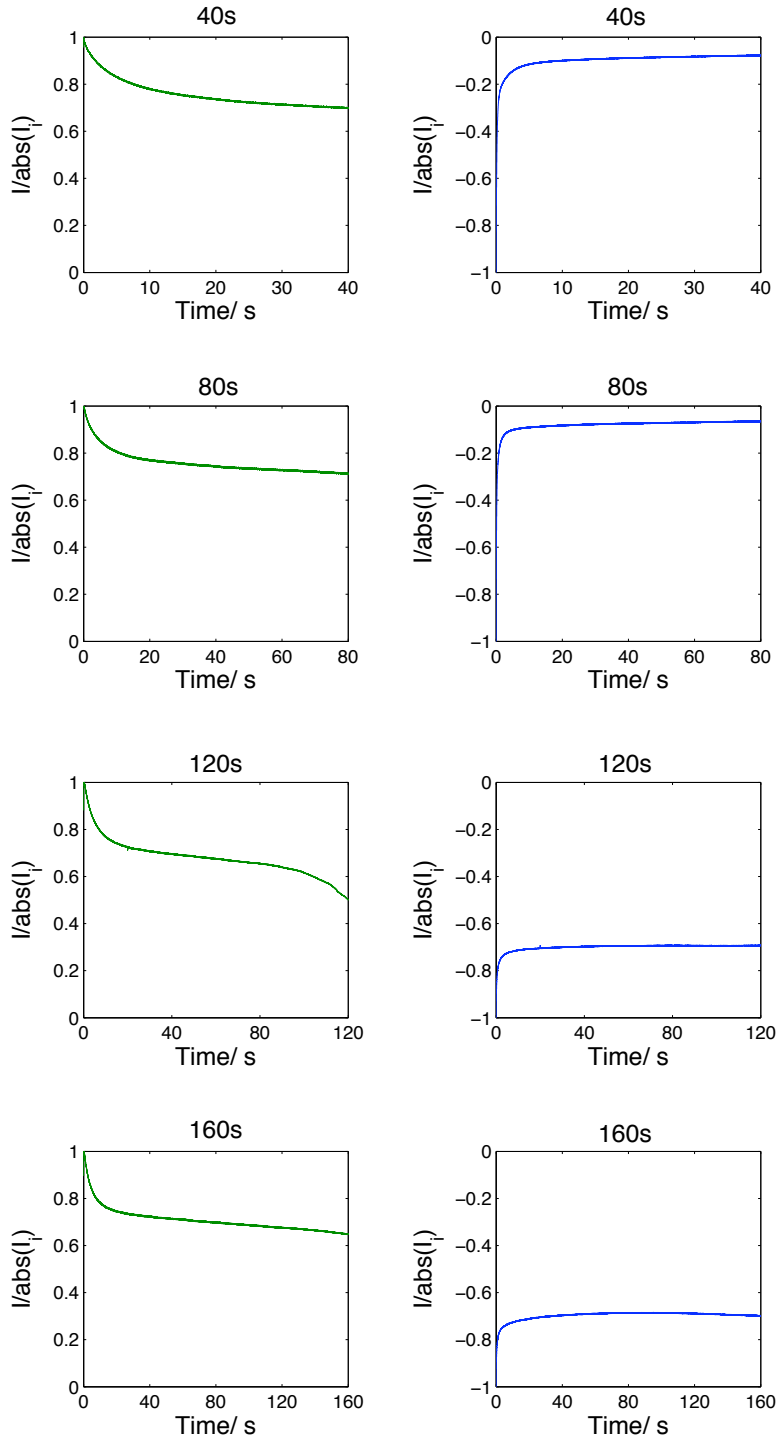


Figure 4.23: *Top to bottom:* Normalised current-time transients resulting from deposition duration experiments (t= 40 s; 80 s; 120; and 160 s) at individual Au coated nanopores using the ICF technique. Both the ionic currents (*green curves*) and the deposition current (*blue curves*) show similar trend as discussed in previous sections. V_{dep} in all cases set to -300 mV; V_{bias}= +200 mV.

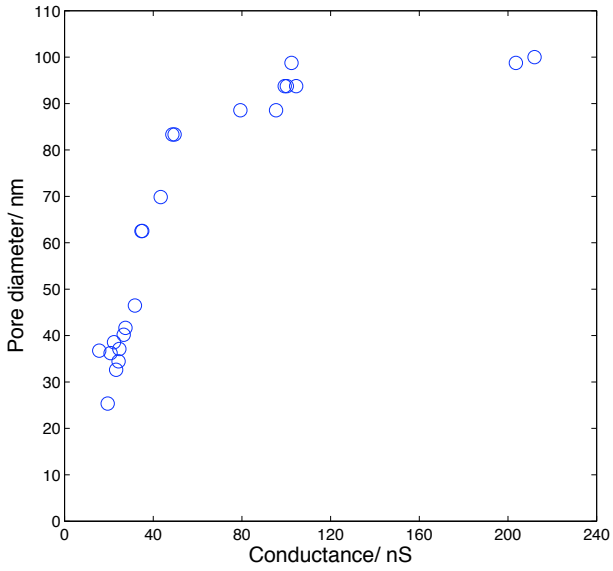


Figure 4.24: Conductance values of 23 individual Pt deposited nanopores as a function of nanopore diameter. Data obtained through I-V measurements in 100 mM KCl, after the deposition process. V_{dep} in all ICF-deposition measurements was set to -300 mV; V_{bias}= +200 mV.

red line) with an effective decay coefficient $1/t_1$ of 3.610^9 mol^{-1} (y= A_1 exp(-x/t_1) + y_0; A_1= 2.53 x10^{-7} S; y_0 = 8.27 x10^{-9} S; t_1 = 2.74 x10^{-10} mol; R^2 = 0.992). However, this is only a phenomenological approach and requires further studies to ascertain a more general relation between pore conductance and the amount of platinum deposited. It should also be noted that for each step, as the deposition potential and all other parameters were kept constant, the amount of platinum deposited should be the same. Hence Figure 4.27 inset plots the deposited platinum for each deposition run and shows the amount of Pt to increase linearly with every step; at a rate of approximately 100 pmol/step.

Figure 4.28 presents the results of the cyclic voltammetry test performed on the nanopore at the end of the final deposition step. SEM images of the nanopore before and after the complete deposition process are also provided in the inset. The final pore diameter was measured to be 18 ±5 nm and the gradient of the I-V plot yields a pore conductance of 27 nS. This compares very well to the 24 nS calculated from the ICF measurements plotted in Figure 4.25. The response is close to ideal with almost no hysteresis and a rectification ratio close to 1. However, based upon the dimensions of the pore observed using the SEM (with values L = 310 nm, d = 18 nm; μ_K= 7.61610^{-8} m^2

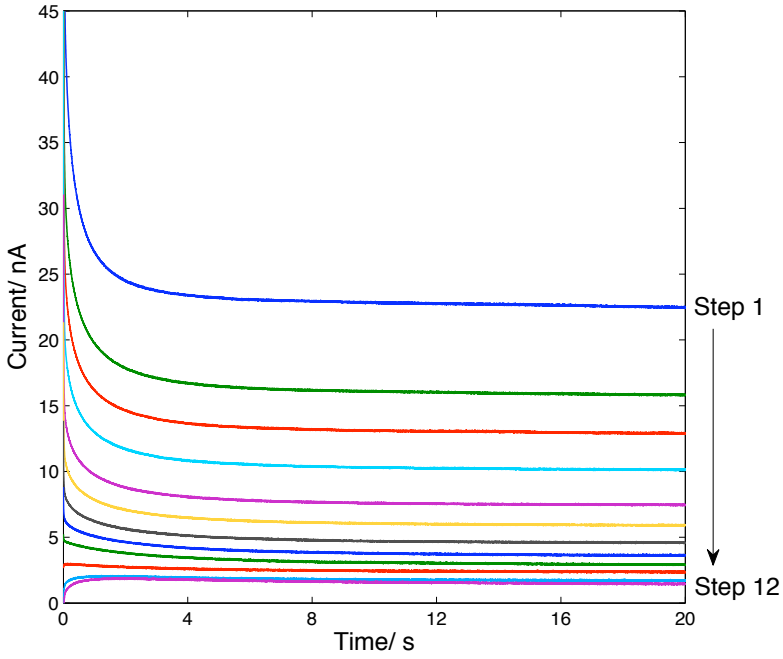


Figure 4.25: Current-time transients of 12 subsequent electrodeposition steps of 20 s duration each, from top to bottom. V_{dep}= -350 mV; V_{bias}= +200 mV in 10 mM K_2PtCl_4) and 100 mM KCl, Ayub et al. (2010).

V^{-1} s^{-1}; μ_{Cl}= 7.90910^{-8} m^2 V^{-1} s^{-1} , Smeets et al., 2006), whilst ignoring the surface charge, Equation 4.5.1 gives a pore conductance of 1.3 nS. This differs greatly from that observed with the ICF and I-V measurements. However certain reservations are appropriate regarding this result; firstly Equation 4.5.1 is only valid for relatively large, cylindrical pores of high aspect ratio L/d. Secondly tolerances in the manufacturing of the membrane may have produced a smaller channel length than 310 nm, further contributing to an under-prediction in conductance. Finally, as the surface charge of the post-deposition membrane is not known, it was not possible at this stage, to calculate its effects using the second term of Equation 4.5.1. Hence the absence of its influence on the modelled conductance also presents a significant source of discrepancy. Also, the SEM imaging experiments provide an estimate of the cross-sectional area of the pore; they do not reveal its three-dimensional structure (including roughness inside the pore). This in turn may affect its charge transport properties. Nevertheless, these findings do not affect the conceptual value of the approach presented here.

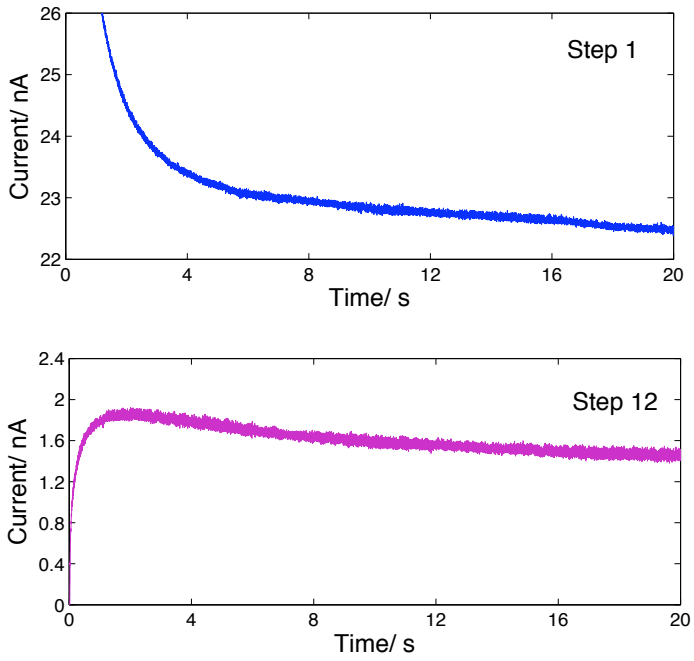


Figure 4.26: Enlarged plot of ICF current-time trace showing steps 1 and 12 from Figure 4.25, respectively, Ayub et al. (2010).

4.5.6 Assessing the reproducibility of the ICF technique

Thus far a series of nanopore sizes and deposition processes were considered in order to evaluate the performance of the ICF method. Here, in order to assess the consistency with which such results can be achieved, all experiments have been repeated, two such sets of repetitions are presented here; one single step and one multi-step.

For the single step experiments, three membranes were subjected to a 40 s deposition period at a V_{dep} of -300 mV. The deposition solution used is as stated previously and the initial pore size for all three membranes was measured at 100 nm using SEM imaging. The V_{bias} was set to +200 mV. The corresponding current-time traces for both the deposition and the ICF measurements are presented in Figure 4.29a and show an identical current-time trace for both measurements of each run. The corresponding conductance values for these runs are presented in Table 4.5 along with the final pore diameters, the relevant charge and thickness values of the deposited Pt.

The SEM images subsequent to deposition are presented in Figure 4.29b and correspond to samples 1 to 3 of the tabulated values. The final pore diameters measured from the SEM images give an average value of 89.3 nm with a maximum deviation of 1.3 nm.

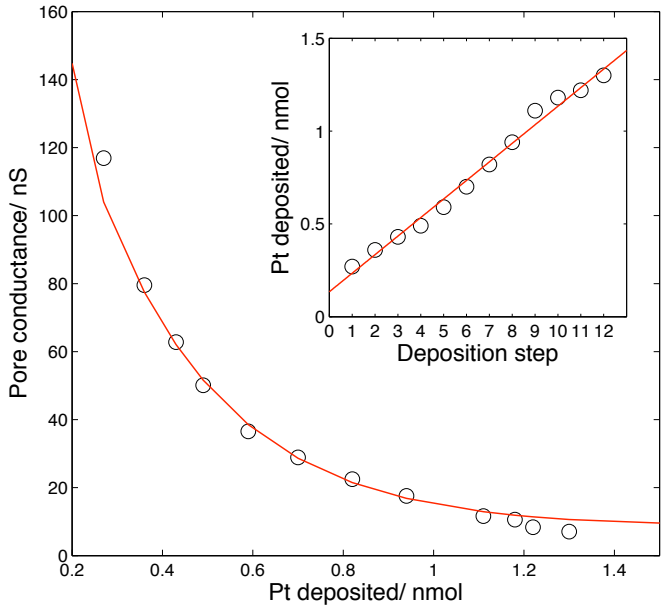


Figure 4.27: Pore conductance G as determined from ICF at t= 20 s versus the amount of Pt deposited. G decreases exponentially with a characteristic decay coefficient of 2.7x10^{-10} mol^{-1} (*red line*). *inset*: total amount of Pt deposited in steps 1-12. On average, 100 pmol of Pt were deposited during each step (linear fit, *red line*), slope: 9.95 x10^{-11} mol, intercept: 1.27 x10^{-10} mol), Ayub et al. (2010).

For the multi-step experiments, three different data sets were compared corresponding to three different nanopore chip devices. These are presented in Figure 4.31. Devices Pt-1 and Pt-2 had an initial pore diameter of 100 nm (black and red circles), the former being the device discussed in Section 4.5.5. Device Pt-3 had an initial pore diameter of 45 nm (blue circles); all initial diameters were determined by SEM imaging. Each data point in the graph represents the conductance values of the corresponding membrane at an interval between each deposition step; hence for Pt-1, 12 steps were performed, 8 steps for Pt-2 and 5 steps for Pt-3. For better comparison, the amount of Pt deposited was normalised by the (geometric) membrane electrode area; 0.07 cm^2 for devices Pt-1 and Pt-2, and 0.65 cm^2 for device Pt-3).

In all cases, ln(G) reduced with an increasing amount of Pt deposition, as shown by fits in Figure 4.31a. The gradients of devices Pt-1 and Pt-2 are very similarly (slope m= -1.72 cm^2 nmol^{-1} (R^2= 0.99) and -1.79 cm^2 nmol^{-1} (R^2 = 0.94), which was expected due their comparable initial dimensions and deposition conditions (V$_{dep}$= +350 mV). This

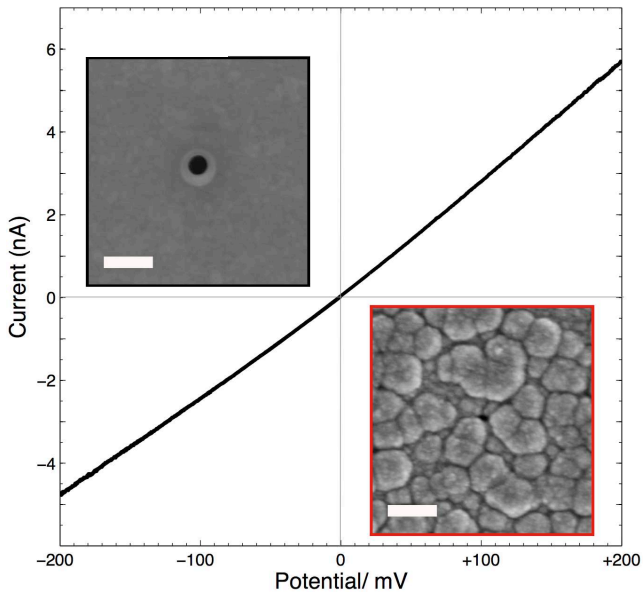
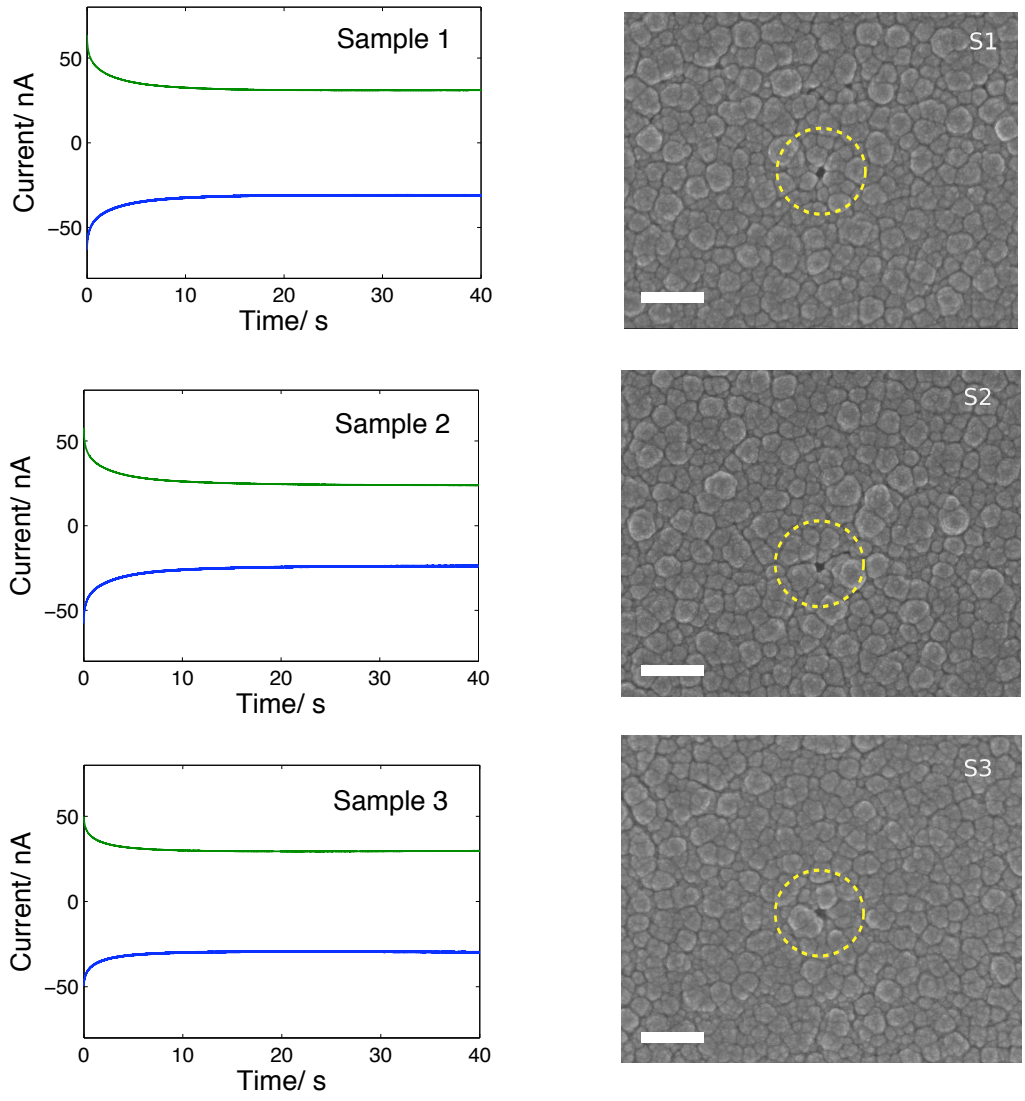


Figure 4.28: I-V traces obtained corresponding to the multi-step measurements carried out at an individual nanopore. Acquired via cyclic voltammetry in 100 mM KCl after Pt deposition. The rectification ratio is close to 1 in the voltage range shown. *inset*: Corresponding SEM images for the initial Au/Si_3N_4 pore (d=100 nm) and post-deposition Pt nanopore, d= ∼18 nm, determined by SEM scale feature. Scale bar= 200 nm, Ayub et al. (2010).

emphasises the good reproducibility of the presented technique. However, in the case of Pt-3, the pore conductance decreased at a lower rate with each deposition step. This is despite the lower deposition potential (note that the deposition potential is negative hence this represents a higher driving force) in this experiment; V_{dep}= -250 mV.

This lower rate of reduction in conductance is confirmed by comparisons of the amount of Pt deposited across the samples at each step; presented in Figure 4.31. Here, the gradients of Pt-1 and Pt-2 also show a strong agreement with deposition rates of 0.071 and 0.053 nmol cm^{-2} s^{-1}, respectively. In comparison, the deposition rate of the Pt-3 sample is calculated to be 0.107 nmol cm^{-2} s^{-1}. This suggests that although more Pt is deposited over the whole membrane electrode for Pt-3, deposition around or inside the pore is less prominent, compared to Pt-1 and Pt-2.

In order to verify the claim that the deposition of Pt is not evenly distributed across the membrane, consider the deposition performed on Pt-1; roughly 100 ±5 pmol of Pt were deposited during each deposition step. For a uniform distribution of deposit, the electrode



(a) (b)

Figure 4.29: *Left:* Current-time transients corresponding to the single-step approach carried out across 3 individual membranes with initial pore diameter of 100 nm. V_{dep}= -300 mV; V_{bias}= +200 mV; t= 40 s. Both the ionic currents (*green curves*) and the deposition current (*blue curves*) show identical trends. *Right:* The respective SEM images post-deposition for all 3 samples are displayed. These exhibit a smooth Pt surface across the membrane with an average pore diameter of 89.3 nm (maximum deviation= 1.3 nm).

Sample	Conductance/ μS	Pore diameter/ nm	Deposited charge/ C	Pt thickness/ nm
1	1.19	88	1.039 x10^{-6}	69 nm
2	1.49	90	1.302 x10^{-6}	87 nm
3	1.50	90	1.286 x10^{-6}	86 nm

Table 4.5: Summary of results obtained for assessing the reproducibility of the single step approach across 3 individual membranes with initial pore diameter of 100 nm. All physical parameters were kept the same including V_{dep}= -300 mV; V_{bias}= +200 mV; t= 40 s.

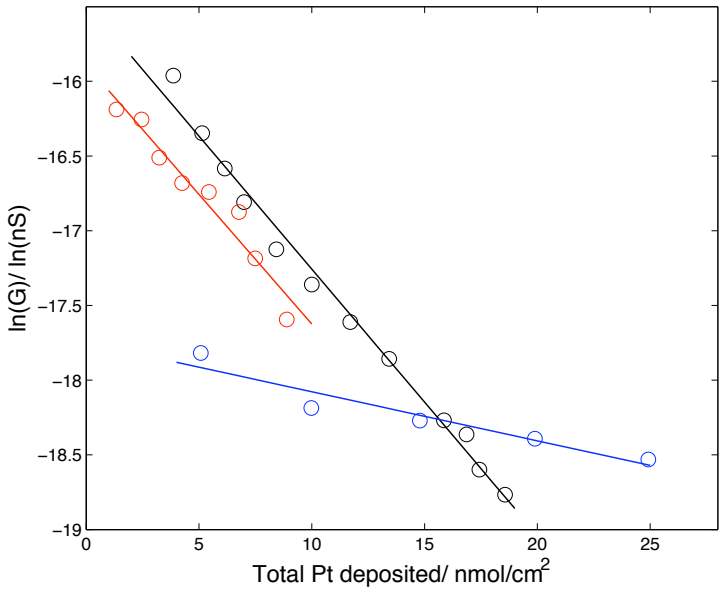


Figure 4.30: Semi-logarithmic plot of the pore conductance G vs. the amount of Pt deposited onto the membrane electrode (in nmol/cm^{-2}), including linear fits. Devices Pt-1 (*black circles*) and Pt-2 (*red circles*): initial pore diameter= 100 nm; V_{dep}= +350 mV. Pt-3 (*blue circles*): initial pore diameter= 45 nm; V_{dep} = -250 mV. V_{bias} in all cases was set to +200 mV.

area (0.07 cm^2) would achieve an increase in its Pt layer thickness of 0.13 nm (Mw(Pt) = 195.08 g/mol; D(Pt) = 21.45 g/cm^3). Such a change in the pore dimensions would not be detected in the ion current measurement (d_{pore}= 20-100 nm; Δd <1%). However, based on the results presented in Figure 4.27, the change in pore diameter is much larger and

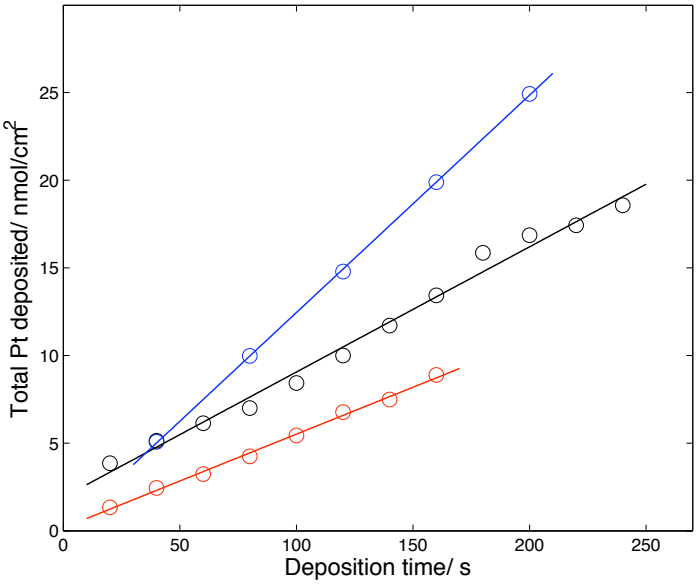


Figure 4.31: Amount of Pt deposited/cm^{-2} as a function of deposition time. The deposition rate for Pt-1 (*black circles*) and Pt-2 (*red circles*) is very similar (0.071 and 0.053 nmol cm^{-2} s^{-1}, respectively), which is expected due to the similar deposition conditions. In the case of Pt-3, however, the deposition rate is higher (0.107 nmol cm^{-2} s^{-1}), in accordance with the lower deposition potential.

on the order of 10 nm.

The origin of this effect is most likely rooted in the transport of reactants to the pore, but further studies are required to gain a full understanding of the complex interplay between the kinetics of the surface reaction and local mass transport.

4.6 Summary

In conclusion a new approach using bi-potentiostatic ion current feedback (ICF) control was developed to fabricate metallic solid-state nanopores with diameters below 20 nm. Preliminary experiments showed that the electrodeposition method developed in Chapter 3 can be employed to shrink solid-state nanopores.

Tests were conducted in this chapter to control this deposition process such that the size of the fabricated nanopores could be controlled in real time. Initial control experiments employed a visual feedback method such that the pore sizes were observed during the deposition process. However, due to constraints in the frame rate of the video monitor

and conflicting requirements with the focusing of the microscope, this approach provided a low level of accuracy in controlling the pore sizes.

In order to provide a more sensitive feedback method, the ionic current through the nanopore was then monitored to assess pore shrinkage in real-time. Tests were conducted on nanopore arrays and on single nanopore membranes. Several studies were performed using both single-step and multi-step deposition approaches at the nanopore surface. It was found that the ICF approach can be employed as a fairly accurate feedback mechanism allowing satisfactory control of the final nanopore size.

4.7 Appendix

4.7.1 Fabrication of PDMS reservoirs

As mentioned in Section 4.4.2, the first generation of flow cells were fabricated with polydimethylsiloxane (PDMS) reservoirs. To prepare a PDMS mould, two components, the base (tetra(trimethylsiloxy)silane) and the curing agent (tetra-methyl-tetra-vinyl-cyclotetra-siloxane), from a SYLGARD 184 Silicone Elastomer Kit (Dow Corning Limited, UK), were thoroughly mixed using a weight ratio of 10:1. The mixture was then poured into a 4 inch petri dish and cured at 65°C for 8 hours. The PDMS was then cut to the dimensions required using a 20 mm scalpel and 0.8 mm fluid inlet and outlet holes were then punched through the top of the PDMS mould for access to both reservoirs.

4.7.2 Fabrication of glass substrates

Holes were drilled onto individual glass substrates of 65 mm x 25 mm dimensions using a 1.6 mm drill bit. Au contact pads were then fabricated onto the glass substrate using standard photolithography techniques, process for which has been previously described for the flat electrodes, used in Chapter 3. The relevant CAD design for patterning is shown in Figure 4.2.

Following this, both the glass substrate and PDMS components were sequentially cleaned in a sonicator bath followed by acetone and isopropanol rinses. The components were then dried under a stream of nitrogen and exposed to an oxygen plasma for two minutes. Subsequently the glass substrate was plasma bonded to the PDMS mould by aligning the two components together.

4.7.3 Wire bonding onto gold contact pads

Wire bonding was used to form an electrical connection between the nanopore chip and the external working electrode terminal. Figure 4.32 shows a simplified schematic of the the wedge bonding technique used for forming electrical connections between the 5 mm^2 nanopore chip and the Au contact pad fabricated on the glass substrate, Section 4.3. For this a manual wire bonder (Kullicke and Soffa 4526 series) was used at the London Centre of Nanotechnology (LCN) facilities, UCL.

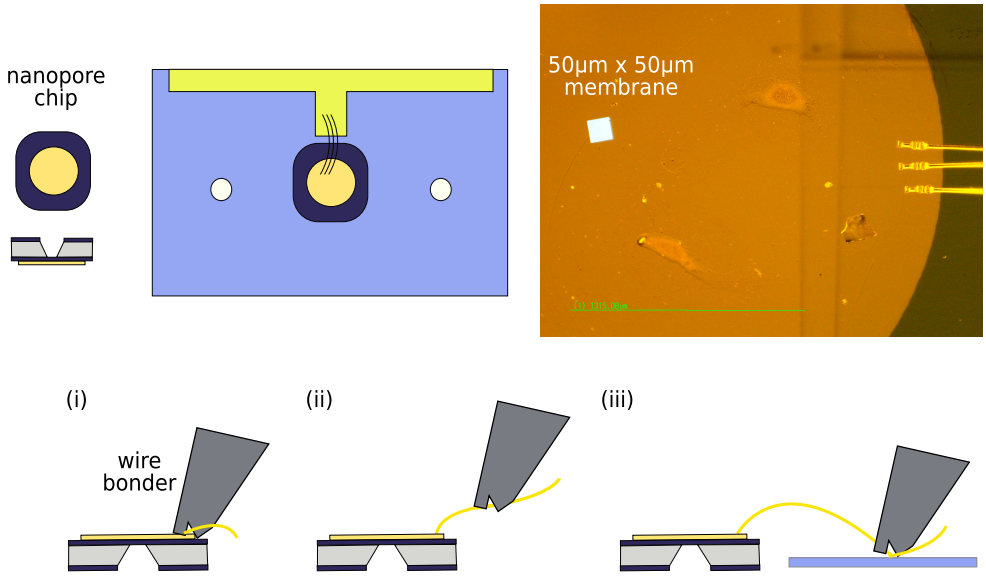


Figure 4.32: Wire bonding for the electrical connection between the Au membrane and contact pad. *Top left:* Schematic of the glass substrate with nanopore affixed for wire bonding. *Top right:* Optical image of Au wedge bonding at the edge of a nanopore chip (front view, *yellow*- gold layer; *green*- silicon nitride layer). The three bonds shown lead towards the contact pad patterned on the glass substrate. Which is externally connected to the WE1 terminal. *Bottom:* Procedure used to form ultrasonic wire bonds between the 5 mm^2 chip and contact pad.

A 25 μm Au wire (Sigma Aldrich) was used for all bonds. As illustrated in Figure 4.32 the Au wire was fed through the tool and manually aligned between the edge of the 5 mm^2 nanopore chip and the work holder. The tool was then lowered to its first search position (10 mm above the nanopore chip). (i) The wire was then pressed against the surface with a pre-determined force of 1.5 pN. Ultrasonic energy was applied for a pre-set time of 3 seconds to make the first bond. (ii) The tool was then raised while the wire was released

out from the spool of wire. Whilst bonded, the work holder was moved to the second bonding site under the tool, by doing so a loop was formed and the tool was lowered to its second search position (the Au contact pad). (iii) Here, the second connecting bond was formed using a force of 1.25 pN. Finally a wire clamp (behind the tool) was used to close and pull back on the wire to break it at the heel of the bond. The tool was then raised, and the end of the wire was fed out underneath the tool for the repeat of cycle.

Chapter 5

Ion transport

Declaration: The work presented in Section 5.1 has been published in M. Ayub et al, 'Nanopore structures for single molecule biosensing'. International Society of Electrochemistry Proceedings, 2010.

The work presented in this thesis has thus far focused upon the fabrication of nanopores for use in single-molecule detection. In this chapter, the ion transport across these pores is evaluated for a wide range of conditions. The aim is to characterise the ionic current for various pore sizes, bias potentials and a range of other factors; hence the sensitivity of ionic current measurements achievable across Pt-deposited nanopores is assessed.

In Sections 5.1 and 5.2 a brief account of the background theory, relevant to the tests conducted in this chapter is presented. The typical experimental set-up and techniques employed during these tests is provided in Section 5.3. This is succeeded by the studies that were conducted as well as discussions on the results achieved. As mentioned above, a wide range of factors were considered to complete a thorough characterisation of the fabricated nanopores. Subsection 5.4.2 considers how varying the salt (ion) concentration affects the ionic current through the pore; this is followed by a study on the performance of different pore sizes. These sections focus upon characterising the influence of the primary factors that determine the ionic current through the pore; the remaining sections then consider various methods of controlling this ionic current via surface modification of the membrane near the pore. As the nanopore is fabricated using Pt, the effects of employing the nanopore as an electrode is considered in sub-section 5.4.4 by a study on the effects of altering surface properties using thiols. Finally the conclusions made through the investigations considered in this chapter are summarised in Section 5.5.

5.1 Pore conductance theory

In order to validate the results of the various investigations conducted in this work, a model is proposed such that the ion transport through the nanopore and associated set-up is approximated as a simplified electric circuit, shown in Figure 5.1. Here the combined effects of a resistor and capacitor; hence the energy-dissipating (resistor) effects are segregated from the energy-storing (capacitor) effects, Bard and Faulkner (2000).

The circuit representing this device consisted of ion solution resistances (R_s) in series to represent the upper and lower chambers. In between which, a capacitance C_{mem} (associated with the membrane) is placed in parallel with a pore resistance R_{pore} – this is of much greater magnitude than R_s due to the constriction of rate of charge carrier (Cl^-) flow in the nanopore. However, various other factors may influence the total capacitance exerted on the ionic current; such as stray capacitance from exposed electrode leads (and other sources), membrane composition, membrane surface roughness and Faradaic reactions on the surface. In this case, C_{mem} may be replaced by a non-ideal capacitance, the constant-phase element (CPE) (Brug et al., 1984) which has two parameters, a magnitude Y_0 and an exponent n. Therefore two models can be constructed, one with a capacitor and another with a CPE.

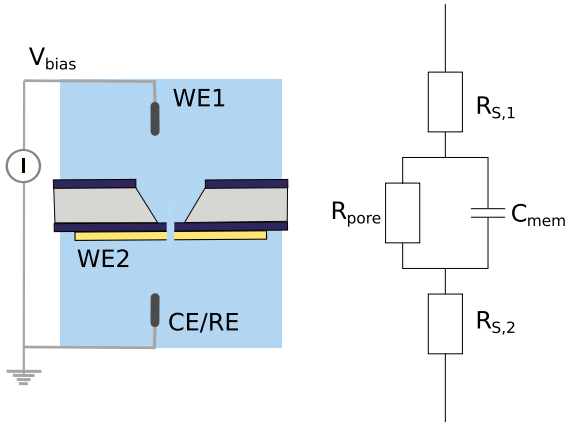


Figure 5.1: Schematic of the electrochemical set-up used for ion transport experiments and its corresponding equivalent circuit. The membrane capacitance C_{mem} here can be replaced by a Constant Phase Element (CPE) to accommodate for non-ideal capacitive behaviour.

In order to reduce the capacitive effects of the electrodes, the choice of ionic solution and composition of the electrodes are chosen such that the electrodes are non-polarisible,

for example Ag/AgCl electrodes in rapid equilibrium with Cl^- ions in solution. Therefore, charge transfer at the electrodes is rapid and thus is not expected to be current-limiting.

For a constant bias voltage V_{bias}, the steady state current flowing through the resistive branch of the circuit is governed by the R_s and R_{pore}. Typically, as R_{pore} is much greater than R_s, the resistive contribution of the solution can be neglected. Hence the primary potential drop across the cell occurs at or in the nanopore ($V_{bias} = \Delta U_{s,1} + \Delta U_{pore} + \Delta U_{s,2}$), where ΔU represents the potential drop:

$$V_{bias} = (R_{s,1} + R_{pore} + R_{s,2}) \times I \approx R_{pore} \times I \tag{5.1.1}$$

To a good approximation, R_{pore} and the pore conductance ($G_{pore} = 1/R_{pore}$) can be calculated from a geometric model, which takes into account the cross-sectional area of the pore d, its channel length L and the conductivity of the solution, ρ, Smeets et al. (2006).

$$G_{pore} = \frac{\pi d^2}{4L}\rho + \pi \frac{d}{L}\sigma_s \mu_i \tag{5.1.2}$$

σ_s is the charge density on the inner pore walls and μ_i is the electrophoretic mobility of the counter ion(s), say K^+ in KCl electrolyte and $\sigma_s < 0$. Note that Equation 5.1.2 is written in terms of the absolute value of σ_s.

For the cases considered in this chapter where the nanopore surface can employed as an electrode (WE2), the potential of WE2 can be controlled independently of the WE1 bias. This modulates the effective charge density on the nanopore surface (σ_s), despite the actual value of σ_s being dependent only upon material and surface structure and hence the potential of zero charge (E_{pzc}). Furthermore, for charged pores, an electric double layer forms to neutralise the charge on the inner pore walls. Under the influence of an electric field, these excess ions also contribute to the overall current and must also be accounted for in the model of G_{pore}; this is particularly important for small pores where this effect is significant. The pore conductance for these cases is given by:

$$G_{pore}(E) = \frac{\pi d^2}{4}\rho + \pi \frac{d}{L}\mu_i C_{edl}(E - E_{pzc}) \tag{5.1.3}$$

In the above E is the (membrane) electrode potential and C_{edl} is the differential capacitance of the electric double layer. The latter takes into account the solvent dielectric

constant, electrolyte concentration and charge, as well as electronic effects at the electrode/solution interface, Schmickler (1996). Indeed, the above equation if valid only if the dependence of C_{edl} on the WE2 potential is insignificant. The second term is strictly valid for long cylindrical pores (i.e. diameter $d << L$), where the electric field lines can be considered to be in parallel, however it often provides a reasonable estimate for other geometries, Siwy and Fulinski (2004b). Equation 5.1.3 implies that G_{pore} has a minimum at $E = E_{pzc}$ and increases linearly (but not necessarily symmetrically) with E for both positive and negative values of E_{pzc}.

Depending on the charge of the pore, the relative contribution of the charged species in solution to the total current will vary. For example, cations will experience a higher activation barrier when entering a positively charged pore than anions, this implies that the latter will carry a larger fraction of the current through the pore. This has been shown experimentally for ions (Siwy and Howorka, 2010), as well as for proteins (Chun et al., 2006).

The resulting arrangement of these components is similar to the Randles circuit, Randles (1947), which has one resistor in series rather than two. Henceforth, in the discussions presented in this chapter, the model circuit proposed here which employs a capacitor will be referred to as 'Randles', whereas the circuit which employs a constant phase element (CPE) will be referred to as 'Randles with CPE'.

5.2 Electrochemical Impedance Spectroscopy (EIS) theory

In previous chapters, tests were performed on the conductance of the fabricated nanopores by applying a Direct Current (DC) potential across the nanopore. For the EIS studies discussed in this chapter, an Alternating Current (AC) is applied. The motivation behind doing so is that the application of an AC potential facilitates the ability to vary its frequency, and so a more comprehensive understanding of the relationship between the ionic current and bias potential can be formed. For example, the variation in potential permits an alternative approach to calculating the conductance of the pores at the potentials previously evaluated (and so serves to validate previous tests), but it can also be employed to form a greater understanding of the resistive and capacitive effects of the nanopore. Indeed, EIS theory is a branch of alternating current theory that illustrates the response of a circuit to an alternating current or voltage as a function of frequency. The technique permits the study of more complex behaviour than cyclic voltam-

metry; for example, frequency-dependent resistance, or impedance, Z may be measured, Barsoukov and Macdonald (2005). From this its possible to produce a modified form of Ohms law, so that whilst for a DC potential the impedance is given by:

$$Z = E(t)/I(t) \tag{5.2.1}$$

for an AC potential, equation 5.2.2 can be employed:

$$Z = \left(E_0 e^{i\omega t}\right) / \left(I_0 e^{i(\omega t - \psi)}\right) \tag{5.2.2}$$

In the above, $E(t)$ is the potential (of known frequency) applied to the electrochemical cell whilst $I(t)$ is the measured current response across the pore. Hence the lag in response between the applied potential and measured current may be used to calculate the phase lag ψ, thus the magnitude of the impedance may be obtained from Equation 5.2.2. Note that i represents an imaginary number, t is time and ω is the frequency of the applied potential. In order to investigate the frequency-dependance of the cell, an expression for the total impedance of the model circuit is required. Hence some basic relations between impedance and the various components employed in the model are presented:

$$\text{Resistor:} \quad Z_R = R \tag{5.2.3}$$

$$\text{Capacitor:} \quad Z_C = 1/\left(i\omega C\right) \tag{5.2.4}$$

$$\text{CPE:} \quad Z_{CPE} = 1/\left(Y_0[i\omega]^n\right) \tag{5.2.5}$$

It should be noted that the impedance of a resistor R is independent of frequency; therefore we would expect any frequency-dependent behaviour in the model to originate from the capacitor or CPE element. Impedances and their inverse, admittances in a circuit are added up in the same way as their DC counterparts: resistances in series and conductances add in parallel. For example with the capacitor circuit:

$$Z_{total} = Z_s + Z_p \tag{5.2.6}$$

$$Z_{total} = 2R_s + 1/\left(1/R_p + i\omega C\right) \tag{5.2.7}$$

$$Z_{total} = 2R_s + R_p/\left(1 + i\omega C R_p\right) \tag{5.2.8}$$

$$Z_{total} = 2R_s + R_p/\left(1 + \omega^2 C^2 R_p^2\right) + \left(i\omega R_p^2 C\right)/\left(1 + \omega^2 C^2 R_p^2\right) = Re\{Z\} + lm\{Z\} \tag{5.2.9}$$

The impedance data can be graphically represented in two ways using Nyquist and Bode plots (Bard and Faulkner, 2000 and Barsoukov and Macdonald (2005)). The most widely used impedance data representation is the Nyquist plot, which plots the imaginary impedance ($Im(Z)$) against their real counterparts ($Re(Z)$), a schematic of this is shown in Figure 5.2. Hence the absolute value of the impedance can be calculated as the hypotenuse of the triangle formed by $Im(Z)$ and $Re(Z)$.

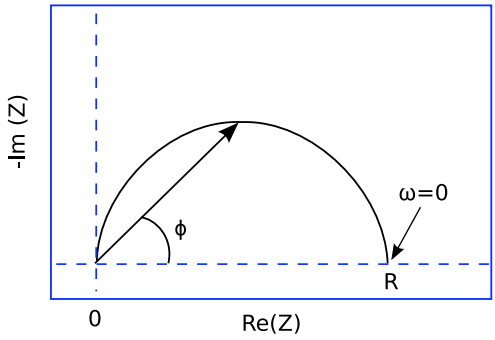


Figure 5.2: Nyquist plot where $Re(Z)$ and $Im(Z)$ are the real and imaginary parts of the impedance, respectively. The phase angle is represented by ϕ.

Even though the Nyquist plot has been widely used for the graphic representation of impedance measurements, it cannot be used to calculate the frequency of the measured impedance. For this, a Bode plot is employed, which typically consists of two sub-plots; the first plots the impedance magnitude as $log_{10}|Z|$ against the frequency as $log_{10}(\mathrm{f})$ whilst the second plots phase difference ψ vs. $log_{10}(\mathrm{f})$. An example of these plots is shown in Figures 5.3. Three distinctive frequency-based regimes can be seen here:

(i) At low frequencies, the behaviour is predominantly resistive. C offers high impedance so the current goes mainly through the two resistive elements. On the $log_{10}|Z|$ plot, the system impedance tends to the sum of R_{pore} and R_s, which is a constant value and independent of frequency. On the phase plot, phase lag tends to zero, which is again characteristic of resistive behaviour.

(ii) At high frequencies the behaviour is again resistive. C provides little impedance, acting as a short circuit, continually charging and recharging. The current tends to go through C rather than R_{pore}; however, in comparison to R_s the impedance of C is negligible. Therefore the total system impedance tends to R_s, which is also a constant value, independent of frequency. Similarly there is zero phase lag on the phase plot.

(iii) At a characteristic frequency to the system, the behaviour becomes significantly

capacitive. The magnitude of the impedance is dependent upon frequency and there is a large phase lag between the voltage applied and the resultant current (although rarely as much as 90 degrees, so not fully capacitive). This frequency may be described as $f = 1(2\pi R_{pore}C)$.

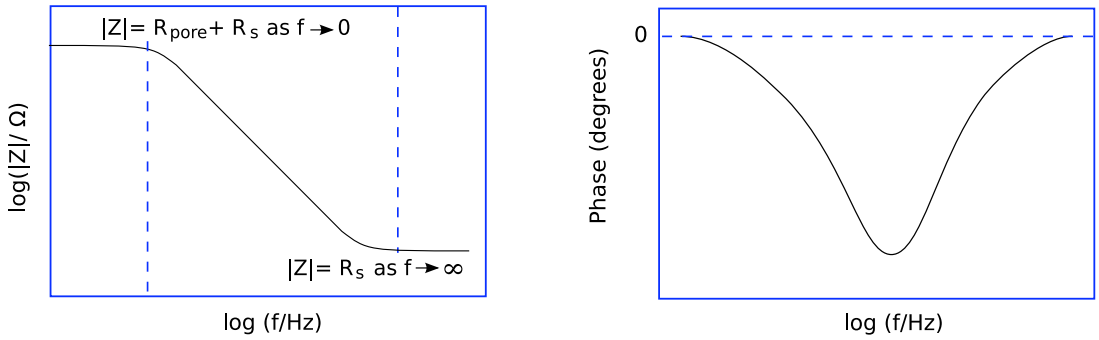


Figure 5.3: *Left*: Bode plot of $log_{10}|Z|$ vs. $\log_{10}$(f). *Right*: Bode plot of phase vs. $\log_{10}$(f).

5.3 Experimental

5.3.1 Buffer solution

KCl solutions of varying concentrations used throughout all measurements were prepared by adding 18 MΩ cm Milli-Q filtered water (Millipore) to an un-buffered (pH= 6.2 ± 0.2) stock solution of 1.0 M potassium chloride (KCl, Fluka, > 99.99%). An un-buffered solution was used to avoid the introduction of additional ionic species into the system. The measurements were carried out starting with the lowest concentration, then increasing this step-wise. This was done to ensure the nanopore device was at its minimum conduction state at the start of each run. Therefore, KCl sweeps were always completed from the lowest concentration to the highest. Before each concentration change, the cell was cleaned as described in Section 2.5.2 and then filled again with the next electrolyte concentration to be used.

5.3.2 Data acquisition and analysis

All I-V and EIS measurements were performed using either a CHI 760c or a Gamry Reference 600 commercial potentiostat. The instrument were controlled via a personal computer (PC) using the CHI 7.20/Echem Analyst softwares. All electrochemical potentials were

measured with respect to a Ag/AgCl reference electrode. The PTFE flow cell was used in all the measurements presented in this chapter. Further details of its design and assembly is provided in Section 2.5. The flow cell was placed in a Faraday cage (constructed in-house) and electrically connected to the ground. The electrolyte solutions were degassed by bubbling high purity argon (Ar) gas for 15 minutes prior to every measurement.

I-V measurements

I-V measurements were conducted using cyclic voltammetry where the data collected consisted of 5 sweeps over a range of both a ±200 mV and a ±500 mV range with a scan rate of either 5 or 50 mV s^{-1}. A three electrode configuration was employed using reversible Ag/AgCl electrodes connected as WE1 and combined CE/RE that were immersed in the buffer solution on either side of the fluid filled nanopore flow cell. A range of pore dimensions were used and are described further in the relevant sections.

AC Impedance Spectroscopy

The electrical performance of metallic nanopores was characterised using AC impedance spectroscopy as described in Section 5.2. For these studies, a 100 nm Au/Si_3N_4 nanopore was fabricated and the KCl concentration was varied to study its effects on the impedance of the nanopore system. Each EIS measurement consisted of a amplitude modulation of 5mV scan with 50 points per decade over 6 decades of frequencies, between 1 Hz to 1 MHz. A setting of 100 points per decade was used for higher concentrations between 500 mM and 1 M. These measurements were conducted with Jessica Clough (summer intern).

EIS modelling

In order to complete the model circuit proposed in Section 5.1, resistance and capacitance values were necessary to represent the effects of the various electrochemical components. These values were obtained by the Echem Analyst model-fitting editor whereby the proposed model circuit was created within the editor and fitted to the I-V and EIS results. Figure 5.4 shows a sequence of screenshots of the EIS model editor which was used to construct the Randles circuit. In order to simplify the model, the solutions resistances are summed and represented in the figure as R_u; as the electrochemical cell is symmetrical $R_{s,1} = R_{s,2} = R_{pore}$. The fitting model employed the Levenberg-Marquardt algorithm

(Gamry), the results of which could then be used to obtain theoretical plots of conductance.

5.3.3 Surface modification using thiols

As a precursor to employing the nanopore surface to influence the electrochemical circuit, preliminary experiments were conducted whereby the Au nanopore surface was chemically modified. Thiol self-assembled monolayers (SAMs) of 6-mercapto-hexan-ol were formed by spontaneous adsorption of chemical molecules onto the Au nanopore surface forming a monolayer (Love et al., 2005 and Schwartz, 2001). This was done to reduce the membranes capacitive effects; Figure 5.5 shows the steps employed for modifying the pores.

The Au coated nanopore membrane consisting of a 100 nm pore was pre-cleaned using ethanol, isopropanol and ultra-pure water followed by exposure to an oxygen plasma for 2 minutes, as described in Section 2.5.1. Subsequently, the membrane was immersed in a 1 mM sealed solution of 6-mercaptohexan-1-ol ($\geq$ 97.0%, Sigma) in isopropanol at room temperature, overnight to form the monolayer. Gentle agitation of the solution was carried out via a rotating 5 mm magnetic stirrer bar. Before measurements, the modified Au membrane was thoroughly rinsed several times with isopropanol and deionised water. These measurements were conducted with Daniel Godfrey (final year undergraduate student).

Characterisation of thiolated nanopores

Once treated, the surface was characterised via cyclic voltammetry. This was done by affixing the modified nanopore membrane to the microfluidic flow cell and filling both reservoirs with a buffer solution of 100 mM NaOH. A three electrode set-up was used where Pt wire was connected as the CE, an Ag/AgCl electrode was used as RE, both immersed into the same reservoir using the inlets of the flow cell. The membrane was connected as WE1 using gold plated adhesive film and potential sweeps between the range of $\pm$ 500 mV were applied to the WE1 at a scan rate of 50 mV s^{-1}.

This technique can also be used to estimate the surface coverage of the thiol monolayer on the Au nanopore surface; Thiol SAMs are known to quantitatively desorb either oxidatively or reductively from Au surface in alkaline media (Sabatani and Rubinstein, 1987 and Schwartz, 2001):

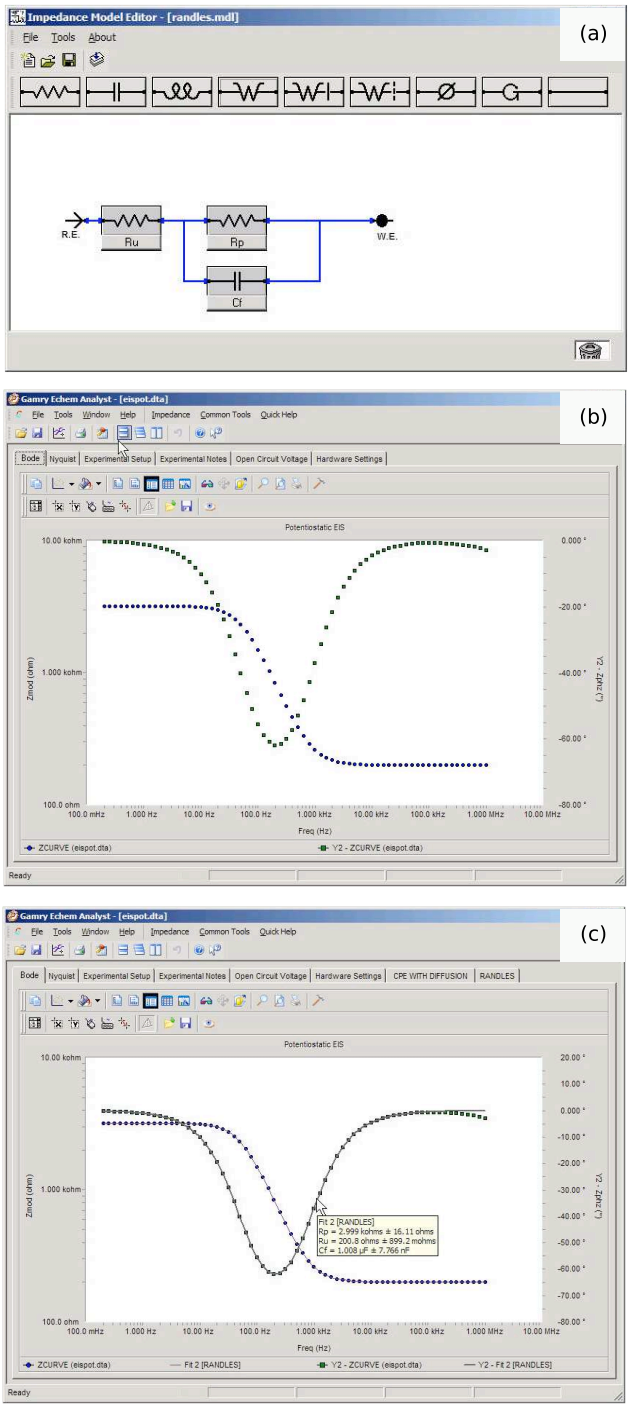


Figure 5.4: Screenshots of model fitting software. (a) construction of the Randles cell circuit. annotations: C_f, Faradaic capacitance in parallel with a polarisation resistance R_{pore}. The solution resistance, displayed as R_u is in series with the R_{pore} and C_f pair. (b) EIS spectrum from measurements. (c) Best fit in accordance with Randle's model.

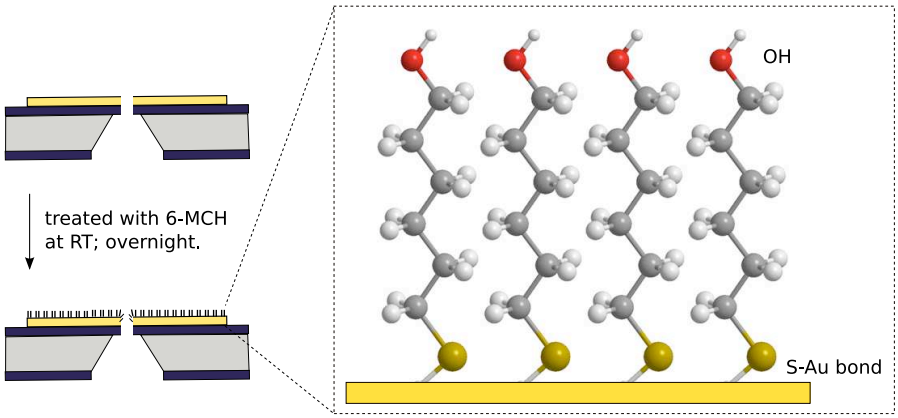


Figure 5.5: *Left*: illustration of process for forming self assembled monolayers of 6-mercaptohexanol onto Au nanopore surfaces. *Right*: enlarged view of 6-MCH adsorption onto Au.

$$Au - SR + 4OH^- \rightarrow Au + RSO_2^- + 2H_2O + 3e^- \quad (5.3.1)$$

$$Au - SR + e^- \rightarrow Au + RS^- \quad (5.3.2)$$

The electrochemical desorption of thiol from gold results in either an oxidative or reductive peak visible in a CV trace. The charge (Q) under this desorption peak was used to calculate the surface coverage (Γ_{SAM} / mol.cm^{-2}) of the SAM using the theoretical relationship in accordance to equation 5.3.3 (Schwartz, 2001):

$$\Gamma_{SAM} = Q/nFA \quad (5.3.3)$$

where n represents the number of electrons involved in the desorption of thiol, F is the Faraday constant and A is the geometric surface area of the Au nanopore electrode.

5.4 Results and discussion

In this section, the ionic current across Pt deposited pores is investigated for a range of solution concentrations, bias potentials and pore sizes. The aim is to assess the sensitivity of the pores as well as characterise their behaviour for a range of given variables. These experiments are conducted whilst employing only a single working electrode (WE1); subsequently, preliminary studies on employing the nanopore to influence the ion transport

were conducted. This consisted of modifying the capacitive effects of the membrane by chemically modifying its surface using thiols, which behaves as an insulating layer and inhibits metal-ion interaction.

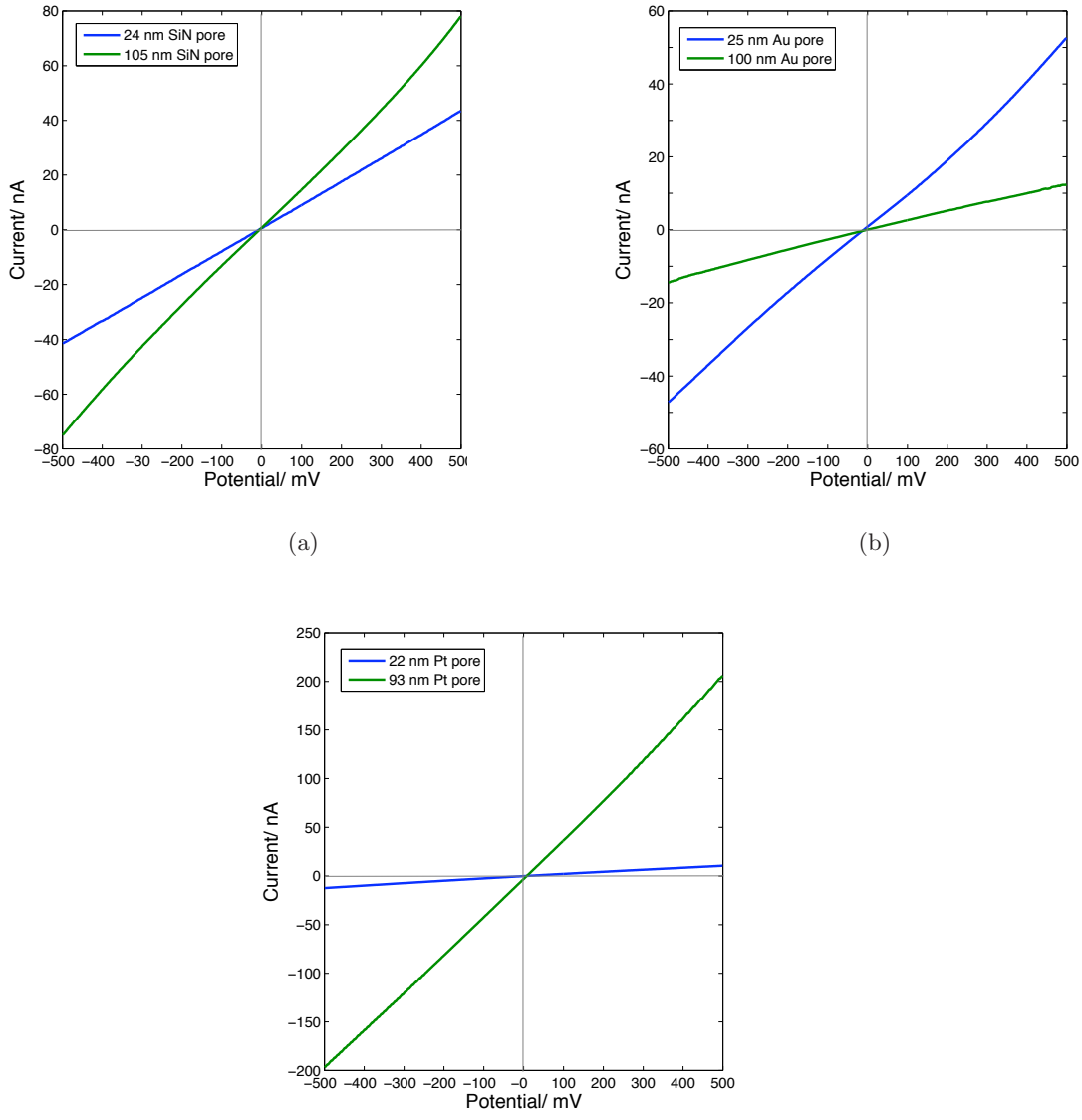
5.4.1 I-V characteristics

In this section, the current-voltage (I-V) characteristics of the nanopores are investigated. Tests were conducted whereby potential sweeps between the range of ±200 mV were applied across the nanopore using cyclic voltammetry and the ionic current was observed. These have been performed on Pt-deposited pores as well as Au and bare Si_3N_4 in 1 M KCl solution.

Figure 5.6 shows a sample of I-V measurements at 1 M KCl of six individual nanopores (2x Si_3N_4; 2x Au and 2x Pt deposited) with different diameters. In all measurements, the I-V curves display a linear relationship, exhibiting ohmic behaviour in the range of ±500 mV. The gradient of linear fits to the data yield the value of nanopore conductance, G_{pore}. It can be observed that these values correlate to the pore dimensions, where a smaller size pore displays a lower conductance. Another noticeable feature is the comparison of metallic nanopores with conventional Si_3N_4 pores; from the results obtained, it is evident that both Au and Pt pores display similar characteristics to Si_3N_4. This suggests that the metallic nanopores tested here do not exhibit excess rectifying behaviour whereby positive and negative potentials of a set value would induce differing current magnitudes. This effect is produced by a conical shaped nanopore, which in this case would be due to an uneven distribution of deposit within the pore. The conical shape of the pore has the effect of selectively restricting the entrance area to the pore on one side in comparison to the other, hence lower ionic current is induced for a negative potential than for a positive one, Siwy and Fulinski (2004b). However as such behaviour is minimal in Figure 5.6, it may be stated that the pore is not conically shaped and hence the metallic surfaces have been evenly distributed through out the pore.

5.4.2 Salt dependence

The ionic current across the nanopore is inherently dependent upon the concentration of ions within the electrolytic solution, hence altering its solution will increase or decrease the observed ionic current. In this section, the KCl concentration is varied from 1 mM to 1 M in order to investigate its effects. These experiments have been conducted not only



(a) (b)

(c)

Figure 5.6: General nanopore characteristics. I-V measurements for (a) Si_3N_4 pores; 24 nm; 105 nm (b) Au pores; 25 nm; 100 nm and (c) Pt deposited pores; 22 nm; 93 nm at 1 M KCl concentration.

for the Pt-deposited nanopores but also on their Si_3N_4 and Au coated counterparts as well as for two different pore diameters of each nanopore.

A summary of the tests conducted and their corresponding results is provided in Table 5.3. These have been plotted in Figures 5.7a and 5.7b for the smaller and larger pore diameters of each pore type respectively. Equation 5.1.2 has been employed to calculate theoretical values of the pore conductance based upon the equivalent circuit model of Figure 5.1 and is also plotted with the experimental results. The plots show the general result that (as expected) increasing the ion concentration results in an increase in charge within the solution, hence pore conductance is seen to increase. It should be noted that despite the diameters of the Pt, Au and Si_3N_4 nanopores being similar, for both the smaller and larger variants; the Pt pores show a significantly higher conductance for all the tested ion concentrations.

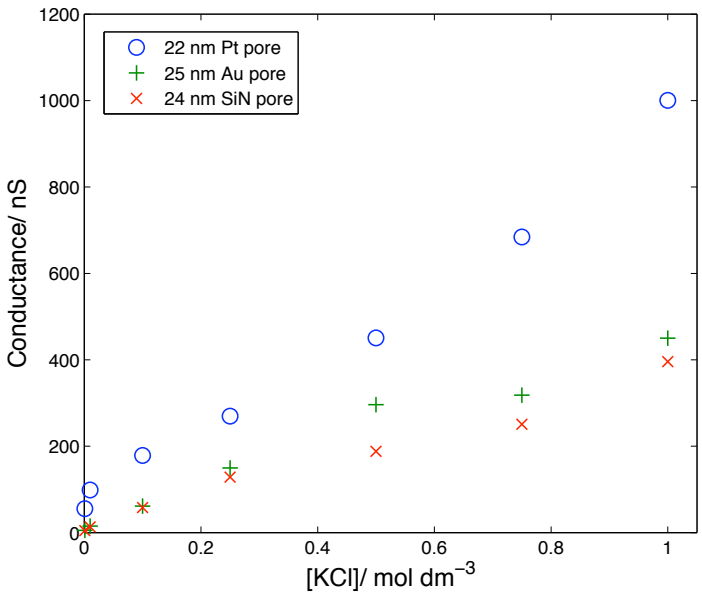
Theoretical values of pore conductance were also calculated from Equation 5.1.2 and are provided in Table 5.3. Clearly, from comparison of the equation conductance values to the experimental data, they do not fit well. This may be due to a number of issues but most notably because of the neglect of the surface charge density term. As it is not currently possible to accurately calculate or estimate its value the term was neglected in Equation 5.1.2. However, it should be noted that other factors may also have contributed to this discrepancy, such as those discussed in Chapter 4.

5.4.3 EIS studies

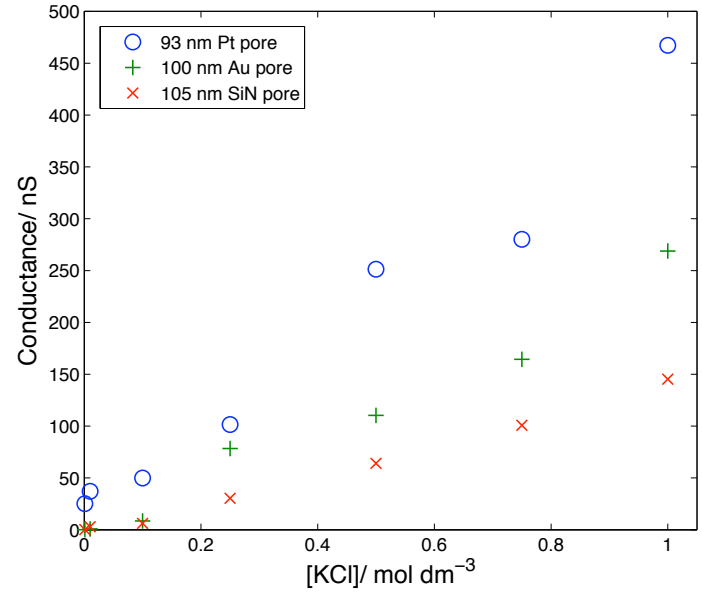
Impedance measurements

As discussed in the theory of EIS studies (Section 5.2), an AC potential was applied to the electrochemical cell in order to characterise its behaviour. In this study, a 100 nm Au/Si_3N_4 nanopore was fabricated and the KCl concentration was varied to study its effects on the impedance of the nanopore system. Each EIS measurement consisted of a scan with 50 points per decade over 6 decades of frequencies, between 1 Hz to 1 MHz. A setting of 100 points per decade was used for concentrations between 500 mM-1 M. The results of the study are provided in Figures 5.8a and 5.8b for the impedance and phase lag, respectively.

The impedance measurements plotted in Figure 5.8a show a decreasing impedance as the ionic concentration in increased. This is due to an increase in charge carriers at higher concentrations, as a result, resistance is lower at all the tested frequencies.



(a)



(b)

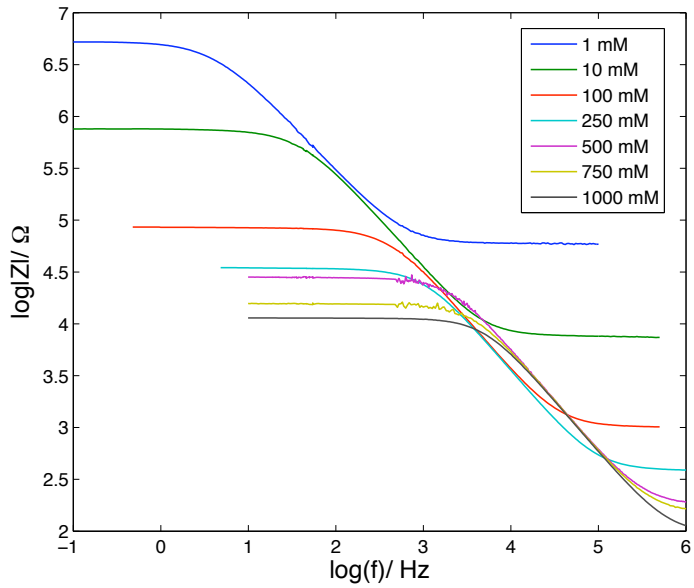
Figure 5.7: Salt concentration dependence of nanopore conductance. (a) small pores and (b) large pores. Individual pore diameters for the different membranes are tabulated in Table 5.3.

KCl/ mol dm^{-3}	Si_3N_4					
	24 nm			105 nm		
	G/ nS	I/ nA	Model/ nS	G/ nS	I/ nA	Model/ nS
0.001	0.16	0.03	0.80	4.58	0.92	4.37
0.010	2.87	0.57	2.90	13.27	2.65	15.41
0.100	6.21	1.24	15.41	58.12	11.62	82.78
0.250	30.44	6.09	40.80	128.33	25.67	218.93
0.500	64.11	12.82	72.70	187.98	37.60	389.72
0.750	100.80	20.16	103.42	250.66	50.13	554.29
1.000	145.21	29.04	121.24	365.80	73.16	649.56

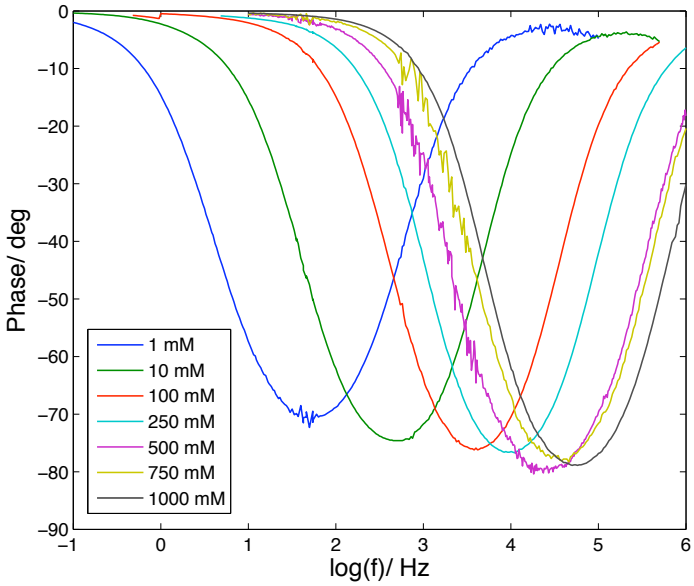
Table 5.1: Summary of results obtained via CV measurements for varying KCl concentrations (1 mM; 10 mM; 100 mM; 250 mM; 500 mM; 750 mM; 1M) in Si_3N_4 nanopores. V_{bias} between WE1 and CE/RE in all measurements was set to +200 mV. Model/ nS= modelled values according to Equation 5.1.2.

KCl/ mol dm^{-3}	Au coated					
	25 nm			100 nm		
	G/ nS	I/ nA	Model/ nS	G/ nS	I/ nA	Model/ nS
0.001	0.11	0.02	0.60	5.09	1.02	6.43
0.010	0.79	0.16	2.11	15.12	3.02	22.54
0.100	8.46	1.69	11.23	61.24	12.25	121.36
0.250	78.44	15.69	29.61	149.76	29.95	320.24
0.500	110.32	22.06	52.66	296.20	59.24	570.12
0.750	164.45	32.89	74.82	318.14	63.63	810.19
1.000	268.88	53.78	87.61	631.05	126.21	950.63

Table 5.2: Summary of results obtained via CV measurements for varying KCl concentrations (1 mM; 10 mM; 100 mM; 250 mM; 500 mM; 750 mM; 1M) in Au coated nanopores. V_{bias} between WE1 and CE/RE in all measurements was set to +200 mV. Model/ nS= modelled values according to Equation 5.1.2.



(a)



(b)

Figure 5.8: Impedance measurements for a 100 nm Au/Si_3N_4 nanopore at 7 different concentrations between 1 mM to 1 M. (a) $\log_{10}|Z|$ vs. $\log_{10}$(f) Bode plot. Resistive behaviour is observed across all concentrations. (b) Correponding phase difference vs. $\log_{10}$(f) Bode plot. As KCl concentration is increased, the frequency at which the maximum phase lag occurs also increases.

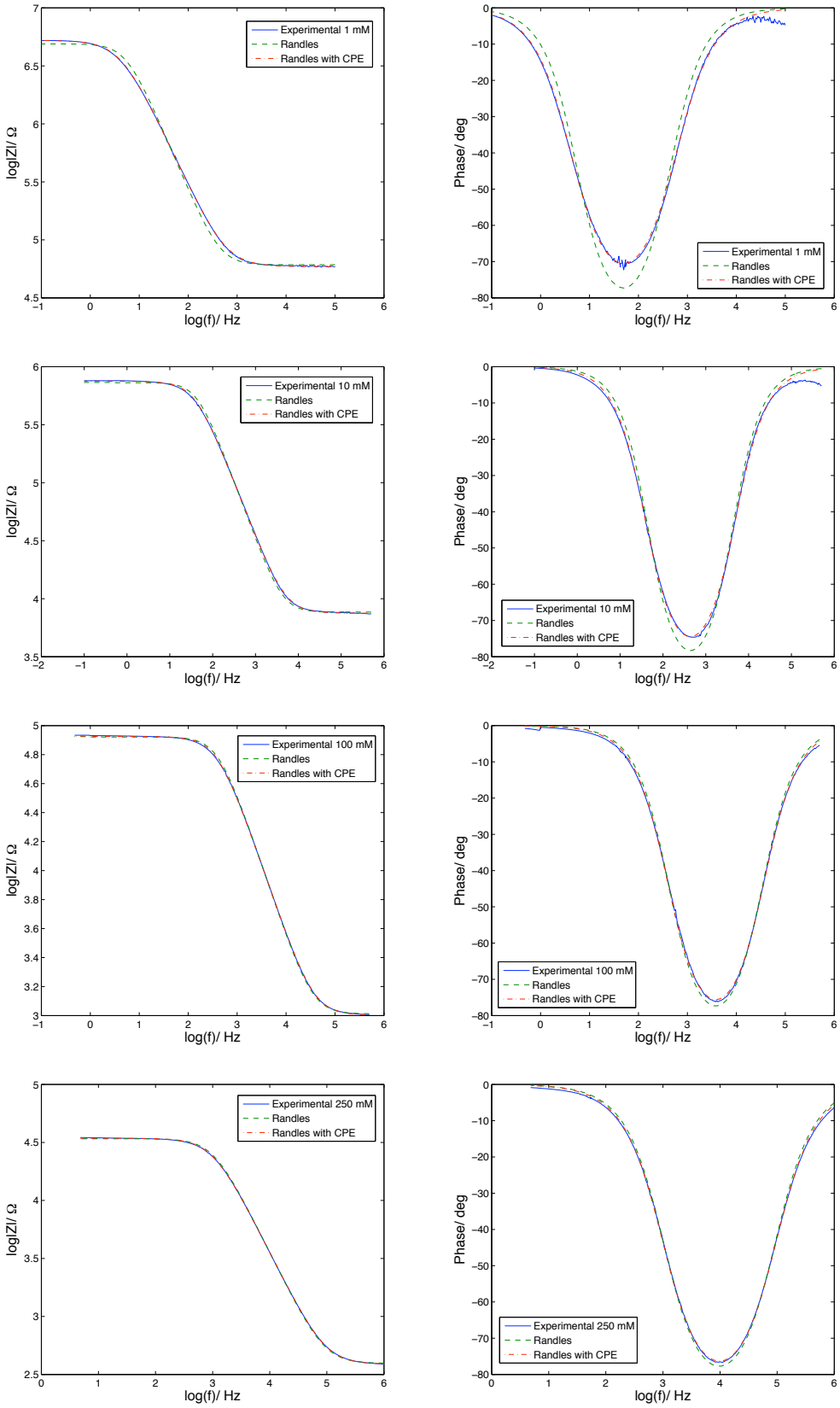


Figure 5.9: Individual $\log_{10}|Z|$ vs. $\log_{10}(\mathrm{f})$ and phase difference Bode plots for KCl concentrations between 1 mM to 250 mM. Experimental data (*blue solid line*); Randles model (*green dotted line*); Randles with CPE model (*red dotted line*).

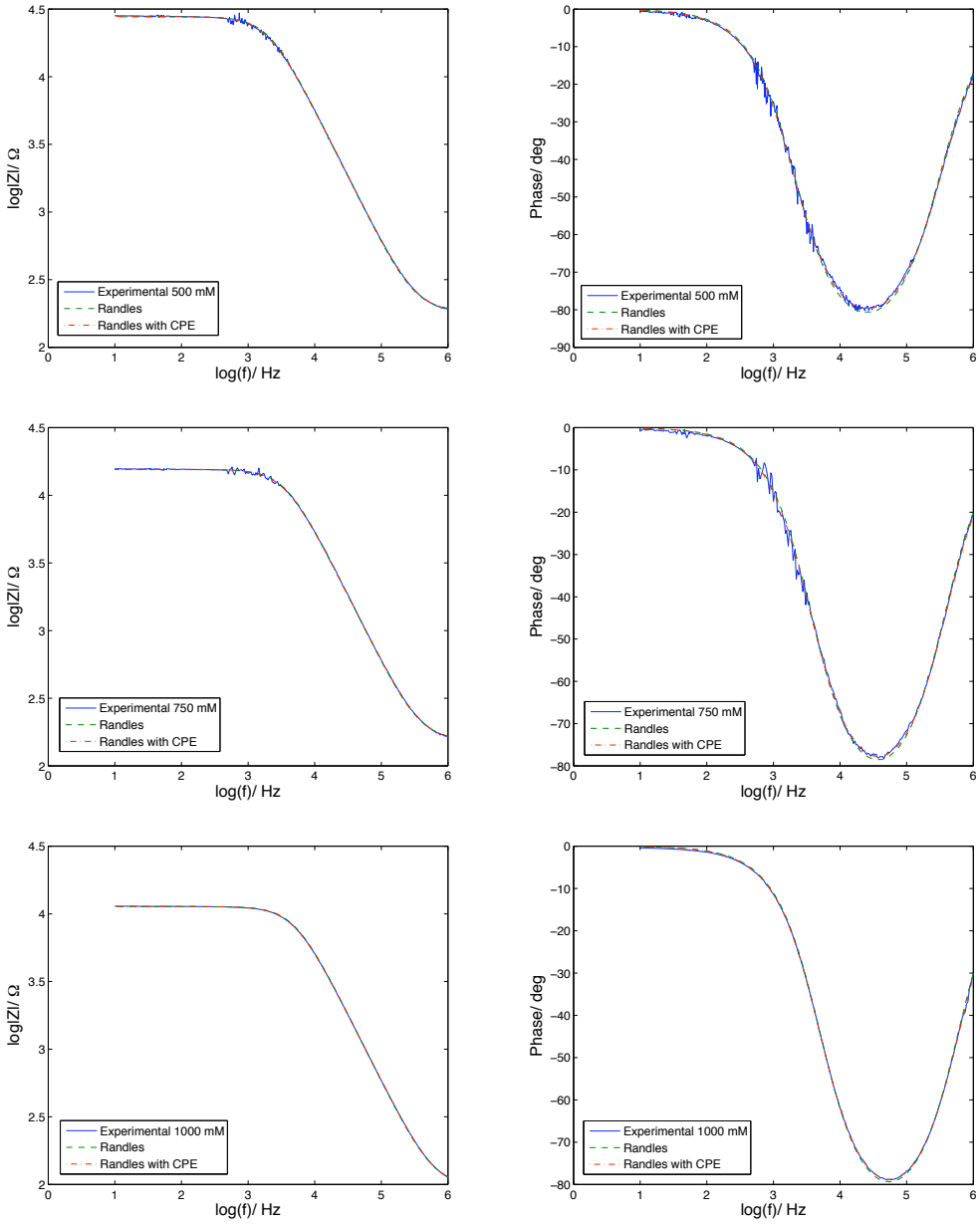


Figure 5.10: Individual $\log_{10}|Z|$ vs. $\log_{10}(\mathrm{f})$ and phase difference Bode plots for KCl concentrations between 500 mM to 1 M. Experimental data (*blue solid line*); Randles model (*green dotted line*); Randles with CPE model (*red dotted line*).

KCl/ mol dm^{-3}	Pt-deposited					
	22 nm			93 nm		
	G/ nS	I/ nA	Model/ nS	G/ nS	I/ nA	Model/ nS
0.001	25.14	5.03	30.25	55.23	11.05	55.91
0.010	37.12	7.42	42.11	98.55	19.71	195.14
0.100	49.90	9.98	57.53	178.67	35.73	104.71
0.250	101.55	20.31	150.11	269.45	53.89	277.16
0.500	251.32	50.26	267.18	450.77	90.15	493.18
0.750	280.12	56.02	380.47	684.21	136.84	701.32
1.000	530.55	106.11	446.20	1000.50	200.10	821.96

Table 5.3: Summary of results obtained via CV measurements for varying KCl concentrations (1 mM; 10 mM; 100 mM; 250 mM; 500 mM; 750 mM; 1M) in Pt deposited nanopores. V_{bias} between WE1 and CE/RE in all measurements was set to +200 mV. Model/ nS= modelled values according to Equation 5.1.2.

The phase vs. $\log_{10}$(f/Hz) plot for the above measurements are presented in Figure 5.8b. The results show that as KCl concentration is increased, the frequency at which the maximum phase lag occurs also increases. However there are two unexpected features observed in the measurements; firstly, some of the concentrations exhibit an oscillatory behaviour and secondly the phase lag values of some concentrations do not return to 0 degrees. The first issue may be a result of noise affecting the EIS readings, however this could not be verified. The source of the latter issue is currently unclear and further investigations are necessary to evaluate its source.

The data collected at each concentration was then compared to the values acquired from the two models (Randles and Randles with CPE). Plots comparing all three results are presented in Figures 5.9 and 5.10 for impedance and phase lag, respectively. For all the plots, it may be observed that the model profiles fit very well to the experimental results, which suggests that the equivalent circuit constructed in Section 5.1 is a good representation of the electrochemical cell. Furthermore, the agreement in profiles also serves to validate the hypothesised behaviour of the electrochemical cell and confirm that there are no spurious current leakages etc.

Pore conductance

In this section the EIS model-fitting method described in section 5.3.2 is studied for a 100 nm pore. The aim is to employ both DC and AC results to the EIS fitting model in order to obtain the values of the various components within the proposed circuit model (Section 5.1). Therefore, DC cyclic voltammetry tests were conducted where bias potentials were applied between WE1 and CE/RE Ag/AgCl electrodes to obtain I-V plots for seven different ion concentrations between 1mM to 1M. The slopes of the I-V plots were then used to calculate the pore conductance of the nanopore system (using equation 5.1.2) for both the capacitor and CPE versions. The R_s and R_{pore} values from the model were substituted into the equation for conductance (Equation 5.1.2). As a result, a series of conductance values were obtained for each concentration and a set for each model.

The three sets of conductances (experimental and two models) are plotted as a function of KCl concentration in Figure 5.11. The raw data values of the experimental results are provided in Table 5.4, whilst the calculated values of the components and conductance based upon the capacitor and CPE model are presented in Tables 5.5 and 5.6 respectively. In order to estimate the error in the model conductances, a simple linear regression analysis was also carried out on the experimental data. The slopes of the system conductance vs. electrolyte concentration obtained by CV and EIS appear to agree within their respective errors. This also suggests that the model circuit satisfactorily represents the electrochemical cell and further validates both its layout and the experimental results.

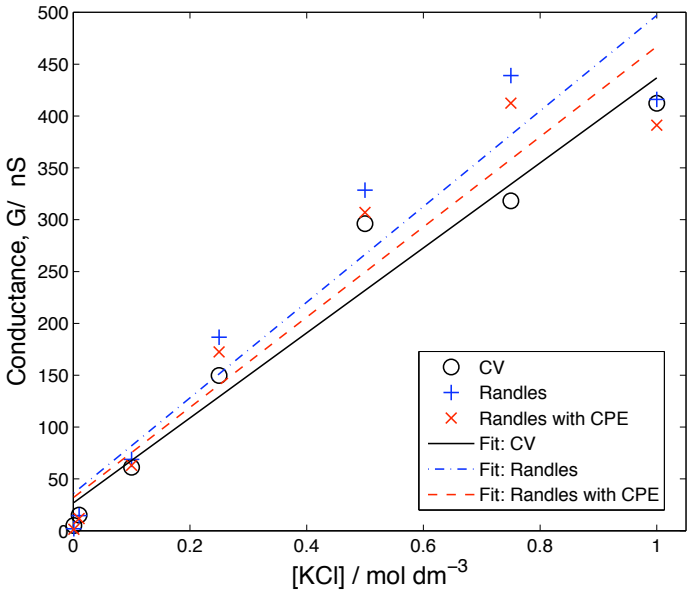


Figure 5.11: Pore conductance, G for a Au/Si_3N_4 nanopore, diameter ~100 nm vs. varying KCl concentration. Three sets of data are plotted, in which conductances have been obtained by: (i) Cyclic voltammetry, slope 410 ± 40 nS mol^{-1} dm^3 (*black circles*) (ii) Model-fitting to Randles circuit (*blue t − cross*), slope 460 ± 60 nS mol^{-1} dm^3 and (iii) Model-fitting to Randles circuit with CPE (*red − cross*), 440 ± 60 nS mol^{-1} dm^3.

KCl/ mol dm^{-3}	G/ nS					Mean	Error in mean
	1	2	3	4	5		
0.001	4.96	4.97	5.24	5.15	5.13	5.09	0.05
0.010	15.00	15.19	15.12	15.19	15.12	15.12	0.04
0.100	59.62	59.65	60.95	64.50	61.46	61.24	0.89
0.250	150.60	148.20	148.60	150.70	150.70	149.76	0.56
0.500	296.00	296.90	294.20	295.50	298.40	296.20	0.70
0.750	317.80	322.60	317.20	317.80	315.30	318.14	1.21
1.000	406.50	412.50	408.20	416.10	418.20	412.30	2.23

Table 5.4: Pore conductance measurements for a 100 nm Au/Si_3N_4 pore at concentrations: 1 mM; 10 mM; 100 mM; 250 mM; 500 mM; 750 mM; 1 M, using the CV technique.

KCl /mol dm^{-3}	R_{pore} ± error /GΩ	$2R_s$ ± error /MΩ	C ± error /nF	R_s /MΩ	$R_{pore} + 2R_s$ /GΩ	$G = 1/(R_{pore} + 2R_s)$ /nS
0.001	508.30 ±2.55	100.50 ±0.23	5.87 ±0.01	50.25	508.40	1.97
0.010	68.25 ±0.21	14.56 ±0.04	3.52 ±0.01	7.28	68.26	14.65
0.100	14.52 ±0.03	1.84 ±0.01	2.35 ±0.01	0.92	14.52	68.86
0.250	5.36 ±0.01	1.58 ±0.01	1.77 ±0.01	0.79	5.36	186.65
0.500	3.04 ±0.01	1.12 ±0.01	1.63 ±0.01	0.56	3.04	328.50
0.750	2.28 ±0.01	1.01 ±0.01	1.68 ±0.01	0.51	2.28	438.98
1.000	2.40 ±0.01	0.87 ±0.01	1.68 ±0.01	0.44	2.40	415.99

Table 5.5: Summary of results obtained from the Randles model.

KCl /mol dm^{-3}	R_{pore} ± error /GΩ	$2R_s$ ± error /MΩ	Y_0 ± error (x10^{-3}) /nS.S^n	n ± error	True C /nF	R_s /MΩ	$R_{pore} + 2R_s$ /GΩ	$G = 1/(R_{pore} + 2R_s)$ /nS
0.001	708.40 ±7.00	95.41 ±0.26	7.49 ±0.02	0.89 ±64.64	8.63	4.77	708.49	1.41
0.010	85.52 ±0.35	13.38 ±0.05	5.69 ±0.02	0.91 ±60.92	5.27	6.69	85.53	11.69
0.100	15.84 ±0.04	1.74 ±0.01	3.89 ±0.02	0.93 ±59.02	3.19	0.87	15.84	63.12
0.250	5.80 ±0.02	1.44 ±0.01	3.93 ±0.03	0.90 ±68.95	2.60	0.72	5.79	172.52
0.500	3.26 ±0.01	0.99 ±0.01	4.00 ±0.02	0.89 ±50.69	2.42	0.49	3.26	306.94
0.750	2.42 ±0.01	0.88 ±0.01	4.18 ±0.02	0.89 ±52.24	2.46	0.44	2.42	412.39
1.000	2.56 ±0.01	0.75 ±0.01	4.09 ±0.03	0.89 ±0.01	2.46	0.38	2.56	391.12

Table 5.6: Summary of results obtained from the Randles with CPE model.

Solution resistivity

The solution resistivity R_s values were also calculated from the two Randles models and have been plotted as their reciprocal (or conductance, G_s) versus the KCl concentration in Figure 5.12. The model values derived for these components are provided in Table 5.7, it should be noted that the gradients of the linear fits agreed to within one σ.

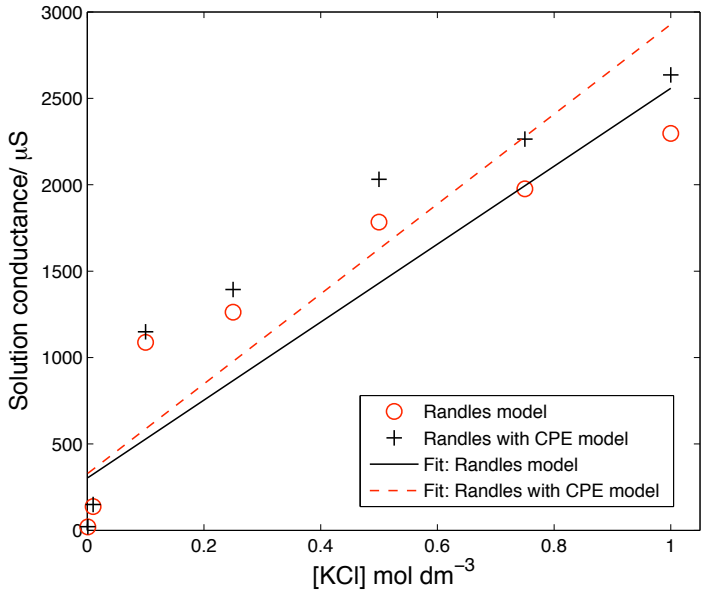


Figure 5.12: KCl solution conductance vs. KCl concentration for the nanopore system of pore diameter ~100 nm, with conductance values calculated from EIS parameters of two models. Randles (*black* $t-cross$); slope= 2601 ± 327 μS mol^{-1} dm^3 and Randles with CPE (*red circle*); slope= 2256 ± 302 μS mol^{-1} dm^3. *black solid line* corresponds to trend fitted to Randles model data and the *red dotted line* to Randles with CPE model data.

Membrane capacitance

The membrane capacitance at each concentration of KCl was also calculated from the two models and is plotted in Figure 5.14. Here it can be seen that the relationship between the capacitance and the salt concentration is more complex than the simple linear dependence displayed by the resistances (R_s and R_{pore}) in the circuit.

For example, the double layer part of the capacitance (C_{dl}) associated with the membrane may be divided into two capacitances in series, corresponding to the Helmholtz

[KCl]	Randles		Randles CPE	
/mol dm^{-3}	R_s/ MΩ	G_s/ μS	R_s / MΩ	G_s/ μS
0.001	50.250	19.90	47.705	20.96
0.010	7.280	137.36	6.690	149.48
0.100	0.920	1087.55	0.870	1149.43
0.250	0.792	1262.63	0.718	1393.73
0.500	0.561	1784.12	0.492	2031.28
0.750	0.506	1976.28	0.442	2264.24
1.000	0.435	2297.27	0.379	2635.39

Table 5.7: Solution resistivity values derived from the Randles and Randles with CPE models.

layers C_H and the diffuse layer C_D, Bard and Faulkner (2000).

$$1/C_{dl} = 1/C_H + 1/C_D \tag{5.4.1}$$

This corresponds to a tiered physical structure in the electrolyte, moving outwards from the surface of the Au membrane: ions absorbed on the surface of the Au in the inner Helmholtz layer; solvated ions in the outer Helmholtz layer and then a diffuse layer of ions. as illustrated in Figure 5.13, Bard and Faulkner (2000). Each of these has a differing dependency on the ion concentration. Simple models describe the diffuse layer as being proportional to $c^{1\backslash 2}$ and the Helmholtz layer is independent of c. As concentration increases, the diffuse layer thickness decreases and so its capacitance increases. The reciprocal $1/C_D$ will become smaller such that C_{dl} will tend to C_H at higher concentrations. The resultant plot may therefore be composed of two separate regimes with different concentration dependencies; a $c^{1/2}$ section at low concentrations and at high concentrations a section which is independent of concentration, representing the Helmholtz layer. However with only three data points in the low concentration range (defined here arbitrarily as 100 mM or less), we cannot accurately describe that relationship. For the four highest concentrations, the mean capacitance was 1.7 nF for the Randles model and 2.5 nF for the Randles CPE model.

In addition to this, the conversion of a CPE magnitude to an experimentally equivalent capacitance is not trivial; its errors have not been accounted for. We must view the system

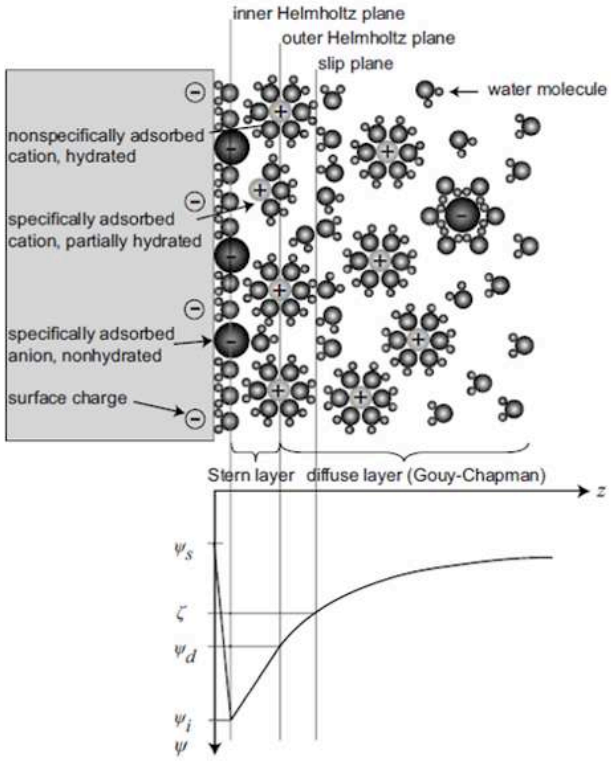


Figure 5.13: Schematic of the electrical double layer (EDL) representing the charge layers that accumulate at a net charged polarisable surface. Adapted from Bard and Faulkner (2000).

as having a distribution of time constants (Barsoukov and Macdonald, 2005) such that:

$$Z = R_{pore}/1 + (iwT)^n \tag{5.4.2}$$

Where n, the exponent of the CPE, is an expression of the deviation from the ideal capacitance and T is an average time constant. Provided that $R_{pore}Y_0 = T^n$ is true, the equation for Z may be used to describe this system. To find the experimentally equivalent capacitance we recognise that the time constant may be written as $R_{pore}C = T$. Substituting for T, we find the equation used to convert the CPE magnitude to be:

$$C = (R_{pore}C)^1/nR_{pore} \tag{5.4.3}$$

This may be evaluated against experimental results, however this is beyond the scope of this project and so is recommended for future work.

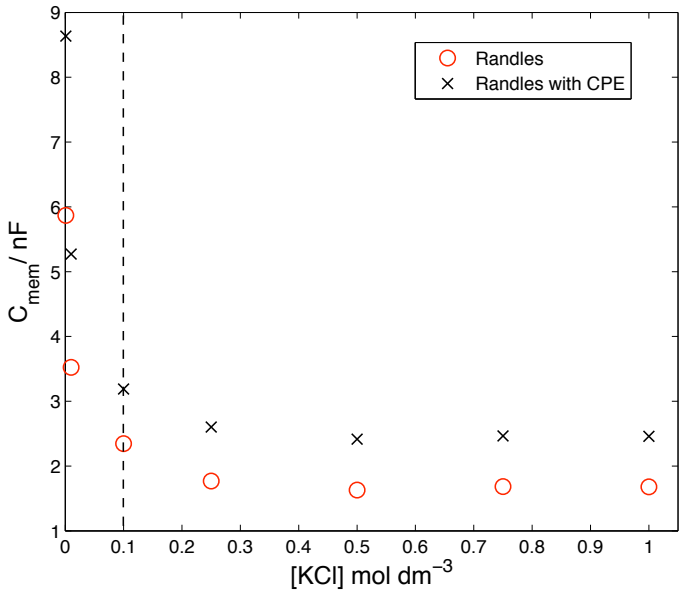


Figure 5.14: Membrane capacitance vs. varying KCl concentration for a 100 nm Au/Si_3N_4 nanopore. Two regimes of concentration dependency may be observed as represented by the dotted line.

5.4.4 Surface modification using thiol chemistry

The study presented in this section looked to modify the chemical properties of the metallic nanopore layer. The objective was to observe the effects of modifying the layers influence on the cell. Here, interest was placed primarily upon reducing the nanopore membranes capacitive effects. For this, thiol self-assembled monolayers (SAMs) of 6-mercapto-hexan-1-ol were formed across the surface by spontaneous adsorption of chemical molecules onto the Au nanopore; hence an ultra thin film was produced, as in Schwartz (2001). Thiols were used due to their strong gold-sulphur (Au-S) covalent bond formation. The method used to prepare these modified nanopores is described in Section 5.3.3.

Figure 5.15 shows the cyclic voltammograms of the 30 nm Au/Si_3N_4 nanopore modified with a SAM of 6-mercapto-hexan-1-ol (MCH) thin layer in 100 mM NaOH. Cyclic voltammograms were typically recorded by sweeping the potential between -500 mV to +500 mV at a scan rate of 50 mV s^{-1} at the Au nanopore surface before treatment and after chemical modification with thiol. The results demonstrate that the electrochemically active Au nanopore surface was fully passivated by the thiol layer which was covalently attached to it – their reductive desorption (release of thiolate is induced by the reduction

of surface Au(1) to Au(0) atoms) gives rise to distinctive peaks. A reductive desorption peak of Au-MCH SAMs is observed at -160 mV, while the bare Au electrode shows the typical features of reduction/oxidation of Au surface at peaks -200 mV; -440 mV and +220 mV, respectively. Once coated on the Au membrane, thiols are known to exhibit a blocking behaviour towards Faradaic processes at the electrode and this phenomenon can be observed in the case shown in Figure 5.15. Here, the CV trace for the thiolated membrane shows the suppression and disappearance of Au Faradaic reactions. Using the thiol modified CV trace, a charge of 3.78 x10^{-5} C is derived by integrating the area under the desorption peak. From this a surface coverage of Γ= 0.56 x10^{-10} mol cm^{-2} is calculated using Equation 5.3.3 with a geometric area, A= 0.07 cm^2.

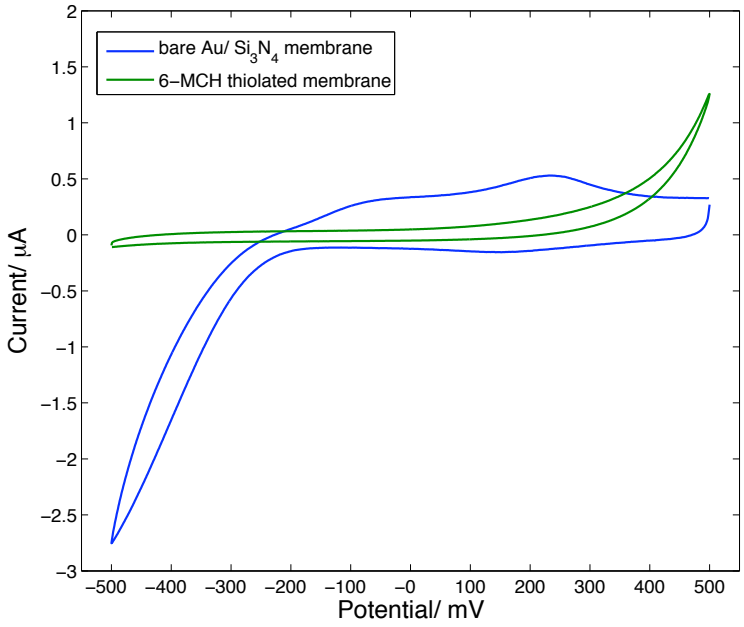


Figure 5.15: Cyclic voltammetry measurements of the Au nanopore surface and the modified thiolated nanopore carried out before (*blue curve*, bare Au membrane) and after modification (*green curve*, Au-MCH modified surface) relative to Ag/AgCl in 100 mM NaOH. Scan rate= 50 mV s^{-1}.

Once the modified Au membrane had been prepared it was assembled into the microfluidic flow cell and filled with 1 M KCl salt solution. Two Ag/AgCl electrodes immersed in the top and bottom reservoir were used to apply a steady state current across the pore. I-V measurements were conducted as described before (by sweeping the potential between

±500 mV). The results of these measurements are plotted in Figure 5.16. In this case, the Au membrane was left floating.

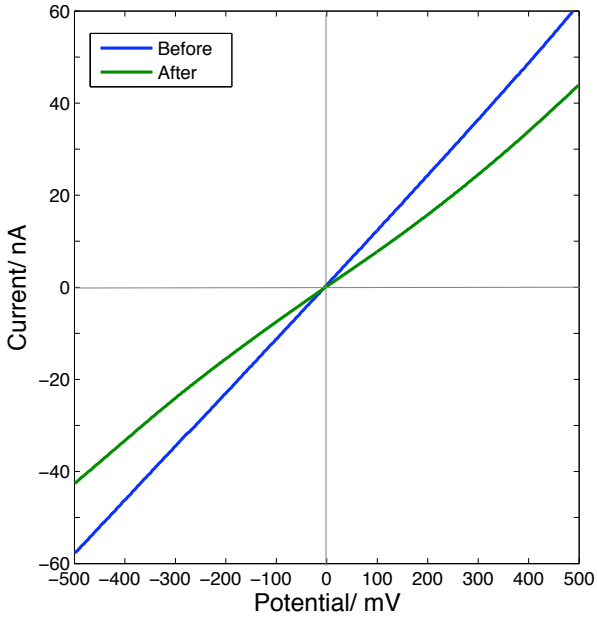


Figure 5.16: Figure: Typical I-V traces obtained through a 30 nm MCH-modified Au nanopore. Acquired via cyclic voltammetry in 1 M KCl; before (*blue curve*) and after (*green curve*) chemical modification.

From these experiments, it is evident that the presence of the thiol layer gives a distinctive curve with a rectification ratio of 1.10. In comparison to the bare Au trace (green curve), a 34% reduction in conductance is observed once the Au is coated with thiol. This decrease in conductance can be explained as a result of the charge transfer inhibition at the Au membrane-electrolyte interface, which occurs through a reduction in intimate contact with the charged surface. As mentioned, this inhibiting behaviour observed in the CV scans is characteristic of thiols, Love et al. (2005). Secondly, the chemically modified Au surface is expected to lead to weaker long range electrostatic interactions between electrolyte and charged surface (Barsoukov and Macdonald, 2005; Schwartz, 2001), thereby mobilising charges in the pore vicinity and potentially exercising a gating effect.

The effects of using a thiol layer at the Au nanopore surface presented in this section can potentially help contribute towards an ohmic, symmetric and controlled potential drop across the membranes cylindrical aperture, where the overall reduction in surface capacitance can be modelled by a classical two plate capacitor, Bard and Faulkner (2000).

5.5 Summary

In this chapter, the metallic nanopores fabricated and discussed previously were characterised for their behaviour under various conditions. Tests were conducted for modifications of four main variables; ionic solution concentration, bias potential, nanopore size and nanopore membrane properties. For the latter, the membrane properties were modified by applying thiols to the surface such that its capacitive effects were inhibited.

The first series of tests considered the effects of varying the ionic concentration for both metallic and Si_4N_4 nanopores. It was observed that an increase in ionic concentration lead to an increase in pore conductance, as expected. Moreover, it was observed that the CV plots of both the metallic and non-metallic nanopores exhibited a linear profile. This suggested that the lack of any rectifying effects, further validating the observations that the applied metal surfaces were evenly distributed within the pore.

The next section considered the effects of varying salt concentration. It was expected that a higher salt concentration would increase the ionic current due to the increase in charge carriers present in the solution. Indeed such a result was observed. Theoretical values of the pore conductance were also calculated from Equation 5.1.2; however due to the neglect of the surface charge density, a large discrepancy between the model and experimental values was observed. Future work should look to consider methods of calculating or estimating the surface charge density so that this term may also be included in future comparisons.

In parallel to these investigations, a model circuit was proposed so that the electrochemical cells behaviour may be modelled by a theoretical circuit. The circuit consisted of two resistors in series (which represented the impedance effects of the ionic solution) and a resistor and capacitor in parallel between them (which represented the energy dissipating and storing effects of the nanopore). In order to calculate the resistive and capacitive values for these theoretical components, electrochemical impedance spectroscopy studies (EIS) were also applied to the cell. These studies consisted of applying an alternating current potential at various frequencies to gauge the cells response. It was found that the results of the model circuit, using the EIS-calculated component values, compared well with the experimental results of the cell.

In the final set of experiments, the surface properties of the nanopore membrane was modified by the addition of thiols. These served to produce an insulating layer on the surface of the membrane and so inhibit its capacitive effects. The results of this section

showed a clear influence of the thiols on the I-V trace suggesting and followed the expected behaviour. This test provided a preliminary investigation into the effects of surface modification for metallic nanopores. Indeed future work should look to applying a potential to the nanopore membrane so that the ionic current can be controlled locally around the pore.

Chapter 6

Detection of DNA using metallic nanopores

This chapter investigates the translocation and detection of λ-DNA molecules through Pt deposited and Si_3N_4 nanopores. In Section 6.1 an overview is presented of the underlying theory of DNA translocation through metallic nanopores. The primary focus of this section is to provide a brief outline of the fundamental theory associated with the drop in ionic current across nanopores that is induced by the translocation of DNA.

Section 6.2 then discusses the experimental set-up of the study presented in this chapter, a brief review of the various chemicals and DNA material employed has been provided as well as a description on the set-up of equipment used to conduct this study. Section 6.3 provides information regarding the data acquisition equipment employed and its set-up as well as the post-processing of the signal recorded during the experiments. Subsequently, Section 6.4 presents a discussion on the results achieved from the experiments. The findings of this study are then summarised in Section 6.5.

6.1 Background theory

Changes in the ionic current

As explained previously in Chapter 1 detection of DNA using a nanopore consists of an experimental set-up whereby a single nanopore provides the only passage between two compartments containing an aqueous electrolyte. By inducing a current across the nanopore, ions are transferred from one compartment to the other. Hence, observations of the current across the nanopore provide the ionic current from one compartment to the

other, as shown in Figure 6.1. By introducing DNA the ionic current passing through the nanopore will decrease as the molecule translocates through the pore. The translocation of each single molecule is observed as a single translocation 'event'.

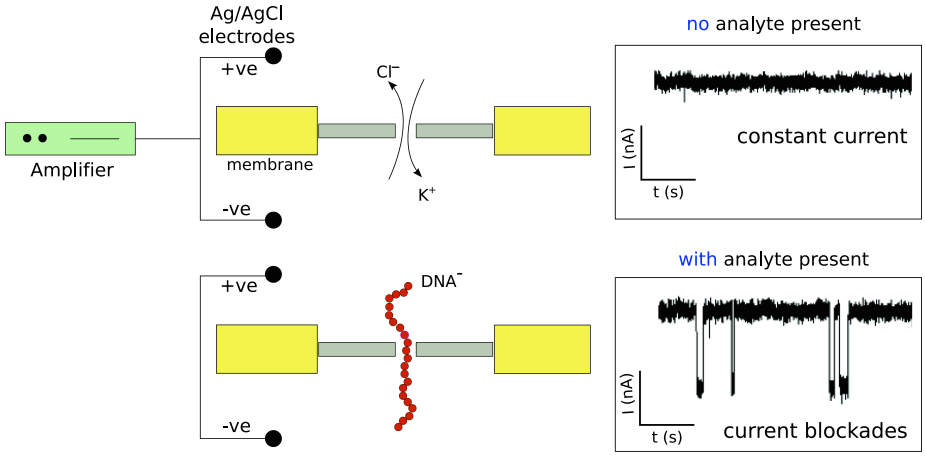


Figure 6.1: General set-up for translocation experiment. A charged polymer is electrophoretically driven through a nanometer-sized aperture, located between two reservoirs kept at a potential difference. *Top*: transmembrane potential causes a constant flow of ions through a single pore. *Bottom*: analytes that pass the pore cause temporary current blockades which are further detected and characterised.

Translocation of a charged molecule such as λ-DNA through a pore can affect the ionic current by (i) changing the effective ionic concentration in the nanopore due to charges carried by the molecule, and by (ii) physically restricting the nanopore cross sectional area (Chang et al., 2004, and Smeets et al., 2006). Since DNA is negatively charged, additional conducting counterions are introduced into the pore when the molecule enters a nanopore, this results in an increase in the ionic current I, (Smeets et al., 2006) given by:

$$I \quad = \quad \mu \, b \, \Delta n \, e \, V / L_{pore}^2, \tag{6.1.1}$$

where Δn is the number of charges introduced uniformly into a nanopore of length L_{pore} with a voltage bias V applied across it, e is the charge of an electron, μ is the ionic mobility, and b is the fraction of counterions that are mobile. This mechanism dominates at low ionic concentrations where the total number of ions in the bulk solution is small. At higher salt concentrations, physical blockage of the nanopore by the DNA molecule dominates, resulting in a current decrease during translocation, Figure 6.1.

To a first order approximation, the reduction in current induced by the physical blockage of the nanopore by the molecule is equivalent to the total ionic current that can be carried by the displaced electrolyte:

$$I_{block} = K\ A\ V_{bias}/L_{pore} \tag{6.1.2}$$

where K is the solution conductivity, V_{bias} the applied voltage, L_{pore} the effective pore length, and A the hydrodynamic cross section of the translocating molecule.

Since it is assumed that the reduction in current is linearly proportional to the hydrodynamic cross section of the translocating material, (Li et al., 2003; Muthukumar, 2007) the translocation events exhibiting only one blockade level can be interpreted as the translocation of a λ-DNA molecule through the pore in a linear, single-file manner. Events exhibiting two or more quantised blockade levels can be interpreted as λ-DNA that translocate through the pore with portions of the molecule folded in on itself, or where two or even three parallel lengths of the λ-DNA translocate through the pore simultaneously, Li et al. (2003).

Frequency of DNA translocations

Each translocation event whereby DNA molecules are transported from a solution on one side of the nanopore to the other side can be divided into three steps: (i) transport of DNA molecules from the solution to the opening of the nanopore, (ii) entrance of the molecule into the nanopore, and (iii) translocation of the molecule across the nanopore to the solution on the other side. The transport of DNA molecules to the nanopore can occur by diffusion, electrokinetic transport, or by convection. Therefore the frequency of arrival of the molecules at the entrance of the nanopore is linearly proportional to the DNA concentration and the electric field at the entrance, (Chen et al., 2004b) and can be given by:

$$f_{arrival} \propto c\ /timesV \tag{6.1.3}$$

where $f_{arrival}$ is the frequency of DNA arrival at the pore entrance, c is the DNA concentration, and V is the applied voltage bias. Entrance of the DNA molecule into the nanopore requires crossing an entropic free energy barrier since the DNA conformation is constrained inside the nanopore when the pore size is smaller than the DNA. Thus the

timescale for translocation depends exponentially on the voltage bias and the free energy barrier, (Henrickson et al., 2000):

$$1/\tau \propto exp(zeV - \Delta G^*/kT) \tag{6.1.4}$$

where z is the number of charges that interact with the electric field, V is the potential difference in the entrance region of the pore, and ΔG^* is the free energy barrier. Thus, the frequency of DNA translocating across the nanopore depends on the applied voltage bias and the mobility of DNA molecules through the nanopore, Chen et al. (2004b), given by $1/\tau_{trans} \propto V$.

6.2 Experimental

6.2.1 DNA material

λ-DNA isolated from bacteriophage lambda (cI857ind 1 Sam 7) was obtained from New England BioLabs. This duplex has a sequence of 48502 base pairs (bp), (Daniels, 1983). For translocation experiments, the DNA samples were dissolved in the buffer solution before use. The samples were manipulated under nuclease-free conditions and materials including water, tips, and tubes were autoclaved prior to use. In a typical experiment, DNA concentrations between 10 to 50 μg/ml were used and added to the cis chamber of the setup, which contained 2 ml of the buffer solution. The buffer solution was made up of 1 M KCl salt solution containing 10 mM Tris-HCl and 1 mM EDTA.

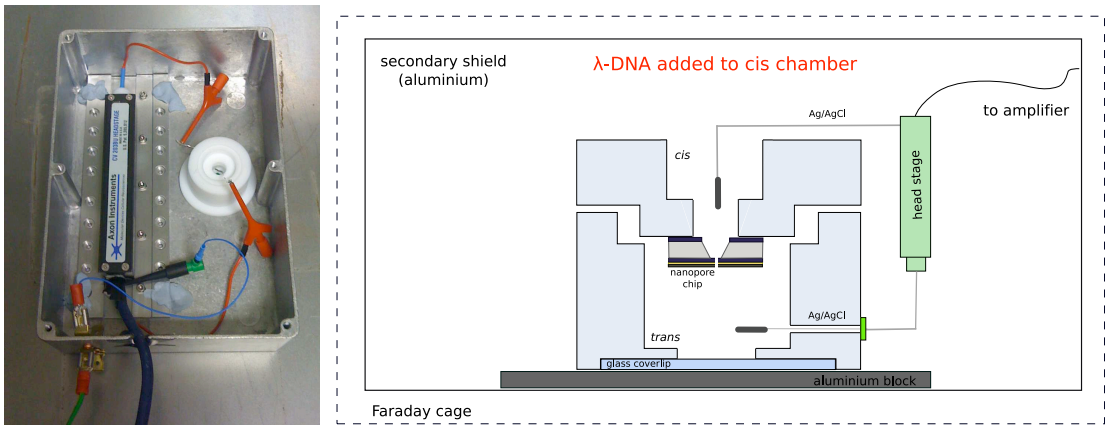
6.2.2 Fabrication of nanopores

A Si_3N_4 membrane was metallised with 10-nm Ti and 100-nm Au. A single pore of 50 nm diameter was then milled using a focused ion beam and further shrunk using the Pt electrodeposition-ICF technique described in Chapter 4. The technique combined electrodeposition with ionic current measurements through the pore to observe the pore shrinking in real time by monitoring the pore conductance simultaenously. This allowed the process to be stopped when the desired dimensions of the pore had been obtained. Pt deposited pores with diameters between 18 nm-22 nm were employed for the experiments involving λ-DNA. Following this a comparative study was carried out with bare Si_3N_4 pores with similar dimensions.

6.2.3 Experimental set-up

The apparatus used for the experiments described here is shown in Figure 6.2. Prior to DNA analysis measurements, the Pt deposited nanopore chips were solvent cleaned with acetone/isopropanol/deionised water (Millipore 18.5 MΩ cm), further details are provided in Section 2.5.1.

The treated pores were aligned and bonded between two chambers of a PTFE microfluidic cell using kwik cast epoxy. This formed a gigaohm seal, thereby reducing fluidic leakage and improving electrical isolation between the reservoirs. The buffer solution of 1 M KCl with 10 mM Tris-HCl, 1 mM EDTA at pH 8.0 was introduced into both reservoirs, where immediate wetting and ionic conduction through the pore was observed. This procedure typically lead to a stable low noise current signal, but additional oxygen plasma cleaning was occasionally necessary to achieve this.



(a) (b)

Figure 6.2: Experimental set up for DNA analysis. (a) image and (b) schematic of design. The microfluidic cell containing the nanopore is mounted into a Faraday cage. A patch-clamp current amplier is used for the ionic-current measurements at high bandwidth. The design employs two layers of electromagnetic (EM) shielding with a use of a double Faraday cage. The headstage from the patch clamp amplifier is mounted onto a custom made aluminium block and connected to the microfluidic cell.

Current was measured by placing newly chloridised Ag/AgCl electrodes in each reservoir with the nanopore forming the only electrical/fluidic connection between the two compartments of the microfluidic flow cell.

The entire setup was housed in a double Faraday cage on a vibration isolation table to

screen external acoustic and electric noise sources. In electrical recordings, sign conventions were used to distinguish between the top and bottom chamber of the microfluidic cell. The chambers were labelled as '*cis*', to which the DNA sample was added; and the Si_3N_4 window was exposed to the *cis* electrolyte. The *cis* chamber was at ground and the transmembrane potential was given as the potential on the '*trans*' side (i.e., the *trans* potential minus the *cis* potential; the latter was zero in the present case). A positive current was one in which positive charge (e.g. K^+) moved through the pore from the *trans* to the *cis* side, or negative charge (e.g. Cl^-) from the *cis* to the *trans* side. The open pore current (I_o) was recorded prior to the addition of λ-DNA for all measurements.

6.3 Data Acquisition and Analysis

6.3.1 Data Digitisation

The ionic current flowing through single solid state nanopores was measured using the commercial Axopatch 200B patch-clamp amplifier (Molecular Devices) and recorded to the hard disk of the computer, Figure 6.3. This instrument transformed the continuous analog current signal that arose into an analog voltage signal, which was fed to the 1440A 16-bit digitiser (Molecular Devices) that converted it into binary numbers with finite resolution (digitisation).

The current signal was measured using the Axopatch 200B low-noise current amplifier (Axon Instruments, USA) operated in resistive feedback mode with the feedback resistor set to $\beta = 1$, which provided both low noise and a large current passing ability of ±20 nA.

The digitiser was connected to a computer that converted and displayed the digitised current information. The dynamic input range of the digitizer is ±10 V, which divides the signal into 2^{16} (65536) values (bins), providing a resolution of 0.305 mV per bin ($20\ V/2^{16}$). If no output gain is applied by the amplifier, this corresponds to a dynamic range of ±10 nA and a resolution of 0.305 pA per bin. However, the output gain can be changed (by up to 500 x) to increase the resolution (decreased bin-width), at the expense of dynamic range. Typically, the output gain was set to 1 x. This corresponds to a dynamic range of ±1 nA and a resolution of 0.0305 pA per bin.

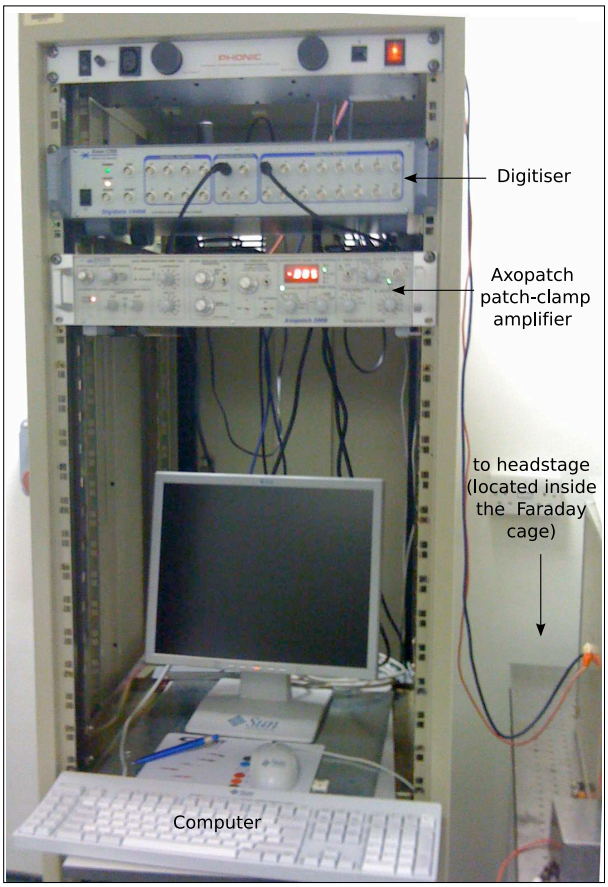


Figure 6.3: Image of the acquisition set-up: the ionic current is measured using the Axopatch 200B patch-clamp amplifier (Molecular Devices) and recorded to the hard disk of the computer. This instrument transforms the continuous analog current signal that arise into an analog voltage signal, which is fed to the 1440A 16-bit digitiser (Molecular Devices) that converts the data. The digitiser is connected to a computer which then converts and displays the digitised current information using Clampex software.

6.3.2 Filtering and sampling

High frequency electrical noise was removed from the signal collected by the amplifier, using an in-built low-pass, 8-pole Bessel filter which limited the bandwidth of the data by eliminating signals above the corner frequency (or cut-off frequency) of the filter. In order to keep errors of current levels to <3%, the applied filter cut-off was set so that it was five times the inverse of the mean event time, (Silberberg and Magleby, 1993).

The Nyquist Sampling Theorem states that the rate at which the filtered signal is sampled (in this case by a 1440A 16-bit digitiser from Molecular Devices) should be twice the cut-off frequency of the applied filter, (Axon-Guide). In practice however, it

was useful to oversample (i.e. sample at a rate that exceeded the Nyquist minimum) (Sakmann and Neher, 1995). Hence, a sampling rate of five times that of the cut-off frequency was used.

6.3.3 Acquisition protocols

The software used to collect and display the current signals was Clampex (version 10.1, Molecular Devices). Clampex was also used to control the 1440A digitiser to apply a potential through the amplifier. Although Clampex has five data acquisition modes, only the 'Gap Free' and 'Episodic Stimulation' modes were used.

In the Gap Free protocol, data were passively and continuously digitised, displayed and saved. This mode was used for all translocation experiments. The Episodic Stimulation protocol was used to output a voltage signal from the digitiser and applied to the nanopore system, while simultaneously acquiring the resulting current signal. This mode was used to apply voltage steps (e.g. when producing I-V curves) and voltage ramps (Dudko et al., 2007).

The DNA sample was added to the cis (top) compartment to a final concentration of typically 400-500 nM. In a typical experiment, initially, +100 mV was applied to the *trans* side for 20 s to drive the negatively charged, DNA molecules through into the pore. The capture of λ-DNA molecules by the nanopore was observed as a stepwise decrease in the open pore current level (I_o) to a lower, current level (I_b), Figure 6.4. The amplified signal (arising from the ionic current passing through the pore) was low-pass filtered at 20 kHz and sampled at 100 kHz (50μs).

Data were analysed and prepared for presentation with pClamp software (version 10.2, Molecular Devices). Single-channel searches were performed to obtain the current level for each individual DNA blockade event (I_b); firstly, pre-defined threshold levels were set for the open pore and blocked pore states, e.g. Level 1 was set to an estimation of the open pore current value and Level 2 was set to an estimation of the blocked pore current level, as shown in Figure 6.4. The event search software detected as the current changed from a Level 1 event (open pore event) to a Level 2 event (blocked pore event) and determined the arithmetic mean of each event from all of the current samples acquired, belonging to a given event.

The open channel current was termed I_o, once the negatively charged DNA was introduced into the *cis* chamber and began to translocate through the pore, sharp decreases

in the blockade current I_b were observed. The duration and amplitude of these I_b events were then used to characterise the translocation of λ-DNA.

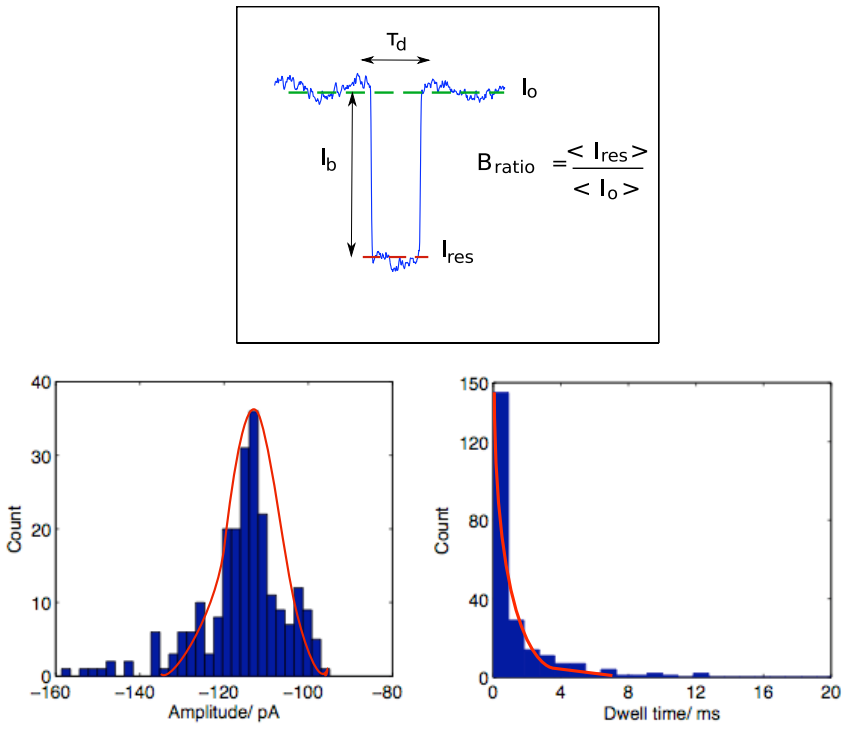


Figure 6.4: *Top*: Typical DNA blockade event analysed by Clampfit software. The current level changes from an open pore event, to a blocked pore event. The software assigns the events and determines the arithmetic mean for both the I_o (*green line*) and the I_b (*red line*) events. *Bottom left*: Histogram displaying amplitude currents I_b for λ-DNA in a typical experiment, the average blockade for the DNA molecule, for this experiment, is taken from the centre of the peak of the fitted Gaussian. *Bottom right*: Histogram of dwell time τ_d, the average dwell time is taken from the mean of the exponential fit from the plot. Events detected= 238.

The I_b values from repeated blockades, for a given DNA sequence had approximately a Gaussian distribution, as the majority of events were of a similar current. The mean I_b value for each DNA event was determined by performing a Gaussian fit to a histogram of all the I_b values from the repeated blockades. The current blockade for each DNA molecule was also described as the residual current (I_{res}), which was expressed as a fraction of the open pore current (I_o): $I_{res} = (I_b/I_o)$, see Figure 6.4.

The dwell time (τ_d) was plotted against the number of events, which gave an exponen-

tial decay. The mean τ_d value was taken from an exponential fit of the plot as shown in Figure 6.4 (Bottom right panel). Errors were calculated through the standard deviation (SD) of the analysed data. The data for each experiment under investigation comprised of at least two separate recordings to ensure its validity. Finally the τ_{on} data, i.e. the duration between events, was used to calculate the frequency of occurrence. τ_{on} was recorded in seconds therefore the inverse of this value ($1/\tau_{on}$) gave the frequency of events.

6.3.4 Noise characterisation

Current-time traces of the Pt deposited and bare Si_3N_4 pores were recorded at constant voltages with the patch-clamp amplier at a sampling frequency of 100 kHz and a low-pass 8-pole Bessel filter with a cutoff frequency of 20 kHz. The power spectral density $S^2(f)$ of 10 seconds of the current noise was obtained by performing Fast Fourier transforms (FFT) of the recorded current-time traces.

The magnitude of the spectral components, S_i, derived by the FFT was given by the sum of the squares of the real, $a_{i(real)}$, and imaginary, $a_{i(imaginary)}$ parts of the coefficients, where:

$$S_i = {a_{i(real)}}^2 + {a_{i(imaginary)}}^2 \tag{6.3.1}$$

Since this is the power averaged over N samples, where N is the transform (window) length and since only $N/2$ of the components are unique, the power at each sampling point (P_i) was scaled such that, for a given sampling frequency, f:

$$P_i = S_i \frac{2N}{f} \tag{6.3.2}$$

The power spectrum was further scaled by the window factor, ϖ, where for a given window function, f_w, the scale factor for a window of length N was calculated by:

$$\varpi = \sum_{n=1}^{N} \frac{{(f_w)}^2}{N} \tag{6.3.3}$$

and the power was expressed in units^2:

$$P_i = S_i \frac{2N}{f\varpi} \tag{6.3.4}$$

Finally the total root mean square (RMS) value was calculated by taking the square root of the integral of the power spectrum, such that:

$$RMS = \sqrt{\sum_{n=1}^{N} P_i \; f/N}, \tag{6.3.5}$$

where f/N was the value of the frequency bin width in Hz, (Axon-Guide).

6.4 Results and Discussion

6.4.1 DNA translocation through Pt deposited nanopores

To test whether the metallised nanopore structures can be used for the sensing of single molecules, DNA translocation experiments were conducted in both Pt deposited and bare Si_3N_4 nanopores. Individual pores of 100 nm diameter were then milled using a focused ion beam and further shrunk using the Pt electrodeposition-ICF technique described in Chapter 4.

The fabricated nanopore was mounted in a microfluidic cell in which it separated two chambers filled with a solution of 1 M KCl, 10 mM Tris-HCl, 1 mM EDTA, at pH 8.0. Ag/AgCl electrodes were immersed in both chambers. The metal layer was left floating during the measurements. λ-DNA was added to the *cis* chamber facing the small-cone opening and a voltage of +300 mV was applied to the *trans* side. This resulted in a constant ionic current of 5.3 $\pm$0.1 nA through the Pt nanopore.

After adding the λ-DNA to the negatively biased *cis* chamber and allowing time for diffusion, intermittent current blockades were observed in the I_o. Figure 6.5 shows part (4.5 s) of a current trace recorded for λ-DNA though an 18 nm Pt pore. Each event is the result of a single molecular interaction with the nanopore and is characterised by its time duration τ_d and its current blockage, I_b. Prior to the addition of DNA, no blockage events were observed during a 10 minute period; one example of the current recorded is plotted between 0-2 seconds in Figure 6.5. Subsequent to the addition of DNA, blockages were observed of the type plotted from 3-7 seconds in the figure. Hence these blockages are attributed to the interaction of individual DNA molecules with the nanopore. The duration of these blockades was on the order of milliseconds which consistently exhibited current reductions to $\sim$10% of the open pore value.

DNA translocation experiments typically ended when the baseline current level suffered an irreversible drop, likely corresponding to DNA sticking to the nanopore surface. Subsequent SEM imaging inspection revealed the presence of additional non-crystalline matter at the nanopore after drying.

Magnified views of the typical current blockades are illustrated in Figure 6.6. The translocation events observed for the passage of λ-DNA through Pt pores usually exhibited a rectangular pulse, similar to what has been observed for SiO_2, Si_3N_4 and Al_2O_3 nanopores in literature, (Storm et al., 2005), (Fologea et al., 2007), (Venkatesan et al.,

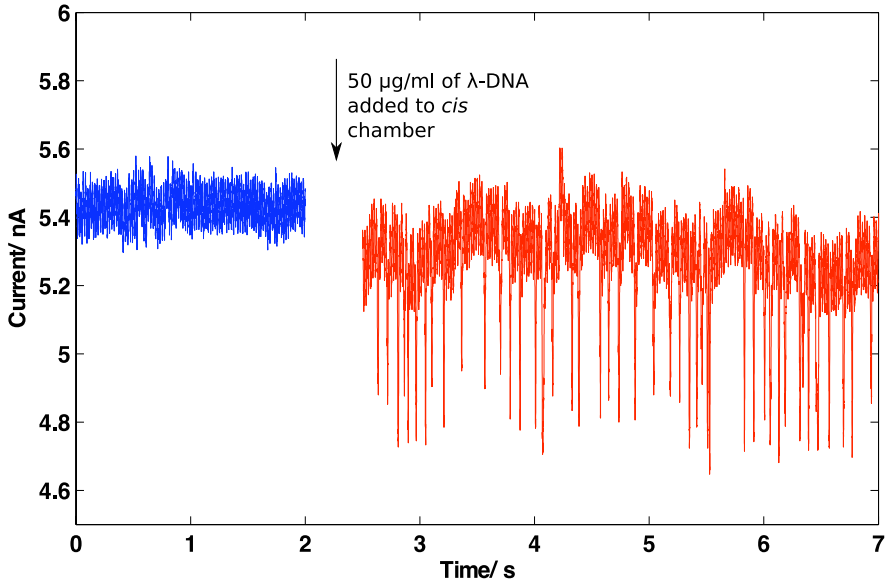


Figure 6.5: Ionic current trace for λ-DNA translocations through a 18 nm Pt deposited nanopore. Typical ionic current signal recorded before (*blue trace*) and after (*red trace*) the addition of λ-DNA test solution to the negatively biased *cis* reservoir, showing extensive current drop spikes.

2009). However ∼30% of all observed events did differ in shape and duration exhibiting a steep onset during which the current dropped within a few milliseconds followed by a slow recovery back to the I_o.

6.4.2 Mean dwell time and amplitude characteristics

A total of 454 events were analysed at a bias potential of +300 mV over a course of 40 seconds and are plotted in Figure 6.7. Figure 6.7 represents a scatter plot of the event amplitude (I_b) against the dwell time (τ_d). The distribution of events are broad and range from an I_b of 0.36 to 0.62 nA ±0.02 nA whilst τ_d ranges from 50 μs to 40 ms ±20μS. However the distribution is clearly not even across that range but instead shows a correlation between I_b and τ_d: where on average, shorter events block the pore less than long events. These events have been represented as histogram plots of I_b and τ_d, which are provided in Figures 6.7. The I_b histogram of Figure 6.7 (left panel) shows the gaussian distribution of event amplitudes with a mean value of 0.47 nA. The histogram of τ_d provided in 6.7 (middle panel) shows a broad exponential tail and has a mean τ_d of 4.4

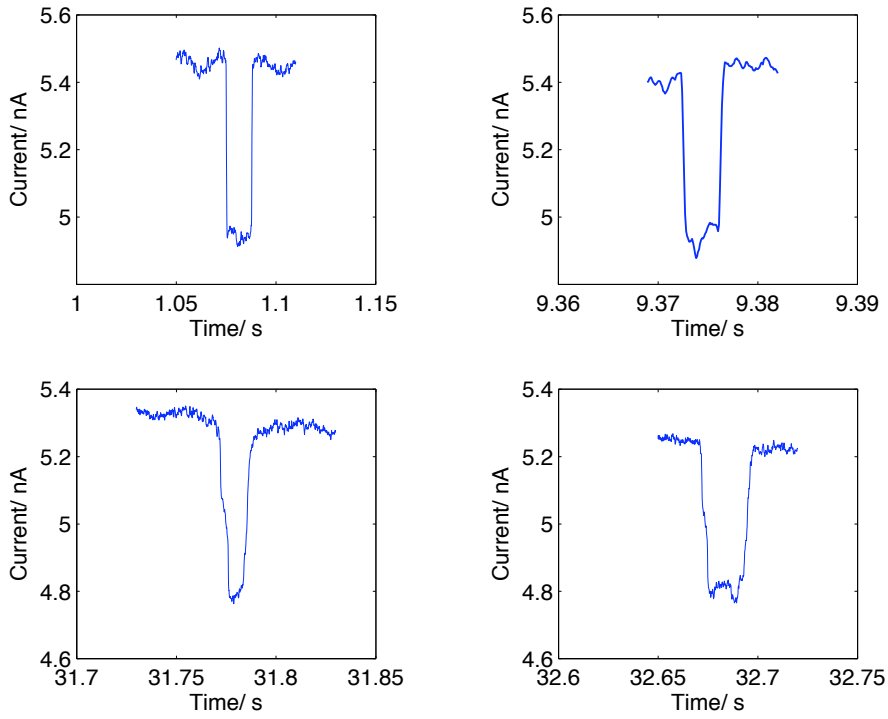


Figure 6.6: Typical current blockades (>70%) characteristic of the λ-DNA translocating through an 18 nm Pt pore. All recordings were taken from a nanopore biased at +300 mV, *trans* side positive.

±0.2 ms. An exponential curve is fitted to the plot and describes the population lifetime of translocation events. The timescale also exhibits strong voltage dependence, suggesting that these events are indeed due to polymer transport through the pore as opposed to rapid, diffusion-driven collisions without translocation.

By calculating the blockage ratio (B_{ratio}= I_{res}/I_o) it could be observed that on average 8% of the open pore current was blocked by the DNA (0.92 ± 0.02) during translocation. The blocked current fraction was ∼5 times larger than expected based on the relative areas of the DNA molecule (A_{DNA}) and the nanopore (A_{pore}); A_{DNA}/A_{pore} = (2.2 nm)^2/(18 nm)^2= 1.5%. The difference in the blocked current fraction could be explained by the relatively large size of the pore, which exhibited a substantial fraction (∼25%) of multiple level events corresponding to partially folded DNA entering the pore or several DNA molecules that traversed through the pore simultaneously.

Further to this, the values obtained from this analysis corresponded to a translocation velocity of 0.4 cm s^{-1}. In comparison to literature values reported by Branton et

al. of 2 cm s^{-1} for a Si_3N_4 and Al_2O_3 pore under comparable translocation conditions (Chen et al., 2004b and Venkatesan et al., 2010). The observed slower DNA translocation rate in these Pt deposited pores were also a good indication of the attractive interactions (ie. adsorption) between the translocating DNA strand and the nanopore surface, which were known to be dependent on the potential of the metal surface, explained in Deamer and Branton (2002), Wanunu et al. (2008). In addition to this, the presence of a larger effective membrane thickness was also reported in (Chen et al., 2004b) to reduce the electric field in the pore region. Whilst the effective membrane thickness in the Pt deposited nanopores is not known accurately, the results of Chen et al. (2004b) and the relative difference in translocation velocity observed in this work seem to suggest that the observed differences could indeed be rationalised in terms of a reduced field strength at the nanopore.

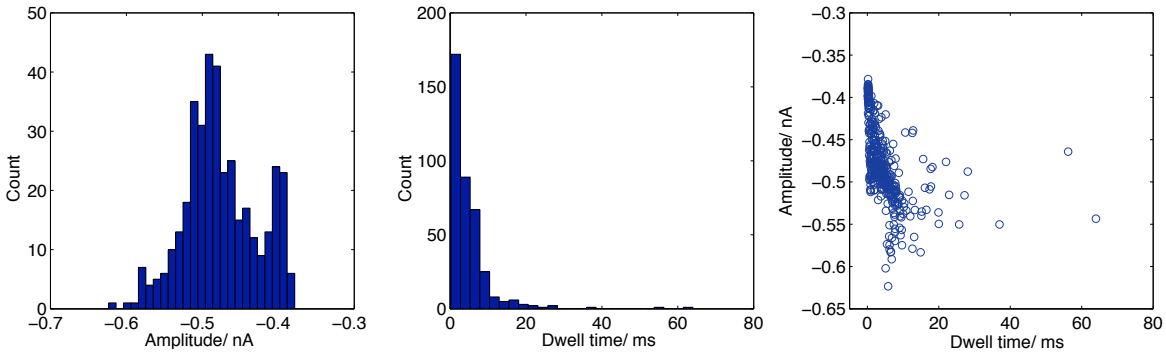


Figure 6.7: *Left*: Amplitude (I_b) and *Middle*: dwell time (τ_d) histograms for an 18 nm Pt deposited nanopore at the applied voltage of +300 mV. *Right*: Scatter plot of I_b versus τ_d.

Varying potential

DNA detection was characterised at varying bias potentials to study the frequency of translocation events and their velocities. The electrophoretic transport of λ-DNA through an 18 nm diameter Pt deposited nanopore was investigated at bias voltages of +100 mV; +200 mV; +300 mV and +500 mV. Example recordings of the observed current are presented in Figure 6.8.

The experimental results are summarised in Table 6.1 and include the open pore current, I_o, mean dwell times, τ_d, the average blockade current, I_b, the total number of

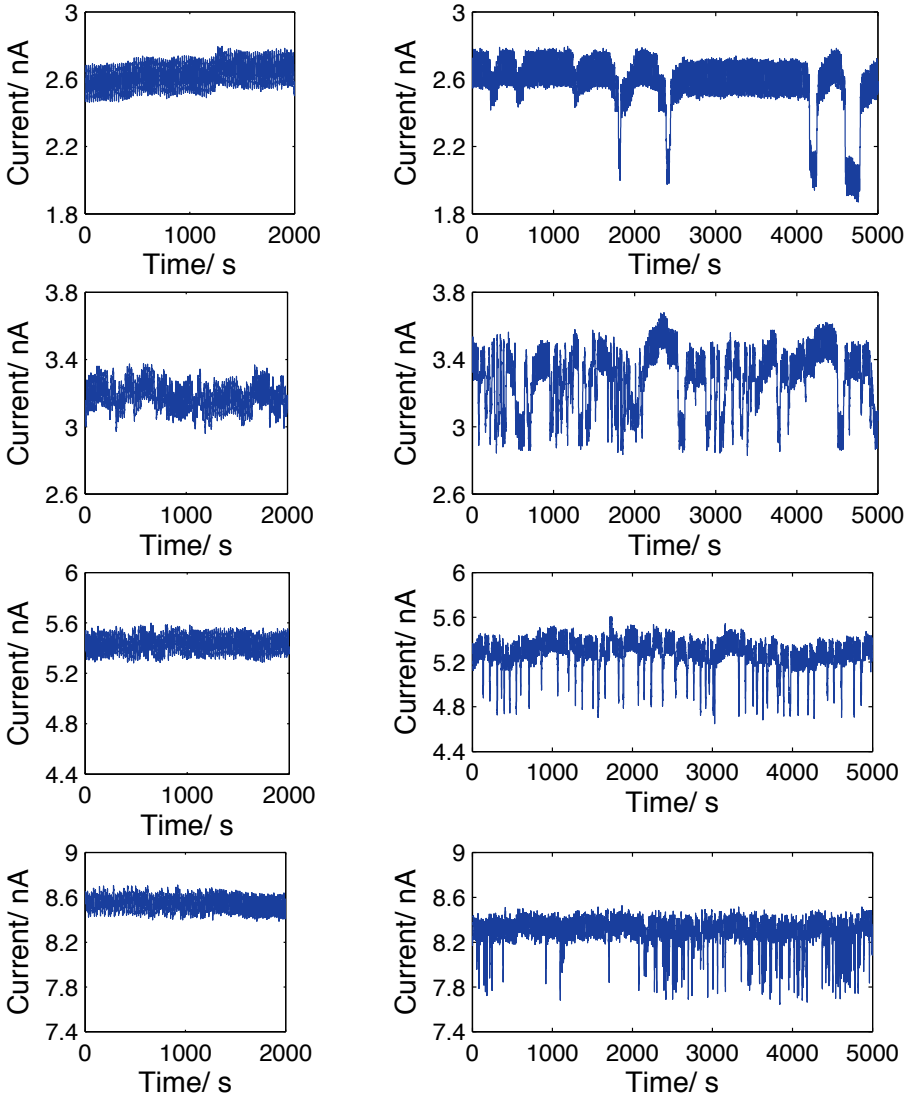


Figure 6.8: Current traces of λ-DNA translocation at each voltage. From *top* to *bottom* (i) +100 mV, (ii) +200 mV, (iii) +300 mV and (iv) +500 mV, including the blockade free open pore current I_o at each voltage prior to the introduction of λ-DNA.

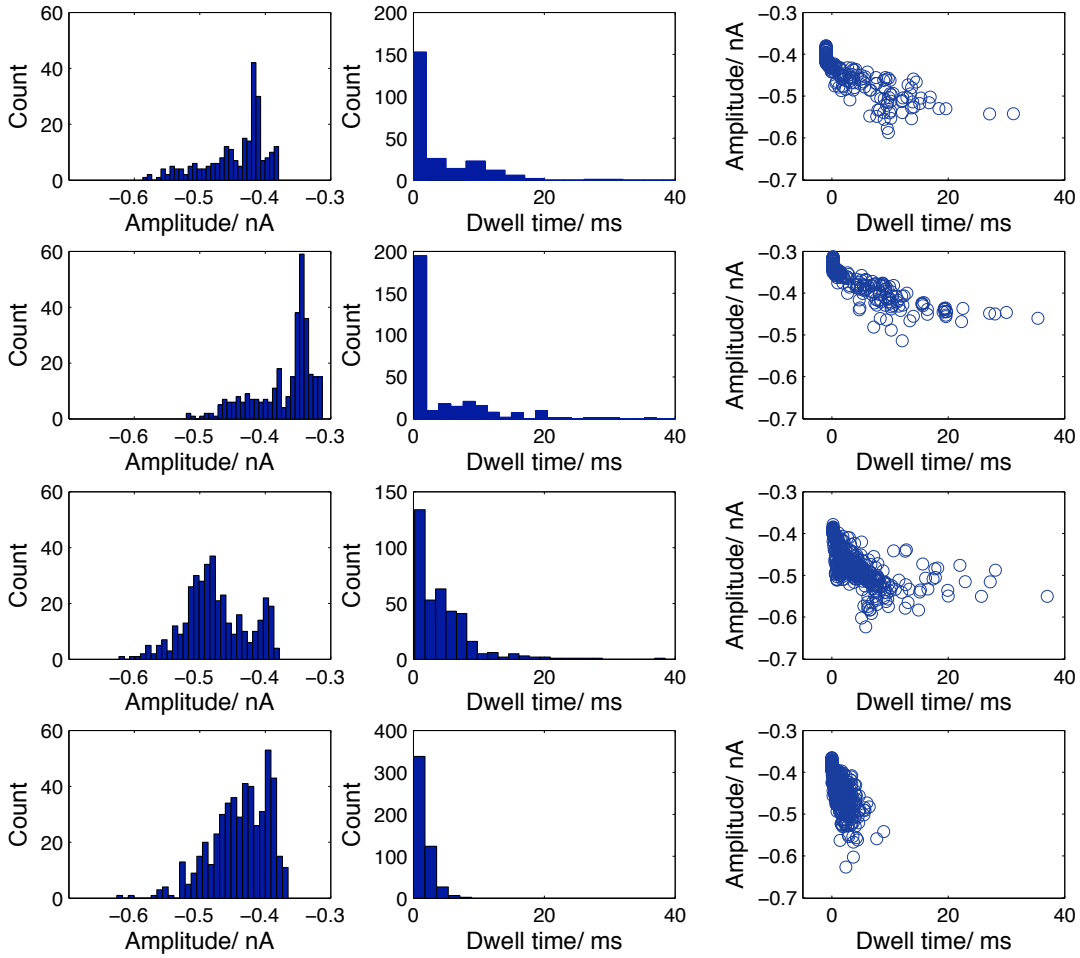


Figure 6.9: Amplitude and dwell time histograms for an 18 nm Pt pore at the applied voltages. From *top* to *bottom* (i) +100 mV,(ii) +200 mV, (iii) +300 mV and (iv) +500 mV. The scatter plots of I_b versus τ_d for each voltage are also displayed.

V_{bias}/ mV	100	200	300	500
I_o ($\pm$0.1 nA)	2.6	3.4	5.3	8.3
I_b ($\pm$0.1 nA)	0.41	0.34	0.48	0.42
τ_d (ms)	8.53 $\pm$ 0.38	3.84 $\pm$ 0.16	4.42 $\pm$ 0.20	1.39 $\pm$ 0.16
n (events)	242	324	454	497
F_{events} (s^{-1})	6.0	8.1	11.3	12.4

Table 6.1: Summary of results for the detection of λ-DNA through an 18 nm nanopore at voltages of +100 mV, +200 mV, +300 mV, and +500 mV. τ_d: is the time DNA resides in the pore. n: total number of events from recording). F_{events}: Frequency of events (s^{-1}) for a 40 s recording at each voltage.

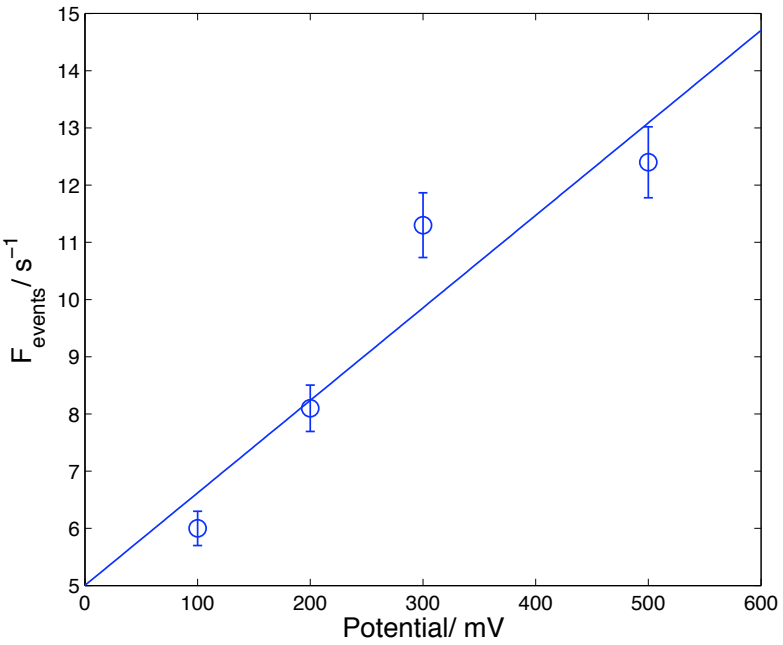


Figure 6.10: Frequency of translocation events (s^{-1}) at varying potentials through an 18 nm Pt pore, calculated using $1/\tau_{on}$. A linear fit is applied which shows a voltage dependence as the bias potential is increased.

events, n and their frequency at each potential. The results indicate that the average dwell time decreases with increasing voltage. As expected, an increase in the applied voltage resulted in an increase in the electrophoretic driving force experienced by the DNA molecule during transit, resulting in higher translocation velocities and shorter dwell times. This voltage-dependent behaviour has also been independently observed in biological α-hemolysin nanopores by Meller et al. (2001) and with Si_3N_4 by (Chen et al., 2004a) and can serve as a complementary method to gel electrophoresis to verify DNA transport through nanometer-sized channels.

A threshold voltage of +80 mV was observed in translocation experiments below which translocation current blockades were not observed, suggesting the presence of a significant activation/entropic barrier associated with λ-DNA transport through Pt deposited nanopores. In addition, the number of events n and the average frequency of events per second (F_{events}) increased linearly with increasing voltage, shown in Tabe 6.1 and plotted in 6.10.

6.4.3 DNA translocation through bare silicon nitride nanopores

The translocation of λ-DNA was also investigated in bare silicon nitride (Si_3N_4) nanopores without the presence of the metal layer. The experimental conditions were kept the same, including buffer, applied potential and DNA concentration. The recordings were acquired at a sampling rate of 100 kHz and filtered at 20 kHz. The single channel recordings for a 24 nm pore is shown in Figure 6.11, at a bias potential of +300 mV. The current trace displays the stable open pore current before the addition of DNA to the *cis* chamber and following introduction of DNA, the pore exhibited similar spikes in current corresponding to DNA translocation events.

A total of 234 events were analysed at a bias potential of +300 mV. Figure 6.12 (right panel) represents the scatter plot of I_b against τ_d for a 24 nm Si_3N_4 nanopore. The events detected using Si_3N_4 nanopores are overall shorter (with a maximum τ_d value of 10 ms) and blocked the pore in the pA range. The distribution of events are broad and range from an I_b of 92 to 160 pA whilst τ_d ranges from 50 μs to 10 ms. The dwell time histogram is presented in Figure 6.11 (middle planel) and shows a mono-exponential decay curve with a mean dwell time of 1.66 $\pm$0.2 ms. The amplitude (I_b) histogram shown in Figure 6.12 (left panel) gave a typical gaussian distribution with the mean value of 114 $\pm$20 pA. This value was comparable to typical experiments carried out with Si_3N_4 nanopores

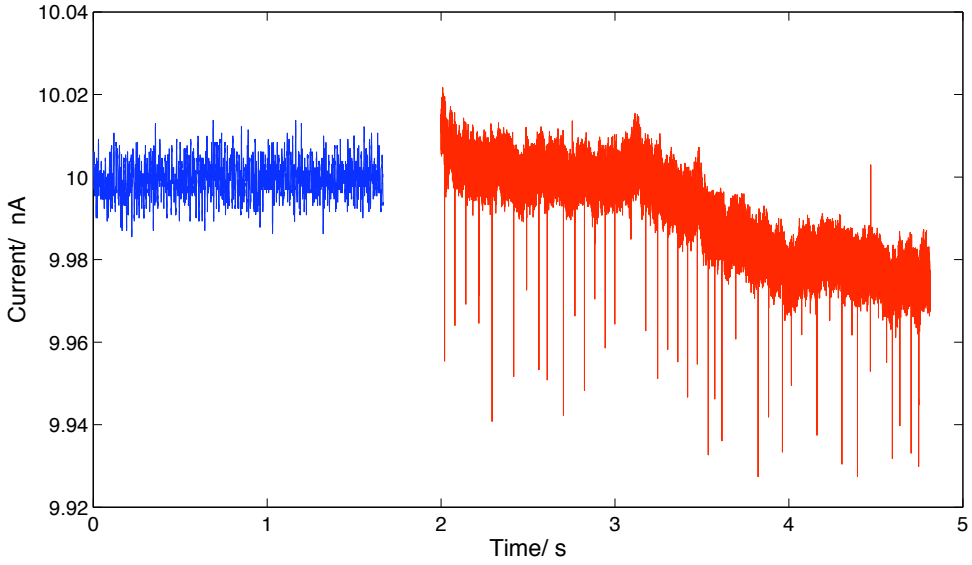


Figure 6.11: Ionic current trace for λ-DNA translocations through a 24 nm Si_3N_4 nanopore. Typical ionic current signal recorded before (*blue trace*) and after (*red trace*) the addition of λ-DNA test solution to the negatively biased *cis* reservoir, showing extensive current drop spikes.

of similar dimensions, Wanunu and Meller (2007). The blocked current fraction here was comparable to the expected value based on the relative areas of the DNA molecule (A_{DNA}) and the nanopore (A_{pore}). The expected value of A_{DNA}/A_{pore} (2.2 nm)^2/(24 nm)^2= 0.84%, compared with a measured blocked current fraction of 1.1%.

The strong attractive interactions observed in the Pt deposited nanopore experiments were not observed in Si_3N_4. This is most likely because the Si_3N_4 exhibited a net negatively charged surface at pH 7.5-8.0, resulting from the deprotonation of surface silanol groups, as described in Hoogerheide et al., 2009 and Wanunu and Meller, 2007. Hydrophobic interactions between DNA bases and the pore surface may also be prevalent in Pt deposited nanopore systems. Such interactions may be enhanced in Pt deposited pore systems as the material undergoes significant surface roughening during electrodeposition, this can be seen as irregular thickness variations across the pore region through SEM imaging, thereby increasing the surface area available for hydrophobic polymer-pore interactions.

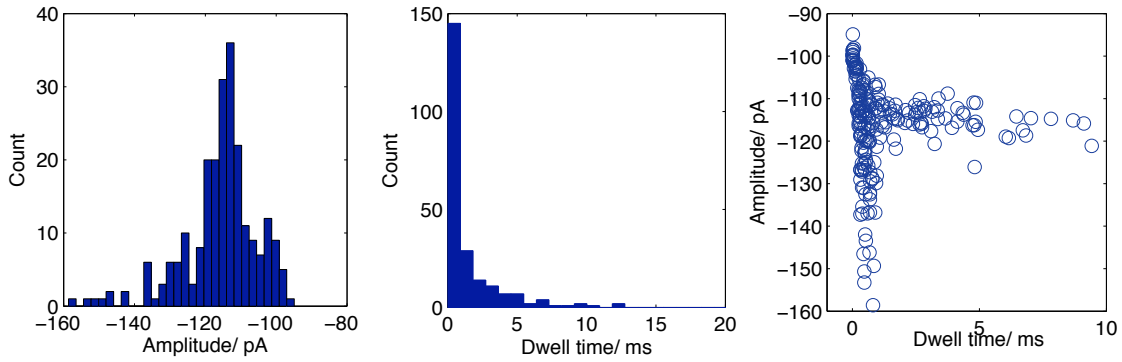


Figure 6.12: *Left*: Amplitude (I_b) and *Middle*: dwell time (τ_d) histograms for a 24 nm Si_3N_4 pore at the applied voltage of +300 mV. *Right*: scatter plots of I_b versus τ_d.

6.4.4 Multiple levels

Quantised levels were observed in many of the blockade events for both Si_3N_4 and Pt deposited nanopores. The multi-level events represented in Figure 6.13 are clearly distinguishable from that produced by λ-DNA translocating through the pore in a single file manner. These levels were attributed to either multiple DNA moving in a linear fashion or as a partially folded molecule. Less than 8% of the translocations were ambiguous or uninterpretable, and such events were excluded from the analysis.

The occurrence of multiple levels was further supported by the state of the DNA molecule at thermal equilibrium. Here the 16.5 μm length of λ-DNA is a flexible molecule that contains 500 persistence lengths and therefore forms a random coil with a radius of gyration of approximately 734 nm. The persistence length, which is a measure of the 'stiffness' of the worm-like coil, is around 33 nm in 1 M salt concentration, (Manning, 1981). Hence, to translocate through a 18 nm pore, this coiled λ-DNA must be at least partially linearised. However the DNA near a voltage biased pore is not at equilibrium and can experience an inhomogeneous electrical field (the closer to the pore, the stronger the electrical driving force) Chen et al. (2004b). By postulating that this inhomogeneous electrical field stretches the DNA towards the pore against the entropic forces that cause it to be randomly coiled at equilibrium, the observation of multiple levels could be explained.

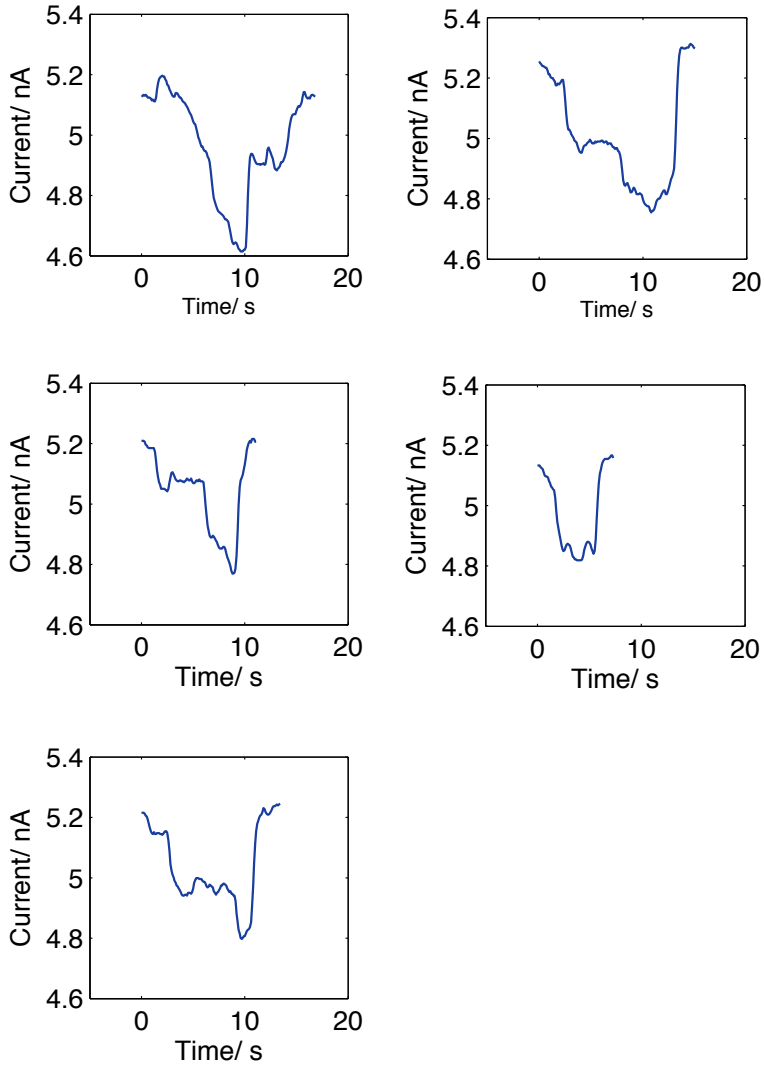


Figure 6.13: Examples of multiple level blockade events produced by λ-DNA molecules translocating through a 18 nm Pt deposited nanopore. All recordings were taken from a nanopore biased at +300 mV, *trans* side positive.

6.4.5 Electrical noise

A pore was deemed inadequate for use as a DNA detector if its total peak-to-peak noise was within approximately one half the expected blockade amplitude for a nanopore translocation. The number of successful DNA detection experiments were limited by the observed excess noise. In most cases the peak-to-peak noise level would completely obscure any DNA signals. Many samples, however, exhibited acceptable noise characteristics for λ-DNA detection.

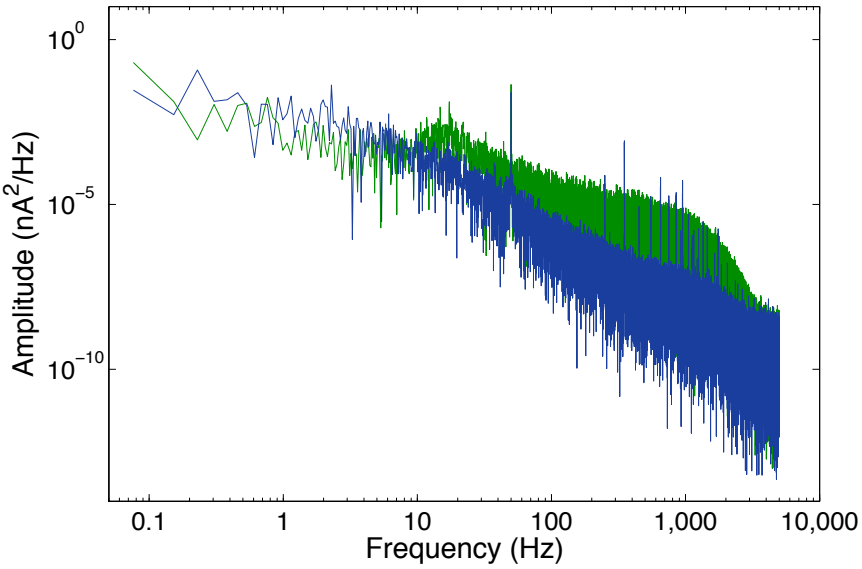


Figure 6.14: The noise power spectral density plots for a 24 nm Si_3N_4 (*green trace*) and a 22 nm Pt pore (*blue trace*) at V= +300 mV. Fourier decomposition of the signals reveals one order of magnitude difference in noise amplitude, and a $1/f$ power spectrum frequency dependence at low frequencies for both nanopores.

The noise power spectral density (PSD) $S^2(f)$ was calculated for each experiment using a fast Fourier transform (FFT) algorithm from a 10 second current-time trace, recorded with the patch-clamp amplifier at a sampling frequency of 100 kHz and 8-pole Bessel-ltered at 20 kHz. Figure 6.14 shows representative current traces of a Si_3N_4 pore (24 nm) and a Pt deposited nanopore (22 nm), with a length (thickness) of 350 nm and 240 nm for Si_3N_4.

The overall noise level is typically higher for Pt deposited nanopores than for Si_3N_4 nanopores tested in the same microfludic cell. The noise spectra mainly differed in the

low frequency $1/f$ noise, where the Pt pore exhibited noise levels that were roughly one order of magnitude higher than the noise of the Si_3N_4 pore.

The two different nanopores featured root-mean-square current variations with RMS values of 6.5 pA for Si_3N_4 and 15.2 pA for the Pt deposited nanopore at a bias voltage of +300 mV. Another source of noise was due to the nanopore capacitance, which converted the measurement amplifiers voltage noise into current noise, which typically dominated at the higher frequencies. As expected, Pt deposited nanopores had a higher capacitance than the Si_3N_4 nanopore devices. The capacitance was higher as the conductive platinum metal layer was capacitively coupled to the electrolyte solution. As a result, the 5 mm x 5 mm nanopore chip with the Pt deposited area exposed to electrolyte could form a capacitor across the Si_3N_4 layers to the underlying silicon and electrolyte.

6.5 Summary

In summary, λ-DNA molecules in 1 M KCl salt concentration were successfully detected in both Si_3N_4 and Pt deposited nanopores with diameters between 18-24 nm. The translocation durations and current amplitudes showed good agreement with simple electrokinetic models and previous work on detection of λ-DNA in nanopores with similar dimensions.

The effect of the applied voltage bias was investigated and found to influence the frequency of translocation events. Here the frequency of events exhibited a linear relationship as the voltage was increased, indicating that the DNA translocation depended strongly on the applied voltage bias and the mobility of DNA molecules through the nanopore. In addition to this it was observed that the existence of a critical driving voltage was necessary to induce translocation of DNA molecules across the nanopore, suggesting the presence of a significant activation/entropic barrier associated with λ-DNA transport. A correlation between I_b and τ_d was also observed for translocation events in both Pt and Si_3N_4 nanopores, where on average, shorter events blocked the pore less than long events. Further to this, multiple level events were seen across all nanopores measured. Which were attributed to multiple molecules passing through the pore and/or a range of conformations the DNA was able to form as it translocated through the pores.

Metallic nanopores are a promising new tool for the study of single-molecule biophysics. The results obtained from these initial experiments suggest that the pores can be employed as robust detectors that are sensitive to individual DNA molecules in their native aqueous environment. They are also versatile enough (through the adjustability of their pore

diameters) to address other interesting biological molecules such as proteins. However in order to understand the mechanism of the translocation process through these metallic nanopores, further experiments with various types and lengths of DNA, RNA and proteins are necessary to fully understand the effects that the metallic layer would contribute to the translocation mechanism.

Chapter 7

Conclusions and Future work

This chapter presents a summary of the work that has been discussed in this thesis. An overview of the motivations is presented below, followed by individual synopses of the contributions made by each chapter. Finally a short discussion is presented on recommendations for future work in order to further develop the techniques introduced here.

7.1 Conclusions

In Chapter 1, the motivation behind employing nanopores for single molecule detection was presented. It was argued that they could potentially provide significant improvements in time and cost over current methods for processes such as DNA sequencing. To illustrate the concept of using nanopores in this fashion, the example of the Coulter counter was provided, which was employed to detect microscale molecules. It was explained that a similar set-up, in which a nanopore was used as the only channel between two electrodes in solution, could be used to detect the translocation of single molecules through it. The background theory was explained such that the passing of a molecule through the pore would produce an appreciable blockage, thus reducing the ionic current between the electrodes. The current state of the art in nanopore technology was then discussed; a review of the strengths and weaknesses of biological nanopores revealed that although they provide greater sensitivity in detecting blockages, they are inherently unstable and so currently not employable within lab-on-a-chip based devices. A review of solid-state pores showed a contradictory characteristic; although inherently stable, they are significantly less sensitive. Examples were given of the use of Si_3N_4 and SiO_2 pores for DNA sequencing before considering the benefits of metallic nanopores. It was argued that a solid-state nanopore

coated with a metal layer would not only provide greater control in the fabrication process (thus achieving smaller nanopores), but that the metal layer could be employed as a third electrode to control the translocation of charged molecules locally – at the pore. This was succeeded by a presentation of the objectives of this work; a novel fabrication method has been developed and characterised such that metallic nanopores can be produced using the electrochemical deposition of Pt. The technique permitted monitoring of the ionic current through the pore during the deposition process and so the pore size could be controlled in real-time. An outline of the thesis was then presented.

Chapter 2 focused upon the presentation of general fabrication and examination techniques that are employed through out the thesis. Particular attention was paid to the creation of the nanopore membrane and the flow cell device, which accommodates the membrane, electrodes and ionic solution during both the fabrication and validation experiments. Sections 2.1 and 2.2 focused upon the fabrication method of the nanopore membrane, where 2.1 discussed the techniques employed for producing free-standing silicon nitride membrane and the technique of applying gold evaporation; subsection 2.2 presented the focused ion beam (FIB) technique used to mill $\sim$ 100 nm pores into the membrane with well defined dimensions. This was followed by the presentation of the main characterisation approaches employed throughout the work – scanning electron microscopy (SEM) and scanning tunnelling microscopy (STM) in Section 2.3 and electrochemical characterisation in Section 2.4. It was explained during the latter section, that such electrochemical studies required a flow cell device, the manufacture and assembly of which was presented in Section 2.5. The device was constructed primarily of PTFE (Teflon ®) and incorporated two chambers for the ionic solution (upper and lower) and a glass cover-slip, which allowed for observation with a microscope. Holes were also drilled into the PTFE to allow the insertion of electrodes during electrochemical studies and deposition. The final Sections, 2.6 and 2.7 discussed the tests and chemicals employed in this work; Section 2.6 elaborated upon the use of the microfluidic flow cell in the fabrication and characterisation studies performed, whilst 2.7 discussed the typical ionic solution employed throughout both the deposition and characterisation studies in this work.

The proposed fabrication process of depositing Pt onto nanopore membrane ($>$ 20 nm) was presented in Chapter 4. In order to characterise this deposition process, tests were conducted on flat gold electrodes without nanopores. This was presented in Chapter 3 and served as a precursor to applying the deposition process to nanopore membranes.

The main objectives of the characterisation investigations was to assess the necessary deposition parameters that produced the desired granularity and distribution of Pt on the Au/Si_3N_4 membrane. Platinum was deposited from a solution of 10 mM K_2PtCl_4 and 100 mM KCl at room temperature. The required growth conditions were such that uniform layers of Pt film would form – so that when applied to a > 20 nm nanopore, the Pt would uniformly and predictably reduce the pore diameter. The effects of parameters such as $PtCl_4^{2-}$ complex concentration; reduction potential and time duration were evaluated. In addition to this, different deposition sequences were also investigated whereby the deposition process would be divided into multiple steps, each of uniform duration. It was found that not only could a uniform, small-grained Pt layer be deposited onto the Au/Si_3N_4 membrane, but that a multi-step approach was most effective at producing such results. This was considered as a multi-step method separated the nucleation and growth stages of deposition, thus interrupting the formation of areas where large quantities of Pt could accumulate and forming a uniform film throughout. The Pt deposited surfaces obtained were smooth and homogenous without cracks or pores; STM measurements gave an average RMS value of $\sim$3.54 nm for a deposition duration of 400 s, indicating a low surface roughness. The grain sizes observed with SEM and STM were between 30-40 nm demonstrating the control achievable over deposits under the conditions investigated.

In Chapter 4, the deposition process discussed in Chapter 3 above was applied to nanopore membranes. However, not only did the work discussed here seek to validate the conclusions of the previous chapter, but it also presented the development of a novel feedback technique to control the pore size in real-time during the deposition process. It was argued in the preamble of this chapter that a feedback mechanism which allowed the pore size to be monitored during fabrication would be beneficial in guaranteeing consistency during their manufacture. Therefore, two versions of feedback mechanisms were assessed; optical and electrochemical. In the former, a microscope was used to observe the light intensity through the pores as Pt was deposited. It was thought that by measuring this intensity and apparent pore size, an accurate reading of the shrinkage could be taken during the deposition process. However, tests revealed that in order to allow the microscope to clearly focus on the membrane, a small lower chamber was necessary. Unfortunately the corresponding reduction in the volume of K_2PtCl_4 interfered with the quality of deposit, hence the pore sizes did not reduce. The latter method – ionic current feedback (ICF) – was then considered; tests were first conducted on nanopore arrays within a single mem-

brane to assess its consistency across multiple pores. It was found that by simultaneously monitoring the ionic current through the pore whilst depositing (via a bi-potentiostatic setup) a satisfactory assessment of the nanopore diameter could be achieved in real-time. This was confirmed by studies conducted on single nanopore membranes, which, as a result of their smaller effective channel area, served as a test of the accuracy of the ICF approach. It was found, based upon the ionic current measurements during deposition and comparisons to SEM images after deposition that the ICF method was effective as a tool to accurately monitor pore shrinkage. To further validate this result, experiments were conducted not only with a single-step deposition process, but also with a multi-step process.

In Chapter 5, the silicon nitride and metallic nanopores fabricated and discussed previously were characterised for their behaviour under various conditions. Tests were conducted for modifications of four main variables; ionic solution concentration, bias potential, nanopore size and nanopore membrane properties. For the latter, the membrane properties were modified by applying thiols to the surface such that its capacitive effects were inhibited. The first series of tests considered the effects of varying the ionic concentration for both metallic and Si_3N_4 nanopores. It was observed that an increase in ionic concentration lead to an increase in pore conductance with both the metallic and non-metallic nanopores exhibiting a linear profile, corresponding to ohmic behaviour. The lack of rectifying behaviour in the metallic pores suggested that metal surfaces were evenly distributed within the pore and compared well with the conventional nanopore platforms. Section 5.4.2 of the chapter further investigated the salt dependence of these nanopores by varying KCl concentration. The results obtained from these measurements showed that high salt concentration gave higher pore conductance values, due to the increase in charge carriers present in the solution. These results were then compared to theoretical values, however due to the neglect of the surface charge density, a large discrepancy between the model and experimental values was noted.

In parallel to these investigations, a model circuit was proposed so that the nanopore electrochemical system behaviour may be modelled by a theoretical circuit. The circuit consisted of two resistors in series (which represented the impedance effects of the ionic solution) and a resistor and capacitor in parallel between them (which represented the energy dissipating and storing effects of the nanopore). In order to calculate the resistive and capacitive values for these theoretical components, electrochemical impedance spec-

troscopy studies (EIS) were also applied to the system. These studies consisted of applying an alternating current potential at various frequencies to monitor the cells response. It was found that the results of the model circuit, using the EIS-calculated component values, compared well with the experimental results of the nanopore system. Following this, Section 5.4.4 of the chapter investigated the surface properties of the metallic nanopores. Preliminary experiments were performed whereby the nanopore surfaces were modified using thiols. These served to produce a well ordered layer on the surface of the membrane which inhibited the capacitive effects of Au. The results of this section showed a clear influence of the thiols on the ion transport across the modified nanopore, which gave a reduced conductance value at 1 M KCl. These test provided a preliminary investigation into the effects of surface modification for metallic nanopores.

The final chapter (Chapter 6) discussed the application of the solid-state metallic nanopores fabricated in the work presented thoughout the thesis to the detecting of DNA translocation. Tests were conducted in which 48.5 kbp λ-DNA molecules were inserted to the 1 M KCl ionic solution and a bias potential was applied across the pore, the resulting ionic current was then monitored. Comparisons of the studies conducted in this chapter were made against simple electrokinetic models and the results of similar published experiments. Primarily, tests were conducted on Pt-deposited pores 18-24 nm in diameter and their equivalent Si_3N_4 versions. The translocation durations and current amplitudes showed good agreement with simple electrokinetic models and previous work on detection of λ-DNA in nanopores with similar dimensions. Thus validating the performance of Pt-deposited pores for known conditions. This was succeeded by an investigation on the effects of varying the bias potential across the pore. It was found that in increase in voltage resulted in an increase in the frequency of translocation events. Moreover, this relationship was found to be linear, suggesting that the DNA translocation depended strongly on the applied voltage bias and the mobility of DNA molecules through the nanopore. It was also observed that the existence of a critical driving voltage was necessary to induce translocation of DNA molecules across the nanopore, suggesting that a significant activation/entropic barrier was present in regards to λ-DNA transport, which needed to be overcome. Assessment of the ionic current-time graph showed that a correlation also existed between the depth of each translocation event (current blockade) and its breadth (translocation duration) in both Pt and Si_3N_4 nanopores. It was found that on average, shorter events produced smaller blockades than long events. This was considered to be

the result of DNA translocating in a single-file manner, whereas for longer durations the DNA may have folded and blocked the pore entirely, thus slowing its translocation speed. Folding of the DNA molecule was also indicated by the observation of multiple current levels in events, which suggested that multiple molecules were passing through the pore and/or the DNA was forming one of a range of conformations as it translocated. DNA transport studies through Pt pores revealed reduction in translocation velocities of 0.4 cm s^{-1} in comparison to Si_3N_4 and SiO_2 architectures, accredited to strong electrostatic binding and adsorption between anionic DNA and metallic nanopore surface. Further to this, the electrical noise of metallic nanopores was found to be remarkably low. This feature along with the favourable surface characteristics of Pt nanopore sensors suggested that the platform may indeed prove to be a viable and functional system ideal for the detection and analysis of ssDNA, dsDNA, RNA secondary structures, and small proteins.

In conclusion, the work presented in this thesis showed that metallic nanopores are a promising new tool for the study of single-molecule biophysics. The results obtained from these initial experiments suggest that the metallic pores can be employed as robust detectors that are sensitive to individual DNA molecules in their native aqueous environment. With an ability to control their pore diameters during fabrication, the metallic pores are versatile enough to address other interesting biological molecules such as proteins. However in order to understand the mechanism of the translocation process through these metallic nanopores further experiments are required, which are detailed below.

7.2 Future work

In order to exploit the full potential of solid-state nanopores for single-biomolecule sensing, precise control of the pore size and geometry is required. Various strategies have therefore been developed, for example based on electron beam-induced shrinking or expansion of the pore or feedback-controlled FIB milling. The feedback mechanisms employed in those studies do not probe the ionic conductance of the pore, which is of key importance in a biosensing experiment in solution. This is a major strength of ICF-controlled electrodeposition, which rests on probing the ionic conductance of the pore directly. Moreover, it operates in real-time and under “in situ” conditions, i.e. in electrolytes that are very similar to those used in a biosensing experiment. Multiplexing the fabrication of many electrode devices in parallel appears to be straightforward and potentially cheaper than producing very small pores with FIB or electron beam drilling in a high-throughput fash-

ion.

ICF-controlled electrodeposition has the potential to produce even single-digit nanometre pores. In fact, the reproducible fabrication of pores with a given ionic conductance in the relevant range (low nS) is relatively straightforward. However, in order to establish a quantitative relation between the measured ion current/pore conductance and the true physical dimension of the pore, a number of challenges remain. For example, since the pore conductance depends on both pore diameter and length, the decrease in ion current during the electrodeposition process cannot solely be related to a change in only one of the two. In fact, two pores with the same ionic conductance may well have different three-dimensional shape and controlling the pore geometry is thus crucial. In addition, the roughness and/or crystallinity of the deposit is expected to affect the properties of the pore, particularly at small pore dimensions and low ionic strength, as well as the device-to-device reproducibility in single-molecule biosensing applications. Both factors depend on the growth conditions during the electrodeposition process. Refinement strategies are well-known for Pt and numerous other metals and can readily be implemented to produce smoother deposits.

Interestingly, the optimisation of the electrodeposition protocol has prospects of fabricating metal pores with varying aspect ratio A_{pore}/L_{pore} by controlling the rates of lateral and vertical growth during the deposition process. Devices with short effective channel length may perform better in fragment sizing applications, where the resolution appears to be limited by the membrane thickness.

For very small pores, it may become crucial to also consider the switching time of the device, i.e. the time constant of the membrane electrode. Ideally, the electrodeposition process is stopped instantaneously, when the ion current reaches the pre-defined value. In an experiment, however, the switching time is given by the electrode capacitance C (including any stray capacitance) and uncompensated resistance R in the electrochemical cell. Within this characteristic time RC, the deposition process continues and may well close the nanopore completely. However, both R and C can be minimised using well-known strategies, for example by decreasing the electroactive area of the membrane electrode or optimising the cell geometry.

Controlling the surface charge is another important parameter, the experiments carried out on the surface modification using thiols provide metallic pores to be compatible with various chemical-modification techniques to further enhance sensitivity and impart

selectivity to the nanopore. Such technologies may find use in drug screening and medical applications involving label-free, real-time kinetic analysis of biomolecular interactions at the single-molecule level. This nanoscale sensor may also serve as a useful tool in studying the mechanisms driving biological processes including DNA – protein interactions, enzyme activity, cell signaling and regulation using gated, selective ion channels. Hence, this technology can find broad application in bionanotechnology.

Bibliography

M. Akeson, D. Branton, J. Kasianowicz, E. Brandin, and D. Deamer. Microsecond time-scale discrimination among polycytidylic acid, polyadenylic acid, and polyuridylic acid as homopolymers or as segments within single rna molecules. *Biophysical Journal*, 77: 3227 – 3233, 1999.

B. Alberts. *Molecular Biology of the Cell*. Garland Publishing, New York, 1994.

W. J Albery. Electrode kinetics. *Philosophical Transactions of the Royal Society of London.*, 302:221–225, 1981.

Axon-Guide. *Molecular Devices*.

M. Ayub, A. Ivanov, J. Hong, P. Kuhn, E. Instuli, J. B. Edel, and T. Albrecht. Precise electrochemical fabrication of sub-20 nm solid-state nanopores for single-molecule biosensing. *Journal of Physics: Condensed Matter*, 22:454128, 2010.

A. J. Bard and L.R Faulkner. *Electrochemical Methods: Fundamentals and Applications*. John, 2000.

E. Barsoukov and J. R. Macdonald. *Impedance spectroscopy: theory, experiment, and applications*. Wiley-Interscience, 2005.

M. E. Baumgartner. The electrodeposition of platinum and platinum alloys. *Platinum Metals Review*, 32:4:188, 1988.

H. Bayley and P. S. Cremer. Stochastic sensors inspired by biology. *Nature*, 413:226–230, 2001.

D. Branton. The potential and challenges of nanopore sequencing. *Nature Biotechnology*, 26:1146–1153, 2008.

G. J. Brug, A.L.G. van den Eeden, M. Sluyters-Rehbach, and J.H. Sluyters. The analysis of electrode impedances complicated by the presence of a constant phase element. *Journal of Electroanalytical Chemistry and Interfacial Electrochemistry*, 176(1-2):275–295, 1984.

J. O. Bustamante, H. Oberleithner, J. A. Hanover, and A. Liepins. Patch clamp detection of transcription factor translocation along the nuclear pore complex channel. *Journal of Membrane Biology*, 146:253–261, 1995.

T. Z. Butler, M. Pavlenok, I. Derrington, M. Niederweis, and J. H. Gundlach. Single-molecule dna detection with an engineered mspa protein nanopore. *Proceedings of the National Academy of Sciences*, 105(52):20647–20652, 2008.

H. Chang, F. Kosari, G. Andreadakis, M. A. Alam, G. Vasmatzis, and R. Bashir. Dna mediated fluctuations in ionic current through silicon oxide nanopore channels. *Nano Letters*, 4(8):1551–1556, 2004.

G. A. T. Chansin, R. Mulero, J. Hong, M. J. Kim, A. J. deMello, and J. B. Edel. Single-molecule spectroscopy using nanoporous membranes. *Nano Letters*, 7(9):2901–2906, 2007.

P. Chen, Brandin E. Gu, J., Y. Kim, Q. Wang, and D. Branton. Probing single dna molecule transport using fabricated nanopores. *Nano Letters*, 4:2293–2298, 2004a.

P. Chen, T. Mitsui, D. B. Farmer, J. Golovchenko, R. G. Gordon, and D. Branton. Atomic layer deposition to fine tune the surface properties and diameters of fabricated nanopores. *Nano Letters*, 4(7):1333–1337, 2004b.

K. Chun, S. Maf, P. Ramrez, and P Stroeve. Protein transport through gold-coated, charged nanopores: Effects of applied voltage. *Chemical Physics Letters*, 418:561 – 564, 2006.

F. S. Collins. A vision for the future of genomics research. *Nature*, 422(6934):835–847, 2003.

S. Conlan, Y. Zhang, S. Cheley, and H. Bayley. Biochemical and biophysical characterisation of ompg: a monomeric porin. *Biochemistry*, 39:11845–11854, 2000.

P. V. Cornish and T. Ha. A survey of single molecule techniques in chemical biology. *ACS Chemical Biology*, 2:53–61, 2007.

W. H Coulter. Means for counting particles suspended in a fluid, 1953.

H. Craighead. Future lab-on-a-chip technologies for interrogating individual molecules. *Nature*, 442 (7191):387–393, 2006.

D.L. Daniels. *Appendix II: Complete Annotated Lambda Sequence, in Lambda II.* 1983.

D. W. Deamer and D. Branton. Characterization of nucleic acids by nanopore analysis. *Accounts of Chemical Research*, 35(10):817–825, 2002.

R. W. DeBlois and C.P. Bean. Counting and sizing of submicron particles by the resistive pulse technique. *Rev. Sci. Instrum.*, 41:909–915, 1970.

C. Dekker. Solid state nanopores. *Nature Nanotechnology*, 2:209–215, 2007.

A. A. Deniz, S. Mukhopadhyay, and E. A. Lemke. Single molecule biophysics: at the interface of biology, physics and chemistry. *Journal of The Royal Society Interface*, 5: 15–45, 2008.

B. Driselkelmann. Translocation of dna across bacterial membranes. *Microbiol. Review*, 58:293–316, 1994.

O. K. Dudko, J. Mathe, A. Szabo, A. Meller, and G. Hummer. Extracting kinetics from single-molecule force spectroscopy: Nanopore unzipping of dna hairpins. *Biophysical Journal*, 92:4188–4195, 2007.

El Dupont. *Teflon data sheet*. 2005.

J. W. Efcavitch and J. F. Thompson. Single molecule dna analysis. *Annual Review of Analytical Chemistry*, 3:109–128, 2010.

J. C. T. Eijkel and Albert van den Berg. Nanofluidics and the chemical potential applied to solvent and solute transport. *Chem. Soc. Rev.*, 39:957–973, 2010.

P. J. Flory. *Principles of Polymer Chemistry*. Cornell University Press, 1953.

D. Fologea, M. Gershow, B. Ledden, D. S. McNabb, A. Golovchenko, and J. L. Li. Detecting single stranded dna with a solid state nanopore. *Nano Letters*, 5(10):1905–1909, 2005a.

D. Fologea, J. Uplinger, B. Thomas, D. S. McNabb, and J. Li. Slowing dna translocation in a solid state nanopores. *Nano Letters*, 5(9):1734–1737, 2005b.

D. Fologea, E. Brandin, J. Uplinger, D. Branton, and J. Li. Dna conformation and base number simultaneously determined in a nanopores. *Electrophoresis*, 28 (18):3186–3192, 2007.

M. Gad-el Hak. *MEMS: Design and Fabrication*. CRC/Taylor & Francis, 2006.

Gamry. Application notes on electrochemistry.

J. I. Goldstein. *Scanning Electron Microscopy and X-Ray Microanalysis*. Springer, 2003.

P. J. Goodhew and J. Humphreys. *Electron microscopy and analysis*. CRC/Taylor & Francis, 2001.

A. E. Guttmacher and F.S. Collins. Genomic medicine - a primer. *New England Journal of Medicine*, 347 (19):1512–1520, 2002.

C. H. Hamann, A. Hamnett, and W. Vielstich. *Electrochemistry*. Wiley-VCH, 2007.

A. P. Han, G. Schurmann, G. Mondin, R. A. Bitterli, N. G. Hegelbach, N. F. de Rooij, and U. Staufer. Label-free detection of single protein molecules and protein protein interactions using synthetic nanopores. *Analytical Chemistry*, 80(12):4651–4658, 2008.

B. Hanss, E. Leal-Pinto, L. A. Bruggeman, T. D. Copeland, and P. E. Klotman. Identification and characterization of a cell membrane nucleic acid channels. *Proceedings of the National Academy of Sciences of the United States of America*, 95(4):1921–1926, 1998.

K. Healy. Nanopore based single molecule dna analysis. *Nanomedicine*, 2:459–481, 2007.

E. A. Heins, Z. S. Siwy, L. A. Baker, and C. R. Martin. Detecting single porphyrin molecules in a conically shaped synthetic nanopore. *Nano Letters*, 5(9):1824–1829, 2005.

J. B. Heng, C. Ho, T. Kim, R. Timp, A. Aksimentiev, Y. V. Grinkova, S. Sligar, K. Schulten, and G. Timp. Sizing dna using a nanometer diameter pores. *Biophysical Journal*, 87:2905–2911, 2004.

S. E. Henrickson, M. Misakian, B. Robertson, , and J. J. Kasianowicz. Driven dna transport into an asymmetric nanometer-scale pore. *Phys. Rev. Lett.*, 85:3057–3060, 2000.

HGP. The human genome project. URL `http://www.ornl.gov/`.

B. Hille. *Ion channels of excitable membranes*. Sinauer Associates, Sunderland, MA, 2001.

D. P. Hoogerheide, S. Garaj, and J. A. Golovchenko. Probing surface charge fluctuations with solid-state nanopores. *Physical Review Letters*, 102(25):256804, 2009.

S. Howorka and Z. Siwy. Nanopore analytics: sensing of single molecules. *Chem. Soc. Rev.*, 38:2360–2384, 2009a.

S. Howorka and Z. Siwy. Nanopores: Generation, engineering, and single molecule applications. In Peter Hinterdorfer and Antoine Oijen, editors, *Handbook of Single Molecule Biophysics*, pages 293–339. Springer New York, 2009b.

Illumina. URL `http://www.illumina.com`.

S. M. Iqbal, D. Akin, and R. Bashir. Solid-state nanopore channels with dna selectivity. *Nature Nanotechnology*, 2:243–248, 2007.

D. J. G. Ives and G. H. Janz. *Reference electrodes: theory and practice*. Academic Press, 1961.

G. Jerkiewicz, G. Vatankhah, J. Lessard, M. P. Soriaga, and Yeon-Su Park. Surface-oxide growth at platinum electrodes in aqueous h2so4: Reexamination of its mechanism through combined cyclic-voltammetry, electrochemical quartz-crystal nanobalance, and auger electron spectroscopy measurements. *Electrochimica Acta*, 49(9-10):1451–1459, 2004.

C. Joo, H. Balci, Y. Ishitsuka, C. Buranachai, and T. Ha. Advances in single molecule fluorescence methods for molecular biology. *Annual Review of Biochemistry*, 77:51–76, 2008.

E. Kalman, O. Sudre, I. Vlassiouk, and Z. Siwy. Control of ionic transport through gated single conical nanopores. *Analytical and Bioanalytical Chemistry*, 394:413–419, 2009.

Nasser Kanani. Processes for the deposition of metallic coatings. In *Electroplating*, pages 87 – 140. Elsevier, Oxford, 2004. ISBN 978-1-85-617451-0.

A. N. Kapanidis and T. Strick. Biology, one molecule at a time. *Trends in Biochemical Sciences*, 34 (5):234–243, 2009.

M. Karhanek, J. T. Kemp, N. Pourmand, R. W. Davis, and C. D. Webb. Single dna molecule detection using nanopipettes and nanoparticles. *Nano Letters*, 5(2):403–407, 2005.

J. Kasianowicz, E. Brandin, D. Branton, and D. Deamer. Characterization of individual polynucleotide molecules using a membrane channels. *Proceedings of the National Academy of Sciences of the United States of America*, 93(24):13770–13773, 1996.

M. J. Kim, M. Wanunu, D. C. Bell, and A. Meller. Rapid fabrication of uniformly sized nanopores and nanopore arrays for parallel dna analysis. *Advanced Materials*, 18 (23): 3149–3153, 2006.

P.T Kissinger and W.R Heineman. *Laboratory Techniques in Electroanalytical Chemistry*. Marcel Inc, 1996.

L. D. Landau and E. M. Lifshitz. *Mechanics, Third Edition*. Oxford: Butterworth-Heinemann, 1976.

R. Lavery. Structure and mechanics of single biomolecules: experiment and simulation. *Journal of Physics: Condensed Matter*, 14 (14):R383–R414, 2002.

J. Li, D. Stein, C. McMullan, D. Branton, M. J. Aziz, and J. A. Golovchenko. Ion beam sculpting at nanometre length scales. *Nature*, 412:166–169, 2001.

J. Li, M. Gershow, D. Stein, E. Brandin, and J. A. Golovchenko. Dna molecules and configurations in a solid state nanopore microscope. *Nature Materials*, 2:611–615, 2003.

I. Lokuge, X. Wang, and P. W. Bohn. Temperature controlled flow switching in nanocapillary array membranes mediated by poly(n isopropylacrylamide) polymer brushes grafted by atom transfer radical polymerization. *Langmuir*, 23:305, 2007.

J. C. Love, L. A. Estroff, J. K. Kriebel, R. G. Nuzzo, and G. M. Whitesides. Self-assembled monolayers of thiolates on metals as a form of nanotechnology. *Chemical Reviews*, 105 (4):1103–1170, 2005.

G. S. Manning. A procedure for extracting persistence lengths from light-scattering data on intermediate molecular weight dna. *Biopolymers*, 20(8):1751–1755, 1981.

C. R. Martin, M. Nishizawa, K. Jirage, and M. Kang. Investigations of the transport properties of gold nanotubule membranes. *Journal of Physcal Chemistry. B*, 105:1925, 2001.

A. Marziali and M. Akeson. New dna sequencing methods. *Annual Review of Biomedical Engineering*, 3:195–223, 2001.

J. Mathe, H. Visram, V. Viasnoff, Y. Rabin, and A. Meller. Nanopore unzipping of individual dna hairpin molecules. *Biophysical Journal*, 87(5):3205–3212, 2004. ISSN 0006-3495.

A. Meller. Dynamics of polynucleotide transport through nanometre-scale pores. *Journal of Physics: Condensed Matter*, 15(17):R581, 2003.

A. Meller, L. Nivon, E. Brandin, J. Golovchenko, and D. Branton. Rapid nanopore discrimination between single polynucleotide molecules. *Proc. Natl. Acad. Sci. USA*, 97 (3):10791084, 2000.

A. Meller, L. Nivon, and D. Branton. Voltage-driven dna translocations through a nanopores. *Phys. Rev. Lett.*, 86(15):3435–3438, 2001.

M. L. Metzker. Sequencing technologies-the next generation. *Nature Reviews Genetics*, 11:31–46, 2010.

W. E. Moerner. New directions in single molecule imaging and analysis. *Proc. Natl. Acad. Sci. USA.*, 4 (31):1259612602, 2007.

P.M. S. Monk. *Fundamentals of Electroanalytical Chemistry*. John Wiley and Sons, New York, 2001.

B. A Movchan. *Surface Engineering*. Maney Press, 2006.

M. Muthukumar. Mechanism of dna transport through pores. *Annual Review of Biophysics and Biomolecular Structure*, 36(1):435–450, 2007.

J. Nakane, M. Wiggin, and A. Marziali. A nanosensor for transmembrane capture and identification of single nucleic acid molecules. *Biophysical Journal*, 87 (1):615–621, 2004.

S. W. Nam, M. J. Rooks, K. B. Kim, and S. M. Rossnagel. Ionic field effect transistors with sub 10 nm multiple nanopores. *Nano Letters*, 9:2044–2048, 2009.

J. Newman and K.E Thomas-Ayea. *Electrochemical Systems*. John Wiley and Sons, New York, third edition, 2004.

M. Nishizawa, V. P. Menon, and C. R. Martin. Metal nanotubule membranes with electrochemically switchable ion-transport selectivity. *Science*, 268:700–702, 1995.

J. Orloff, L. Swanson, and M. W. Utlaut. *High Resolution Focused Ion Beams: FIB and Applications*. Springer, 2005.

M. Paunovic and M. Schlesinger. *Fundamentals of Electrochemical Deposition*. John Wiley and Sons, New York, 2006.

R.M. Penner. Brownian dynamics simulations of the growth of metal nanocrystal ensembles on electrode surfaces in solution: 2. the effect of deposition rate on particle size dispersion. *Journal of Physcal Chemistry. B*, 105:8672–8678, 2001.

A. Piruska, M. Gong, V. Sweedler, and P. W. Bohn. Nanofluidics in chemical analysis. *Chem. Soc. Rev.*, 39:1060–1072, 2010.

R. D. Purves. *Microelectrode methods for intracellular recording and ionophoresis*. Academic Press, 1981.

J. E Randles. Kinetics of rapid electrode reactions. *Discuss. Faraday Society*, 11, 1947.

C. R. K. Rao and D. C. Trivedi. Chemical and electrochemical depositions of platinum group metals and their applications. *Coordination Chemistry Reviews*, 249(5-6):613 – 631, 2005. ISSN 0010-8545.

E. Raub and K. Muller. *Fundamentals of Electrodeposition*. Elsevier, 1967.

L. Reimer. *Scanning Electron Microscopy: Physics of Image Formation and Microanalysis*. Springer, 2nd edition, 1998.

R. Rigler and H. Vogel. *Single Molecules and Nanotechnology*. Springer Series in Biophysics, Vol. 12, 2008.

T. Riley, C. Tomlinson, and A. M. James. *Principles of Electroanalytical Methods*. John Wiley and Sons, New York, 1987.

C A Ross. Electrodeposited multilayer thin films. *Annual Review of Materials Science*, 24(1):159–188, 1994.

I. Rubinstein. *Physical Electrochemistry: Principles, Methods, and Applications*. Marcel Dekker, New York, 1995.

E. Sabatani and I. Rubinstein. Organized self-assembling monolayers on electrodes. 2. monolayer-based ultramicroelectrodes for the study of very rapid electrode kinetics. *The Journal of Physical Chemistry*, 91(27):6663–6669, 1987.

B. Sakmann and B. Neher. *Single-channel recording*. Plenum Press, New York, 1995.

H. Salman, D. Zbaida, Y. Rabin, D. Chatenay, and M. Elbaum. Kinetics and mechanism of DNA uptake into the cell nucleus. *Proceedings of the National Academy of Sciences of the United States of America*, 98(13):7247–7252, 2001.

A. F. Sauer-Budge, J. A. Nyamwanda, D. K. Lubensky, and D. Branton. Unzipping kinetics of double-stranded dna in a nanopores. *Phys. Rev. Lett.*, 90(23):238101, Jun 2003.

B. Scharifker and G. Hills. Theoretical and experimental studies of multiple nucleation. *Electrochimica Acta*, 28(7):879 – 889, 1983. ISSN 0013-4686.

G. Schatz and B. Dobberstein. Common principles of protein translocation across membranes. *Science*, 271(5255):1519–1526, 1996.

A. Scheludko and M. Todorova. *Bull. Acad. Bulg. Sci. Phys.*, 3:61, 1952.

M. Schlesinger and M. Paunovic. *Modern electroplating*. John Wiley, New York, fourth edition, 2000.

W. Schmickler. Electronic effects in the electric double layer. *Chemical Reviews*, 96(8): 3177–3200, 1996.

F. Scholz. *Electroanalytical Methods: Guide to Experiments and Applications*. Springer, 2002.

D. K. Schwartz. Mechanisms and kinetics of self-assembled monolayer formation. *Annual Review of Physical Chemistry*, 52(1):107–137, 2001.

P. R. Selvin and T Ha. *Single-Molecule Techniques: A Laboratory Manual*. Cold Spring Harbor Laboratory Press, 2008.

T J Shaffner and R D Van Veld. 'charging' effects in the scanning electron microscope. *Journal of Physics E: Scientific Instruments*, 4(9):633, 1971.

D. F Shriver and P. W. Atkins. *Inorganic Chemistry*. Oxford University Press, Oxford, 1990.

Y. Shufang, L. Sang Bok, and C. R. Martin. Electrophoretic protein transport in gold nanotube membranes. *Analytical Chemistry*, 75:1239–1244, 2003.

S. D. Silberberg and K. L. Magleby. Preventing errors when estimating single channel properties from the analysis of current fluctuations. *Biophysical Journal*, 65:1570–1584, 1993.

Z. Siwy and A. Fulinski. A nanodevice for rectification and pumping ions. *American Journal of Physics*, 72:567–574, 2004a.

Z. Siwy and A. Fulinski. A nanodevice for rectification and pumping ions. *American Journal of Physics*, 72(5):567–574, 2004b.

Z. Siwy, P Apel, D. Baur, D. Dobrev, Y. Korchev, R. Neumann, R. Spohr, C. Trautmann, and K. Voss. Preparation of synthetic nanopores with transport properties analogous to biological channels. *Surface Science*, 532-535:1061–1066, 2003a.

Z. Siwy, P Apel, D. Dobrev, R. Neumann, R. Spohr, C. Trautmann, and K. Voss. Ion transport through asymmetric nanopores prepared by ion track etching. *Nuclear Instruments and Methods in Physics Research Section B: Beam Interactions with Materials and Atoms*, 208:143–148, 2003b.

Z. Siwy, L. Trofin, P. Kohli, L. A Baker, C. Trautmann, and C. R. Martin. Protein biosensors based on biofunctionalized conical gold nanotubes. *Journal of the American Chemical Society*, 127:5000–5001, 2005.

Z. S. Siwy and S. Howorka. Engineered voltage-responsive nanopores. *Chemical Society Reviews*, 39:1115–1132, 2010.

R. M. M. Smeets, U. F. Keyser, D. Krapf, M. Y Wu, N. H. Dekker, and C. Dekker. Salt dependence of ion transport and dna translocation through solid state nanopores. *Nano Letters*, 6(1):89–95, 2006.

R. M. M. Smeets, U. F. Keyser, N. H. Dekker, and C. Dekker. Noise in solid state nanopores. *Proceedings of the National Academy of Sciences*, 105:417–421, 2008.

L. Song, M. R. Hobaugh, C. Shustak, S. Cheley, H. Bayley, and J. E Gouaux. Structure of Staphylococcal Alpha-Hemolysin, a Heptameric Transmembrane Pore. *Science*, 274 (5294):1859–1865, 1996.

A. Sparreboom, W. van den Berg and J. C. T. Eijkel. Principles and applications of nanofluidic transport. *Nature Nanotechnology*, 4:713–720, 2009.

J. A. Sprague and C. M. Gilmore. Effects of atom energy on metal-on-metal film nucleation and growth. *Surface and Coatings Technology*, 65(1-3):71–76, 1994. ISSN 0257-8972.

A. J. Storm, J. H. Chen, X. S. Ling, H. W. Zandbergen, and C. Dekker. Fabrication of solid state nanopores with single nanometre precision. *Nature Materials*, 2:537–540, 2003.

A. J. Storm, J. H. Chen, H. W. Zandbergen, and C. Dekker. Translocation of double strand dna through a silicon oxide nanopore. *Phys. Rev. E*, 71(5):51903, May 2005.

I. Szabo, G. Bathori, F. Tombola, M. Brini, A. Coppola, and M. Zoratti. Dna translocation across planar bilayers containing bacillus subtilis ion channels. *Journal of Biological Chemistry*, 272(40):25275–25282, 1997.

T. J. Talisman, J. T. Novatt, A. S. McKenney, A. Zilman, R. Peters, M. P Rout, and B. T. Chait. Artificial nanopores that mimic the transport selectivity of the nuclear pore complex. *Nature*, 457:1023–1027, 2009.

M. Taniguchi, M. Tsutsui, K. Yokota, and T. Kawai. Fabrication of the gating nanopore device. *Applied Physics Letters*, 95(12):123701, 2009.

J. Tegenfeldt, C. Prinz, H. Cao, R. Huang, R. Austin, S. Chou, E. Cox, and J. Sturm. Micro- and nanofluidics for dna analysis. *Analytical and Bioanalytical Chemistry*, 378: 1678–1692, 2004.

M. Ueda, H. Dietz, A. Anders, H. Kneppe, A. Meixner, and W. Plieth. Double-pulse technique as an electrochemical tool for controlling the preparation of metallic nanoparticles. *Electrochimica Acta*, 48(4):377 – 386, 2002. ISSN 0013-4686.

J. A. Venables, G. D. T. Spiller, and M. Hanbucken. Nucleation and growth of thin films. *Reports on Progress in Physics*, 47(4):399, 1984.

B. M. Venkatesan, Dorvel B, S. Yemenicioglu, N. Watkins, I. Petrov, and Bashir R. Highly sensitive, mechanically stable nanopore sensors for dna analysis. *Advanced Materials*, 21:271–2776, 2009.

B. M. Venkatesan, A. B. Shah, J-M. Zuo, and R. Bashir. Dna sensing using nanocrystalline surface-enhanced al2o3 nanopore sensors. *Advanced Functional Materials*, 20:1266–1275, 2010.

J. C. Venter. The sequence of the human genome. *Science*, 291 (5507):1304, 2001.

F. C. Walsh. *Trans. Inst. Metal Finish.*, 69:111, 1991.

N. G. Walter, C. Y. Huang, A. J. Manzo, and M. A. Sobhy. Do it yourself guide: how to use the modern single molecule toolkit. *Nature Methods*, 5:475–489, 2008.

G. Wang, B. Zhang, J. R. Wayment, J. M. Harris, and H. S. White. Electrostatic-gated transport in chemically modified glass nanopore electrodes. *Journal of the American Chemical Society*, 128(23):7679–7686, 2006.

J. Wang. *Analytical Electrochemistry*. VCH Publishers Inc. New York, 1994.

M. Wanunu and A. Meller. Chemically modified solid-state nanopores. *Nano Letters*, 7 (6):1580–1585, 2007.

M. Wanunu, J. Sutin, B. McNally, A. Chow, and A. Meller. Dna translocation governed by interactions with solid-state nanopores. *Biophysical Journal*, 95(10):4716–4725, 2008. ISSN 0006-3495.

M. Wanunu, V. Soni, and A. Meller. Single molecule studies of nucleic acid interactions using nanopores. In Peter Hinterdorfer and Antoine Oijen, editors, *Handbook of Single Molecule Biophysics*, pages 265–291. Springer New York, 2009.

J. D. Watson and F. H. C. Crick. A structure for deoxyribose nucleic acid. *Nature*, 171: 737, 1953.

O. C. Wells. *Scanning electron microscopy*. McGraw Hill, 1974.

S. Yu, S-B Lee, and C. R. Martin. Electrophoretic protein transport in gold nanotube membranes. *Analytical Chemistry*, 75(6):1239–1244, 2003.

C. Zeiss. *Crossbeam manual*. 2007.

Y. Zhang, B. Zhang, and H. S White. Electrochemistry of nanopore electrodes in low ionic strength solutions. *Journal . Phys. Chem. B*, 110:1768–1774, 2006.

Appendicies

Journal Publications

The list of publications given below are presented in the following pages.

M. Ayub et al, *Precise electrochemical fabrication of sub-20 nm solid-state nanopores for single-molecule biosensing*, Journal of Physics: Condensed Matter, 2010, Volume 22, 454128.

M. Ayub et al, *Nanopore/electrode structures for single-molecule biosensing*, Electrochimica Acta, 2010, Volume 55, 8237-8243.

M. Ayub et al, *Nanopore structures for single molecule biosensing*, International Society of Electrochemistry Proceedings, 2010.

Conference Publications

M. Ayub, J. Hong, T. Albrecht, J. B. Edel, *"Fabrication of metallised solid-state nanopores using electrodeposition with ionic current feedback"*. Biophysical Society 54^{th} Annual Meeting, February 2010, San Francisco, California, USA.

M. Ayub, J. Hong, T. Albrecht, J. B. Edel, *"Electrochemical size control of solid-state nanopores with ionic current feedback"*. MicroTAS (μTAS) 2009, 13^{th} International Conference on Minituarised Systems for Chemistry and Life Sciences, November 2009, Jeju, South Korea.

M. Ayub, J. Hong, T. Albrecht, J. B. Edel, *"Electrically gated nanopores for single molecule separation"*. 237^{th} American Chemical Society (ACS) National Meeting & Exposition, Annual International Conference, March 2009, Salt Lake City, Utah, USA.

M. Ayub, T. Albrecht, J. B. Edel, *"Development of solid-state nanopore biosensors"*. HITS 2008: Bioanalysis, Microfluidics and Nanotechnology, Annual International Conference, April 2008, Imperial College London, London, UK.

J. Phys.: Condens. Matter **22** (2010) 454128 (8pp) doi:10.1088/0953-8984/22/45/454128

Precise electrochemical fabrication of sub-20 nm solid-state nanopores for single-molecule biosensing

Mariam Ayub[1,2], Aleksandar Ivanov[1,2], Jongin Hong[1,2], Phillip Kuhn[1,2,3], Emanuele Instuli[1,2], Joshua B Edel[1,2,4] and Tim Albrecht[1,4]

[1] Department of Chemistry, Imperial College London, Exhibition Road, London SW7 2AZ, UK
[2] Institute of Biomedical Engineering, Imperial College London, Exhibition Road, London SW7 2AZ, UK

E-mail: joshua.edel@imperial.ac.uk and t.albrecht@imperial.ac.uk

Received 19 May 2010, in final form 23 July 2010
Published 29 October 2010
Online at stacks.iop.org/JPhysCM/22/454128

Abstract

It has recently been shown that solid-state nanometer-scale pores ('nanopores') can be used as highly sensitive single-molecule sensors. For example, electrophoretic translocation of DNA, RNA and proteins through such nanopores has enabled both detection and structural analysis of these complex biomolecules. Control over the nanopore size is critical as the pore must be comparable in size to the analyte molecule in question. The most widely used fabrication methods are based on focused electron or ion beams and thus require (scanning) transmission electron microscopy and focused ion beam (FIB) instrumentation. Even though very small pores have been made using these approaches, several issues remain. These include the requirement of being restricted to rather thin, mechanically less stable membranes, particularly for pore diameters in the single-digit nanometer range, lack of control of the surface properties at and inside the nanopore, and finally, the fabrication cost. In the proof-of-concept study, we report on a novel and simple route for fabricating metal nanopores with apparent diameters below 20 nm using electrodeposition and real-time ionic current feedback in solution. This fabrication approach inserts considerable flexibility into the kinds of platforms that can be used and the nanopore membrane material. Starting from much larger pores, which are straightforward to make using FIB or other semiconductor fabrication methods, we electrodeposit Pt at the nanopore interface while monitoring its ionic conductance at the same time in a bi-potentiostatic setup. Due to the deposition of Pt, the nanopore decreases in size, resulting in a decrease of the pore conductance. Once a desired pore conductance has been reached, the electrodeposition process is stopped by switching the potential of the membrane electrode and the fabrication process is complete. Furthermore, we demonstrate that these pores can be used for single-biomolecule analysis, such as that of λ-DNA, which we use in a proof-of-concept study. Importantly, our approach is applicable to single nanopores as well as nanopore arrays, and can easily be extended to deposits of metal other than Pt.

S Online supplementary data available from stacks.iop.org/JPhysCM/22/454128/mmedia

(Some figures in this article are in colour only in the electronic version)

1. Introduction

Nanometer-sized pores ('nanopores') in recent years have emerged as versatile single-molecule sensors for the detection

[3] Present address: Department of Chemistry and Applied Biosciences, ETH Zurich, CH-8093 Zurich, Switzerland.
[4] Authors to whom any correspondence should be addressed.

 © 2010 IOP Publishing Ltd Printed in the UK & the USA

and analysis of biopolymers such as DNA, RNA and polypeptides (Dekker 2007, Wanunu and Meller 2007, Branton *et al* 2008). In a pioneering experiment performed in 1996, Kasianowicz *et al* used α-hemolysin, embedded in a lipid bilayer membrane, as a biological pore to measure the length of single-stranded DNA (ssDNA) molecules (Kasianowicz *et al* 1996). The authors could detect the ionic blockage current during the translocation of ssDNA as it was electrokinetically driven through the nanopore. This demonstration of 'stochastic' single-biomolecule sensing opened a new area of research, suggesting that nanopores could be used to sense and analyze nucleic acids with prospects for applications in ultra-fast DNA sequencing (Deamer and Akeson 2000).

Since then, the α-hemolysin pore has proven to be a powerful analysis tool. For example, a wealth of information on the molecules' properties, length, composition and interactions with other biomolecules can be extracted (Kasianowicz *et al* 1996, Deamer and Akeson 2000, Meller *et al* 2000, Howorka *et al* 2001, Deamer and Branton 2002, Meller and Branton 2002, Chen *et al* 2004a, Kim *et al* 2007b, Kasianowicz *et al* 2008). Being embedded in a rather fragile lipid bilayer membrane biological pores are perhaps less compatible with the requirements for a robust total-analysis system, for example with a view on point-of-care diagnostics outside the research laboratory. To overcome these limitations, recent efforts have been directed towards the development of solid-state nanopores using semiconductor fabrication techniques to replace or complement the biological pores (Li *et al* 2001, Storm *et al* 2003, Polk *et al* 2004, Wu *et al* 2005, Chang *et al* 2006, Harrell *et al* 2006, Kim *et al* 2006, Lo *et al* 2006). Nanopores fabricated from solid-state materials exhibit improved mechanical and chemical stability (Li *et al* 2001, Storm *et al* 2003, Kim *et al* 2006, Lo *et al* 2006), are compatible with a large pH and temperature range, and offer greater flexibility with regards to the pore dimensions (Li *et al* 2001, Polk *et al* 2004, Kim *et al* 2006, Dekker 2007, Wanunu and Meller 2007, Branton *et al* 2008). The latter point is an important feature, since the pore size has to roughly match or more precisely be somewhat larger than the size of the analyte for optimal sensor performance (Kasianowicz *et al* 1996, Dekker 2007, Wanunu and Meller 2007, Branton *et al* 2008). With greater flexibility in the pore size, nanopore-based sensing can thus be extended towards analyte molecules other than DNA, such as protein/DNA complexes, large proteins or nanoparticles.

Solid-state nanopores can further be functionalized by fabricating electrode structures close to or inside the nanopore using well established micro- and nanofabrication techniques (Siwy and Howorka 2010). Such pore/electrode geometries offers possibilities for external switching of the pore properties (e.g. by modulating the potential) for improved sieving or sensing performance (Nishizawa *et al* 1995, Ramirez *et al* 2003, Wang *et al* 2006, Gracheva *et al* 2007), controlling the speed of analyte translocation, and/or determining the composition of the translocating analyte (Gracheva *et al* 2006, Sigalov *et al* 2008). The latter two points are in fact related as high translocation speed and poor control of the translocation process represent major challenges, negatively affecting the performance of nanopore sensor devices (Wanunu *et al* 2008).

The most powerful techniques for fabricating solid-state pores employ focused electron (TEM) and ion beams (FIB) to drill holes with diameters as low as 1 nm in thin SiO_2, Si_3N_4 or other membranes, see below (Mussi *et al* 2010, Li *et al* 2001, Storm *et al* 2003, 2005, Wu *et al* 2005, Kim *et al* 2006, Lo *et al* 2006, Fischbein and Drndic 2007, Kim *et al* 2007a, Patterson *et al* 2008, Nagoshi *et al* 2009, Venkatesan *et al* 2009, Vlassiouk *et al* 2009). Ion track etching can be used to fabricate pores in polymeric films, even though achieved pore diameters are typically not quite as small and it is much more difficult to control the location of the pore on the membrane surface (Ai *et al* 2010, Apel *et al* 2001, Harrell *et al* 2006, Kovarik *et al* 2009). Furthermore, electron-beam lithography in combination with reactive ion etching (Petrossian *et al* 2007), stimulated chemical vapor deposition (Schenkel *et al* 2003, Nilsson *et al* 2006), atomic layer deposition (Chen *et al* 2004b), as well as electroless and electrodeposition from solution (Nishizawa *et al* 1995, Chen *et al* 2004b, Polk *et al* 2004) have also been successfully used to fabricate small solid-state pores.

The chemical etching of membranes directly in solution is interesting in the present context, since the pore conductance can be monitored during the fabrication process by measuring the ion current between two reservoirs. As long as the membrane is intact, the two reservoirs are separate and the ion current is essentially zero. Once a pore has opened, the ion current increases and is proportional to the geometry of the pore, *vide infra*. The process is usually terminated by a chemical etch stop and can either be promoted or suppressed by the applied electric field, depending on its direction (Apel *et al* 2001). However, polymer membranes tend to have thicknesses on the order of micrometers and pore fabrication typically requires a heavy-ion source to produce the initial ion tracks in the polymer. Both factors may render this type of nanopore device less suitable for high-resolution translocation studies and mass production of devices. Park *et al* have recently reported on the fabrication of very small nanopores with different geometries in pre-etched silicon membranes, which also makes use of a combination of chemical etching and electric current feedback (Park *et al* 2007). The reproducibility of the final pore dimensions were shown to depend critically on the pre-etching step, the local crystal structure, the local concentration of the etchant, and may thus be difficult to control to low-nanometer levels. Finally, various approaches for fabricating ultra-small nanopores in glass with high precision using ion current feedback have been developed ('nanopipettes') (Shim *et al* 2007, White *et al* 2007, Zhang *et al* 2007, Ervin *et al* 2008), even though these devices are perhaps less suitable for mass production.

At present, TEM or FIB-based methods can be applied to plain dielectric as well as composite membranes (including metal layers) (Dimitrov *et al* 2010, Storm *et al* 2005, Wu *et al* 2005, Patterson *et al* 2008, Nagoshi *et al* 2009) for individual nanopores and arrays (Schiedt *et al* 2010). Moreover, depending on the beam parameters, the membrane material, thickness, and pore size can be increased and decreased under the influence of the beam (electron or ion beam sculpting) (Li *et al* 2001, Storm *et al* 2003). The process is controlled

either by visual feedback or, more elegantly, by detecting the electron/ion current on the backside of the membrane in real-time (Li *et al* 2001, Patterson *et al* 2008, Nagoshi *et al* 2009). The latter in particular gives a high degree of control, even though the feedback signal does not directly correspond to the ionic conductance of the pore in solution. While the precision of nanopores fabricated with TEM and FIB is unmatched, the process does put constraints on the membrane thickness (Storm *et al* 2003). Very small pores are usually only achieved with thin membranes with thicknesses on the order of 50 nm, even though some efforts have been made to overcome these constraints recently (Patterson *et al* 2007). Such thin membranes ultimately affect the mechanical stability of the device, reduce the flexibility of the design and ultimately limit their use as biomedical sensors outside the research laboratory. Finally, the drilling of nanopore directly into a metallic films is problematic and has, to the best of our knowledge, only been achieved with FIB (diameter 30 nm, film thickness 3 mm) (Nagoshi *et al* 2009).

In this paper we present a new method for the facile, inexpensive and reproducible fabrication of metallic solid-state nanopores with diameters below 20 nm based on electrodeposition in a bi-potentiostatic setup and with real-time feedback control. As one of the key features of this approach, the electrodeposition process can be controlled precisely by modulating the potential applied to the membrane electrode, which is being operated as a second independent working electrode. The final diameter of the pore is largely independent of constraints from the membrane thickness, and its geometry mainly determined by the diffusion field in or close to the pore. The approach can easily be extended to the deposition of layered or composite materials.

The fabricated metal pores are suitable for single-molecule biosensing applications, as we demonstrate by performing proof-of-concept translocation experiments with λ-DNA. The metallic pores shown here offer interesting prospects towards facile chemical modification of the nanopore surface, e.g. employing thiol-based self-assembled monolayers, and external (electric) switching of the nanopore properties to modulate their translocation characteristics. Finally, the fabrication method can be easily scaled up to nanopore arrays, which have recently been used for optical detection of DNA translocations and plasmonic applications (Soni *et al* 2010, Chansin *et al* 2007, Hong *et al* 2008).

2. Experimental methods

Free-standing (200 nm thick) Si_3N_4 membranes are fabricated using standard photolithography and KOH wet etching as described elsewhere (Chansin *et al* 2007, Kim *et al* 2007b). The membrane is then coated with a 10 nm thick titanium adhesion layer, followed by 100 nm of gold by thermal evaporation. The overall membrane thickness, including adhesion layer, thus amounts to 310 nm.

Nanopores with a relatively large diameter of 100 nm or more were milled through the Au/Si_3N_4 membrane using a focused ion beam (FIB, Carl Zeiss XB1540 Cross-Beam; ion acceleration voltage = 30 kV; milling current = 1 pA). This part of the fabrication process is routine and can be performed on membranes with a wide range of different thicknesses and membrane materials.

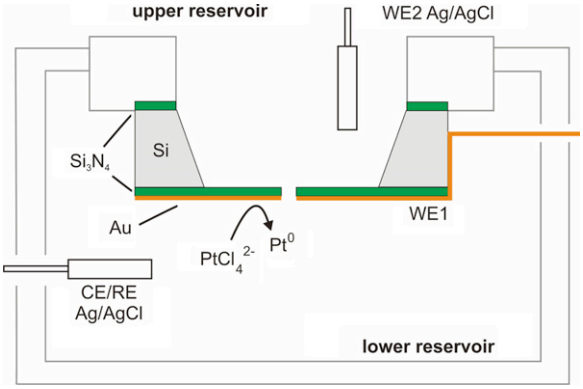


Figure 1. Schematic diagram of the four-electrode cell used for the ion current feedback (ICF) experiments: two Ag/AgCl electrodes constitute working electrode two (WE2) and the combined counter/reference electrode (RE/CE). The Au film on the membrane is connected as working electrode one (WE1). A bias voltage is applied between WE2 and CE/RE, driving an ion current through the pore. The potential of WE1 is set independently to control the electrodeposition process on the membrane. Electrical contact is made to membrane electrode using gold adhesive film. Note that the Si surface is coated with Kwik-Cast™ epoxy resin for electrical insulation (not shown).

Prior to mounting the nanopore device into a custom-made PTFE flow cell, figure 1, the membrane is subjected to oxygen plasma for 2 min and then flushed with ethanol in order to remove any organic contaminants and to enhance the hydrophilicity of the nanopore surface. Gold-plated adhesive film (250 μm thick, 3 M Farnell) is used to form the electrical contact to the membrane electrode. The PTFE flow cell consists of two compartments (top and bottom reservoirs). The nanopore membrane is affixed between the two compartments with Kwik-Cast™ epoxy resin (World Precision Instruments) rendering the nanopore the only electric connection between the top and bottom reservoirs. The epoxy resin is also used to cover and electrically isolate the sides of the silicon. The Ag/AgCl electrodes were prepared according to published procedures (Ives 1961) and were 400 μm thick, 30 mm long and located 5–10 mm away from the membrane. Under these conditions, the measured ion currents were found to be independent of the relative electrode–membrane distance, confirming that the majority of the potential drop across cell indeed occurs at the nanopore. A grounded Faraday cage was used to shield the cell from electrical interference. All chemicals used in this work were purchased from Sigma-Aldrich, unless noted otherwise.

Bi-potentiostatic electrodeposition experiments were performed with a CH Instruments 760c bi-potentiostat (CH Instruments, Austin/Texas, USA) under aerobic conditions. Employing a bi-potentiostat allows one to modulate the potential (or in fact the potential drop across the electrode/solution interface) of two working electrodes independently with respect to a common reference electrode. The membrane electrode is connected as working electrode one (WE1), the two Ag/AgCl

electrodes as WE2 and combined counter/reference electrode (CE/RE), respectively. Hence, the electrodeposition process on the membrane surface can be initiated (or stopped), while maintaining a constant bias voltage between WE1 and CE/RE to monitor the ion current.

For the electrodeposition experiments, both reservoirs are filled with a solution containing 10 mM K_2PtCl_4 and 100 mM KCl. A constant potential of $E(\mathrm{WE1}) = 0.35$ V versus CE/RE is applied to WE1, driving the electrodeposition of Pt^0 on the gold surface according to the reaction; $PtCl_4^{2-} + 2e^- \rightarrow Pt + 4Cl^-$. A bias voltage $V_{\mathrm{bias}} = 0.2$ V between WE2 and CE/RE is applied to monitor the pore current at the same time.

As a result of the electrodeposition process, the diameter of the nanopore decreases and its length increases (Ayub *et al* 2010). This leads to a decrease in the pore conductance, cf equation (1), and thus a decrease in the pore current (Smeets *et al* 2006). Once a desired value has been reached, the potential of WE1 can be switched to a higher potential, where the electrodeposition process no longer takes place, completing the fabrication process.

$$G = \frac{\pi}{4}\frac{d^2}{L}(\mu_{\mathrm{K}} + \mu_{\mathrm{Cl}})n_{\mathrm{KCl}}e + \pi\frac{d}{L}\sigma\mu_{\mathrm{K}} \qquad (1)$$

d is the pore diameter, μ_{K} and μ_{Cl} are the electrophoretic mobilities of K^+ and Cl^-, n_{KCl} is the number density of K^+ or Cl^- ions, σ is the surface charge density and e the elementary charge. The pore length L corresponds to the membrane thickness in our devices. Note that equation (1) only provides an estimate for the pore conductance and applies to cylindrical nanopores with a net negative surface charge density, high aspect ratios (L/d), and diameters larger than the Debye screening length (Siwy and Fulinski 2004).

DNA translocation experiments were performed at room temperature in a buffer solution containing 1 M KCl, 10 mM Tris-HCl and 1 mM EDTA at pH 8.0 in both the top and bottom reservoirs (using the same setup as shown in figure 1). Ag/AgCl electrodes are immersed on both sides of the pore to measure changes in ionic current at a 100 μs sampling rate and low pass filtered at 2 kHz using an Axopatch 200B amplifier (Molecular Devices, Sunnyvale/CA, USA). The cell is placed in a double Faraday cage enclosure to reduce electrical noise.

3. Results and discussion

Figure 2(A) illustrates the implementation of a typical real-time ICF experiment. We performed 12 subsequent deposition steps (20 s deposition time each), starting with a 100 nm nanopore drilled in an Au/Si_3N_4 membrane (thickness 310 nm). As described above, a potential of $E(\mathrm{WE1}) = 0.35$ V versus CE/RE is applied to the membrane electrode, in order to drive the deposition of Pt on the electrode. At the same time, a bias voltage of $V_{\mathrm{bias}} = 0.2$ V is applied between WE2 and CE/RE to produce an ion current, the magnitude of which depends on the pore conductance G. As expected, the ion current decreases during each step (while electrodeposition is taking place) and importantly begins roughly at the same current level in the subsequent step (the initial phase of increased currents is due to the formation of a diffusion layer). This confirms that the deposition process is stopped, when $E(\mathrm{WE1})$ is switched back to high potentials.

The ion current/time traces for deposition steps 1 and 12 are shown in figure 2(B). For large pore sizes (step 1), the ion current through the pore dominates the overall current in the system, as a monotonous decay is observed over the duration of the deposition step. On the other hand, in step 12 the pore dimensions and the pore current are much smaller resulting in capacitive charging dominating the overall current response between 0 and 2 s. Only after this initial phase does the current decrease in accordance with equation (1). We note that the exact shape of the ion current/time trace depends on details of the deposition process (mass transport versus kinetic control) and the three-dimensional geometry of the pore during the process. Modeling this process is outside the scope of the present work and will be treated elsewhere.

The pore conductance was determined from the steady-state ion current at the end of each run and plotted against the amount of Pt deposited. The latter was determined from integrating the deposition current $I(\mathrm{WE1})$, taking into account the stoichiometry of the deposition reaction. No corrections were made for capacitive charging and Pt deposition is assumed to be the only Faradaic process occurring. As shown in figure 2(C), the pore conductance can be approximated to follow an exponential decay (dashed red line) with an effective decay coefficient $1/t_1$ of 3.6×10^9 mol^{-1} ($y = A_1 \exp(-x/t_1) + y_0$; $A_1 = 2.53 \times 10^{-7}$ S; $y_0 = 8.27 \times 10^{-9}$ S; $t_1 = 2.74 \times 10^{-10}$ mol; $R^2 = 0.992$). This is only a phenomenological approach and more detailed modeling studies are required to establish the exact functional dependence, see above. The total amount of Pt deposited increases approximately linearly with each step, as is shown in figure 2(C) (inset). From the slope of the regression line, we obtain an average of 100 ± 5 pmol of Pt deposited/step.

Figure 2(D) shows a typical ion current/bias curve for a Pt metal pore in 0.1 M KCl solution (i.e. without Pt complex in solution; two subsequent cycles), prepared using ICF-controlled deposition. SEM imaging reveals an effective pore diameter of 18 ± 5 nm, cf inset in figure 2(D). The slope of the ion current/bias trace yields a pore conductance of 27 nS, which compares well with the corresponding value of 24 nS obtained from the ion current/time trace at constant bias (not shown). The response is close to ideal with almost no hysteresis and a rectification ratio close to 1.

Using the nominal dimensions of the nanopore in equation (1) ($L = 310$ nm, $d = 18$ nm; $\mu_{\mathrm{K}} = 7.616 \times 10^{-8}$ m^2 V^{-1} s^{-1}; $\mu_{\mathrm{Cl}} = 7.909 \times 10^{-8}$ m^2 V^{-1} s^{-1} (Smeets *et al* 2006); ignoring the surface charge contribution), we obtain a pore conductance of 1.3 nS. This is in poor agreement with experimental result, but some reservations are appropriate. Firstly, equation (1) is only valid for relatively large, cylindrical pores of high aspect ratio L/d. For the metallic pores shown, these assumptions do not hold and deviations from the theoretical value are expected. Secondly, since Pt is deposited locally on the Au, rather than along the whole pore channel, the effective pore length L is most likely quite different from the initial value of 310 nm (cf below). Depending on the deposition conditions (diffusion field during

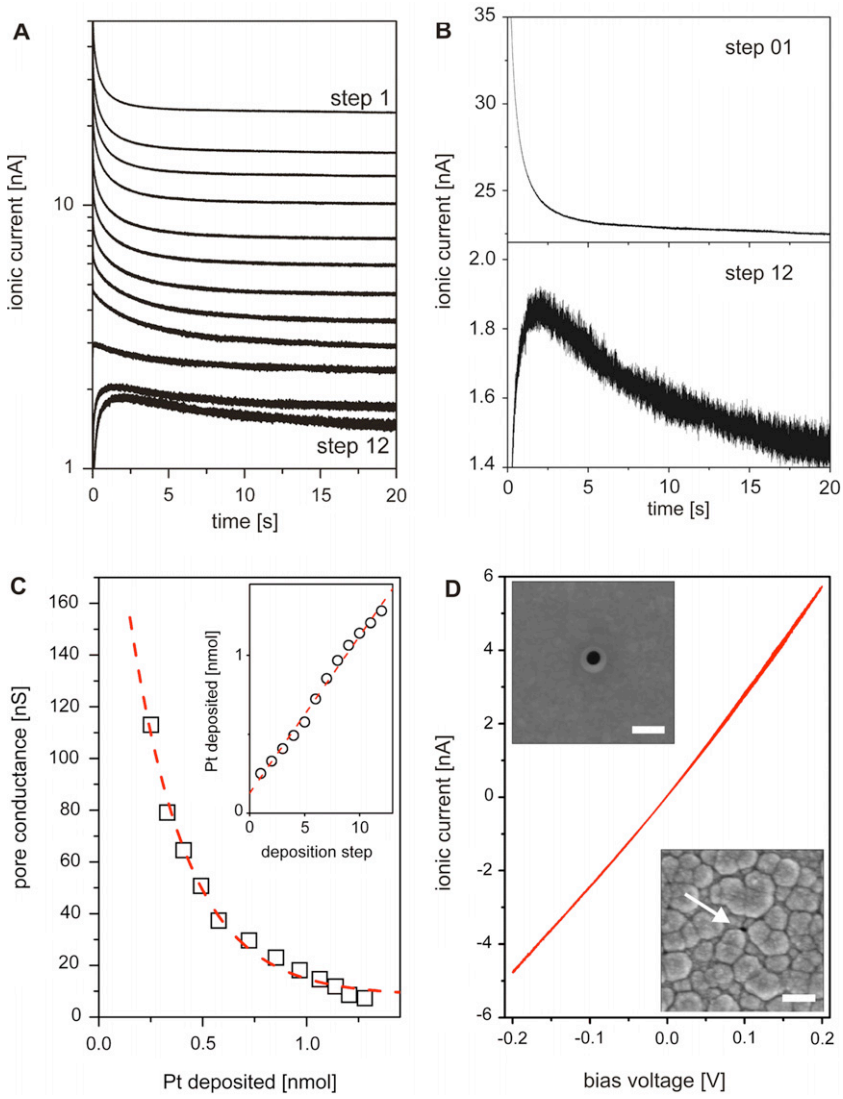


Figure 2. (A) Semi-logarithmic ion current/time $I_c(t)$ transient for 12 subsequent electrodeposition steps of 20 s duration each, from top to bottom (E(WE1) = +0.35 V versus CE/RE; V_{bias} = 0.2 V; 0.1 M KCl + 0.01 M K_2PtCl_4). (B) Enlarged plot of $I_c(t)$ for steps 1 and 12, respectively (linear scale). (C) Pore conductance G as determined from I_c at t = 20 s versus the amount of Pt deposited. G decreases exponentially with a characteristic decay coefficient of 2.7×10^{-10} mol^{-1} (dashed red line). Inset: total amount of Pt deposited in steps 1–12. On average, 100 pmol of Pt were deposited during each step (linear fit (red dashed line), slope: 9.95×10^{-11} mol, intercept: 1.27×10^{-10} mol). (D) Characteristic I_c/V_{bias} plot for a Pt nanopore of ∼18 nm apparent diameter as determined from SEM imaging. The rectification ratio is close to 1 in the voltage range shown above. Insets: SEM images before and after electrodeposition (scale bar: 200 nm).

the process, concentration of Pt complex, and deposition overpotential), L could well be a factor of ten smaller if for example mass transport to the pore entrance is much more efficient than along the channel length or due to the local potential distribution, cf below for further discussion. Finally, our SEM imaging experiments so far only allow us to estimate the cross-sectional area of the pore, but do not reveal its three-dimensional structure (inc. roughness inside the pore), which in turn affect its charge transport properties. In any case, this finding does not affect the conceptual value of our approach. On the contrary, it may suggest that pores with very small effective channel length can be fabricated with this method.

In order to assess the device-to-device reproducibility; we compare three different data sets in figure 3, corresponding to three different nanopore chip devices. Devices 1 and 2 had an initial pore diameter of 100 nm (black squares and red circles), the former being the device discussed above and in figure 2. Device 3 had an initial pore diameter of 45 nm (blue triangles); all initial diameters were determined by SEM imaging. For better comparison, the amount of Pt deposited was normalized to the (geometric) electrode area (0.07 cm^2 for devices 1 and 2, 0.65 cm^2 for device 3).

In all cases, ln(G) decays linearly with the normalized amount of Pt deposited, as shown by the fits in figure 3(A). Devices 1 and 2 behave very similarly (slope m = −1.72 cm^2 nmol^{-1} (R^2 = 0.99) and −1.79 cm^2 nmol^{-1} (R^2 = 0.94), respectively), which is expected due their comparable initial dimensions and deposition conditions (deposition potential E(WE1) = +0.35 V versus CE/RE). This testifies to the good reproducibility of the technique.

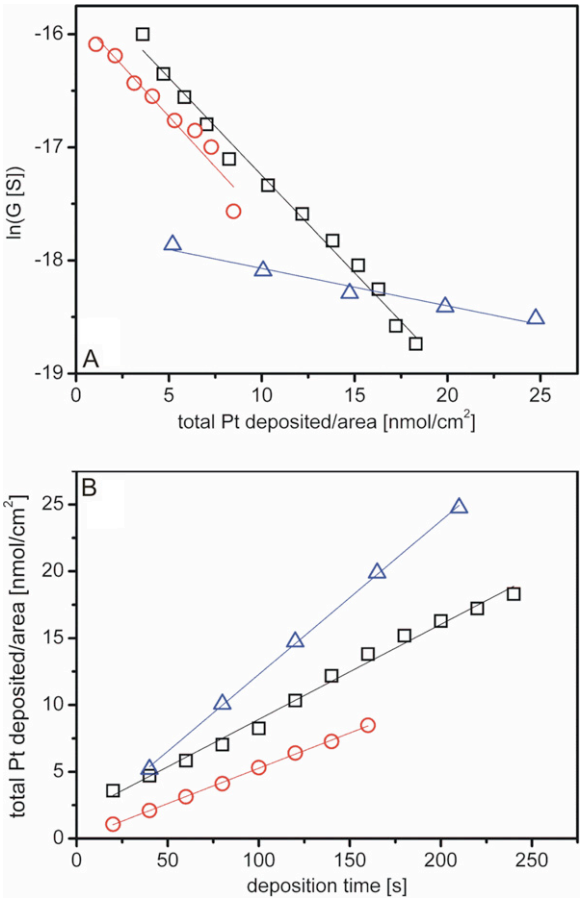


Figure 3. (A) Semi-logarithmic plot of the pore conductance G versus the amount of Pt deposited onto the membrane electrode (in nmol cm^{-2}), including linear fits. Devices 1 (black squares) and 2 (red circles): initial pore diameter = 100 nm; E(WE1) = +0.35 V versus CE/RE. Device 3 (blue triangles): initial pore diameter = 45 nm; E(WE1) = −0.25 V versus CE/RE. (B) Amount of Pt deposited cm^{-2} as a function of deposition time. The deposition rate for devices 1 (black squares) and 2 (red circles) are very similar (0.071 and 0.053 nmol cm^{-2} s^{-1}, respectively), which is expected due to the similar deposition conditions. In the case of device 3, however, the deposition rate is higher (0.107 nmol cm^{-2} s^{-1}), in accordance with the lower deposition potential.

However, in the case of device 3, the pore conductance decreases more slowly, despite the lower deposition potential (higher driving force) in this experiment (E(WE1) = −0.25 V). This is surprising, since using a lower (more negative) deposition potential, a faster deposition rate and pore shrinking is expected. However, this turns out to be the case, when comparing the amount of deposited Pt (over the whole membrane) versus the deposition time, as in figure 3(B). Again, devices 1 and 2 display similar behavior with deposition rates of 0.071 and 0.053 nmol cm^{-2} s^{-1} respectively, while the rate is increased in the case of device 3 (0.107 nmol cm^{-2} s^{-1}). Even though more Pt is deposited over the whole membrane electrode for device 3, deposition around or inside the pore is less prominent, compared to devices 1 and 2.

The following estimate confirms that the growth conditions at the pore are significantly different compared to the membrane surface. Taking device 1 as an example, roughly 100 ± 5 pmol of Pt were deposited during each deposition step, cf above. Provided that this amount were deposited uniformly over the whole electrode area (0.07 cm^2); the increase in the Pt layer thickness would only amount to 0.13 nm (MW(Pt) = 195.084 g mol^{-1}; ρ(Pt) = 21.45 g cm^{-3}). Such a change in the pore dimensions would not be detected in the ion current measurement (d_{pore} = 20–100 nm; Δd < 1%). On the other hand, based on equation (1) and the experimental decrease in the pore conductance during one deposition step, figure 2(C), the change in pore diameter is much larger and on the order of 10 nm.

The origin of this effect is most likely rooted in the transport of reactants to the pore, but further studies are required to gain a full understanding of the complex interplay between the kinetics of the surface reaction and local mass transport. Importantly, the device fabrication strategy is functional in all three devices.

The same approach can also be used to uniformly shrink nanopores in an array format. The total pore conductance is then just the sum of the conductances of the individual pores and the feedback signal becomes insensitive to pore-to-pore variation. However, as we show in the supporting information (available at stacks.iop.org/JPhysCM/22/454128/mmedia), the pore shrinking is still quite uniform for arrays of up to 16 pores in total. We are confident that the array size can be scaled up further, as long as the field distribution across the membrane is homogeneous.

Finally, in order to evaluate the suitability of these Pt nanopores for applications in single-molecule biosensing, we performed translocation experiments using λ-DNA as a test system (48.5 kbp, c = 50 μg ml^{-1}; pore diameter: 18 nm; V_{bias} = 0.3 V). Figure 4 shows the results including statistical analysis based on 440 translocation events. This number is relatively low compared to other studies focusing on DNA analysis (Kasianowicz *et al* 2008), but deemed sufficient for a feasibility study presented here. Panel A (top) compares the ion current in the absence (black) and in the presence of λ-DNA (red). Upon introduction of the DNA, current blockade events become apparent. Prior to statistical analysis using a template search (cf inset, figure 4(B)), the current traces were filtered (8-pole Bessel, 2 kHz low pass) and background corrected manually.

The two-dimensional histogram, plotting the abundance of given blockade time and current values and their respective one-dimensional projections, is shown in figure 4(B). The translocation histograms peak at a translocation time of ∼4 ms and a blockage current of 0.5 nA (∼10% decrease). This corresponds to a translocation speed of 0.4 cm s^{-1}, which is slightly lower than the value of 2 cm s^{-1} reported by Branton *et al* under comparable translocation conditions for an Al_2O_3-modified Si_3N_4 nanopore (Chen *et al* 2004a, Venkatesan *et al* 2010). In the latter study, the Al_2O_3 layer reduced the electrical noise and improved the capture rate of DNA compared to an unmodified Si_3N_4 pore. Once again this highlights the importance of the surface properties. The observed slower DNA translocation rate in our device are attributed to the following two reasons: one is a reduced electric field in the pore region (due to a larger effective membrane thickness

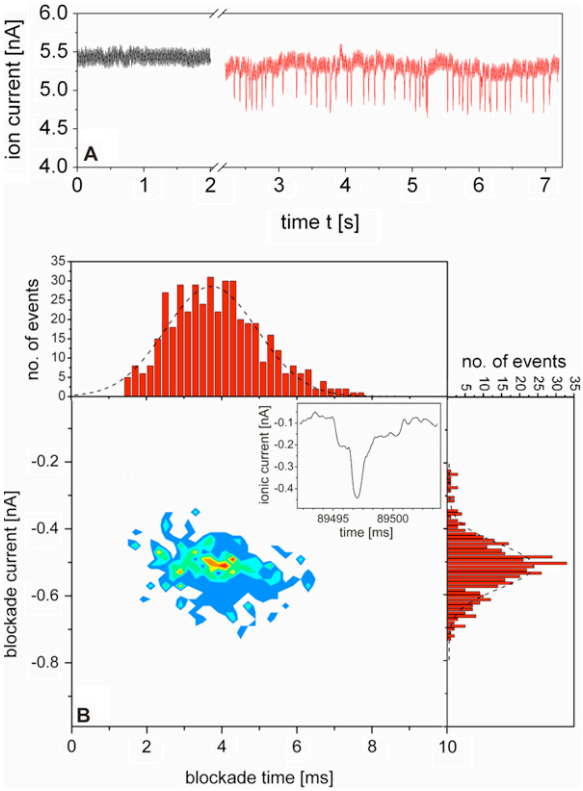


Figure 4. (A) Ion current/time trace before (black) and after introduction of λ-DNA, when blockage events start to occur. (B) 2D histogram of the translocation data (440 events; linear color scheme: one event (blue) to ten events (red) [grayscale: dark and light gray, respectively]) after a template search (inset), including 1D projections of blockage time and blockage current histograms, respectively. See main text for further details.

at the same bias voltage); the other involves interactions (i.e. adsorption) between the translocating DNA strand and the nanopore surface, which is known to be dependent on the potential of the metal surface (Demers *et al* 2002, Wanunu *et al* 2008). While the effective membrane thickness in our devices depends on the exact shape of the metal deposit and is not known accurately, comparison with Chen *et al* (2004a) seems to suggest that the observed difference could indeed be rationalized in terms of a reduced field strength at the nanopore. Branton *et al* specify the membrane thickness in the pore region to be on the order of 10 nm, which by linear extrapolation implies that the effective membrane thickness in our devices is approximately 50 nm, roughly in line with the characteristics of the deposition process. Future studies will address this point in more detail, namely by characterizing the three-dimensional geometry of the metallic pore and how far the potential applied to the membrane electrode affects DNA translocation (Demers *et al* 2002).

4. Conclusions

In conclusion, we show that bi-potentiostatic ion current feedback (ICF) control represents a new approach to fabricating metallic nanopores with diameters below 20 nm without being constrained to using very thin, potentially less stable membranes. Importantly, monitoring the nanopore conductance in real-time during the fabrication process and under '*in situ*' conditions allows for precise control of the final pore dimensions. The method applies to both individual nanopores as well as arrays.

With λ-DNA as a test system, we show that the metallic nanopores fabricated with the ICF approach can be used for single-biomolecule analysis and sensing. The results are in line with previous work, in terms of the translocation characteristics of the DNA, but also offer interesting prospects towards controlling the speed of translocating analytes by the potential applied to the metallic pore and surface modification.

Following on from the present proof-of-concept study, further work will be directed towards optimizing the deposition conditions to control the three-dimensional pore geometry (e.g. by optimizing mass transport to the edges of the pore) and the smoothness of the deposit; the deposition of materials other than Pt and composite materials (Cole *et al* 2009); as well as surface modification and functionalization.

Acknowledgments

This work is supported by the EPSRC, HFSP, and Royal Society. The authors would like to thank C Ahn, National NanoFab Center, Daejeon/Korea, for some support of the nanofabrication procedures. J Hong would like to acknowledge partial financial support by the Korea Research Foundation Grant funded by the Korean Government (KRF-2006-214-D00056).

References

Ai Y *et al* 2010 Effects of electroosmotic flow on ionic current rectification in conical nanopores *J. Phys. Chem.* C **114** 3883–90

Apel P Y *et al* 2001 Diode-like single-ion track membrane prepared by electro-stopping *Nucl. Instrum. Methods Phys. Res.* B **184** 337–46

Ayub M, Ivanov A, Instuli E, Cecchini M, Chansin G, McGilvery C, Hong J, Baldwin G, McComb D, Edel J B and Albrecht T 2010 Nanopore/electrode structures for single-molecule biosensing *Electrochim. Acta* **55** 8237–43

Branton D *et al* 2008 The potential and challenges of nanopore sequencing *Nat. Biotechnol.* **26** 1146–53

Chang H *et al* 2006 Fabrication and characterization of solid-state nanopores using a field emission scanning electron microscope *Appl. Phys. Lett.* **88** 103109

Chansin G A T *et al* 2007 Single-molecule spectroscopy using nanoporous membranes *Nano Lett.* **7** 2901–6

Chen P *et al* 2004a Probing single DNA molecule transport using fabricated nanopores *Nano Lett.* **4** 2293–8

Chen P *et al* 2004b Atomic layer deposition to fine-tune the surface properties and diameters of fabricated nanopores *Nano Lett.* **4** 1333–7

Cole R M *et al* 2009 Engineering SERS via absorption control in novel hybrid Ni/Au nanovoids *Opt. Express* **17** 13298–308

Deamer D W and Akeson M 2000 Nanopores and nucleic acids: prospects for ultrarapid sequencing *Trends Biotechnol.* **18** 147–51

Deamer D W and Branton D 2002 Characterization of nucleic acids by nanopore analysis *Acc. Chem. Res.* **35** 817–25

Dekker C 2007 Solid-state nanopores *Nat. Nanotechnol.* **2** 209–15

Demers L M *et al* 2002 Thermal desorption behavior and binding properties of DNA bases and nucleosides on gold *J. Am. Chem. Soc.* **124** 11248–9
Dimitrov V *et al* 2010 Nanopores in solid-state membranes engineered for single molecule detection *Nanotechnology* **21** 065502
Ervin E N *et al* 2008 Simultaneous alternating and direct current readout of protein ion channel blocking events using glass nanopore membranes *Anal. Chem.* **80** 2069–76
Fischbein M D and Drndic M 2007 Sub-10 nm device fabrication in a transmission electron microscope *Nano Lett.* **7** 1329–37
Gracheva M E *et al* 2006 Simulation of the electric response of DNA translocation through a semiconductor nanopore-capacitor *Nanotechnology* **17** 622–33
Gracheva M E *et al* 2007 p–n semiconductor membrane for electrically tunable ion current rectification and filtering *Nano Lett.* **7** 1717–22
Harrell C C *et al* 2006 Conical nanopore membranes: controlling the nanopore shape *Small* **2** 194–98
Hong J *et al* 2008 Design of a solid-state nanopore-based platform for single-molecule spectroscopy *Nanotechnology* **19** 165205
Howorka S *et al* 2001 Sequence-specific detection of individual DNA strands using engineered nanopores *Nat. Biotechnol.* **19** 636–9
Ives D J G and Janz G J (ed) 1961 *Reference Electrodes, Theory and Practice* (New York: Academic Press)
Kasianowicz J J *et al* 1996 Characterization of individual polynucleotide molecules using a membrane channel *Proc. Natl Acad. Sci. USA* **93** 13770–3
Kasianowicz J J *et al* 2008 Nanoscopic porous sensors *Annu. Rev. Anal. Chem.* **1** 737–66
Kim M J *et al* 2006 Rapid fabrication of uniformly sized nanopores and nanopore arrays for parallel DNA analysis *Adv. Mater.* **18** 3149
Kim M J *et al* 2007a Characteristics of solid-state nanometre pores fabricated using a transmission electron microscope *Nanotechnology* **18** 205302
Kim Y R *et al* 2007b Nanopore sensor for fast label-free detection of short double-stranded DNAs *Biosens. Bioelectron.* **22** 2926–31
Kovarik M L *et al* 2009 Effect of conical nanopore diameter on ion current rectification *J. Phys. Chem.* B **113** 15960–6
Li J *et al* 2001 Ion-beam sculpting at nanometre length scales *Nature* **412** 166–9
Lo C J *et al* 2006 Fabrication of symmetric sub-5 nm nanopores using focused ion and electron beams *Nanotechnology* **17** 3264–7
Meller A and Branton D 2002 Single molecule measurements of DNA transport through a nanopore *Electrophoresis* **23** 2583–91
Meller A *et al* 2000 Rapid nanopore discrimination between single polynucleotide molecules *Proc. Natl Acad. Sci. USA* **97** 1079–84
Mussi V *et al* 2010 DNA-functionalized solid state nanopore for biosensing *Nanotechnology* **21** 145102
Nagoshi K *et al* 2009 Direct fabrication of nanopores in a metal foil using focused ion beam with *in situ* measurements of the penetrating ion beam current *Rev. Sci. Instrum.* **80** 125102
Nilsson J *et al* 2006 Localized functionalization of single nanopores *Adv. Mater.* **18** 427
Nishizawa M *et al* 1995 Metal nanotubule membranes with electrochemically switchable ion-transport selectivity *Science* **268** 700–2
Park S R *et al* 2007 Fabrication of nanopores in silicon chips using feedback chemical etching *Small* **3** 116–9
Patterson N, Carter H V, Vasile M J, Adams D P, Chen Z and Brinker C J 2007 *Direct Focused Ion Beam Drilling of Nanopores* (Warrendale, PA: Materials Research Society Meeting)
Patterson N *et al* 2008 Controlled fabrication of nanopores using a direct focused ion beam approach with back face particle detection *Nanotechnology* **19** 235304
Petrossian L *et al* 2007 Fabrication of cylindrical nanopores and nanopore arrays in silicon-on-insulator substrates *J. Microelectromech. Syst.* **16** 1419–28
Polk B J *et al* 2004 Microelectroplating silver on sharp edges toward the fabrication of solid-state nanopores *J. Electrochem. Soc.* **151** C559–66
Ramirez P *et al* 2003 Synthetic nanopores with fixed charges: an electrodiffusion model for ionic transport *Phys. Rev.* E **68** 011910
Schenkel T *et al* 2003 Formation of a few nanometer wide holes in membranes with a dual beam focused ion beam system *J. Vac. Sci. Technol.* B **21** 2720–3
Schiedt B *et al* 2010 Direct FIB fabrication and integration of 'single nanopore devices' for the manipulation of macromolecules *Microelectron. Eng.* **87** 1300–3
Shim J H *et al* 2007 Glass nanopore-based ion-selective electrodes *Anal. Chem.* **79** 3568–74
Sigalov G *et al* 2008 Detection of DNA sequences using an alternating electric field in a nanopore capacitor *Nano Lett.* **8** 56–63
Siwy Z and Fulinski A 2004 A nanodevice for rectification and pumping ions *Am. J. Phys.* **72** 567–74
Siwy Z S and Howorka S 2010 Engineered voltage-responsive nanopores *Chem. Soc. Rev.* **39** 1115–32
Smeets R M M *et al* 2006 Salt dependence of ion transport and DNA translocation through solid-state nanopores *Nano Lett.* **6** 89–95
Soni G V *et al* 2010 Synchronous optical and electrical detection of biomolecules traversing through solid-state nanopores *Rev. Sci. Instrum.* **81** 014301
Storm A J *et al* 2003 Fabrication of solid-state nanopores with single-nanometre precision *Nat. Mater.* **2** 537–40
Storm A J *et al* 2005 Translocation of double-strand DNA through a silicon oxide nanopore *Phys. Rev.* E **71** 051903
Venkatesan B M *et al* 2009 Highly sensitive, mechanically stable nanopore sensors for DNA analysis *Adv. Mater.* **21** 2771
Venkatesan B M, Shah A B, Zuo J-M and Bashir R 2010 DNA sensing using nanocrystalline surface-enhanced Al_2O_2 nanopore sensors *Adv. Funct. Mater.* **20** 1266–75
Vlassiouk I *et al* 2009 Versatile ultrathin nanoporous silicon nitride membranes *Proc. Natl Acad. Sci. USA* **106** 21039–44
Wang G L *et al* 2006 Electrostatic-gated transport in chemically modified glass nanopore electrodes *J. Am. Chem. Soc.* **128** 7679–86
Wanunu M and Meller A 2007 Chemically modified solid-state nanopores *Nano Lett.* **7** 1580–5
Wanunu M *et al* 2008 DNA translocation governed by interactions with solid-state nanopores *Biophys. J.* **95** 4716–25
White R J *et al* 2007 Single ion-channel recordings using glass nanopore membranes *J. Am. Chem. Soc.* **129** 11766–75
Wu M Y *et al* 2005 Formation of nanopores in a SiN/SiO_2 membrane with an electron beam *Appl. Phys. Lett.* **87** 113106
Zhang B *et al* 2007 Bench-top method for fabricating glass-sealed nanodisk electrodes, glass nanopore electrodes, and glass nanopore membranes of controlled size *Anal. Chem.* **79** 4778–87

Electrochimica Acta 55 (2010) 8237–8243

Contents lists available at ScienceDirect

Electrochimica Acta

journal homepage: www.elsevier.com/locate/electacta

Nanopore/electrode structures for single-molecule biosensing

Mariam Ayub[a,b], Aleksandar Ivanov[a,b], Emanuele Instuli[a,b], Michael Cecchini[a,b], Guillaume Chansin[a,b], Catriona McGilvery[c], Jongin Hong[a,b], Geoff Baldwin[d], David McComb[c], Joshua B. Edel[a,b,**], Tim Albrecht[a,*,1]

[a] Imperial College London, Department of Chemistry, South Kensington Campus, Exhibition Road, London SW7 2AZ, UK
[b] Imperial College London, Institute of Biomedical Engineering, Exhibition Road, London SW7 2AZ, UK
[c] Imperial College London, Materials Department, Exhibition Road, London SW7 2AZ, UK
[d] Imperial College London, Division of Molecular Biosciences, Exhibition Road, London SW7 2AZ, UK

ARTICLE INFO

Article history:
Received 21 November 2009
Received in revised form 15 March 2010
Accepted 15 March 2010
Available online 23 March 2010

Keywords:
Nanopore sensing
Solid-state
DNA sequencing
Electrochemical nanoscience
Ion transport

ABSTRACT

Biological and solid-state nanopores have recently attracted much interest as ultrafast DNA fragment sizing and sequencing devices. Their potential however goes far beyond DNA sequencing. In particular, nanopores offer perspectives of single-molecule (bio)sensing at physiologically relevant concentrations, which is key for studying protein/protein or protein/DNA interactions. Integration of electrode structures into solid-state nanopore devices moreover enables control and fast switching of the pore properties, e.g. for active control of biopolymer transport through the nanopore. We present some of recent work in this area, namely the fabrication and characterization of nanopore/electrode architectures for single-(bio)molecule sensing. Specifically, we introduce a new technique to fabricate ultra-small metal nanopores with diameters smaller than 20 nm based on ion current feedback (ICF) controlled electrodeposition. It offers precise control of the pore conductance, is easily multiplexed, and can be extended to a wide range of different metals.

© 2010 Elsevier Ltd. All rights reserved.

1. Introduction

Biological and artificial 'solid-state' nanopores have attracted enormous interest over the past 15 years due to the potential to develop applications in 'stochastic' single-molecule biosensing [2–4]. Original research in this area focused around the electric recording of single ion channel activity embedded in biological membranes or lipid bilayers [5,6]; however, experiments in the mid 1990s indicated their potential for single-molecule biosensing applications in general, and DNA fragment sizing and sequencing in particular [7,8].

Biological nanopores comprise different classes of pore-forming proteins and protein assemblies, including ion channels, porins, and bacterial toxins. Alpha-hemolysin is a representative of the latter class and perhaps the most widely used model system in the area to date. The term 'solid-state' nanopore generally refers to nanometre-scale openings in solid-state membranes, e.g. made of glass, polymers or Si_3N_4 [2,3,9–26]. Depending on the membrane material, thickness and required pore size, different pore fabrication techniques have been employed, including electron and focused ion beams (FIB), and heavy ion bombardment/track etching.

For both biological and solid-state nanopores, the operating principle of a translocation experiment is the same: the membrane splits a fluidic system into two compartments, which only communicate through the small nanometre-sized opening in the membrane. These two compartments are filled with an electrolyte solution and contain one non-polarisable electrode each (e.g. Ag/AgCl electrodes for chloride containing electrolytes). By applying a constant voltage between the two electrodes, an electrochemical potential difference is established and a steady-state ion current flows through the cell. The resistance of the nanopore is usually large compared to the solution resistance; therefore, most of the (Faradaic) potential drop occurs at or in the vicinity of the pore. Ions and any other charged species, such as DNA or proteins, are transported according to this potential gradient. Once a protein or DNA molecule enters the pore, the effective pore conductance and thus the steady-state ion current changes (drops in most cases; see however [1]). When the species exits the pore again, the original ion current is re-established. The frequency, duration, amplitude and in some cases even the shape of the current/time trace of the blockage event can then be used to derive information about the translocation process and the

* Corresponding author. Tel.: +44 020 75943704.
** Corresponding author. Tel.: +44 020 759 40754.
E-mail addresses: joshua.edel@imperial.ac.uk (J.B. Edel), t.albrecht@imperial.ac.uk (T. Albrecht).
[1] ISE Member.

0013-4686/$ – see front matter © 2010 Elsevier Ltd. All rights reserved.
doi:10.1016/j.electacta.2010.03.051

translocating species itself [2,7,27]. This is very similar in spirit to the much older Coulter counter principle of voltage-driven transport through pores [28,29], but there are subtle, yet important differences for pore diameters in the low nanometre range. These include surface conductance effects, in addition to the bulk contribution, and explicit consideration of "chemical" interactions during biopolymer translocation, e.g. binding equilibria in the pore interior and chemical signatures in the current noise [30–39].

The translocation process itself is generally rather complicated and any comprehensive physical description has to take into account details of the ion transport process in solution (e.g. diffusion, electrokinetic and hydrodynamic effects), the pore geometry as well as the properties of the translocating biopolymer (these include but are not limited to, co- and counter ion effects; entropic effects; and polymer dynamics) [40–46].

The respective advantages and disadvantages of biological and solid-state nanopores will not be discussed in detail here. The reader is referred to the recent review by Howorka and Siwy for a deeper discussion and further references [3]. We will just briefly mention some important points, as far as they are deemed important in the present context.

Advantages of biological pores include the high reproducibility of the pore dimensions and geometry. This is essentially dictated by the protein's structure and self-assembly properties. The protein pores can easily be mass-produced via biochemical routes, including altering their amino acid composition by site-directed mutagenesis or chemical modification [27,47]. Due to the low capacitance of the lipid bilayer membrane, biological pores typically exhibit lower electrical noise, which is particularly important in detecting fast translocation events at low currents. The difficulties in working with biological pores lie in their controlled integration into the bilayer membrane, the protein mobility within the membrane (i.e. two-dimensional lateral diffusion), limited potential for multiplexing, the long-term stability of the device (inc. membrane), their integration into MEMS devices, e.g. with a view on applications in point-of-care diagnostics.

The advantages of solid-state pores are somewhat complementary and include increased device stability and better portability; flexibility in terms of the pore diameter and length; potential for multiplexing; and relatively straightforward routes to mass production of nanopore membranes. Device-to-device reproducibility is still not trivial for small solid-state nanopores (diameters < 5–10 nm); however, it is these dimensions which are most interesting for single-molecule biosensing applications. As a unique feature of solid-state nanopore membranes, further functionality can be added using micro- and nanofabrication techniques. For example electrode structures can easily be integrated to be localized at the pore interface. The surface properties of these electrodes can be modified by molecular self-assembly or switched externally. This can simply be done by modulating the pore charge applying a time-dependent gated field, or by the local generation of electroactive species. Such routes can be exploited for novel sensing applications [22,48–55].

Somewhat surprisingly, electrochemical approaches to nanopore fabrication and functionalisation have just begun to emerge and their full potential still remains to be explored [3,22,24,26,49,55]. In this paper, we give a brief overview of some of our work in this area and introduce a new electrochemical method for the fabrication of ultra-small metal nanopores, namely ion current feedback (ICF) controlled electrodeposition. ICF control allows for the preparation of metallic nanopores with a precise and pre-defined pore conductance, offering interesting perspectives towards the application of ultra-small metal pores in single-molecule biosensing.

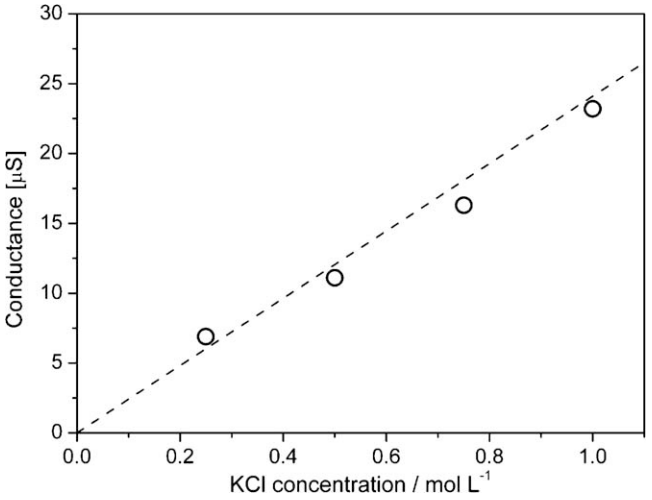


Fig. 1. Conductance of a 5150 nm × 75 nm × 250 nm ($w \times h \times L$) slit in a Si_3N_4 membrane as a function of KCl concentration (circles), including a theoretical estimate based on Eq. (1a) (n(KCl) = 6.02×10^{25} m^{-3}; $\mu_K = 7.616 \times 10^{-8}$ m^2/(V s); $\mu_K = 7.909 \times 10^{-8}$ m^2/(V s); [1] surface effects not included). The length and width were taken from SEM image (inset); the membrane thickness was estimated from the optical reflection of the Si_3N_4 layer.

2. A brief review of nanopore conductance

The ionic conductance of a nanopore can be expressed as the superposition of the bulk conductivity and the surface conductivity. The latter generally occurs for charged nanopores, where the surface charge is compensated by an equivalent amount of counterions in solution (excess charge). These counterions respond to an external electric field (electrophoresis) and add to the total pore conductance. Eq. (1) expresses the pore conductance G for a negatively charged cylindrical pore of high aspect ratio with a length (L) much greater than the diameter (d) immersed in a KCl containing electrolyte solution [1,40,56]:

$$G = \frac{\pi}{4} \cdot \frac{d^2}{L} \cdot (\mu_K + \mu_{Cl}) \cdot n_{KCl} \cdot e + \pi \cdot \frac{d}{L} \cdot \sigma \cdot \mu_K \quad (1)$$

where μ_K and μ_{Cl} are the electrophoretic mobilities of K^+ and Cl^-, n_{KCl} is the number density of K^+ or Cl^- ions, σ is the surface charge density and e the elementary charge. Note that the pore length nominally corresponds to the membrane thickness in our devices. A similar expression holds for slit geometries, where w and h are the width and height of the slit (cross-sectional area $= w \cdot h$) [40]:

$$G = \frac{w \cdot h}{L} \cdot n_{KCl} \cdot e \cdot (\mu_K + \mu_{Cl}) + 2 \cdot \frac{w}{L} \cdot \mu_K \cdot \sigma \quad (1a)$$

The agreement between the theoretically predicted values based on Eqs. (1) and (1a) and experimental data is surprisingly good [1]. This is illustrated in Fig. 1, which compares the experimental and theoretically expected conductance of a micrometer-sized rectangular opening as a function of KCl concentration, based on Eq. (1a) and the nominal dimensions of the slit in the Si_3N_4 membrane. Surface charge effects have been neglected in the calculation, due to the large size of the slit, cf. below for a more detailed discussion.

Note that Eq. (1) ignores any diffusive or convective contributions to the pore conductance, as well as ion/ion interactions. The latter potentially complicate matters significantly as they affect the effective concentration of the ions, their electrophoretic mobility (in both the bulk and surface contributions), and the surface charge density σ. Modifications to the theory are well established in the electrochemical literature and could readily be incorporated [40,57].

The contribution of surface effects to the total pore conductance depends on the pore dimension and the ionic strength of

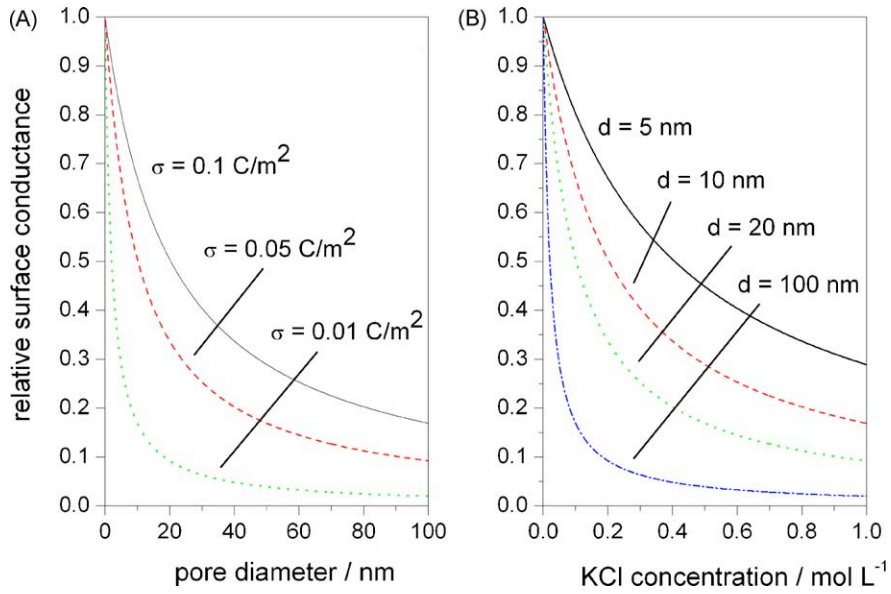


Fig. 2. Surface conductance relative to total pore conductance based on Eq. (1); (A) as a function of diameter for different surface charge σ (c(KCl) = 0.1 mol/L); (B) as a function of KCl concentration for different pore diameters d (σ = 0.1 C/m^2). L = 310 nm, $\mu_K = 7.616 \times 10^{-8}$ m^2/Vs, $\mu_{Cl} = 7.909 \times 10^{-8}$ m^2/Vs.

the electrolyte. This is illustrated in Fig. 2, which shows the relative contribution of the surface conductance as a function of pore diameter (panel A, c(KCl) = 0.1 mol/L) and KCl concentration (panel B, σ = 0.1 C/m^2), respectively, according to Eq. (1). For a given electrolyte concentration, the surface contribution decreases rapidly with increasing pore diameter and decreasing surface charge. This is expected from Eq. (1), where the bulk contribution scales with d^2, while the surface contribution scales only linearly with d. Even for large σ = 0.1 C/m^2, the latter contribution is smaller than 20% for pores on the order of 100 nm in diameter and the total conductance is dominated by the bulk (panel A).

At given σ, the surface contribution is large for small electrolyte concentrations and small pore diameters (panel B). For c(KCl) = 0.1 mol/L and $d \approx 20$ nm, which is the parameter range in the experiments shown below, this fraction is still on the order of 50% and thus cannot be neglected. Note that the Debye screening length is only about 1 nm under these conditions and thus significantly smaller than the pore diameter. Within this simple model, the length of the pore L does not affect the ratio between bulk and surface contribution (cf. Ref. [48] for a more elaborate treatment).

Moreover, the shape of the pore has an effect on the nanopore conductance. For a pore with radial symmetry and ignoring surface effects, the differential resistance can be expressed as

$$dR(z) = \frac{\rho}{\pi} \cdot \frac{dz}{r(z)^2} \tag{2}$$

ρ is the resistivity of the solution, r and z are the pore radius and the axial coordinate relative to the pore entrance, as defined in

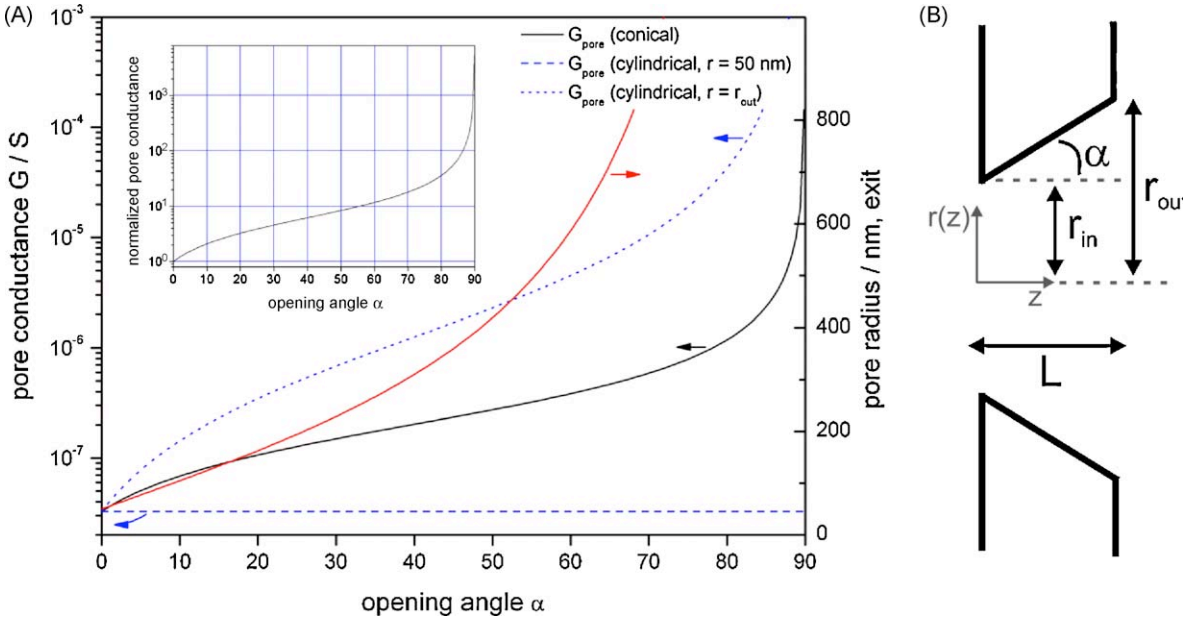


Fig. 3. (A) Pore conductance $G(\alpha) = 1/R(\alpha)$, Eq. (3), as a function of opening angle α (left ordinate, solid (black) line); pore radius r_{in} = 50 nm, L = 310 nm; c = 0.1 M KCl. Dashed and dotted (blue) lines: conductance of cylindrical pores with r = 50 nm and $r = r_{out}(\alpha)$, respectively. Right ordinate: pore radius at the "exit" side, depending on α. Inset: $G(\alpha)/G_{cyl}$ (r = 50 nm) for different α. (B) Illustration of the parameters in Eqs. (2) and (3). (For interpretation of the references to color in this figure legend, the reader is referred to the web version of the article.)

Fig. 3B. Integrating over the length L of the pore and introducing the opening angle α, the pore resistance R becomes [56]:

$$R(\alpha) = \frac{\rho}{\pi} \cdot \frac{L}{(r_{in} + L \cdot \tan(\alpha)) \cdot r_{in}} = \frac{\rho}{\pi} \cdot \frac{L}{r_{out} \cdot r_{in}} \quad (3)$$

r_{in} is the radius of the pore entrance and r_{out} the pore radius at the exit, $r_{out} = r_{in} + L \cdot \tan(\alpha)$.

With increasing opening angle α at constant "inner" pore radius r_{in}, the effective pore size and conductance increase as shown in Fig. 3A. For $r_{in} = 50$ nm and a pore length of 310 nm, the pore conductance approximately doubles for $\alpha = 10^{\circ}$; the "outer" pore radius has increased to $r_{out} = 105$ nm. Fig. 3A (inset) compares the expected conductance at given α, with the conductance of a perfectly cylindrical pore with $r = r_{in} = r_{out}$.

Thus, for small to moderate opening angles, the effect on the relative pore conductance is not large. Nevertheless, changes by a factor of 2–5 are not uncommon and the exact geometry of the pore needs to be taken into account when comparing experimental data with theoretical estimates.

3. Experimental

All chemicals used in this work were purchased from Sigma–Aldrich and of highest available purity grade, unless otherwise noted. For our electrodeposition experiments, free standing silicon nitride membranes (thickness: 250 nm) [58] were fabricated using standard photolithography, metalized by e-beam evaporation and etched by KOH wet etching as described elsewhere [59,60]. A 100 nm Au layer and 10 nm Ti or Cr adhesion layer was deposited on top of the membrane making the total membrane thickness 360 nm.

Nanopores were drilled into the membrane by bombarding the surface with Ga^+ ions using a focused ion beam (FIB, Carl Zeiss XB1540 Cross-Beam) at an acceleration potential of 30 kV and 1 pA and exposure time of 20–40 s. The beam diameter had a minimal width of 8 nm. The actual pore dimensions obtained are determined by SEM imaging from the top side and from the backside of the membrane. The membrane is then mounted into a flow cell using a glass platform and affixed with Kwik-Cast epoxy resin (World Precision Instruments). Electrodes are wire-bonded to an Au contact pad. The membrane platform is then sealed between two patterned PDMS chambers. Importantly, the pore is the only connection between the top and bottom reservoir, Fig. 4.

Prior to sealing, the nanopore membranes are flushed with ethanol and subjected to oxygen plasma for 2 min. This process removes any organic contaminants and enhances the hydrophilicity of the membrane surface. Alternatively, we have also used an equivalent, custom-built setup based on PTFE cells (cf. Fig. 1, inset); the results were the same within experimental error.

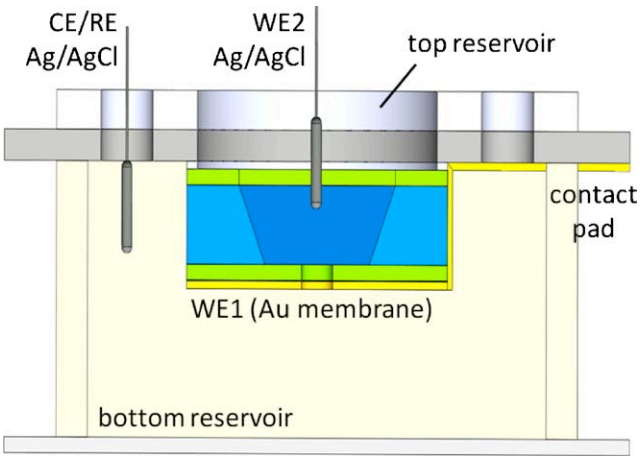


Fig. 4. Nanopore membrane devices in a bipotentiostatic configuration, side view. Epoxy resin around the Si layer was used for electrical insulation (not shown).

Electrochemical experiments, including pore conductance measurements, were performed on a CHI 760c bipotentiostat (CH Instruments, Austin, USA), Gamry Reference 600 potentiostats (Gamry, Warminster, USA) or an Axopatch 200B patch clamp instrument (Molecular Devices, Sunnyvale, USA). In the bipotentiostatic experiments, the Au coated nanopore membrane serves as working electrode 1 (WE1), while two newly prepared Ag/AgCl pseudo-reference electrodes were connected as working electrode 2 (WE2) and combined counter/reference electrode (CE/RE). A bias between WE2 and CE/RE establishes an ionic current, while electrodeposition of Pt on the membrane electrode is controlled separately by the potential of WE1. Platinum is deposited from a solution containing 0.01 M K_2PtCl_4 and 0.1 M KCl (Sigma–Aldrich, ACS grade) at room temperature according to $[PtCl_4]^{2-} + 2e^- \rightarrow Pt^0 + 4Cl^-$.

In this proof-of-principle study, we chose platinum as the depositing metal mainly because of its electrochemical inertness. This is an important factor, since we have observed corrosion effects for more reactive metals, such as Al, particularly close to the nanopore and at high ionic currents, Fig. 5. The composition of the plating bath was kept as simple as possible to avoid potential complications in the pore conductance measurements. Protocols providing smoother deposits are well known and could be implemented, if necessary [61].

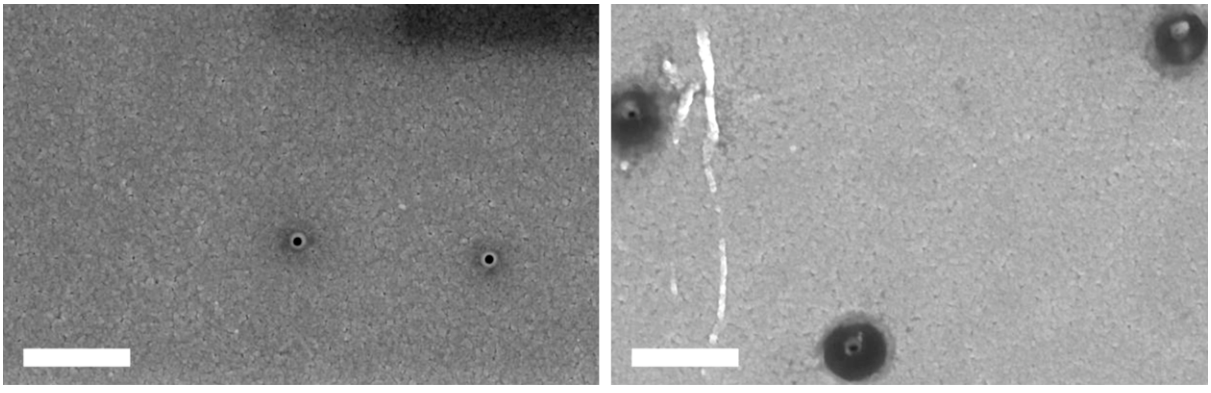


Fig. 5. SEM images showing corrosion effects. Si_3N_4/Al membrane with 100 nm wide pores, before (left) and after (right) several experiments in 1 mM KCl using Ag/AgCl electrodes at bias voltages up to 140 mV. The scale bar is 1 μm in both images.

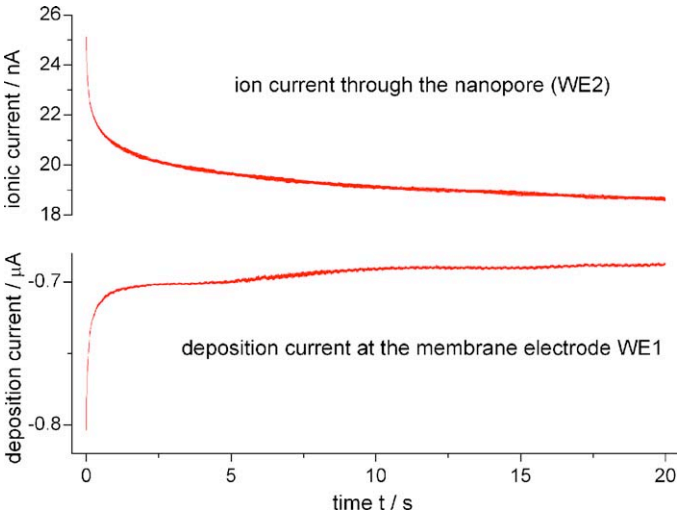


Fig. 6. Pore current and deposition current for a typical pore shrinking experiment under ICF control (upper and lower panel, respectively). Electrolyte: 0.1 KCl + 0.01 M $K_2[PtCl_4]$; bias voltage (WE2 vs. CE/RE) = 0.2 V; deposition potential E(WE1) = 0.35 V vs. CE/RE.

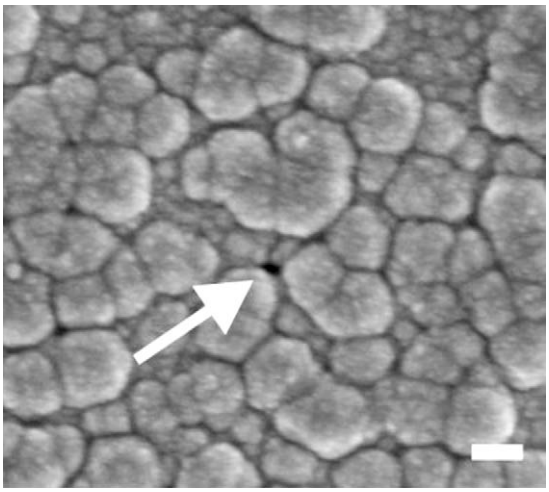


Fig. 7. SEM image of an electrodeposited Pt pore. Scale bar: 200 nm. Identification of the pore based on larger scale reference points.

4. Results and discussion

The bipotentiostatic configuration shown in Fig. 4 comprises an interesting feature that allows for feedback-controlled fabrication of electrodeposited metal pores. Since the potentials of the two working electrodes E(WE1) and E(WE2) are controlled independently with respect to a common reference electrode (CE/RE), a bias voltage between WE2 and CE/RE can be imposed to induce an ionic current governed by the conductance of the nanopore, while the potential of WE1 remains fixed. The potential gradient across the cell is maintained by conversion of chloride and AgCl at the Ag/AgCl electrodes, but all other ions in solution are transported through the pore accordingly. If no chemical reaction occurs on the membrane electrode WE1, its only contribution to the total current is due to (transient) capacitive charging. With $[PtCl_4]^{2-}$ present in solution, Pt deposition takes place, when E(WE1) is set to a sufficiently low value. The deposition of material on the membrane surface will decrease the pore diameter and alter the effective pore length. In accordance with Eq. (1), the nanopore conductance and the pore current decrease until the membrane is eventually covered with Pt and the pore fully blocked. Since the ionic current between CE/RE and WE2 can be monitored in real-time during the experiment, it can also be used as a feedback mechanism to stop the deposition process. This constitutes the basis of ion current feedback (ICF) controlled electrodeposition as a new and powerful tool to fabricate ultra-small (metallic) nanopores of pre-defined conductance. The new approach allows for the precise control of the fabrication process in real-time and has thus significant advantages over previously employed techniques to use metal deposition for this purpose [51,53,62]. The working principle is illustrated in Fig. 6, which shows the ion current across the nanopore for a typical deposition experiment (20 s step; upper panel) and the deposition current on the membrane electrode (WE1, deposition potential: 0.35 V vs. CE/RE; lower panel). The initial pore diameter and the membrane thickness were 80 and 360 nm, respectively. The ion current traces are composed of at least two phases: the first includes transient capacitive charging and equilibration of the deposition process (formation of a depletion layer), implying that more material is being deposited on the membrane during the first few seconds. The pore shrinking process subsequently enters a steady-state regime, where the pore conductance decreases with a constant rate (after ~5 s in Fig. 6).

The amount of Pt deposited during the experiment shown in Fig. 6 was determined by integrating the deposition current. No corrections were made for capacitive charging and Pt deposition was assumed to be the only Faradaic process occurring. On average, $14.3 \pm 1.4\,\mu C$ ($\pm 1\sigma$, on the basis of 8 deposition experiments) were deposited during a 20 s deposition step, corresponding to 74 pmol of Pt on a geometric electrode area of $7 \times 10^{-2}\,cm^2$. If metal deposition occurred homogenously over the whole membrane area, including the area around the pore, this would correspond to a Pt layer of ~1 nm in thickness. The current decrease shown in Fig. 6, however, suggests that the pore diameter has changed by approximately 20 nm (based on Eq. (1); L = const.), implying that the deposition around the pore is more efficient and in fact not homogeneous over the whole membrane area. SEM imaging data of the electrodeposited nanopores seem to confirm this hypothesis, also showing that the roughness of the deposit is on the same length scale as the pore diameter, Fig. 7. Further studies are on the way to elucidate the local potential distribution in or at the nanopore.

5. Conclusions

In order to exploit the full potential of solid-state nanopores for single-biomolecule sensing, precise control of the pore size and geometry is required. Various strategies have therefore been developed, for example based on electron beam-induced shrinking or expansion of the pore or feedback-controlled FIB milling [63,64]. The feedback mechanisms employed in those studies do not probe the ionic conductance of the pore, which is of key importance in a biosensing experiment in solution. This is a major strength of ICF-controlled electrodeposition, which rests on probing the ionic conductance of the pore directly. Moreover, it operates in real-time and under "*in situ*" conditions, i.e. in electrolytes that are very similar to those used in a biosensing experiment. Multiplexing the fabrication of many electrode devices in parallel appears to be straightforward and potentially cheaper than producing very small pores with FIB or electron beam drilling in a "high-throughput" fashion.

ICF-controlled electrodeposition has the potential to produce even single-digit nanometre pores. In fact, the reproducible fabrication of pores with a given ionic conductance in the relevant range (low nS) is relatively straightforward. However, in order to establish a quantitative relation between the measured ion current/pore conductance and the true physical dimension of the pore, a number of challenges remain. For example, since the pore con-

ductance depends on both pore diameter and length, the decrease in ion current during the electrodeposition process cannot solely be related to a change in only one of the two. In fact, two pores with the same ionic conductance may well have different three-dimensional shape and controlling the pore geometry is thus crucial. In addition, the roughness and/or crystallinity of the deposit is expected to affect the properties of the pore, particularly at small pore dimensions and low ionic strength, as well as the device-to-device reproducibility in single-molecule biosensing applications. Both factors depend on the growth conditions during the electrodeposition process. Refinement strategies are well known for Pt and numerous other metals and can readily be implemented to produce smoother deposits [61]. Interestingly, the optimization of the electrodeposition protocol has prospects of fabricating metal pores with varying aspect ratio A_{pore}/L_{pore} by controlling the rates of lateral and vertical growth during the deposition process. Devices with short effective channel length may perform better in fragment sizing applications, where the resolution appears to be limited by the membrane thickness.

For very small pores, it may become crucial to also consider the switching time of the device, i.e. the time constant of the membrane electrode. Ideally, the electrodeposition process is stopped instantaneously, when the ion current reaches the pre-defined value. In an experiment, however, the switching time is given by the electrode capacitance C (inc. any stray capacitance) and uncompensated resistance R in the electrochemical cell. Within this characteristic time R·C, the deposition process continues and may well close the nanopore completely. However, both R and C can be minimized using well-known strategies, for example by decreasing the electroactive area of the membrane electrode or optimizing the cell geometry.

Controlling the surface charge is another important parameter, which can however be varied systematically in the bipotentiostatic setup used in our experiments [22]. Future work will thus explore the influence of the surface charge and surface modification on the transport properties of the nanopore.

In summary, we have presented a brief overview of our recent work on the fabrication of electrode/nanopore structures for applications in single-molecule biosensing. Applying established electrochemical approaches, such as electrodeposition or bipotentiostatic control, in this new context offers a range of so far largely unexplored opportunities in electrochemical nanoscience and single-molecule sensing. We introduce ion current feedback (ICF) controlled electrodeposition as a new tool to fabricate ultrasmall metal nanopores with interesting perspectives towards fast switching of pore properties, deposition of a wide range of other electroactive metals, and surface modification.

Acknowledgements

The authors would like to thank Dr Chiwon Ahn, National NanoFab Centre, Dajeon/Korea, for support in some of the nanofabrication procedures. J. Hong was partially supported by the Korea Research Foundation Grant funded by the Korean Government (KRF-2006-214-D00056).

References

[1] R.M.M. Smeets, U.F. Keyser, D. Krapf, M.Y. Wu, N.H. Dekker, C. Dekker, Nano Letters 6 (2006) 89.
[2] C. Dekker, Nature Nanotechnology 2 (2007) 209.
[3] S. Howorka, Z. Siwy, Chemical Society Reviews 38 (2009) 2360.
[4] D. Branton, D.W. Deamer, A. Marziali, H. Bayley, S.A. Benner, T. Butler, M. Di Ventra, S. Garaj, A. Hibbs, X. Huang, S.B. Jovanovich, P.S. Krstic, S. Lindsay, X.S. Ling, C.H. Mastrangelo, A. Meller, J.S. Oliver, Y.V. Pershin, J.M. Ramsey, R. Riehn, G.V. Soni, V. Tabard-Cossa, M. Wanunu, M. Wiggin, J.A. Schloss, Nature Biotechnology 26 (2008) 1146.
[5] E. Neher, B. Sakmann, Nature 260 (1976) 799.
[6] B. Sakmann, E. Neher (Eds.), Single-Channel Recording, Plenum Press, New York, 1995.
[7] E. Brandin, D. Branton, D. Deamer, J. Kasianowicz, Proceedings of the National Academy of Sciences of the United States of America 93 (1996) 13770.
[8] M. Zwolak, M. Di Ventra, Reviews of Modern Physics 80 (2008) 141.
[9] K. Sint, B. Wang, P. Kral, Journal of the American Chemical Society 130 (2008) 16448.
[10] Z. Siwy, P. Apel, D. Baur, D.D. Dobrev, Y.E. Korchev, R. Neumann, R. Spohr, C. Trautmann, K.O. Voss, 7th International Conference on Nanometer-Scale Science and Technology (NANO-7)/21st European Conference on Surface Science (ECOSS-21), Malmo, Sweden, 2002, p. 1061.
[11] Z. Siwy, Y. Gu, H.A. Spohr, D. Baur, A. Wolf-Reber, R. Spohr, P. Apel, Y.E. Korchev, Europhysics Letters 60 (2002) 349.
[12] E.N. Ervin, R. Kawano, R.J. White, H.S. White, Analytical Chemistry 80 (2008) 2069.
[13] D. Klenerman, Y. Korchev, Nanomedicine 1 (2006) 107.
[14] Y.E. Korchev, C.L. Bashford, M. Milovanovic, I. Vodyanoy, M.J. Lab, Biophysical Journal 73 (1997) 653.
[15] J.D. Piper, R.W. Clarke, Y.E. Korchev, L.M. Ying, D. Klenerman, Journal of the American Chemical Society 128 (2006) 16462.
[16] H.S. White, A. Bund, Langmuir 24 (2008) 12062.
[17] R.J. White, E.N. Ervin, T. Yang, X. Chen, S. Daniel, P.S. Cremer, H.S. White, Journal of the American Chemical Society 129 (2007) 11766.
[18] B. Zhang, J. Galusha, P.G. Shiozawa, G.L. Wang, A.J. Bergren, R.M. Jones, R.J. White, E.N. Ervin, C.C. Cauley, H.S. White, Analytical Chemistry 79 (2007) 4778.
[19] E.R. Cruz-Chu, T. Ritz, Z.S. Siwy, K. Schulten, Faraday Discussions 143 on Soft Nanotechnology, London, England, 2009, p. 47.
[20] M. Davenport, A. Rodriguez, K.J. Shea, Z.S. Siwy, Nano Letters 9 (2009) 2125.
[21] C.C. Harrell, Z.S. Siwy, C.R. Martin, Small 2 (2006) 194.
[22] Y. He, D. Gillespie, D. Boda, I. Vlassiouk, R.S. Eisenberg, Z.S. Siwy, Journal of the American Chemical Society 131 (2009) 5194.
[23] K. Healy, B. Schiedt, Z. Siwy, A.P. Morrison, R. Neumann, 49th Annual Meeting of the Biophysical-Society, Long Beach, CA, 2005, p. 660A.
[24] E.B. Kalman, O. Sudre, I. Vlassiouk, Z.S. Siwy, Analytical and Bioanalytical Chemistry 394 (2009) 413.
[25] Z. Siwy, P. Apel, D. Dobrev, R. Neumann, R. Spohr, C. Trautmann, K. Voss, 5th International Symposium on Ionizing Radiation and Polymers (IRaP 2002), St Adele, Canada, 2002, p. 143.
[26] Z. Siwy, D. Dobrev, R. Neumann, C. Trautmann, K. Voss, Applied Physics A-Materials Science & Processing 76 (2003) 781.
[27] H. Bayley, L. Jayasinghe, Molecular Membrane Biology 21 (2004) 209.
[28] W. H. Coulter, "Means for counting particles suspended in a fluid", US patent US2656508 (A), 1953.
[29] R.W. Deblois, C.P. Bean, Review of Scientific Instruments 41 (1970) 909.
[30] M. Kotulska, S. Koronkiewicz, S. Kalinowski, 48th Annual Meeting of the Biophysical Society, Baltimore, MD, 2004, p. 383A.
[31] R.M.M. Smeets, U.F. Keyser, N.H. Dekker, C. Dekker, Proceedings of the National Academy of Sciences of the United States of America 105 (2008) 417.
[32] V. Tabard-Cossa, D. Trivedi, M. Wiggin, N.N. Jetha, A. Marziali, Nanotechnology 18 (2007).
[33] J.D. Uram, K. Ke, M. Mayer, ACS Nano 2 (2008) 857.
[34] A. Ridi, E. Scalas, A. Gliozzi, European Physical Journal E 2 (2000) 161.
[35] E. Scalas, A. Ridi, M. Robello, A. Gliozzi, Europhysics Letters 43 (1998) 101.
[36] F. Wohnsland, R. Benz, Journal of Membrane Biology 158 (1997) 77.
[37] O. Braha, B. Walker, S. Cheley, J.J. Kasianowicz, L.Z. Song, J.E. Gouaux, H. Bayley, Chemistry & Biology 4 (1997) 497.
[38] S. Cheley, H.Z. Xie, H. Bayley, Chembiochem 7 (2006) 1923.
[39] S. Howorka, S. Cheley, H. Bayley, Nature Biotechnology 19 (2001) 636.
[40] R.B. Schoch, J.Y. Han, P. Renaud, Reviews of Modern Physics 80 (2008) 839.
[41] S. van Dorp, U.F. Keyser, N.H. Dekker, C. Dekker, S.G. Lemay, Nature Physics 5 (2009) 347.
[42] Y. Rabin, M. Tanaka, Physical Review Letters 94 (2005) 4.
[43] L. Brun, M. Pastoriza-Gallego, G. Oukhaled, J. Mathe, L. Bacri, L. Auvray, J. Pelta, Physical Review Letters 100 (2008) 4.
[44] M. Muthukumar, Annual Review of Biophysics and Biomolecular Structure 36 (2007) 435.
[45] M. Pastoriza-Gallego, G. Gibrat, B. Thiebot, J.M. Betton, J. Pelta, Biochimica et Biophysica Acta-Biomembranes 1788 (2009) 1377.
[46] J.B. Heng, A. Aksimentiev, C. Ho, P. Marks, Y.V. Grinkova, S. Sligar, K. Schulten, G. Timp, Biophysical Journal 90 (2006) 1098.
[47] G. Maglia, M.R. Restrepo, E. Mikhailova, H. Bayley, Proceedings of the National Academy of Sciences of the United States of America 105 (2008) 19720.
[48] C. Amatore, I.O. Alexander, I. Svir, Chemphyschem 10 (2009) 211.
[49] M. Nishizawa, V.P. Menon, C.R. Martin, Science 268 (1995) 700.
[50] K.Y. Chun, S. Mafe, P. Ramirez, P. Stroeve, Chemical Physics Letters 418 (2006) 561.
[51] P. Ramirez, S. Mafe, V.M. Aguilella, A. Alcaraz, Physical Review E 68 (2003) 8.
[52] Z. Siwy, I.D. Kosinska, A. Fulinski, C.R. Martin, Physical Review Letters 94 (2005) 4.
[53] Z. Siwy, L. Trofin, P. Kohli, L.A. Baker, C. Trautmann, C.R. Martin, Journal of the American Chemical Society 127 (2005) 5000.
[54] A.A. Kornyshev, Soviet Electrochemistry 24 (1988) 385.
[55] M.E. Gracheva, D.V. Melnikov, J.P. Leburton, ACS Nano 2 (2008) 2349.
[56] Z. Siwy, A. Fulinski, American Journal of Physics 72 (2004) 567.

[57] A.K.N.R. John, O'M. Bockris, Modern Electrochemistry, Plenum Press, New York, 1998.
[58] J. Henrie, S. Kellis, S.M. Schultz, A. Hawkins, Optics Express 12 (2004) 1464.
[59] G.A.T. Chansin, R. Mulero, J. Hong, M.J. Kim, A.J. Demello, J.B. Edel, Nano Letters 7 (2007) 2901.
[60] M.J. Kim, B. McNally, K. Murata, A. Meller, Nanotechnology 18 (2007).
[61] C.R.K. Rao, D.C. Trivedi, Coordination Chemistry Reviews 249 (2005) 613.
[62] B.J. Polk, M. Bernard, J.J. Kasianowicz, M. Misakian, M. Gaitan, Journal of the Electrochemical Society 151 (2004) C559.
[63] J. Li, D. Stein, C. McMullan, D. Branton, M.J. Aziz, J.A. Golovchenko, Nature 412 (2001) 166.
[64] A.J. Storm, J.H. Chen, X.S. Ling, H.W. Zandbergen, C. Dekker, Nature Materials 2 (2003) 537.

Nanopore/electrode structures for single molecule biosensing

M. Ayub[*], A. Ivanov[*], E. Instuli[*], D. Godfrey[*], J. B. Edel[*,***], and T. Albrecht[*]

[*]Imperial College London, [*]Department of Chemistry, Exhibition Road, London SW7 2AZ, UK, t.albrecht@imperial.ac.uk
[**] Imperial College London, Materials Department, Exhibition Road, London SW7 2AZ, UK
[***]Imperial College London, Institute of Biomedical Engineering, Exhibition Road, London SW7 2AZ, UK

ABSTRACT

In this contribution we present some of our recent work on solid-state nanopores, the fabrication of nanopore/electrode structures and how these can be used for single-molecule biosensing applications (DNA, proteins etc.). Examples include bi-potentiostatic experiments with Au/Si_3N_4 nanopore membranes and a new way of fabricating small metal nanopores with diameters below 20 nm and well-defined pore conductance, based on electrodeposition and ion-current feedback control.

Keywords: solid-state nanopores, biosensing, single-molecule, electrodes, electrochemistry

1 INTRODUCTION

Solid-state nanopores have attracted enormous attention over the past 10-15 years with a view on single-molecule biosensing in general and high-throughput DNA sequence analysis in particular[1-3]. The idea is conceptually simple: A highly-insulating SiO_2, Si_3N_4 or polymer membrane with a nanometer-sized hole separates two compartments filled with electrolyte solution and the analyte of interest (e.g. DNA or proteins). The nanopore allows for ion transport across the membrane and is thus the only electric connection between the two reservoirs. One electrode is placed in each compartment and, upon application of an electric field, an ion current starts to flow. After some initial equilibration phase, this results in a steady-state ion current that is proportional to the conductivity of the electrolyte, the dimensions of the pore (cross-sectional area, channel length) and the magnitude of the electric field. Once an analyte molecule enters the pore opening, the conductance and thus the ion current is decreased. The ion current returns to the initial value, when the analyte molecule leaves the pore again - either into the opposite compartment ("translocation") or into the initial one. In the simplest case, this results in a telegraphic noise pattern in the current/time trace with distinct "on" and "off" states, corresponding to the open and partly blocked pore. In reality, however, the signal is often more complex and comprises molecular detail of the translocation event[4-5]. Accordingly, the idea of using biological or solid-state nanopores for DNA sequencing is based on resolving base-specific current modulations in real-time as the DNA translocates through the pore. With characteristic translocation times per base on the order of 1 µs and below, this opens up perspectives of a very simple and inexpensive high-throughput sequencing device. Unfortunately, plain nanopore devices have not been used successfully for DNA sequencing, partly due to the speed of the translocation process, the lack of specificity, and the low spatial resolution of the device.

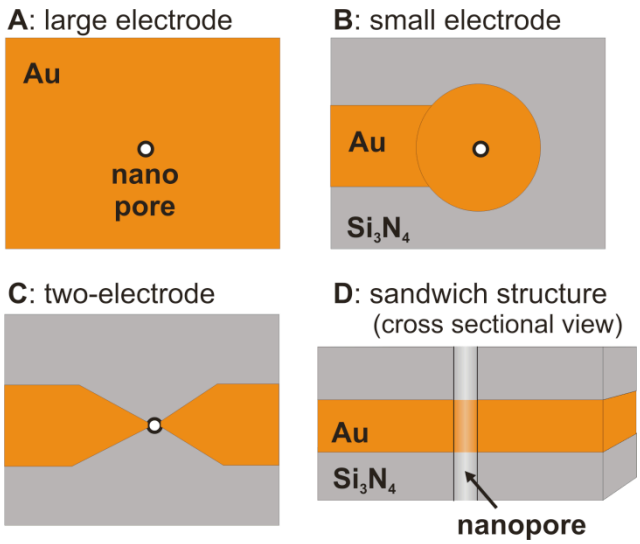


Figure 1: Electrode/nanopore architectures, schematic not to scale, A-C (top view) and D (cross-sectional view). In our devices, the nanopore diameter is 1-200 nm, the membrane thickness between 30 and 400 nm.

These three main issues are currently being addressed in different ways, for example by modifying the analyte or by modulating the properties of the pore itself. In this context, solid-state nanopores offer an advantage over biological pores: Since these devices are typically fabricated using semi-conductor processing technology (lithography, reactive ion etching etc.), semiconducting or metallic layers/electrodes can easily be integrated with the nanopore. Chemical modification using self-assembled monolayers or external electric switching of the surface properties is then straightforward, offering enhanced control of the translocation process (gating) or potentially even the

specificity required for DNA sequencing applications (aligned nanopore/tunneling junction devices)[6-15].

Depending on the application, however, the type of nanopore/electrode architecture is different. Figure 1 gives an overview of structures our research group has been working with recently, including large- and small-area single electrode devices, two-electrode junctions, and embedded electrode structures. After a short section on the physical basis of ion transport through nanopores, we will give examples of some experimental work using these devices.[16]

2 THEORETICAL BACKGROUND

In the simplest case, the current flow through the electrochemical cell can be modeled by an equivalent circuit composed of the solution resistance R_s, the pore resistance R_{pore} and the membrane capacitance C_{mem}, figure 2. C_{mem} can be convoluted by stray capacitance from the electrode leads and other sources; in principle, membrane composition, surface roughness and Faradaic reactions on the membrane surface can add further complications to the interpretation of C_{mem}. In these cases, C_{mem} may be replaced by a non-ideal capacitance, the constant-phase element or "CPE"[17].

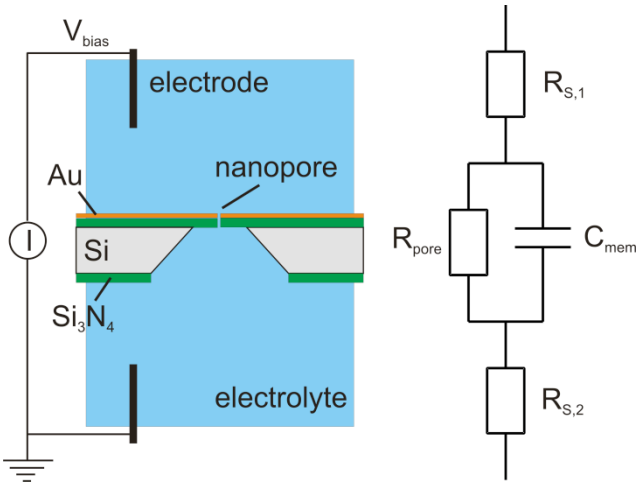


Figure 2: Electrochemical setup including an equivalent circuit. The membrane capacitance C_{mem} may be replaced by a CPE to accommodate for on-ideal capacitive behavior.

The electrodes are usually chosen to be non-polarizable, for example Ag/AgCl electrodes in rapid equilibrium with Cl^- ions in solution. This implies that the potential drop across the metal/solution interface is small and capacitive charging negligible. Charge transfer at the electrodes is rapid and thus not expected to be current-limiting (unless perhaps the electrodes are very small).

At constant bias voltage V_{bias}, the steady-state current passes through the resistive branch of the circuit and is governed by R_s and R_{pore}. Since usually $R_{pore} >> R_s$, the solution contribution can normally be neglected; most of the potential drop across the cell thus occurs at or in the nanopore ($V_{bias} = \Delta U_{s,1}+\Delta U_{pore}+\Delta U_{s,2}$):

$$V_{bias} = (R_{s,1} + R_{pore} + R_{s,2})\cdot I \approx R_{pore}\cdot I \qquad \text{eq. (1)}$$

To a good approximation, R_{pore} or its inverse, the pore conductance G_{pore} can be calculated based on a geometric model, taking into account the cross-sectional area of the pore A, the channel length L and the conductivity of the solution σ. For charged pores, an electric double layer forms to neutralize the charge on the inner pore walls. Under the influence of an electric field, these excess ions also contribute to the overall current, which is accounted for by the second term on the right-hand side of equation 3 (important for small pores). The latter is strictly valid for long cylindrical pores (i.e. diameter d << L), where the electric field lines can be considered to be in parallel, but it often provides a reasonable estimate for other geometries[18].

$$G_{pore} = \frac{\pi}{4}\cdot\frac{d^2}{L}\cdot\sigma + \pi\cdot\frac{d}{L}\cdot\sigma_S\cdot\mu_i \qquad \text{eq. (2)}$$

σ_S is the charge density on the inner pore walls and μ_i is the electrophoretic mobility of the counter ion(s), say K^+ in KCl electrolyte and $\sigma_S < 0$. Note that eq. (2) is written in terms of the absolute numerical value of σ_S.

In cases where an additional electrode is integrated with the nanopore, e.g. as the Au layer in figure 1, the potential of this electrode can be controlled externally. This modulates the surface charge density σ_S, although the actual value of σ_S depends on the potential of zero charge E_{pzc} and is thus material- and surface structure-dependent. The differential capacitance of the electric double C_{edl} takes into account the solvent dielectric constant, electrolyte concentration and charge, as well as electronic effects at the electrode/solution interface[19]. Provided the potential-dependence of C_{edl} is small, equation (2) can be re-written in terms of the (membrane) electrode potential E:

$$G_{pore}(E) = \frac{\pi}{4}\cdot\frac{d^2}{L}\cdot\sigma + \pi\cdot\frac{d}{L}\cdot\mu_i\cdot C_{edl}\cdot(E - E_{pzc}) \qquad \text{eq. (3)}$$

Thus, G_{pore} has a minimum at $E = E_{pzc}$ and increases linearly (but not necessarily symmetrically!) with E on both sides of E_{pzc}.

Depending on the charge of the pore, the relative contribution of the charged species in solution to the total current will vary. For example, cations will experience a higher activation barrier when entering a positively charged pore than anions, implying the latter carry a larger fraction of the current through the pore. This has been shown experimentally for ions[6] as well as for proteins [20].

When operated in bi-potentiostatic mode, the potential drop across the electrode/solution interface of two working electrodes can be controlled precisely and largely independently with respect to a common reference electrode. As a consequence, a constant V_{bias} between the

two Ag/AgCl electrodes may be maintained, while at the same time the membrane electrode is switched between electrochemically 'active' (deposition) and 'in-active' potentials (no deposition), respectively. This feature can, for example, be exploited to fabricate very small metallic nanopores by electrodeposition with pore conductance feedback, cf. below[16].

3 RESULTS

If the membrane electrode WE2 were an ideal polarizable electrode, no Faradaic process should occur at its interface and any change in applied potential results in interfacial charging. The current between the two (ideal non-polarizable) Ag/AgCl electrodes is then only affected by the effective charge of the nanopore surface, according to equation (3). In a real electrochemical system, however, charge transfer does occur at the electrode interface, depending on its potential, and may affect the current distribution in the cell. In order to test this effect, we performed a range of control experiments; some of which are shown in figures 3 and 4.

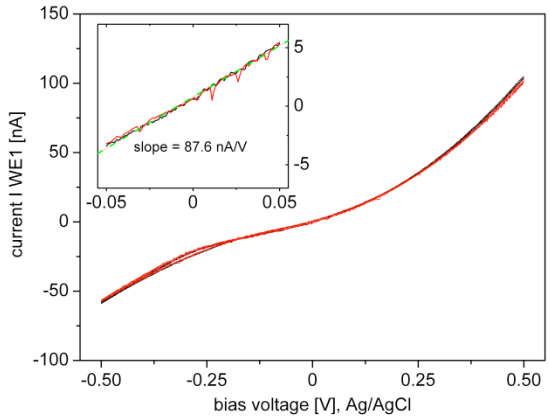


Fig. 3: Ion current between WE1 (Ag/AgCl) and CE/RE with the Au membrane electrode disconnected (black) and connected (red, no potential applied). Inset: The same data in the low V_{bias} region, inc. linear fit (green).

Figure 3 compares the ion current through a nanopore (diameter 110 nm) in a gold/Si_3N_4 membrane (thickness 310 nm), when the membrane electrode is disconnected (black) and connected, but without applying a potential (red). In the latter case, the potential drop between the membrane electrode and the solution is essentially determined by chemical equilibria, ion adsorption and so forth (open circuit potential, ocp).

As expected, there is no difference between the two curves within experimental error. The nanopore conductance amounts to 88 nS, as determined from the slope of the I/V_{bias} trace. This is somewhat higher than the theoretical value of ~ 50 nS obtained from equation (3) and may indicate that the (effective) channel length is smaller than the nominal value given above. Since Au and Si_3N_4 are likely to respond differently to the Ga^+ beam during the fabrication process, the pore shape may be considerably different from the cylindrical model geometry underlying equations (2) and (3). Work is currently ongoing to investigate this effect.

The same device was then investigated with the Au membrane electrode connected as WE2. This implies that the potentiostat will drive sufficient current through WE2 to maintain a pre-defined potential difference with respect to CE/RE.

Figure 4 displays the results for E(WE2) = 0 V: Panel A, current recorded at WE2 (Au membrane); panel B, current at WE1 (Ag/AgCl). The first set of data (black) was measured at the beginning of the experiment. The second set (green) was recorded after excursions to higher and lower E(WE2) and re-equilibration. The current through WE2 (panel A) is much larger than current through WE1 (panel B), due to the large size of the membrane electrode (and thus small resistance); it is however independent of the potential applied to WE1.

The current at WE1 is roughly linearly dependent on V_{bias}. The pore conductance was determined from the slope as before and amounts to 177 nS. This is approximately twice as large as the value determined previously and may be related to cross-talk between WE1 and WE2. The small, but significant off-set of I(WE1) at V_{bias} = 0 V of ~ -100 nA supports this hypothesis. Note that, even if E(WE2) = 0 V vs. CE/RE, I(WE2) is not necessarily zero, but rather depends on the presence of Faradaic processes at this potential.

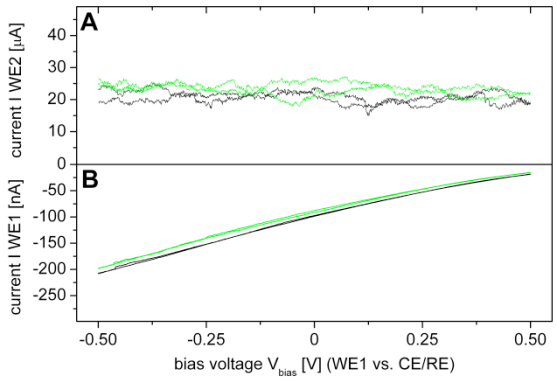


Fig. 4: Bi-potentiostatic experiment with E(WE2) = 0 V (1st dataset (black); 2nd data set (green)), V_{bias} is swept from -0.5 to + 0.5 V. Panel A: I(WE2), panel B: I(WE1).

The same approach can be used to control an electrochemical reaction on the surface. As an example, figure 5 shows a gold/Si_3N_4 nanopore membrane before and after electrodeposition of Pt from 10 mM $K_2[PtCl_4]$/0.1 M KCl solution. As long as E(WE2) is kept sufficiently high, no deposition takes place. When E(WE2) is lowered to below the reduction potential of $[PtCl_4]^{2-}$, however, the Pt

complex is reduced according to $[PtCl_4]^{2-} + 2e^- \rightarrow Pt^0 + 4Cl^-$ and Pt deposited onto the membrane. Interestingly, this also reduces the diameter of the pore allowing one to adjust the pore dimensions to a defined pore conductance *in situ*, i.e. by measuring the ion current through WE1[16].

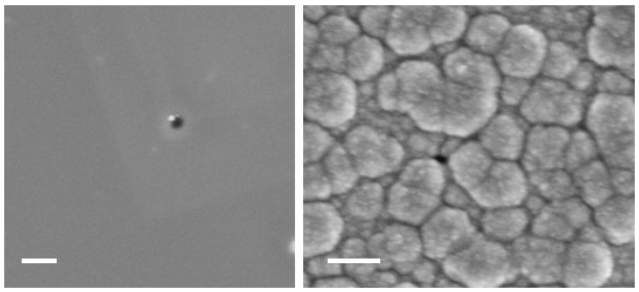


Figure 5: SEM images before (left, backside; magnification 100KX) and after Pt deposition (right, front side; magnification: 150KX). Scale bar: 200 nm

In the case shown above, the effective pore diameter was reduced from 95 nm to ~22 nm. The pore conductance of the Pt nanopore was determined to be 12 ± 3 nS (0.1 M KCl), which is in reasonable agreement with the expected value. In principle, the pore diameter could be reduced even further, offering a simple mechanism to fabricate (metallic) nanopores for single-molecule biosensing.

4 EXPERIMENTAL PROCEDURES

All chemicals used in this work were purchased from Sigma–Aldrich and of highest available purity grade, unless otherwise noted. For our electrodeposition experiments, free standing silicon nitride membranes (thickness: 250 nm) were fabricated using standard photolithography, metalized by e-beam evaporation and etched by KOH wet etching as described elsewhere[21-23]. A 100nm Au layer and 10nm Ti or Cr adhesion layer was deposited on top of the membrane resulting in a total membrane thickness of 360 nm. Nanopores were drilled into the membrane by exposing the surface to Ga^+ ions in a focused ion beam (FIB, Carl Zeiss XB1540 Cross-Beam; acceleration potential 30 kV, beam current 1 pA, exposure time of 20–40 s). The beam diameter had a minimal width of 8 nm. The actual pore dimensions obtained are determined by SEM imaging from the top side and from the backside of the membrane. The membrane is then mounted into a flow cell using a glass platform and affixed with Kwik-Cast™ epoxy resin (World Precision Instruments). Electrodes are wire-bonded to an Au contact pad. The membrane platform is then sealed between two patterned PDMS chambers. Prior to sealing, the nanopore membranes are flushed with ethanol and subjected to oxygen plasma for 2 minutes. This process removes any organic contaminants and enhances the hydrophilicity of the membrane surface. Alternatively, we have also used custom-built setup based on PTFE cells (not shown); the results were the same within experimental error. Electrochemical experiments were performed on a CHI 760c bipotentiostat (CH Instruments, Austin, USA) or on Gamry Reference 600 potentiostats (Gamry, Warminster, USA). In the bipotentiostatic experiments, the Au coated nanopore membrane serves as working electrode 2 (WE2), while two newly prepared Ag/AgCl pseudo-reference electrodes were connected as working electrode 1 (WE1) and combined counter/reference electrode (CE/RE).

REFERENCES

[1] J. J. Kasianowicz et al., Proc. Nat. Acad. Sci. USA, 93, 13770-13773, 1996

[2] C. Dekker, Nature Nanotechnol., 2, 209-215, 2007.

[3] D. Branton et al., Nature Biotechnology, 26, 1146-1153, 2008.

[4] J. Mathé et al., Biophys. J., 87(5) 2004.

[5] U. Bockelmann, V. Viasnoff, Biophys. J., 94(7), 2716-2714.

[6] Z. Siwy, S. Howorka, Chem. Soc. Rev., 39, 1115-1132, 2010.

[7] M. Nishizawa et al., Science, 268, 700-702, 1995.

[8] R. M. M. Smeets et al., Nano Lett., 6, 89-95, 2006.

[9] M. E. Gracheva et al., Nano Lett., 7, 1717-1722, 2007.

[10] G. Sigalovet al., Nano Lett., 8, 56-63, 2008.

[11] M. Di Ventra et al., Nano Lett., 6, 779-782, 2006; Zhang et al., Biophys. J. 91, L04–L06, 2006.

[12] D. Collins et al., Sensors and Actuators B: Chemical, 132, 593-600, 2008.

[13] T. Oshiro, Y. Umezawa, Proc. Nat. Acad. Sci. USA, 103, 10-14, 2006.

[14] H. Tanaka, T. Kawai, Nature Nanotechnol. 4, 518-522, 2009; M. Tsutsui et al., Nature Nanotechnol. 2010, DOI: 10.1038/NNANO.2010.42.

[15] S. Lindsay et al., Nat. Nanotechnol. 4, 297-301, 2009; S. Lindsay et al., Nanotechnology 2009, 20, 075102-075110; S. Lindsay et al., Nano Letters 2010, DOI: 10.1021/nl1001185.

[16] M. Ayub, et al., Electrochim. Acta 2010, doi:10.1016/j.electacta.2010.03.051, 2010.

[17] G. J. Brug et al., J. Electroanal. Chem., 176, 275-295, 1984.

[18] Z. Siwy, A. Fulinski, Amer. J. Physics, 72, 567-574, 2004.

[19] W. Schmickler, Chem. Rev. 96, 3177-3200, 1996.

[20] K. Y. Chun et al., Chemical Physics Letters, 418, 561-564, 2006.

[21] J. Henrie, S. Kellis, S.M. Schultz, A. Hawkins, Optics Express 12 (2004) 1464.

[22] G. A. T. Chansin et al., Nano Letters 7 2901-2906, 2007.

[23] M. J. Kim, B. McNally, K. Murata, A. Meller, Nanotechnology 18, 205302-6, 2007.